UNIVERSITÀ degli STUDI di CATANIA

IMM Istituto per la Microelettronica e Microsistemi
Consiglio Nazionale delle Ricerche

Molybdenum Disulfide Heterostructures

Preparation and Electronic transport

PhD Candidate
Salvatore Ethan Panasci

PhD Tutors
Prof. Franco Gelardi
Dr. Filippo Giannazzo
Prof. Simonpietro Agnello

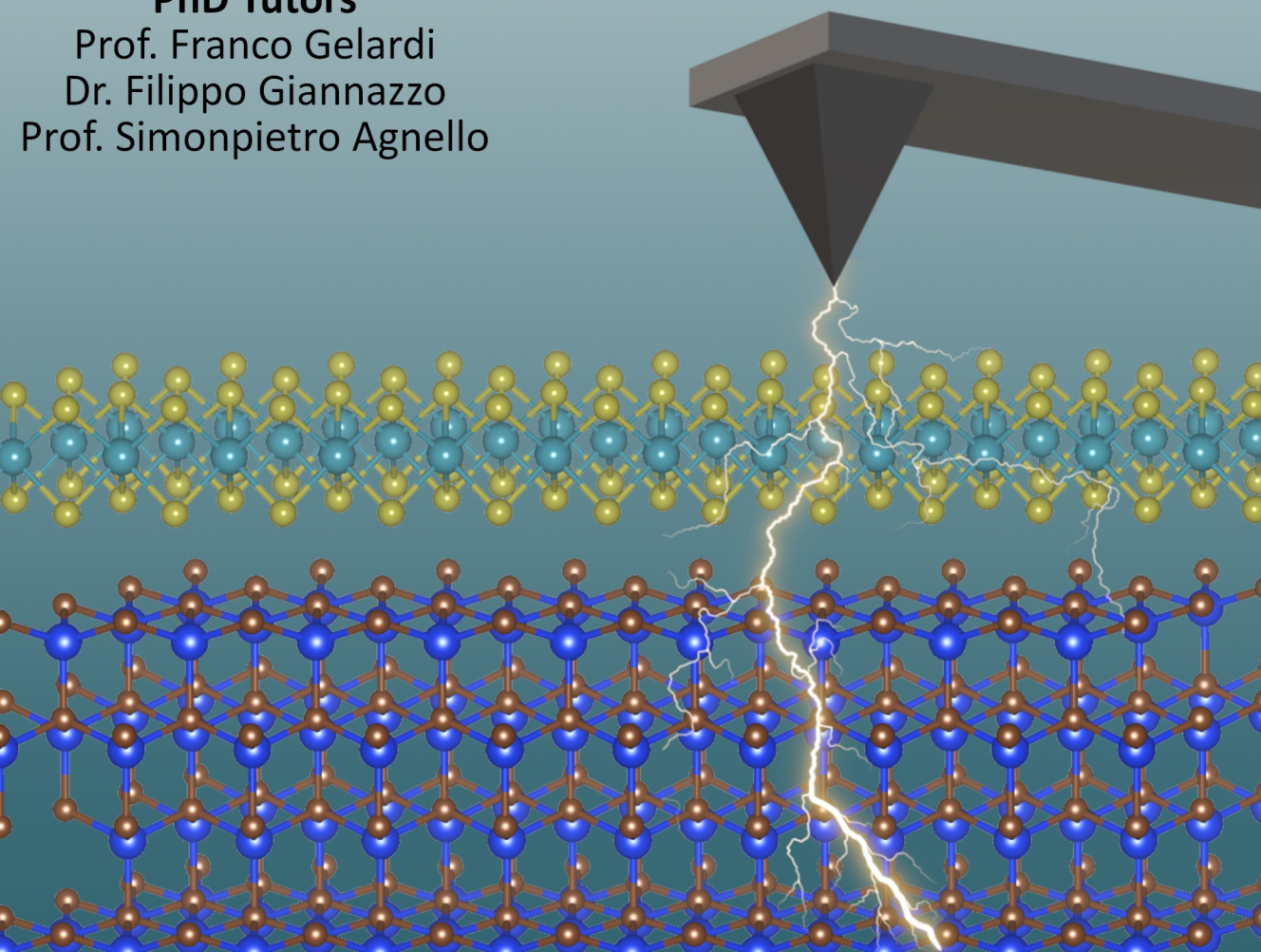

Università degli studi di Catania

Ph.D. Materials Science and Nanotechnology

XXXV cycle

Molybdenum disulfide heterostructures: preparation and electronic transport

Salvatore Ethan Panasci

Coordinator: Prof. G. Compagnini (UniCT)

Supervisors: Prof. F. M. Gelardi (UniPa)
Dr. F. Giannazzo (CNR-IMM, Catania)
Prof. S. Agnello (UniPa)

CONTENTS

List of Figures

List of Tables

List of Acronyms and physical variables

2D	Two-dimensional
3D	Three-dimensional
4H-SiC	4H polytype – Silicon Carbide
ABF	Annular Bright Field
Al_2O_3	Aluminium Trioxide
ALD	Atomic Layer Deposition
ARPES	Angle-Resolved inverse PhotoEmission Spectroscopy
Au	Gold
BG	Band Gap
BTBT	Band-To-Band Tunneling
C-AFM	Conductive Atomic Force Microscopy
CMOS	Complementary Metal Oxide Semiconductor
CVD	Chemical Vapor Deposition
DC	Direct current
DFT	Density Functional Theory
DT	Direct Tunneling
E_{BD}	Break-Down Electric-Field
EDS	Energy Dispersive X-ray Spectroscopy
E_F	Fermi Level Energy
E_G	Band-gap Energy
EOT	Equivalent Oxide Thickness
FBZ	First Brillouin Zone
FE	Field Emission
FET	Field-Effect Transistor
FFT	Fast-Fourier Transform
FIB	Focused Ion Beam
FL	Few Layers
FWHM	Full Width at Half Maximum
GaN	Gallium Nitride
GB	Grain Boundaries
GGA	General Gradient Approximation

Gr	Graphene
H_2O	Water
HAADF	High Angle Annular Dark Field
h-BN	hexagonal Boron nitride
HfO_2	Hafnium Dioxide
HfS_2	Hafnium Disulfide
I_d	Drain Current
InN	Indium Nitride
I-V	Current-Voltage
LED	Light Emitting Diode
MBE	Molecular Beam Epitaxy
Mo	Molybdenum
MOCVD	Metal-Organic Chemical Vapor Deposition
MoO_2	Molybdenum Dioxide
MoO_3	Molybdenum Trioxide
$MoO_{3-x}S_y$	Molybdenum (3-x)Oxide y-Sulfide
MoO_x	Molybdenum X-oxide
MoS_2	Molybdenum Disulfide
MOSFET	Metal-Oxide-Semiconductor Field-Effect Transistor
Nb	Niobium
NDR	Negative Differential Resistance
Ni	Nickel
PBE	Perdew-Burke-Ernzerhof
PL	Photoluminescence
PLD	Pulsed Laser Deposition
PMDS	PolyDiMethylSiloxane
PMMA	Poly (Methyl MethAcrylate)
Pt-coated	Platinum coated
ReS_2	Rhenium Disulfide
RHEED	Reflection High-Energy Electron Diffraction
RMS	Rout Mean Square
SEM	Scanning Electron Microscopy
Si	Silicon
SiO_2	Silicon Dioxide

STEM	Scanning Transmission Electron Microscopy
TAT	Trap-Assisted Tunneling
TEM	Transmission Electron Microscopy
TiS_2	Titanium Disulfide
TMD	Transition Metal Dichalcogenides
TRT	Thermal Release Tape
UV	Ultra-violet
VBM	Valence Band Maximum
V_d	Drain Voltage
vdW	van der Waals
V_G	Gate Voltage
V_s	Sulfur Vacancies
V_{th}	Threshold Voltage
V_{tip}	Voltage applied to the tip
WBG	Wide Band Gap
WS_2	Tungsten Disulfide
WSe_2	Tungsten Diselenide
XPS	X-Ray Photoemission Spectroscopy
ZrS_2	Zirconium Disulfide

INTRODUCTION

Two-dimensional (2D) materials represent one of the most widely investigated research topics in condensed matter physics in the last two decades. The history of this research field dates back to the pioneering experiments by the Manchester research group in 2004, leading to the first isolation of a single layer Graphene (Gr) by exfoliation from graphite and the discovery of its unique electronic properties. The subsequent international success for the Nobel prize awarded to Novoselov and Geim in 2010, generated explosive interest in the research of Gr and other 2D materials[1-6].

To date, the 2D materials family counts more than 150 components characterized by different physical properties for application in the Moore and More than Moore domains of electronics [7]. **Figure 0.1**(a) shows a table with the classification of 2D layered materials existing in nature as bulk crystals [1]. All these materials are characterized by strong in plane bonds and weak van der Waals (vdW) interaction

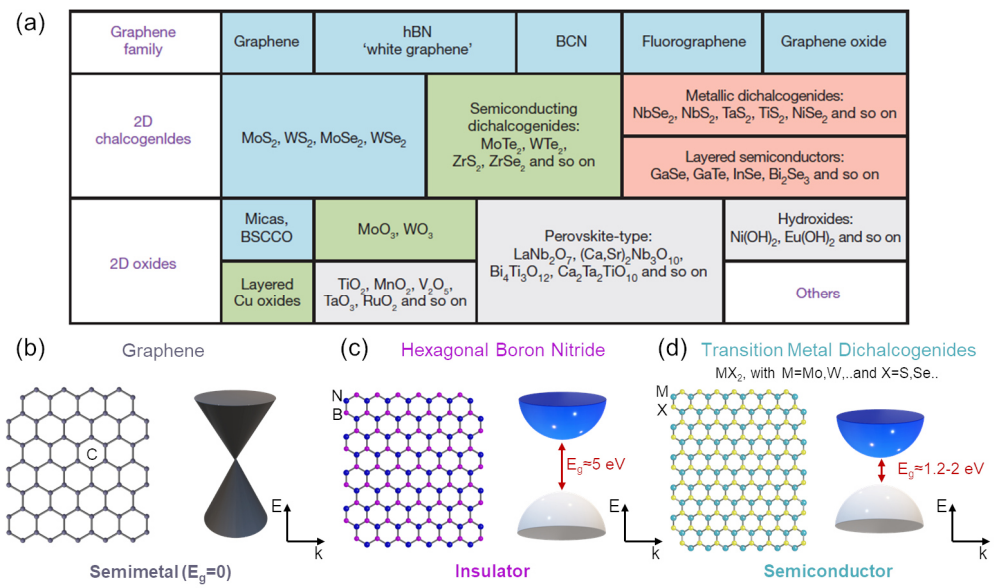

Figure 0.1.- (a) Current 2D materials library. Those monolayer materials stable in ambient conditions are shaded in blue, while those probably stable in air are shaded in green. The red squares represent monolayer unstable in air but stable in inert atmosphere and in the end the gray squares represent materials exfoliated from bulk to monolayers but of which there are not further information. (b) Graphene planar structures and its semimetal band structure. (c) Hexagonal Boron Nitride planar structure and its insulator band structure with a band gap of around 5 eV. (d) Monolayer Transition metal dichalcogenides 3D view and their semiconductive band structure with a band gap in a range between 1.2-2 eV. Fig.(a) reproduced from Ref. [1].

between the stacked layers of which they consist. Hence, single or few layers membranes can be exfoliated from the parent bulk crystals using the same approach initially used for Gr. Besides layered materials existing in nature in the bulk form, other 2D materials (commonly unstable under ordinary conditions) have been demonstrated in the last decade by using particular synthesis/deposition approaches on specific substrates. These include, among the others, the so-called X-enes, such as silicene (2D silicon) [8], germanene (2D germanium) [9], borophene (2D boron) [10], and MXenes (2D carbides/nitrides) [11].

From application perspectives, one of the most intriguing features of the 2D family is that it includes different materials covering the entire range of electrical properties, including semi-metals, semiconductors and insulators [1].

Graphene is the first and most popular example of 2D material with a semi-metallic electrical behaviour. In particular, its electronic structure is characterized by a valence and conduction bands with linear E-k dispersion relation (Dirac cones) merging in a single point (Dirac point), as illustrated in **Figure 0.1**(b). This peculiar electronic structure is at the origin of many unique physical properties of Gr, such as the high optical transparency in a wide wavelength range (interesting for optoelectronic applications) and the ambipolar behaviour of the transfer characteristics of Gr field effect transistors (FETs) with very high carrier (electrons/holes) mobility values (up to ~10^5 $cm^2V^{-1}s^{-1}$) [12]. The excellent mobility makes Gr FETs appealing for high frequency applications, requiring very fast modulation of electrical signals. On the other hand, the absence of a bandgap in the Gr bandstructure results in a small ratio between the on-state and off-state currents (I_{on}/I_{off}), making Gr FETs unsuitable for switching applications. Although strategies for opening a gap in the Gr energy bandstructure have been explored, including nanostructuring and functionalization treatments [13-15], the bandgap values obtainable by these approaches are in the range of ~300 meV and a degradation of the mobility with respect to ideal Gr values is typically observed [16-23].

The most widely investigated 2D material with insulating properties is the hexagonal Boron Nitride (h-BN), which exhibits an hexagonal planar structure analogous to the Gr one, with B and N atom replacing C atoms, as illustrated in **Figure 0.1**(c). Due to its atomically flat surface and excellent structural affinity to Gr, combined to the relatively high energy bandgap $E_g \approx 5$ eV, h-BN has been employed as the ideal insulating substrate or encapsulation layer for Gr, enabling the achievement of outstanding mobilities in Gr FETs, by suppressing roughness and charge-impurity scattering of electrons/holes [24-26].

Finally, the layered transition metal dichalcogenides (TMDs) are the most widely investigated semiconducting 2D materials. As illustrated in **Figure 0.1**(d), the individual TMD layer has the chemical formula MX_2, where M is the transition metal (6-fold coordinated) from groups IV B, V B, VI B, VII B (Ti, Zr, Hf, V, Nb, Ta, Mo, W, Tc, Re), sandwiched between two chalcogen atoms X (3-fold coordinated) from group VI A (S, Se, Te) [27,28]. Molybdenum disulfide (MoS_2) is the most widely investigated among layered TMDs. It can be found in nature with two semiconductor polytypes, i.e. the hexagonal 2H-MoS_2 and the rhombohedral 3R-MoS_2. Another polytype with metallic behaviour, i.e. 1T-MoS_2, can be obtained from 2H-MoS_2 using chemical treatments [29,30]. In the following, we will indicate as MoS_2 the 2H-MoS_2 phase, since it is the most widely investigated one. One of the peculiar properties of this polytype is the thickness dependent bandgap. In particular, bulk or few layers MoS_2 exhibit an indirect bandgap of 1.2 eV, whereas the monolayer counterpart shows a direct band gap of 1.8-1.9 eV [31,32]. These sizable bandgap values, combined to a decent carrier mobility (~400 $cm^2V^{-1}s^{-1}$ under proper conditions), make MoS_2 a promising candidate to replace Si in ultra-scaled thin films transistors. Owing to the direct bandgap, 1L-MoS_2 is also appealing for optoelectronic and photovoltaic applications. Furthermore, the large surface-to-volume ratio of 1L-MoS_2, its high flexibility and mechanical strength similar to Gr[33], make MoS_2 very remarkable to be employed in diverse fields, like sensing and photocatalysis [34-36].

The availability of a complete set of 2D materials with complementary electronic properties (semimetallic, insulator and semiconductors) has inspired research efforts aimed at the realization of electronic or optoelectronic devices based on artificial van der Waals (vdW) heterojunctions obtained by the sequential stacking of exfoliated flakes. Prototypes of functional devices entirely composed by 2D materials have been reported in the literature, including lateral field effect transistors, tunnel diodes, photodetectors and light emitting diodes [37-39]. Although this research field is highly appealing for basic studies and for the demonstration of new device concepts, this fabrication approach is not suitable for practical applications.

The following main requirements can be identified for future industrial applications of 2D materials in the fields of electronics and optoelectronics:

(i) the availability of optimized synthesis methods of 2D materials, enabling precise control of the thickness, crystalline quality, doping, strain on large area, i.e. from cm^2 scale to entire wafers;

(ii) the heterogeneous integration of 2D materials with bulk (3D) semiconductors commonly used in electronics, including silicon and wide-bandgap (WBG) semiconductors (SiC, GaN and related materials).

This thesis work will be focused on the investigation of 2H-MoS_2, as the main representative of the semiconducting TMDs family. In particular, some relevant top-down and bottom-up approaches have been developed for the production of uniform monolayer and few layer MoS_2 films suitable for electronic applications. Furthermore, the integration of MoS_2 with hexagonal WBG semiconductors (SiC and GaN) has been explored and the electronic transport across the interfaces of these heterostructures have been investigated [40-42]. Several complementary morphological, structural, electrical, chemical and optical characterizations both at micro and nanoscale have been employed in these experimental studies. The activities on MoS_2 preparation and integration with insulating and semiconductor substrates, and nanoscale morphological/electrical analyses based on scanning probe microscopy have been carried out at CNR-IMM in Catania, whereas photoluminescence and Raman spectroscopy investigations were carried out at the Department of Physics and Chemistry "E. Segrè" of the University of Palermo. Furthermore, the PhD thesis also took benefit of the involvement of the PhD student in the activities of the European Project "ETMOS: Epitaxial Transition Metal dichalcogenides Onto wide bandgap hexagonal Semiconductors for advanced electronics", which gave access to additional materials growth and characterization facilities.

The thesis is composed by the following 4 chapters:

Chapter 1 "Molybdenum Disulphide physical properties" will initially provide a basic overview of the structural properties, electronic transport behavior, optical emission, and vibrational properties of single and multilayer MoS_2.

Chapter 2 "Preparation methods and integration of MoS_2 for electronics" will describe the state-of-the-art preparation methods (top-down and bottom-up) of MoS_2 thin films for application in electronics. The peculiarities of each method, including advantages and disadvantages, will be discussed. Furthermore, the main challenges for the integration of MoS_2 with the state-of-the-art semiconductor materials used in electronics, Si and wide bandgap semiconductors (GaN and SiC), will be discussed. In particular, an overview of literature results on the physical properties of MoS_2/GaN and MoS_2/SiC heterostructures (e.g. band alignment) will be presented and examples of heterojunction diodes will be discussed. In the end, the beneficial

role of the high-κ integration on MoS_2 will be discussed, focusing on the main issues related to the Atomic Layer Deposition (ALD) on 2D materials.

Chapter 3 "Strain, doping and electric transport of large area MoS_2 exfoliated on gold and transferred on an insulting substrate" will present the experimental results obtained in this thesis on the preparation and characterization of large area MoS_2 membranes by the gold-assisted exfoliation method. It will be composed of four parts.

In the first part, the experimental method employed to obtain a monolayer of MoS_2 by mechanical exfoliation assisted by gold and the subsequent transferring on an insulting substrate (Al_2O_3) will be described.

In the second part, the vibrational and light emission properties of the MoS_2 membranes will be extensively investigated by μ-Raman and μ-Photoluminescence analyses, highlighting the effects of the substrates (Au and Al_2O_3) on the strain and doping of MoS_2.

In the third part, the vertical current transport in the MoS_2-Au system will be characterized by conductive atomic force microscopy (C-AFM), whereas the lateral current transport of 1L-MoS_2 on Al_2O_3/Si will be investigated by electrical analyses on a field-effect transistor.

In the final part, we will present the results on ALD of ultra-thin films (3-4 nm) of high-κ dielectrics (Al_2O_3) on 1L-MoS_2 exfoliated on gold and transferred onto an insulating substrate. In particular, the beneficial role of the Au-MoS_2 interaction on the nucleation and growth of uniform Al_2O_3 films on the dangling-bond free MoS_2 surface will be demonstrated. The excellent insulating properties of the dielectric film will be confirmed by C-AFM characterization.

Chapter 4 "Integration of large-area MoS_2 on wide-band gap semiconductors by sulfurization of ultrathin Mo film"

This final chapter reports the experimental results on the growth and characterization of ultra-thin (1L or 2L) films of MoS_2 on the surface of WBG semiconductors (4H-SiC and GaN) by a bottom-up method, consisting in the sulfurization of a pre-deposited Mo film. This approach was found to ensure uniform coverage on large area (up to wafer scale) by controlling the initial film thickness. This chapter is composed of three parts.

The first part is focused on the optimization of the Mo film deposition by sputtering and its morphological (AFM) and compositional analysis (XPS). This preliminary study allowed to define the optimal conditions of magnetron sputtering (time, current and pressure of deposition) for the reproducible deposition of ultrathin (1-2 nm) Mo films with a low roughness. Furthermore, XPS analyses revealed that the as-deposited films are completely oxidized in the form of MoO_x.

The second part is focused on the sulfurization process for the conversion of the ultrathin MoOx films deposited on a SiO_2 reference substrate to MoS_2. In particular, AFM and Raman analyses demonstrated that the controlled and reproducible growth of a single or bilayer MoS_2 by sulfurization of MoOx films with thickness from 1.1 to 1.8 nm at a temperature of 700°C.

In the third part, the integration of ultra-thin MoS_2 on SiC and GaN was investigated by applying these optimized sulfurization conditions. The structural and compositional properties of the vdW interfaces of MoS_2 on these WBG semiconductors have been investigated in detail by atomic resolution TEM analyses and by macroscopic XPS characterization, whereas the strain and doping distribution in the MoS_2 membranes was evaluated by Raman mapping. Finally, the vertical current injection at MoS_2 heterojunction diodes with n^- and n^+ doped 4H-SiC and with n- bulk GaN have been investigated by conductive atomic force microscopy. Some peculiar transport phenomena, like band-to-band tunneling (Esaki diode behavior) at the heterointerface between 1L-MoS_2 and n^+ SiC have been observed and modeled.

CHAPTER 1

MOLYBDENUM DISULPHIDE PHYSICAL PROPERTIES

As discussed in the Introduction, molybdenum disulfide (MoS_2) is the most investigated member of the 2D layered transition metal dichalcogenides (TMDs) family. Owing to the large abundance in nature of the molybdenite bulk crystal, its stability under ambient conditions, and its semiconductor behavior with a thickness dependent bandgap, MoS_2 is very interesting for electronics and optoelectronics applications, such as field-effect transistors (FETs), diodes and photodetectors.

This first chapter, composed by three different parts, is aimed to provide a basic overview on the physical properties of MoS_2.

In the first part, the structural properties of MoS_2, such as the vdW interaction between the layers and its polytypes will be treated.

In the second part, the electronic transport properties of semiconducting MoS_2 will be discussed considering the back-gated FET characteristics, and compared to those of semimetal graphene. Furthermore, some key aspects for the performance of MoS_2 transistors will be presented, such as the beneficial impact of the high-κ dielectrics deposition on top of MoS_2 on the carrier mobility, and the role of metal/MoS_2 contact resistance.

Finally, in the third part, the optical and vibrational properties of MoS_2 will be discussed, focusing on how they are affected by strain, doping and density of defects induced by the growth conditions or by the interaction with the substrates.

1.1 MoS_2 STRUCTURAL PROPERTIES

A single layer of MoS_2 is composed by a central Molybdenum (Mo) atom covalently bonded to two Sulphur (S) atoms, as shown in **Figure 1.1**(a). Multilayers of MoS_2 or bulk molybdenite crystals are formed by the stacking along the z-axis of several monolayers (**Figure 1.1** (b)) bonded by weak van der Waals (vdW) interactions, with typical energies of 0.1-10 kJ mol^{-1}, i.e. ~3 orders of magnitude lower than the intra-layer S-Mo-S covalent bonds (~10^2-10^3 kJ mol^{-1}) [43,44]. Hence, the vdW bonds can be overcome using an appropriate force, allowing the separation of single or few layers MoS_2 from bulk crystals, as in the scotch tape exfoliation method employed to separate Gr from graphite [45]. The vdW interaction between two atoms as a function of their distance can be described by the Lennard-Jones potential, as illustrated in **Figure 1.2**(a), where the energy minimum corresponds to the vdW distance (d_{vdW}) between the centres of the two interacting atoms at the equilibrium. Furthermore, the vdW gap (Δ_{vdW}) in layered crystals formed by two planes of atoms can be defined as:

$$\Delta_{vdW} \approx d_{vdW} - r_a - r_b \qquad (1)$$

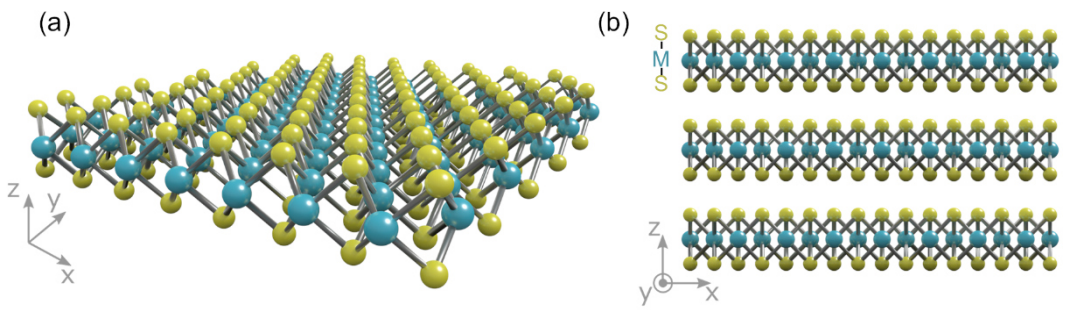

Figure 1.1.- Three-dimensional view of a MoS_2 single layer (a) and in a multilayer structure (b).

where r_a and r_b represent the covalent radius of the two atoms, as schematically illustrated in the insert of **Figure 1.2**(a).

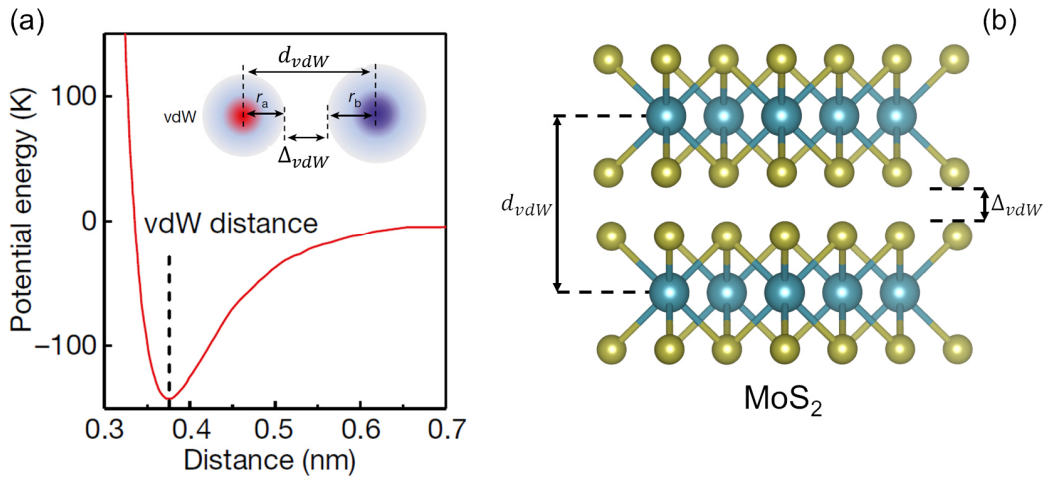

Figure 1.2.- (a) Lennard-Jones potential to model the vdW interaction between two atoms a and b. The vdW distance (d_{vdW}), corresponding to the minimum of the L-J potential, the covalent radius of the two atoms (r_a and r_b) and the vdW gap (Δ_{vdW}) are indicated in the insert of **Figure 1.2** (a). (b) 2L-MoS_2 cross section representation showing the vdW gap between the two adjacent sulphur atoms and the spacing between two consecutive molybdenum atoms. Fig.(a-b) reproduced from Ref. [43].

Figure 1.2(b) shows a schematic illustration of a bilayer of MoS_2, with the indication of the equilibrium distance between the two monolayers, corresponding to the spacing between the two rows of Mo atoms (~0.62 nm) [43], and of the vdW gap between the two adjacent S atoms (~0.18 nm) [43]. Generally, both the parameters show a certain variability for different 2D materials. Calculations carried out by Liu et al. [43] on different 2D materials, reported in the **Table 1**, show that MoS_2 exhibits similar values of the vdW gap to Gr and h-BN, whereas the spacing between Mo atoms in bilayer MoS_2 is clearly larger than the vdW distances in Gr and h-BN bilayers.

Material	Spacing	vdW gap
BN	0.33 nm	0.19 nm
Graphene	0.34 nm	0.20 nm
MoS_2	0.62 nm	0.18 nm

Table 1. – Summary of the spacing and vdW gap calculated for different 2D layered materials [43].

Layered MoS_2 can be found as three different polytypes (2H, 3R and 1T), which differ for the coordination of the sulphur atoms with respect to the central molybdenum atom within the layers or for the stacking order of the layers [46], as shown in **Figure 1.3**. For this reason, the polytypes are denoted by a number that identifies the number of layers per repeated unit and by a letter describing the crystallographic structure of the individual layers. In particular, the 2H-MoS_2 polytype presents hexagonal symmetry (H) with a trigonal prismatic Mo-S coordination within each layer and two layers per repeated unit . It is the most stable form of MoS_2 with lattice parameters $a = 3.15$ Å and $c = 12.30$ Å [47]. Instead, the 3R-polytype shows a rhombohedral symmetry with a trigonal prismatic Mo-S coordination and three layers per repeated unit. Its lattice parameters are $a = 3.17$ Å and $c = 18.38$ Å [47]. From the electronic point of view, these two polytypes are semiconductors. Finally, the 1T polytype presents a tetragonal symmetry with octahedral coordination and one layer per repeated unit. Its lattice parameters are $a = 5.60$ Å and $c = 5.99$ Å [47]. Differently from the 2H- and 3R-MoS_2 semiconductor polytypes, the 1T-polytype exhibits a metallic behaviour. Furthermore, it is a metastable form commonly not found in nature, which can be obtained by chemical treatments [48-50]. As an example, it has been demonstrated that the typical semiconducting 2H- or 3R- crystallographic phases can be converted into the metallic 1T- one through a Lithium intercalated chemical exfoliation

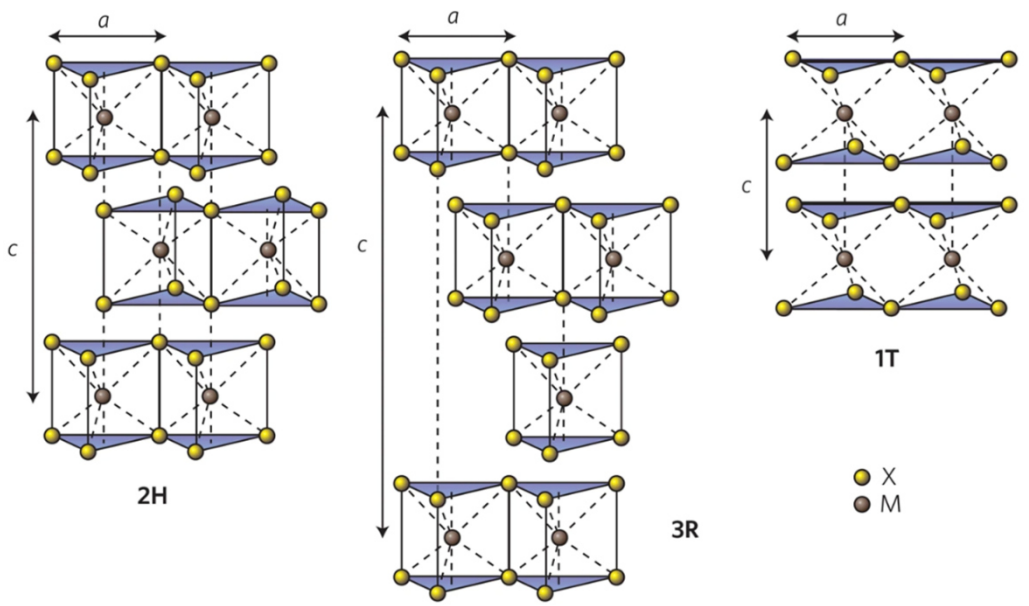

Figure 1.3- MoS_2 polytypes: hexagonal (2H), rhombohedral (3R) and tetragonal (1T) symmetry. Figure reproduced from Ref. [174].

approach[29,30]. This phase transition process is reversible by an annealing process at 300° C, which restores the Mo coordination from the octahedral (1T-) to the trigonal prismatic (2H) one[29]. **Table 2** resumes the features for each MoS_2 polytypes.

In the following, the discussion will be focused on the semiconductor 2H-MoS_2 phase. Concerning the mechanical properties, freestanding 1L-MoS_2 shows exceptional high in-plane stiffness corresponding to an effective Young modulus of 270±100 GPa, comparable to that of steel. Indeed, it shows a breaking strength of 15±3 Nm^{-1}, namely it breaks after the application of a strain in a range between 6-11%. The highest values are obtained when the material is highly crystalline in absence of defects. These peculiar features make it suitable also for flexible electronic applications and incorporation in composites[3,51].

Polytype	Stacking order	Lattice parameters	Mo-S coordination	Symmetry	Point Group	Physical properties
2H-MoS_2	AbA BaB	a= 3.15 Å c= 12.30 Å	Trigonal Primastic	Hexagonal	D_{3h}	Semiconductive
3R-MoS_2	AbA BcB CaC	a= 3.17 Å c= 18.38 Å	Trigonal Primastic	Rhombohedral	D_{3h}	Semiconductive
1T-MoS_2	AbC	a= 5.60 Å c= 5.99 Å	Octahedral	Tetragonal	O_h	Metallic

Table 2.- Summarized MoS_2 polytypes characteristics: stacking order, lattice parameters, Mo-S coordination, symmetry, point group and physical properties. Reproduced from Ref. [47].

1.2 MOLYBDENUM DISULFIDE ELECTRONIC TRANSPORT PROPERTIES

The electronic transport properties of single or few layer 2H-MoS_2 membranes have been the object of high research interests in the last decade, owing to their semiconducting behaviour, which is highly promising for the replacement of silicon in the next generation of ultra-scaled field effect transistors (More Moore applications) [7], as well as for novel device concepts with advanced architectures and functionalities (More than Moore applications) [7].

Since the first pioneering studies on Gr, the back-gated transistor configuration has been adopted as the easiest approach to evaluate the electronic transport in atomically thin 2D materials by investigating the field effect modulation of their conductivity [52]. In its most basic implementation, the back-gated FET was fabricated on a highly doped Si substrate coated by an insulating film (e.g. SiO_2, or high-κ dielectrics, such

as Al_2O_3, HfO_2,..), working as the back-gate contact and gate insulator, respectively. The 2D materials were exfoliated or deposited on the insulating film, with properly chosen thickness to maximize the visibility of the ultra-thin 2D membranes by optical interference contrast. Source and drain metal contacts were finally deposited on the 2D material channel, allowing to probe the conductivity variation as a function of the back-gate electric field.

To illustrate the different transport properties between a semi-metallic and a semiconducting 2D material, two back-gated FETs with Gr and 1L-MoS_2 channels are illustrated in **Figure 1.4**(a,b) respectively, while the comparison between two typical transfer characteristics (i.e. the drain current I_d vs the backgate bias V_{bg} for a fixed value of the drain voltage V_d) of the two devices is reported in **Figure 1.4** (c-d). These experimental curves are taken from the pioneering papers of Lemme et al. [53] and Radisavljevic et al. [2] on Gr and 1L-MoS_2 field effect transistors.

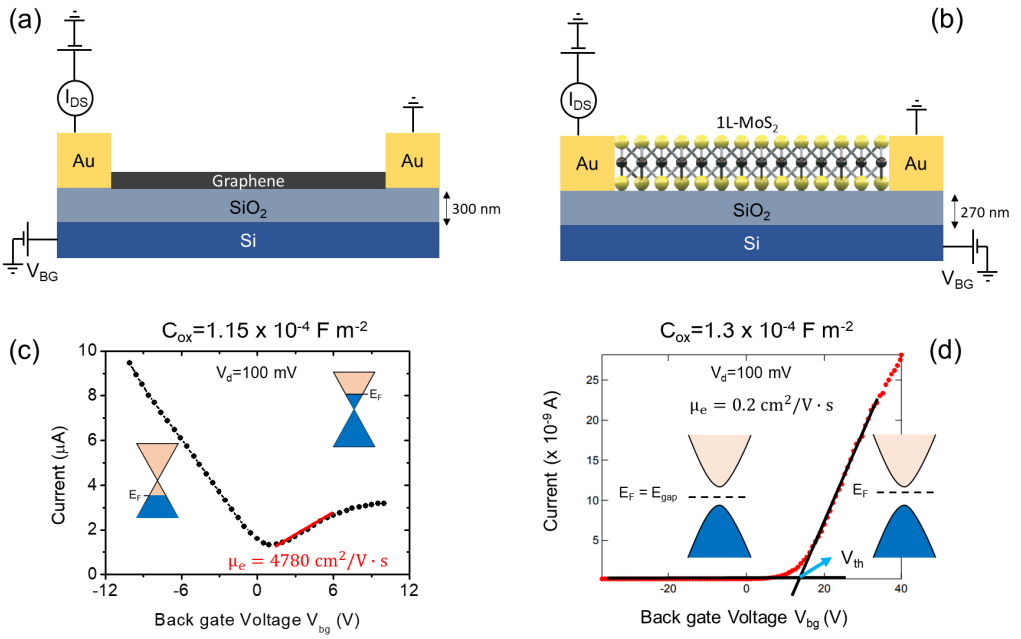

Figure 1.4.- (a) Back-gated field-effect transistor (FET) composed by a single layer of graphene as a channel. (b) Back-gated FET composed by a single layer of MoS_2 as channel. (c) Linear transfer characteristic of FET with graphene and the corresponding mobilities and the Dirac cone for each side of the voltage corresponding to a different doping (p-type left-side, n-type right side). (d) Linear transfer characteristic of 1L-MoS_2 and its mobility and the corresponding threshold voltage (V_{th}). Fig.(c) and (d) are adapted from Ref. [53] and [2].

The I_D-V_G curve for a backgated FET with a monolayer Gr channel (see **Figure 1.4** (c)) exhibits a typical ambipolar behaviour, showing both the holes and electron conduction branches associated to the field effect induced shift of the Fermi level in the valence and conduction band. These two branches are separated by a minimum of the conductivity, corresponding to the Fermi level at the Dirac point of the Gr bandstructure [53]. A very small current modulation (lower than a factor of 10) is typically observed for Gr FETs. The field effect mobility for electrons and holes can be evaluated from the slopes (dI_{ds}/dV_{bg}) of the I_d-V_{bg} characteristics in the linear region of the holes and electron branches, according to the equation:

$$\mu = \frac{dI_{ds}}{dV_{bg}} \times \frac{L}{WC_{ox}V_{ds}} \qquad (2)$$

where L and W are the channel length and width, respectively, and $C_{ox}=\varepsilon_0\varepsilon_{ox}/t_{ox}$ is the backgate insulator capacitance, with ε_0 the vacuum permittivity, ε_{ox} the insulator dielectric constant and t_{ox} its thickness. Similar values of the field effect mobility for holes (μ_h =4790 cm^2/V) and for electrons (μ_e =4780 cm^2/V) were obtained for this device structure.

A very different behaviour is observed for the transfer characteristics of back-gated FETs with a MoS_2 channel, as shown in the typical I_d-V_{bg} curve reported in **Figure 1.4** (d). In this case, a negligible current flow is observed below a back-gate threshold voltage (V_{th}), followed by a nearly-linear increase of I_D above this value. This monotonic trend of the current in the considered bias range indicates that conduction is due only to one type of majority carriers (i.e. electrons), and the conductivity increase above the threshold voltage V_{th} is explained by their accumulation in the semiconducting 1L-MoS_2 channel induced by the back-gate bias. A similar behaviour has been also observed for back-gated multilayer MoS_2 FETs [54].

The unipolar (n-type) current transport typically observed in monolayer or multilayer MoS_2 FETs is explained by two physical reasons:

(i) an unintentional n-type doping of MoS_2 thin films produced by exfoliation or other methods.

(ii) a Fermi level pinning close to MoS_2 conduction band at the interface between MoS_2 and most of the metals, used as source/drain contacts.

The unintentional n-type doping commonly observed in MoS_2 samples is typically ascribed to the presence of native defects (such as sulphur vacancies) in the MoS_2 crystal structure[55,56]. In this regard, realizing a controlled n- or p-type doping of MoS_2 and, in general, of the 2D materials represents a challenging task. In fact, common methods (such as ion-implantation) used for selective area doping of bulk semiconductors cannot be employed to dope these ultra-thin membranes without altering their crystal quality (i.e. introducing high density of defects)[57,58]. Differently, these membranes are strongly affected by their substrates and by the growth conditions that can induce doping. N-type doping can be obtained coupling the MoS_2 with TiO_2[59] or removing sulphur atoms by plasma treatments[60]. Otherwise, p-type doping of MoS_2 can be induced by oxygen plasma treatments, leading to MoO_3 formation, or by introducing substitutional Niobium (Nb) atoms during sulfurization or CVD growth[61-63]. The first approach induced an extraction of electrons from MoS_2 to MoO_3, due to the very large electron affinity of this material. On the other hand, Nb substitution introduced holes because the Nb has one-less d-electrons compared to Mo[64]. It is highly desirable to control the doping on large area MoS_2 for electronic applications. For this reason, different approaches to induce doping on MoS_2 will be faced in the experimental sections in Chapter 3-4.

Besides doping, the realization of ideal metal-semiconductor contacts on MoS_2 is still a challenging issue. **Figure 1.5**(a) shows the ideal band alignment between the bandgap of multilayers of MoS_2 and the Fermi levels of different metals with low work function (Scandium, Titanium) and high work function (Nickel, Platinum). According to this diagram, it should be possible to realize Ohmic contacts on n-type MoS_2 by choosing low work function metals, whereas the high work function metals should be chosen for Ohmic contacts on p-type doped MoS_2. The real experimental

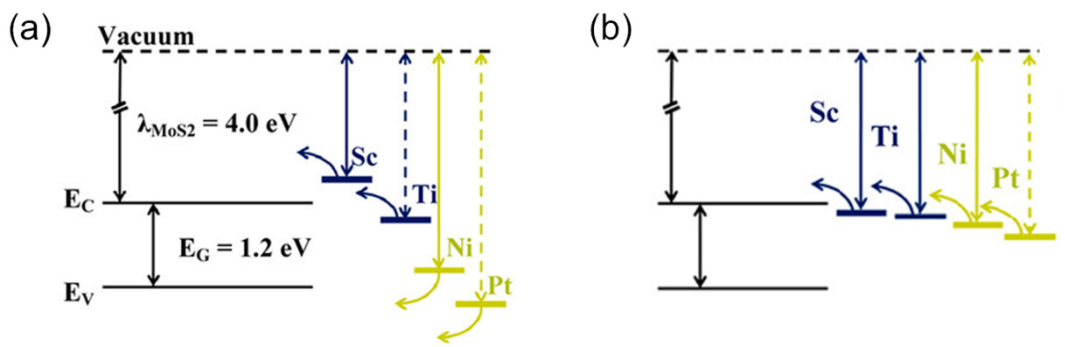

Figure 1.5.- Ideal charge transfer effect on 1L-MoS_2 with different work function metals (Sc, Ti, Ni and Pt). (b) Real situation of charge transfer effect on 1L-MoS_2 limited by Fermi-level pinning near the CB of the MoS_2 for all the different work function metals. Fig.(a-b) reproduced from Ref. [66].

situation is instead depicted in **Figure 1.5** (b), showing that the Fermi level of metals is typically pinned close to the conduction band of MoS_2.

The origin of the Fermi level pinning effect is still debated, since it can be partially ascribed to MoS_2 native defects[65,66] and partially to the surface damage produced by the deposition (evaporation/sputtering) of metals on MoS_2[66-68] . The main consequence of the Fermi level pinning is the presence of a low Schottky barrier $\Phi_{B,e}$ for electrons (from tens to few hundreds meV) at MoS_2/metal interfaces. This barrier is responsible of a contact resistance $R_c \propto \exp[\alpha \Phi_{B,e}]$ which partially limits the performances of the MoS_2 transistor.

The electron field effect mobility μ_e for the back-gated MoS_2 FET can be evaluated according to Eq.(2), from the slope of the I_d-V_{bg} curve in the linear region above V_{th}, as illustrated in **Figure 1.4**(d). It is worth mentioning that the first back-gated 1L-MoS_2 devices reported in the literature[2,4] were affected by a relatively low electron mobility, in the range between ~0.1 to ~10 $cm^2V^{-1}s^{-1}$, much lower than the theoretical expectation (200-500 $cm^2V^{-1}s^{-1}$) at room temperature[2,69].

A major advancement in this field was the demonstration of a significant improvement of μ_e after encapsulating the 1L-MoS_2 channel with high-κ dielectrics films, as illustrated in **Figure 1.6**(a) . The I_d-V_{bg} curve of 1L-MoS_2 back-gated FET with the MoS_2 channel coated by ~30-nm-thick HfO_2 (with nominal dielectric constant ε=25) grown by thermal atomic layer deposition (ALD)[70,71] is reported in **Figure 1.6**(c). The large improvement of the electron mobility (μ_e~217 $cm^2V^{-1}s^{-1}$) with respect to the backgated transistor without high-κ capping (see **Figure 1.4**(b)) was ascribed to two main physical mechanisms:

(i) a strong reduction of the Coulomb scattering between electrons in MoS_2 channel and charged impurities (Q) thanks to the higher dielectric permittivity ε_r of the environment, being the Coulomb interaction $U_{Coul} \propto Q/\varepsilon_r\varepsilon_0$;

(ii) a modification of the electron-phonon interaction in 1L- MoS_2[72].

The ~30 nm thick HfO_2 capping layer was also used as a top-gate dielectric, after the deposition of a local gate contact on the MoS_2 channel, as reported in **Figure 1.6**(b). **Figure 1.6** (d) shows the transfer characteristics of the top gated 1L- MoS_2 FET, where the drain current I_d is measured as a function of the top-gate voltage (V_{tg}) and the Si backgate bias is set to V_{bg}=0 V. The three transfer characteristics in **Figure**

1.6 (d), collected at three fixed V_{ds} bias values of 10 mV, 100 mV and 500 mV, are reported in a semilog scale, showing an exponential dependence of the subthreshold current on the gate bias, with an on/off current ratio of ~10^6 and a subthreshold swing S of 74 mV/decade. This latter parameter defines the switching performance of the FET, and its ideal value at room temperature is ~60 mV/decade.

Beneficial effects of capping layer have been observed using other high k-dielectrics, such as Al_2O_3 [73].

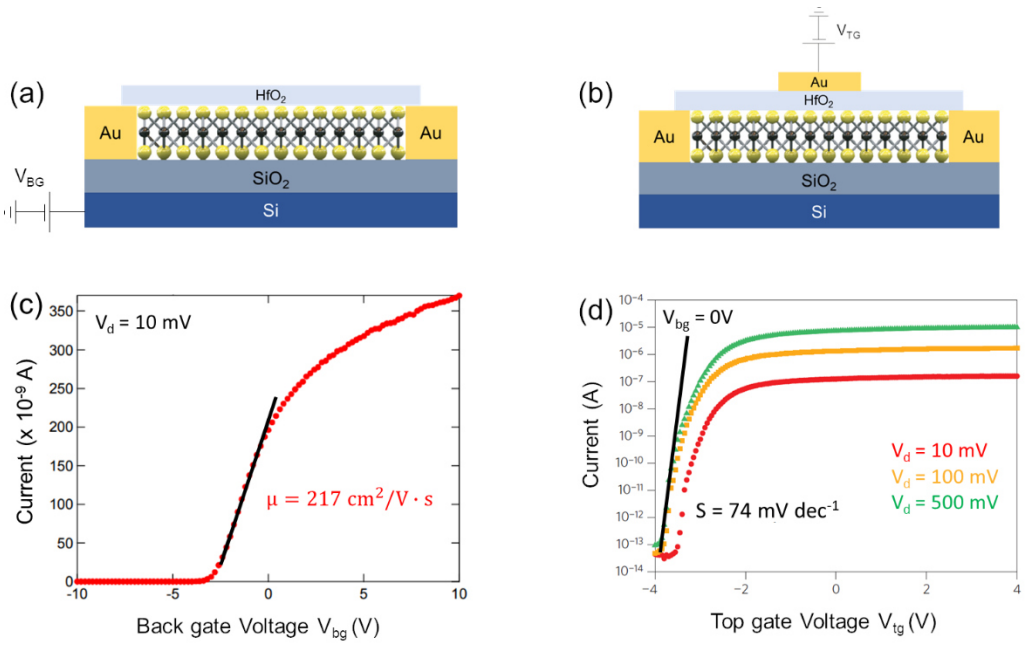

Figure 1.6.- Scheme of the 1L-MoS_2 FET integrated on the surface with 30 nm of HfO_2: without (a) and with (b) top-gate metal contacts. (c) I_d-V_{bg} transfer characteristics of the FET when is applied a V_d=10 mV. (d) I_d-V_{tg} transfer characteristics of the FET for different V_d values (from 10 to 500 mV) when the V_{bg} is set to zero. Fig.(c) and (d) adapted from Ref. [2].

In this context, relatively thick high-κ films were employed in the first pioneering studies on MoS_2 transistors to achieve a uniform coverage of MoS_2 surface, thus minimizing the gate leakage current. However, the real application of MoS_2 FETs in next generation logic devices requires an aggressive scaling of the channel length and, consequently, of the high-κ dielectric thickness.

In the Chapter 3 of this thesis, we will report the study on the integration of an ultra-thin Al_2O_3 film (3.6 nm thick) deposited by ALD on 1L-MoS_2, evidencing the potentialities of this procedure for applications in devices.

1.3 MOLYBDENUM DISULFIDE OPTICAL AND VIBRATIONAL PROPERTIES

Besides the field-effect phenomenon described in the previous section, also the optical and vibrational spectroscopy (such as Photoluminescence and Raman) are versatile techniques employed to characterize 2D materials. In this section, the MoS_2 electronic band structure and its vibrational properties will be explored in relation to the electrical properties previously reported.

1.3.1 Electronic band structure and photoluminescence

In 2011 Mak and Splendiani et al.[31,32] reported for the first time one of the most important features of MoS_2 in terms of the optical properties and their correlation

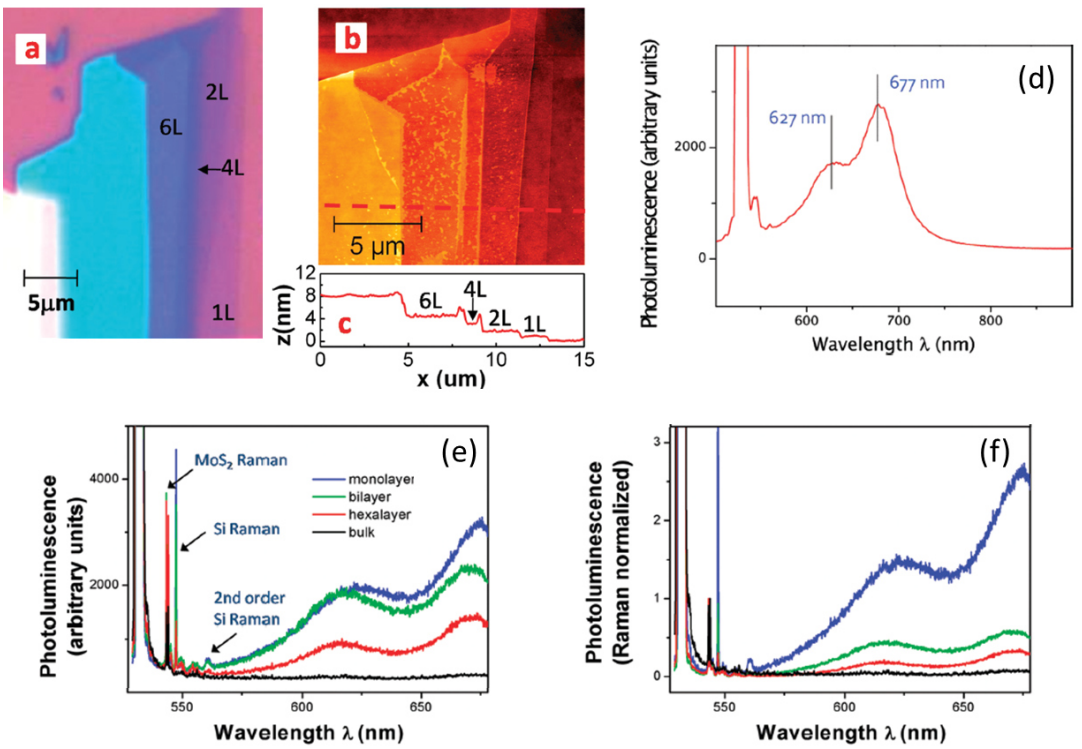

Figure 1.7.- (a) Optical image of exfoliated flake of MoS_2 at different thickness (1L, 2L, 4L and 6L). (b) Corresponding AFM image for the different MoS_2 thickness. Their steps are reported in (c). (d) Photoluminescence of MoS_2 flake with its main peaks centered at 627 and 677 nm. (e) Photoluminescence of 1L, 2L and 6L-MoS_2 and (f) PL after the normalization of the MoS_2 Raman peak. Fig. (a-f) are adapted from Ref. [32].

with thickness. MoS_2 films with variable number of layers were exfoliated on SiO_2 and the layer thickness was evaluated by optical contrast and AFM morphology, as shown in **Figure 1.7**(a-c). Photoluminescence (PL) analyses were carried out using a laser source with a wavelength of 532 nm. A typical PL spectrum of 1L MoS_2, reported in **Figure 1.7** (d), shows two main peaks at 627 and 677 nm, associated to the B and A excitonic transitions respectively, as discussed in the following. The thickness dependence of the PL spectra was also investigated, as reported in **Figure 1.7**(e). While the bulk crystal shows a flat PL intensity in the considered visible spectral region, the two prominent peaks appear with decreasing the number of layers. For a better quantification of this effect, the PL spectra were normalized with respect to the MoS_2 Raman peak intensity (**Figure 1.7** (f)), showing an evident rise of the PL intensity from 6L to a 1L-MoS_2. This normalization removes external effects on the PL intensity, such as laser excitation intensity, quantity of material, and local electric fields, and finally provides an intrinsic value of the quantum efficiency of the analysed area[32]. Hence, a single layer of MoS_2 showed the highest luminescence quantum efficiency.

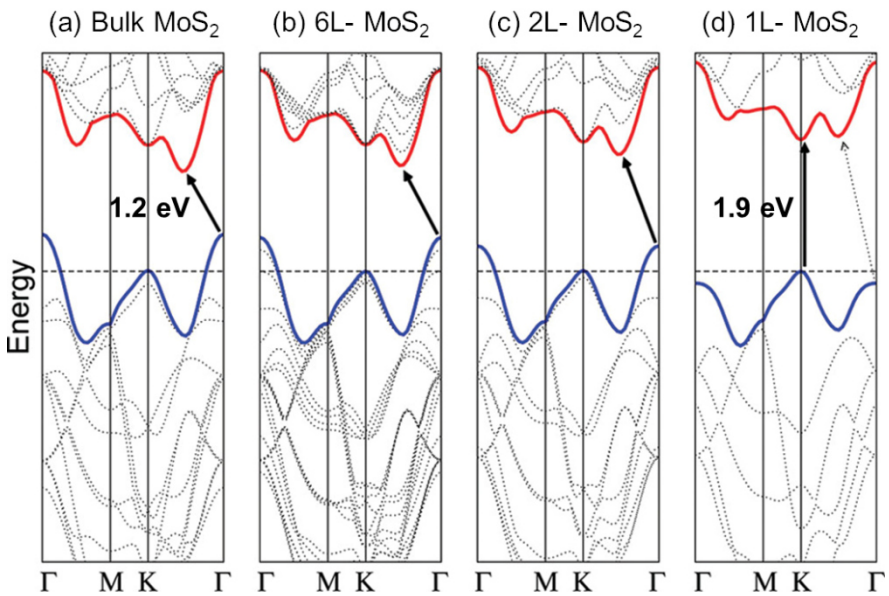

Figure 1.8.- Band structure of (a) Bulk, (b) hexalayer (6L), (c) bilayer (2L) and (d) monolayer (1L) MoS_2. Figure adapted from Ref. [32].

To explain the origin of this layer dependent behaviour, extensive calculations have been performed by different groups to determine the electronic band structure of both bulk crystals and MoS_2 monolayer [74-76].**Figure 1.8** shows the band structures in the First Brillouin Zone (FBZ) for bulk, 6L, 2L and 1L MoS_2, obtained by first-principle

calculations based on the density functional theory (DFT), with the exchange and correlation terms described using general gradient approximation (GGA) in the scheme of Perdew-Burke-Ernzerhof (PBE) [76].

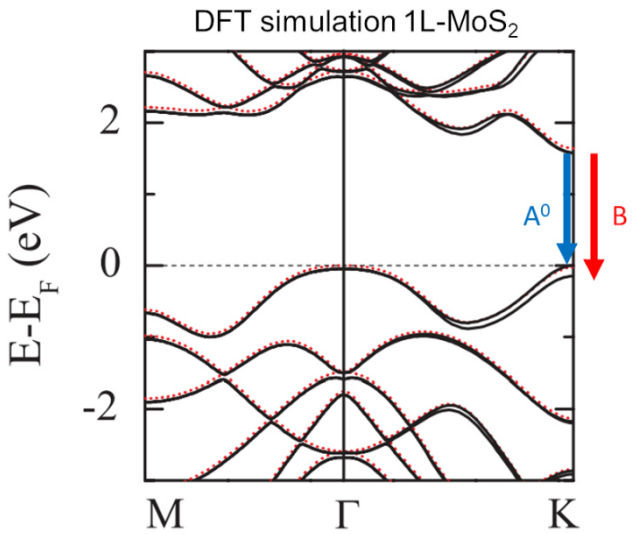

Figure 1.9.- (a) DFT simulation of the 1L-MoS_2 band structure including (black solid line) or not (dotted line) the spin-orbit coupling. This consideration permits to evaluate the splitting of the VB in K point. Figure adapted from Ref. [77].

For the bulk MoS_2 an indirect bandgap of ~1.2 eV was obtained between the top of the valence band (at the Γ point) and the bottom of the conduction band. Decreasing the number of layers, the bandgap increases and achieves a maximum value of 1.8-1.9 eV, with the top of the VB and the bottom of the CB at the K point, in the monolayer case.

It is worth to point out that these DFT calculations did not include the spin-orbit coupling, that causes a splitting in the valence band at K point. Later on, Zhu et al.[77] performed fully relativistic first-principles calculations based on DFT including the spin-orbit interaction. The calculated band structures of the 1L-MoS_2 including (black solid line) and excluding (red dotted line) the spin-orbit contribution are displayed in **Figure 1.9**. According to these results, a maximum spin-splitting of 148 meV at the top of the valence (K point) was estimated for 1L-MoS_2. Calculations also showed a larger splitting value for another TMD monolayer, i.e. 1L WSe_2, since the magnitude of the spin-orbit splitting increases for heavier atoms [77].

The two excitonic transitions, indicated with A^0 and B in **Figure 1.9**, gives rise to the corresponding peaks in the PL spectra of 1L-MoS_2, as illustrated in **Figure 1.10**.

The PL spectra were characterized employing a 532 nm laser wavelength. It is important to note that a more detailed interpretation is obtained from an appropriate deconvolution of the PL spectra. In fact, as shown in **Figure 1.10**, the deconvolution

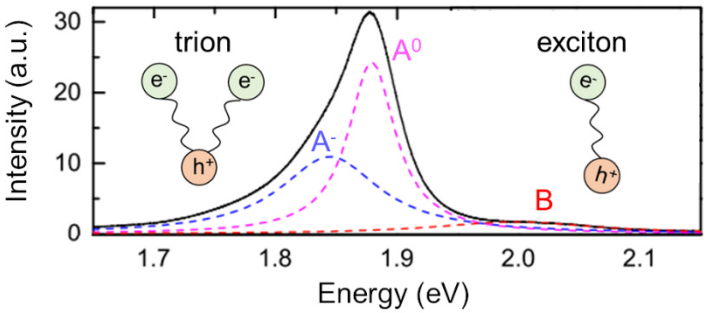

Figure 1.10.- Deconvolution of a freestanding 1L-MoS_2 PL spectrum. Three different components are visible: two excitonic peaks, A_0 and B, and the Trion (A-). Figure adapted from Ref. [78].

of the PL peak gives rise to three different components. In addition to the A and B exciton peaks, a further peak at lower energy can be associated to the charged excitons (or trions) [78]. These quasi-particles are composed by two identical charge carriers and an unpaired one with opposite sign, as two electrons and a hole (A^-) or two holes and one electron (A^+). The kind of the combination between the three excited particles depends on the doping, provided for example by the substrate[54,79].

The switching from indirect to direct bandgap passing from 2L to 1L MoS_2 allows to explain the strong increase in the photoluminescence intensity.

In general, the luminescence quantum efficiency can be expressed as [32]:

$$\eta_{lum} \approx \frac{k_{rad}}{k_{rad} + k_{def} + k_{relax}} \qquad (3)$$

where the k_{rad}, k_{def} and k_{relax} are the radiative recombination rate, the defects trapping rate, and the electron intraband relaxation rate, respectively. The first term (k_{rad}) represents the recombination of an electron in conduction band with a hole in valence band, resulting in the emission of a photon. The second term (k_{def}) describes the non-radiative trapping of photoexcited electrons by typical defects in MoS_2, such as as sulphur vacancies, molybdenum vacancies and substitutional oxygen atoms. Finally, the latter term (k_{relax}) describes the transition of electrons at lower energy

levels inside the same valence (or conduction) band. Moving from the bulk MoS_2 structure to a monolayer, the intraband relaxation k_{relax} rate is significantly reduced and approaches to zero. Furthermore, in the case of an ideal defects-free material, also the k_{def} contribution tends to zero. Hence, in the ideal case the quantum efficiency reaches its maximum value for a single layer of MoS_2 [32]. In the real case of monolayer MoS_2, these two contributions are not zero but are very small compared to the bulk counterpart. In fact, according to Eq.(3), for 1L MoS_2, the electron relaxation probability becomes k_{relax} =0, whereas the luminescence quantum efficiency can be limited by the presence of defects (k_{def}≠0).

The bandstructure of 1L-MoS_2 has been evaluated not only theoretically, but also experimentally, using the micro angle-resolved photoluminescence spectroscopy (ARPES) technique with synchrotron ultraviolet radiation[80,81], as reported in **Figure 1.11**. This technique is based on the photoelectric effect, in which an electron is ejected from a material after the interaction with a photon of a certain energy. An electron spectrometer is exploited to measure the kinetic energy, and the emission angle distribution of the photoelectrons emitted. In this way, it is possible to rebuild the Fermi level surface and the band structure of the analysed material. The colour bar represents the electrons counts per kinetic energy and emission angle. A good agreement between the ARPES electronic valence band dispersion along the K directions of the FBZ and the DFT calculations on the maximum of VB [77], indicated as red lines, can be observed. In particular, the maximum of the valence band for 1L-MoS_2 was located at the K point, confirming theoretical predictions. However, due

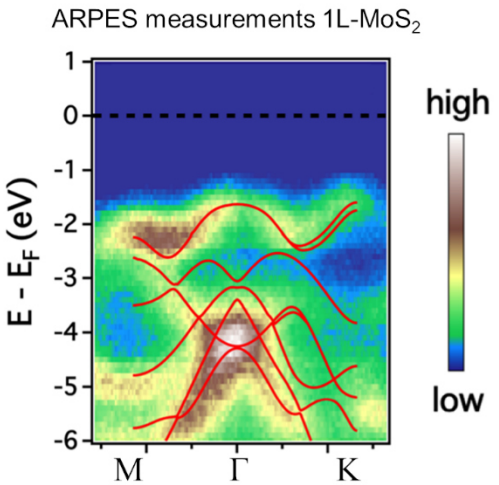

Figure 1.11.- Angle-resolved photoluminescence spectroscopy (ARPES) measurement realized on 1L-MoS_2 along the M-Γ directions. The red curves represent the theoretical calculations overlapped to the experimental band structure. Figure reproduced from Ref. [80].

to an insufficient energy resolution, ARPES measurements were not able to resolve the spin-orbit splitting near K point. Noteworthy, in the experimental dispersion, the Fermi level (E_F) is located ~1.5 eV above the valence band maximun, indicating an electron doping of the exfoliated MoS_2 that was also experimentally observed in many works[77,82-83].

1.3.2 Vibrational properties and Raman spectra of MoS_2

The most widely used and powerful technique employed to characterize the vibrational modes for the 2D materials is the Raman Spectroscopy, based on the inelastic scattering of a laser light incident on a crystal structure. The general principles of this techniques are discussed in the Appendix A.

In particular, two main vibrational modes (i.e., the E_{2g} and A_{1g} modes) characterize the Raman spectra of the MoS_2. Looking at the schematic in **Figure 1.12**(a), these

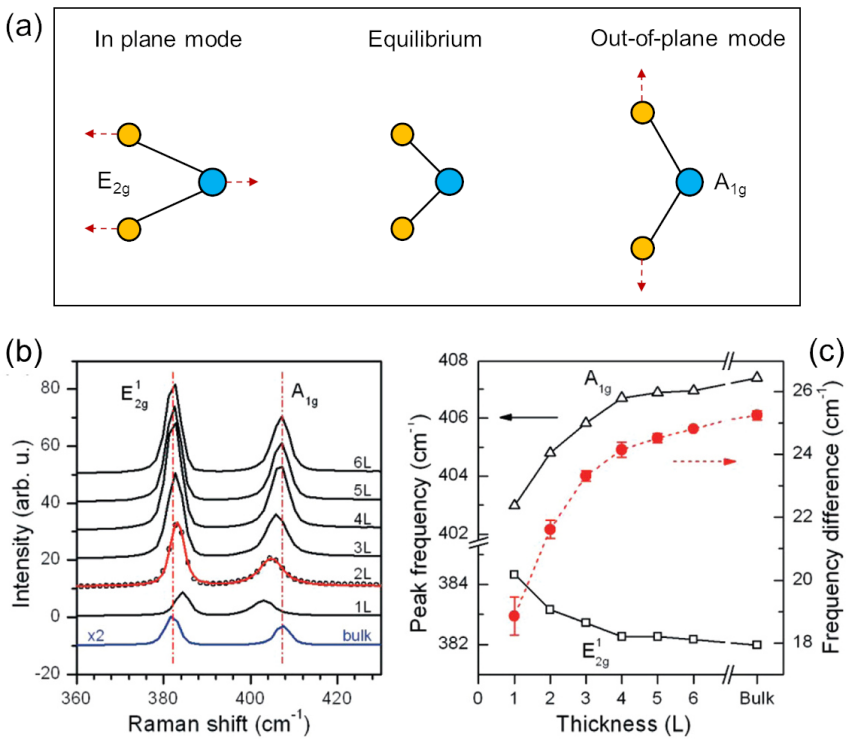

Figure 1.12.- (a) Vibrational modes and (b) Raman spectra of MoS_2 from Bulk to 1L with the characteristics vibrational peaks E_{2g} and A_{1g}. (c) Trend of the two peaks (black lines) as a function of the thickness and their difference $\Delta\omega$ (red points and dashed line) as a function of the thickness. Fig.(b) and (c) reproduced from Ref. [84].

represent the in-plane and out-of-plane vibrational modes of the S-Mo-S system, respectively. From the denomination point of view, the E_{2g} and A_{1g} names are typically used to identify the two modes in bulk or multilayer MoS_2, whereas the names E' and A'_1 are sometimes used to indicate the same modes in monolayer MoS_2.

A characteristic dependence of the frequencies for these two peaks as a function of the number of layers was observed experimentally for the first time in 2010 by Lee et al. [84]. **Figure 1.12** (b) shows the Raman spectra obtained in that work using a laser light source at a wavelength of 532 nm on bulk MoS_2 and on MoS_2 flakes with different thickness (ranging from 1 to 6 layers) exfoliated on a SiO_2/Si substrate. A blue-shift of the E^1_{2g} peak at higher frequencies values and a red-shift of the A_{1g} peak at lower frequencies were observed with decreasing the number of layers. The trends of the two Raman modes frequencies as a function of the number of layers are represented in **Figure 1.12** (c), left scale. Furthermore, the dependence of the peak frequency difference ($\Delta\omega$) on the number of layers is reported in **Figure 1.12** (c), right scale, by the red circular points. The observed monotonic increase of $\Delta\omega$ with the thickness represents a straightforward way to evaluate the number of MoS_2 layers, especially for very thin MoS_2 films (1 to 5 L). Due to the saturating trend of $\Delta\omega$ for larger thickness, alternative characterization methods (e.g. AFM step height measurements and TEM) are required for thicker samples.

1.3.3 Strain, doping and defects effect on PL and Raman spectra

In addition to the dependence on the thickness, PL and Raman spectra of MoS_2 are influenced by other effects, such as:

- Uniaxial/biaxial strain induced on the MoS_2
- Density of charge carriers (doping) of the MoS_2
- Density of defects presents on the MoS_2.

1.3.3.1 Strain effects on Raman and PL spectra

The optical and vibrational properties of the MoS_2 are particularly influenced by external perturbation induced on the material, as for example strain and charge transfer [85-87]. The strain (ε) describes the percent change of the volume of a material in response to an external mechanical perturbation[88]. In the last years, several papers

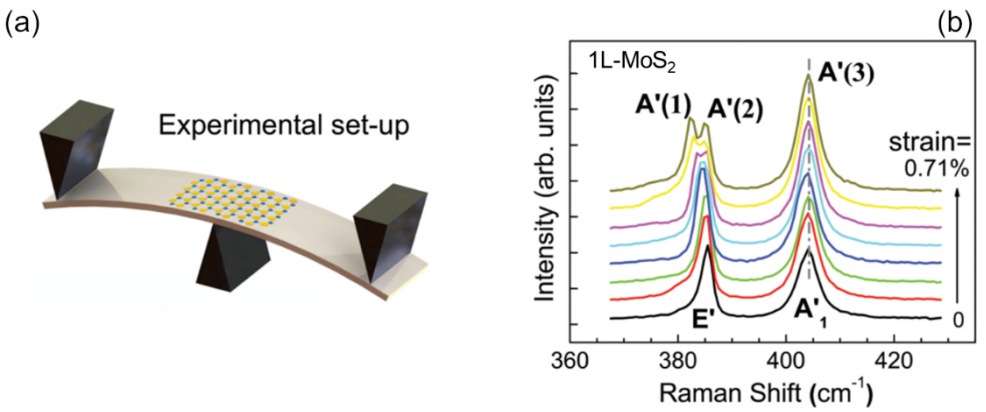

Figure 1.13.- Experimental set-up for (a) uniaxial strain applied on 1L-MoS_2. (b) Raman spectra of 1L-MoS_2 at different uniaxial strain steps. Fig(a-b) adapted from Ref. [89].

investigated the effects of uni- or biaxial strain on the Raman spectra of thin films of MoS_2.

The application of uniaxial strain to MoS_2 has been realized using the experimental set-up reported in **Figure 1.13**(a).

In this case, 1L-MoS_2 membrane is exfoliated on a flexible polymeric substrate that can be bended in a controlled way, resulting in the application of a tensile uniaxial-strain. The corresponding effects on the E' and A_1' vibrational modes are reported in **Figure 1.13** (b). In particular, a splitting of the E' peak is observed for applied strain values above ~0.5%. In detail, while the in-plane E' mode of 1L-MoS_2 is degenerate at strain ε=0, the isotropic symmetry in the x-y plane is broken when a uniaxial strain is applied [89], resulting in the loss of the degeneracy and the experimentally observed splitting in the two peaks A'(1) and A'(2) [89].

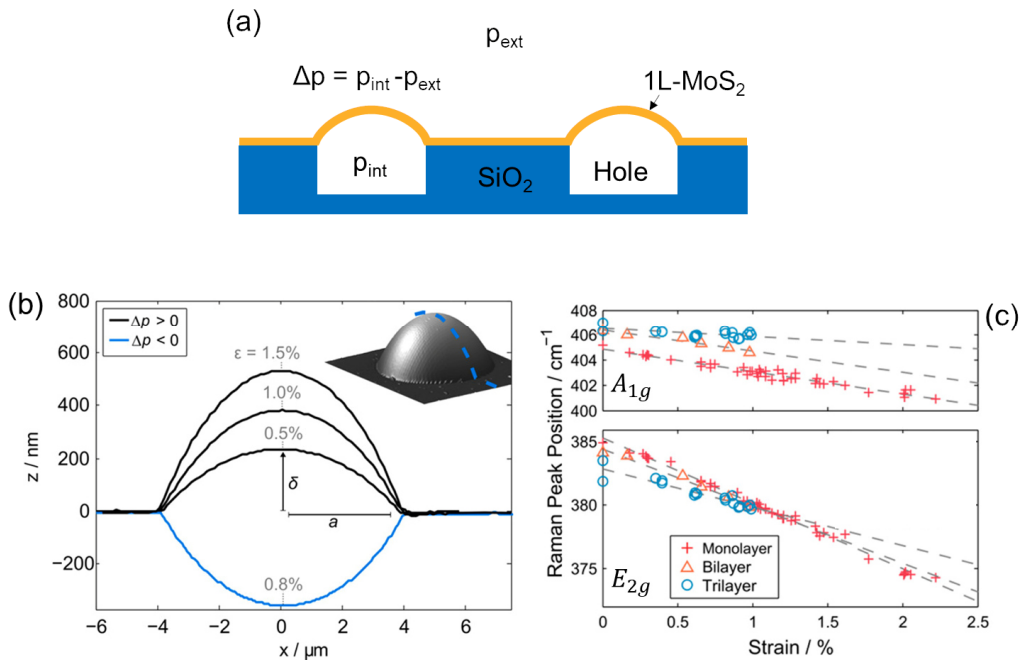

Figure 1.14.- (a) Scheme of the SiO_2 micro-holes array in which is exfoliated the 1L-MoS_2 for the biaxial strain treatments. (b) AFM profile of the MoS_2 film after the application of an internal pressure (and therefore a difference of pressure with the external pressure Δp) at which corresponds a different extension (δ) of the membrane at and thus a different biaxial strain applied. (c) Raman peak position of the E_{2g} and A_{1g} for 1L, 2L and 3L-MoS_2 as a function of the strain in a range between 0 and 2.5%. Fig.(a-c) are adapted from Ref. [90].

An experimental approach to apply a biaxial strain to a MoS_2 membrane is represented in **Figure 1.14** (a-b). Here, 1L-MoS_2 is exfoliated on a substrate with an array of micro-holes [90]. By introducing an inert gas within these holes, a pressure difference is created between the hole cavity and the external ambient, separated by

the 1L-MoS_2 membrane. The result is a deformation of the membrane, i.e. a biaxial strain, which can be evaluated by AFM morphological measurements, as shown **Figure 1.14** (b) Raman spectra collected on the MoS_2 membranes subjected to this biaxial strain exhibit a significant red-shift of the E_{1g} peak and a smaller red-shift of the A_{1g} peaks. Differently from the uniaxial case, no splitting of the E_{1g} peak is observed for MoS_2 membranes subjected to biaxial strain. **Figure 1.14**(c) and (d) show the experimental behaviour of the E_{1g} and A_{1g} peak positions as a function of the strain for 1L, 2L and 3L MoS_2 membranes.

In most of the experimental conditions, MoS_2 membranes are subjected to a biaxial strain, e.g. by interaction with the substrate. Hence the experimental results in the **Figure 1.14**(c-d) are extremely useful to evaluate this strain from the Raman shift of the peaks with respect to an ideally unstrained MoS_2 membrane.

According to the previous results, it is possible to extract the Grüneisen parameters, defined as the effect of changing of the volume of the crystal lattice on the variation of the vibrational peaks position [91]. In the case of variation of the volume induced by an applied strain on a 2D material, the following relationship describes the effects on the Raman peaks [91-96]:

$$\gamma_m = \frac{1}{\omega_m^0}\frac{\partial \omega_m^h}{\partial \varepsilon_h} \qquad (4)$$

where the m-index identifies a particular vibrational mode (E' or A'_1 in the case of 1L-MoS_2), ω_m^0 and ω_m^h are the position of the specific mode at zero strain and after the application of a strain, respectively. In the end, ε_h represents the total hydrostatic strain contributions due by the sum of the parallel ε_{ll} and perpendicular ε_{tt} components to the applied strain. When it is considered a uniaxial strain, these two components are not equal, and this justifies the splitting effect on the E_{2g} peak observed experimentally [92].

Differently when a biaxial strain is applied on the material, the strain components are equal $\varepsilon_h = \varepsilon_{ll} = \varepsilon_{tt}$ and in the case of the E_{2g} peak, there is not a splitting. Thus, the previous relation can be reduced for both the 1L-MoS_2 Raman peaks in the following general expression:

$$\Delta\omega_m = -2\gamma_m^{\text{biax}}\omega_m^0\varepsilon \quad (5)$$

This correlation between the strain and the vibrational modes, can be thought because of the molecular bond length increase (or decrease) that causes a red-shift (or blue-shift) mainly in the in-plane mode [88]. In this way it is possible to understand and quantify the effects of external perturbations on the crystal lattice of MoS_2, after the knowledge of the Grüneisen parameters and the positions of the vibrational peaks for the specific 2D materials.

The same authors of Ref. [90] carried out the optical characterization of biaxial strained 1L-MoS_2 employing a 532 nm laser excitation wavelength, as illustrated in **Figure 1.15**. By increasing the biaxial strain in the range from 0 to 2%, a red shift of the main PL peak and a significant decrease of the PL intensity (see the insert) were observed. In particular, a shift rate of -99 ± 6 meV/% of the PL peak was evaluated both for mechanical exfoliated and CVD grown 1L-MoS_2. These values are comparable with theoretical predictions of 105 meV/% [97].

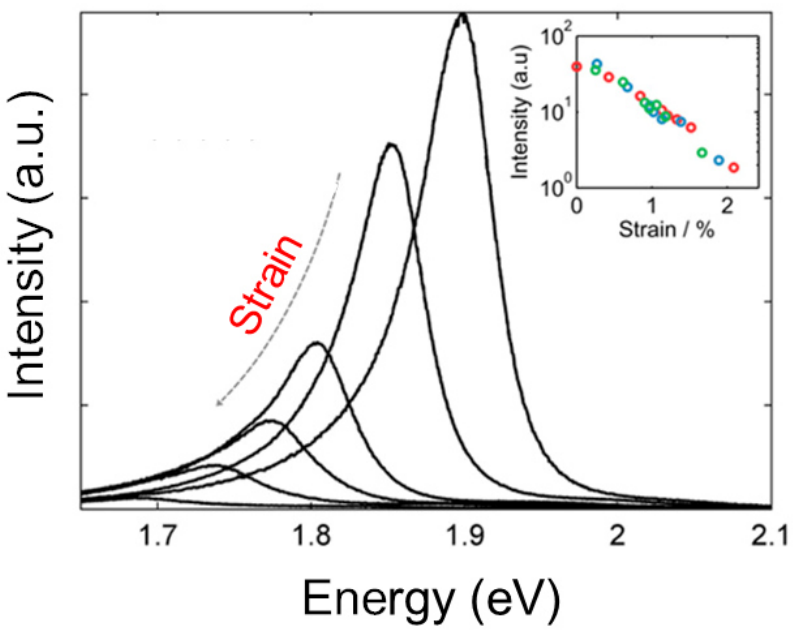

Figure 1.15.- Effect of the biaxial strain on the PL intensity and position of monolayer MoS_2. Increasing the strain the PL peak decreases in intensity and undergoes a red-shift. Figure adapted from Ref. [90].

A similar trend was observed for PL spectra of 1L-MoS_2 subjected to uniaxial strain, but with a lower shift-rate of the peak of ~45 meV/% [96].

The observed red-shift of PL peaks with the strain can be ascribed to a variation of the overlap between the Mo and S orbitals. More specifically, tensile strain causes a reduction of the distance between the S atoms and an increase of the distance between the Mo and S atoms. According to simulations, these effects give rise to a modification of the energy band structure for 1L-MoS_2, with the rise of valence band maximum and a decrease of the bottom of the conduction band, resulting in a reduction of the band gap [98].

1.3.3.2 Doping effects on Raman and PL spectra

MoS_2 vibrational peaks are also influenced by the doping in this 2D semiconducting material. The dependence of the E_{2g} and A_{1g} peaks frequencies on the carrier density

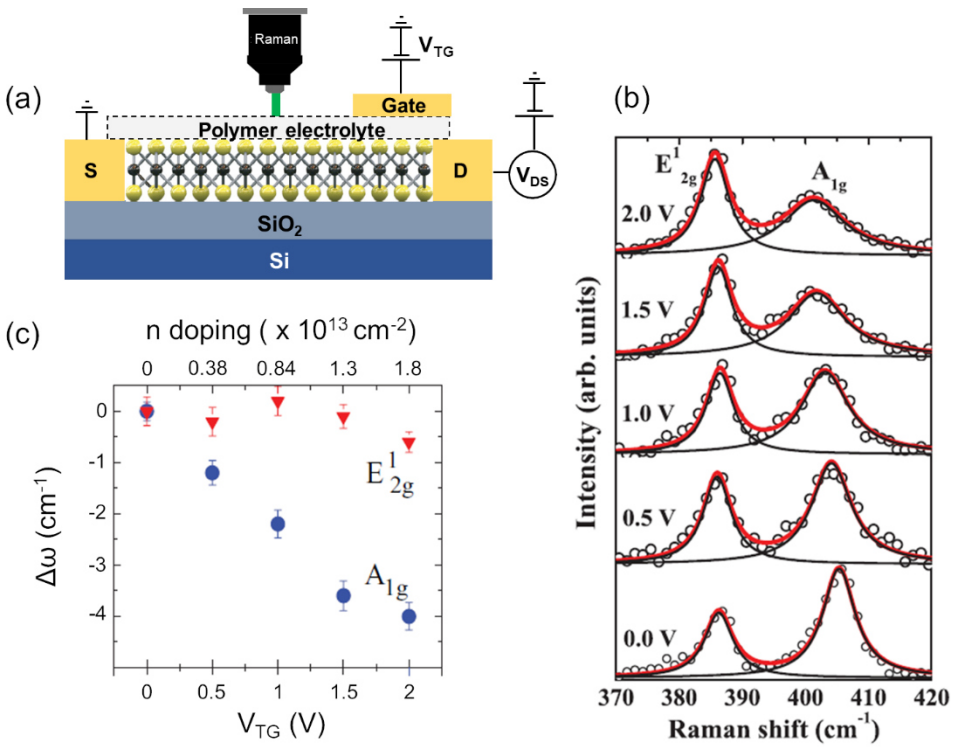

Figure 1.16.- (a) Top-gated transistor with 1L-MoS_2 combined with a polymer electrolyte. (b) 1L-MoS_2 Raman spectra at different top-gate voltage applied. (c) Shift rate of the two vibrational peaks positions as a function of the applied voltage. Fig. (a-c) adapted from Ref. [87].

in 1L-MoS_2 has been experimentally evaluated by Chakraborty et al. [87], by performing Raman measurements on 1L-MoS_2 field effect transistor with a polymer electrolyte top-gate, as schematically illustrated in **Figure 1.16**(a). This polymer was chosen as the top gate for its high capacitance, allowing a field modulation of the MoS_2 carrier density over a wide range, and its transparency, enabling to realize simultaneously Raman and electrical measurements [99]. Applying different top-gate voltages on the 1L- MoS_2, an evolution of the peaks intensity and positions can be observed in **Figure 1.16**(b). Specifically, a redshift and a broadening of the A_1' peak is observed for increasing values of V_{TG}, while the in-plane mode experiences lower effects in terms of spectral position and width. To associate a particular value of carrier concentration to an applied top-gate voltage, the authors used the following expression:

$$n = C_{TG}(V_{tg} - V_{th})/\mathrm{q} \qquad (6)$$

In this relationship, V_{tg} represents the value of the voltage applied to the top-gate of the transistor, V_{th} (~ 0.1 V) represents the threshold voltage , C_{tg} (~ 1.5 µF/cm^2) is the top-gate capacitance [99]. Thus, it was possible to realize the graph of the variation of the peaks position as a function of the voltage applied to the top-gate (or the corresponding carrier density n as shown in **Figure 1.16** (c). Here, the strong influence of the carrier concentration on the A_1' compared to the E' peak is clearly visible from the two different trends. From their slopes the shift rates of the two modes with carrier concentration were extracted, resumed in the following general expression for the m-th mode:

$$\Delta\omega_m = k_m n \qquad (7)$$

From a physical point of view, this charge transfer dependence on the A_1' position is associated, in literature, to a strong electron-phonon coupling [87,100-103]. We will see in the experimental section that the solutions of the equations Eq.(5) -(7) can give quantitatively information on the strain and doping induced by the substrate or by growth conditions on the 1L-MoS_2.

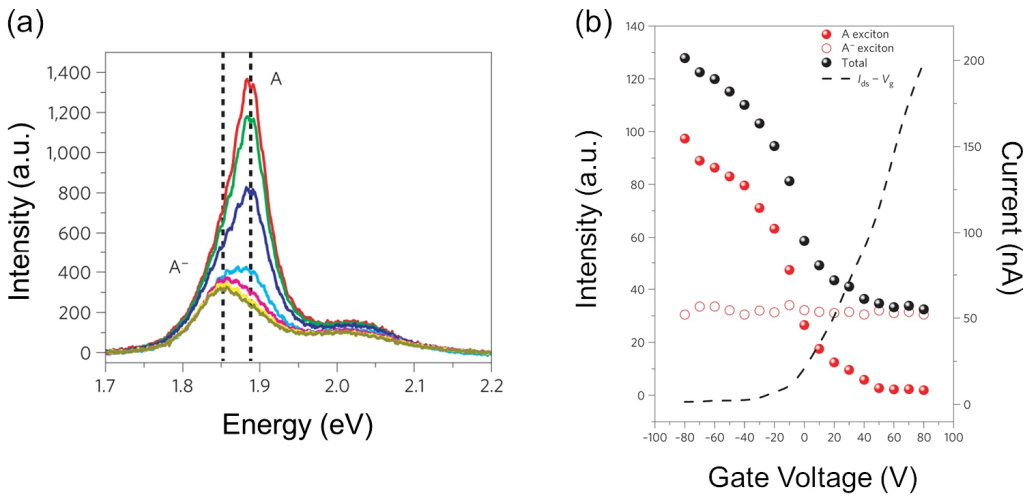

Figure 1.17.- (a) Photoluminescence spectra of 1L-MoS_2 at different gate voltage from -70 V to 80 V. (b) Intensity and current of the three components (A^-, A^0 and B) as a function of the gate voltage. Fig.(a-b) reproduced from Ref. [55].

Also, the optical properties of the 1L-MoS_2 are influenced by doping. Applying different voltage to a transistor like that reported previously (in **Figure 1.16** (a)), it is possible to note that the exciton peak A^0 decrease radically passing from -70 V to 80 V, as shown in **Figure 1.17** (a). This effect causes the raising of the A^- peak compared to the exciton counterpart [55]. Thus, a decreasing trend of the peak intensity is observed for the A^0 and B peaks passing from negative to positive voltage values, as shown in **Figure 1.17** (b). Differently the A^- peak remains constant for all the voltage values applied to the 1L-MoS_2. However, applying different values of doping (and varying the charge carriers extracted or introduced in the MoS_2)

		ω^0_{E2g} (cm^{-1})	ω^0_{A1g} (cm^{-1})	γ_{E2g} (a.u.)	γ_{A1g} (a.u.)	k_{E2g} (x10^{-13} cm)	k_{A1g} (x10^{-13} cm)
Exfoliated	1L-MoS_2	385	405	0.68	0.21	-0.33	-2.2
	2L-MoS_2	384.4	406.3	0.55	0.16	--	--
	3L-MoS_2	382.9	406.4	0.39	0.09	--	--
CVD	1L-MoS_2	--	--	0.40	0.21	--	--
	2L-MoS_2	--	--	0.43	0.18	--	--
DFT	1L-MoS_2	--	--	0.56	0.13	--	--
	2L-MoS_2	--	--	0.58	0.17		

Table 3.- Summary of the Raman peak positions, the Grüneisen parameters and shift rate as a function of the doping for the monolayer, bilayers, and trilayer MoS_2. Collected from Ref. [87,90].

induces a control of the MoS_2 optical properties. A similar situation is also observed in the PL of chemically treated 1L-MoS_2 [56] or in vanadium doped CVD-grown MoS_2 [104]. The E_{2g}, A_{1g} peaks positions references, their corresponding Grüneisen parameters and shift-rates with doping employed in this thesis for 1L-, 2L- and 3L-MoS_2 are summarized in **Table 3**.

1.3.3.3 Defects effects on PL and Raman spectra

The effect of defects and, more generally, crystalline disorder on the Raman spectra of MoS_2 have been experimentally investigated in the past by performing ion bombardment on the surface of 1L-MoS_2 [105]. As an example, the implantation was performed using different ion doses between 10^{12}-10^{14} ions/cm^2, corresponding to inter-defect distances (L_D) in the range between 10 and 1 nm. As shown in **Figure 1.18**(a), evident changes of the Raman spectra are associated to the increasing of the density of ions implanted (or the decreasing of L_D). Indeed, the longitudinal acoustic peak LA(M) is observed to increase in intensity as decreasing the L_D, while the two main vibrational modes E' and A'$_1$ move away from their starting positions and become wider after the implantation process. At once the second-order longitudinal acoustic mode (2LA(M)) decreases at higher doses and vanishes when the L_D is near 1-1.3 nm. Other details are obtained in this work after the deconvolution analysis on the two main vibrational active modes. As reported in **Figure 1.18**(b), each of the two broader modes is constituted by two different components, and in the specific, the in-plane longitudinal optical mode (LO(M)) has been associated to the peak at around 357 cm^{-1}, and the out-of-plane optical mode (ZO(M)) to the other one at 411

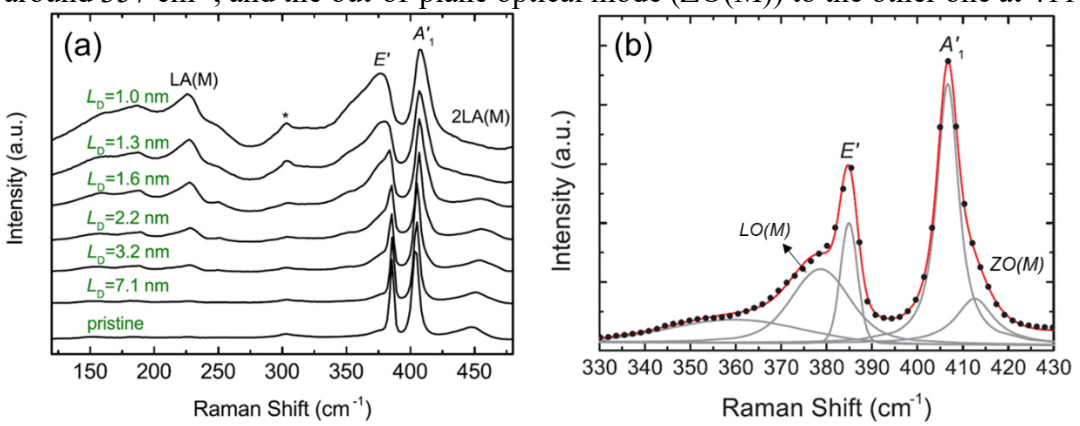

Figure 1.18.- (a) Raman spectra of 1L-MoS_2 by varying the inter-defects distance L_D. (b) Deconvolution of the two main vibrational peaks E' and A'1 after the ion beam bombardments. Fig. (a-b) adapted from Ref. [105].

cm^{-1}. The presence of these modes is associated to the activation of phonons at the edge of the First-Brillouin zone by the contribution of the defect's momentum [106]. For this reason, these peaks are defined as defect-activated peaks. The last result found in this work is the experimental correlation between the intensity ratio of the LA(M) and E' (or A_1') peaks and L_D, that can be extracted using the following relationship:

$$\frac{I(LA)}{I(X)} = \frac{C(X)}{L_D^2} \quad (8)$$

where X=E' or A_1' and C(E') =1.11 ± 0.08 nm^2 and C(A_1') = 0.59 ± 0.03 nm^2 are two values that depend strongly on the laser power used for the Raman characterization. The authors deduced the C(X) values supposing that the inter-defects distance is proportional to the inverse of the square of the density of ions impacting on the surface ($L_D \propto \frac{1}{\sqrt{\sigma}}$). Thus, it is possible to employ this equation to find the density of defects in material grown by other methods or affected by other factors.

Also, the PL spectrum is influenced by the presence of high density of defects in 1L-MoS_2. As reported in Ref. [60], the two typical PL peaks (A and B) undergo a rapid decrease until a total quenching after hydrogen plasma treatments. This kind of treatment results in the formation of sulfur vacancies in the 1L-MoS_2. As reported in **Figure 1.19**(a), the as-grown 1L-MoS_2 spectrum (black line) decreases after 10 minute and reaches a total quenching after 30 minutes (blue line) of plasma exposure, as shown in the inset of **Figure 1.19**(a). Indeed, an evident change of the PL shape emerges after some minutes of treatments. Thus, the authors realized a deconvolution of the spectrum before (as-grown), after 10 and 20 minutes, reported respectively in **Figure 1.19** (b-d). It can be appreciated that the three typical components (A^-, A and B) are present before the plasma treatments. Meanwhile, the B-peak became the dominant feature, and a further peak (X_D) appears after the desulfurization process. X_D is defined as the defect-induced exciton and its presence is due to an increasing of the density of defects (sulfur vacancies) in the 1L-MoS_2. The decreasing of the trion (A^-) and exciton (A) components in favor of the B-peak enhancement results from raising of non-radiative recombination of the exciton due to the high density of

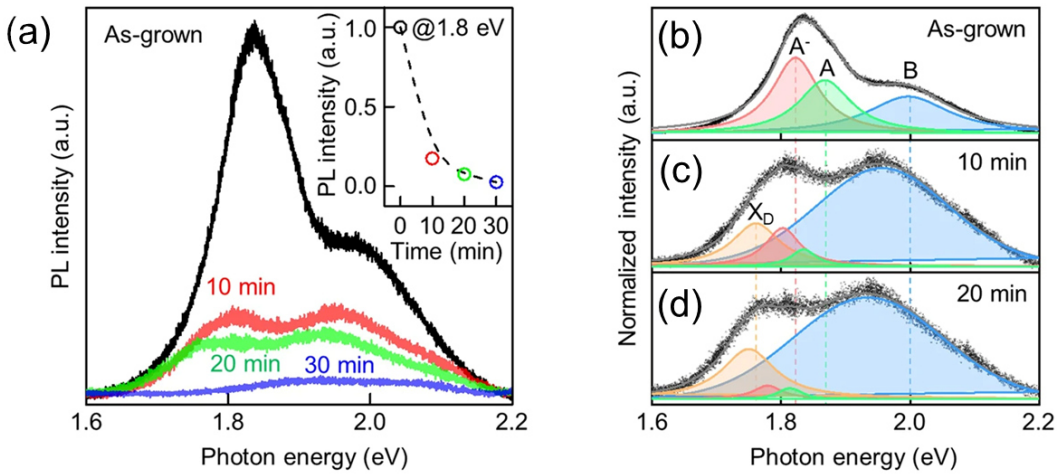

Figure 1.19.- (a) PL spectra of 1L-MoS_2 after different time of hydrogen plasma treatments. Deconvolution of the PL spectra for the (b) as-grown 1L-MoS_2, (c) after 10 and (d) 20 minutes of plasma treatments. Fig.(a-b) reproduced by Ref. [60].

defects [107,108]. This phenomenon reduces mainly the A lifetime in contrast to the B-peak that is moderately affected [108].

CHAPTER 2

PREPARATION METHODS AND INTEGRATION OF MoS_2 FOR ELECTRONICS

As discussed in the Chapter 1, MoS_2 holds very interesting structural, electronic and optical properties, which can find several applications in the development of advanced electronic/optoelectronic devices and sensors. Most of the initial studies on this material have been carried out on flakes obtained by mechanical exfoliation from bulk crystal. On the other hand, scalable production approaches are needed for the development of real applications. Furthermore, the heterogeneous integration of MoS_2 with the state-of-the-art bulk (3D) semiconductors, such as Si and wide-bandgap semiconductors (SiC, GaN) represents a promising strategy to develop advanced devices, exploiting the functional properties of this 2D material with the well assessed semiconductor technology .

This chapter is composed by two parts. The first part is a brief overview of the state-of-the-art preparation methods to produce single and few layers of MoS_2. These will be classified as top-down and bottom-up methods, and the main advantages/disadvantages of each approach will be discussed. In the second part, the status of MoS_2 heterogeneous integration with semiconductors, in particular silicon, gallium nitride and silicon carbide will be discussed. Furthermore, another key issue for electronic applications of MoS_2, i.e. the deposition of ultrathin high-κ dielectric on its surface, will be discussed.

2.1 MoS_2 PRODUCTION BY TOP-DOWN APPROACHES

2.1.1 Mechanical exfoliation from bulk molybdenite

The simplest top-down method to produce 2D materials is represented by mechanical exfoliation from the corresponding bulk crystal. This approach was employed for the first time to obtain graphene from bulk graphite. In a similar way, starting from a

crystal of molybdenite, single or few layers of MoS_2 have been produced simply peeling an undefined number of layers with a scotch-tape [109], as schematically depicted in **Figure 2.1** (a). Although the mechanical exfoliation approach still provides the MoS_2 samples with the best crystalline and electronic quality, the difficulty in controlling the thickness of the flakes, the limited exfoliation yield and the small lateral size of the flakes (typically, few micrometers, as illustrated in **Figure 2.1** (b) makes this method not suitable for large scale production of MoS_2.

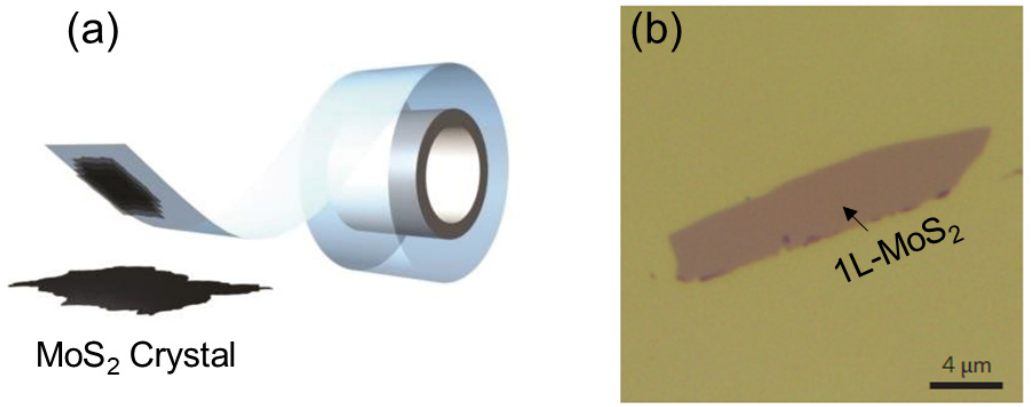

Figure 2.1.- (a) Scheme of the mechanical exfoliation from a MoS_2 crystal by scotch-tape. (b) Few micrometers-area of 1L-MoS_2 obtained by the mechanical exfoliation. Fig. (b) reproduced from Ref. [174].

2.1.2 Exfoliation in liquid

The exfoliation yield of MoS_2 and, more generally, of 2D materials from bulk samples has been greatly enhanced by the development of exfoliation methods in liquid [110,111]. In the case of MoS_2, liquid exfoliation is favoured by the intercalation of the crystal layers with ionic species, as shown in **Figure 2.2**(a-b). A typical procedure is the immersion of the MoS_2 crystal in a solution of lithium compounds, such as n-butyllithium, for more than one day to allow the lithium ions to intercalate between the layers. Next, this solution is mixed to water, which strongly reacts with the intercalated lithium by production of H_2 gas, resulting in the separation of the MoS_2 layers by mechanical action [29,112,113]. This chemical exfoliation allows to produce mixed nano-sheets of mono- and few-layers MoS_2, as illustrated in **Figure 2.2**(c), that are different from the bulk in terms of structural and electronic properties[29]. In fact, as previously explained in the section 1.1, this process changes

the properties of MoS_2 from semiconducting to metallic and the Mo-S coordination, forming the 1T-MoS_2. Hence, post exfoliation treatments are needed to reconvert the metallic 1T-MoS_2 to the 2H- semiconducting phase [114].

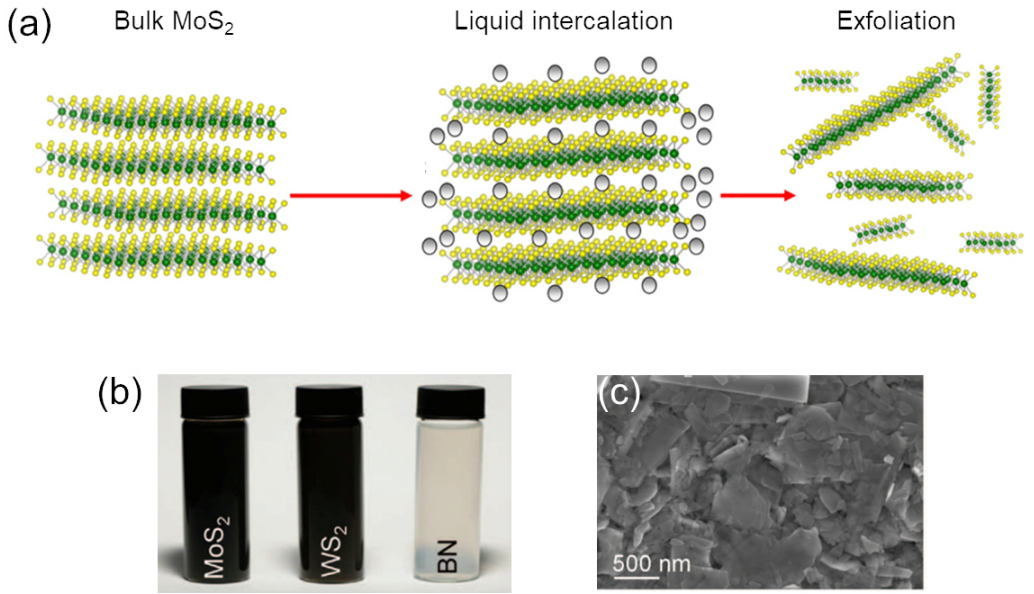

Figure 2.2.- (a) Scheme of the liquid-exfoliation method for a bulk MoS_2. (b) Photograph of phials containing liquid exfoliated MoS_2, WS_2 and BN. (c) SEM image of liquid exfoliated MoS_2 at high magnification. Fig. (a), (b) and (c) reproduced from [111], [110] and [110], respectively.

The main advantage of the liquid exfoliation methods is clearly its scalability. However, the MoS_2 films obtained by spin coating or inkjet printing of the liquid solutions are composed by a network of overlapped nano-sheets. The electrical resistance associated to these nanosheets junctions, combined to defectivity originating from the exfoliation process, make these MoS_2 films not suitable for electronic/optoelectronic applications. On the other hand, they proved to be very useful for catalysis and/or sensing applications[109,115,116].

2.1.3 Gold-assisted mechanical exfoliation

Recently, different research groups explored an alternative top-down approach to overcome the limitations of the mechanical exfoliation (i.e. small flakes size and poor control of the thickness), while maintaining its main advantages in terms of crystalline quality of produced MoS_2 [117-126]. This method, named “gold-assisted mechanical exfoliation”, exploits the strong bonds naturally established between the

gold and sulphur atoms at the nanoscale [127] to achieve the exfoliation of large area monolayer MoS_2 membrane by simply pressing a MoS_2 bulk crystal onto a flat gold substrate (as schematically illustrated in **Figure 2.3** (a)). Under perfect conditions of an ultra-flat and contaminations-free Au surface, the S-Au interaction exceeds the interlayer vdW force of the MoS_2 bulk crystal, resulting in the exfoliation of the MoS_2 monolayer directly in contact with Au. Ideally, the lateral extension of the exfoliated MoS_2 membrane is only limited by the area of the starting molybdenite crystal. **Figure 2.3** (b) shows an optical microscopy image of a MoS_2 membrane exfoliated on a gold surface [124], where the light-yellow contrast is associated to Au, the dark yellow to 1L MoS_2, and the blue and violet contrast to multilayers of MoS_2. A very large extension (~82 mm^2) of the 1L MoS_2 area can be deduced from this image.

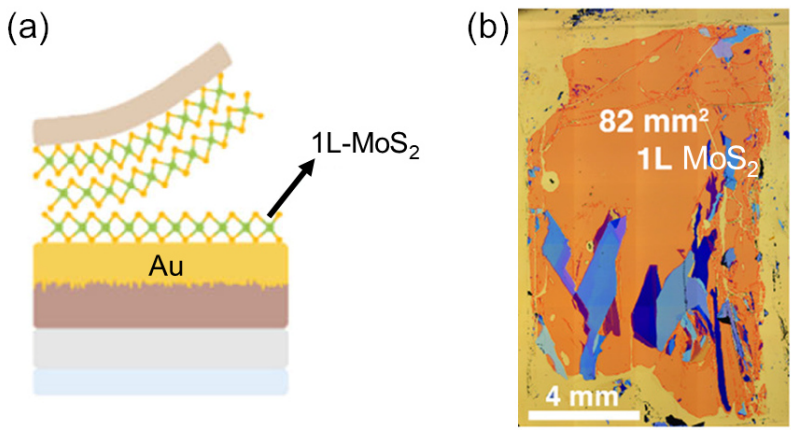

Figure 2.3.- (a) Schematic of the mechanical exfoliation assisted by gold substrate. (b) Optical image of a large area (mm^2) 1L-MoS_2 exfoliated on gold. Fig.(a-b) adapted from Ref. [120].

Velicky et al. [119], recently investigated the exfoliation of MoS_2 on the surface of thin Au films deposited by evaporation. They demonstrated how the monolayer exfoliation yield critically depends on the degree of contamination of the Au surface, due to the exposure to the air after the deposition.

As schematically illustrated in **Figure 2.4**, the presence of organic contaminants, e.g. adventitious carbon, at the interface between the two materials gradually reduces the exfoliation yield of a MoS_2 monolayer. Besides the surface cleanness, another key parameter that can influence the yield of the exfoliation is the Au surface roughness. The authors compared the MoS_2 exfoliation on the surface of three Au films with different roughness obtained by different techniques, i.e. e-beam evaporation, sputtering and peeling on a polymeric substrate, as described by AFM images in **Figure 2.5** (a-c) respectively. In the thinner film characterized by a lower surface

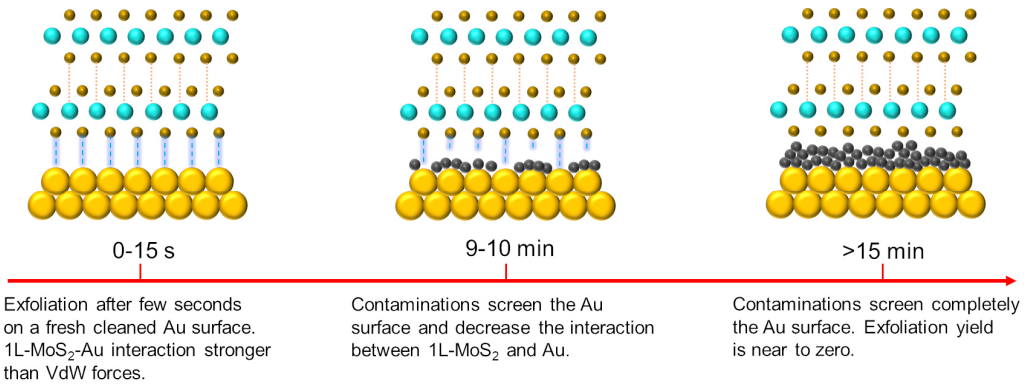

Figure 2.4. - Au-assisted exfoliation yields as a function of the time of gold exposition at air.

roughness of 0.8 nm a larger exfoliation yield of 1L-MoS_2 (~95%) is obtained compared to that obtained on thicker Au substrate with a higher roughness of 5.1 nm[119,121]. The interaction between 1L-MoS_2 and Au with different roughness has also consequences in the optical and vibrational properties of the material. In fact, as observed in **Figure 2.5** (d), the authors reported an anomalous splitting of the A'_1 and a large red-shift of the E', observed on both on a thinner (7 nm) and a thicker (15 nm peeled) gold substrate [121,124]. The main differences between the two cases are the intensity ratio between the two A'_1 components and a further small splitting for the E' when a thicker Au substrate is employed. A further discrepancy, compared to the exfoliated 1L-MoS_2 on SiO_2, is the photoluminescence quenching of the 1L-MoS_2 when it is exfoliated on gold [119,121,124], as shown in **Figure 2.5** (e). These effects have been associated to the strong interaction with Au, but it is still a debated topic. In fact other authors did not observe the anomalous splitting of the A'_1 peak [117-119,122] and a total quenching of the PL when the MoS_2 is supported on Au[128,129].

Overall, the gold assisted approach permits to obtain single-crystalline monolayer MoS_2 on relatively large area (from mm^2 to cm^2) typically limited by the size of the available bulk molybdenite samples. Furthermore, the exfoliation process can be repeated several times in a reproducible way, as shown in the photographs reported in **Figure 2.6** (a). This method is not only limited to MoS_2, but can be extended to other TMDs, as illustrated in **Figure 2.6** (b), which reports a set of 32 optical microscopy images of different layered materials successfully exfoliated on Au thin films.

A main issue for practical applications of the large area TMDs membranes obtained by this approach is their detachment from the gold substrate and transfer to an insulating one, without significant degradation of the membranes' quality. Different

approaches have been presented in the literature to address this point, although a well-established method to transfer 1L-TMDs from Au to other substrates is not currently available. It is worth to note that, notwithstanding the above issues, some applications of as-exfoliated MoS_2 membranes on gold, without any transfer procedure, have been recently proposed [128].

In this context, the strong interaction between the gold substrate and a single thin membrane of MoS_2 is still under study. Also, the vibrational and optical effects induced by the Au on the MoS_2 are source of debate both for their observations and interpretations.

Indeed, it is fundamental to characterize the strain, the doping, and the electrical properties of the exfoliated MoS_2 in contact with Au. In fact, as previously observed in the introductive Chapter1, all these aspects influence severely the optical, vibrational, and electrical properties of the device realized with a single layer of MoS_2. These points will be covered in Chapter 3 and 4 of the experimental sections.

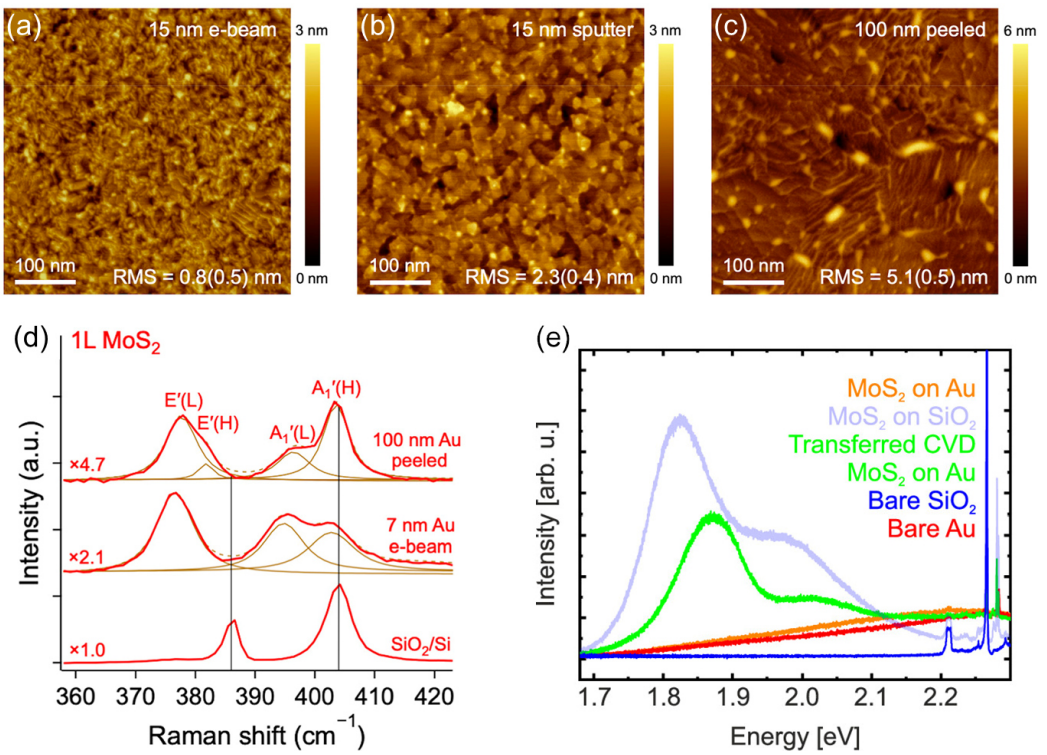

Figure 2.5.- AFM of the Au morphology realized by different technique: (a) e-beam evaporator, (b) sputtering and (c) peeled. (d) Effect of the strong interaction between the MoS_2 and Au (for the peeled and e-beam cases) compared to the SiO_2 counterpart on the Raman spectra. (e) Effect on PL quenching in the MoS_2 on Au compared to the exfoliated and CVD grown MoS2 on SiO_2. Fig.(a-d) adapted from Ref. [121]. Fig.(e) reproduced from Ref. [124].

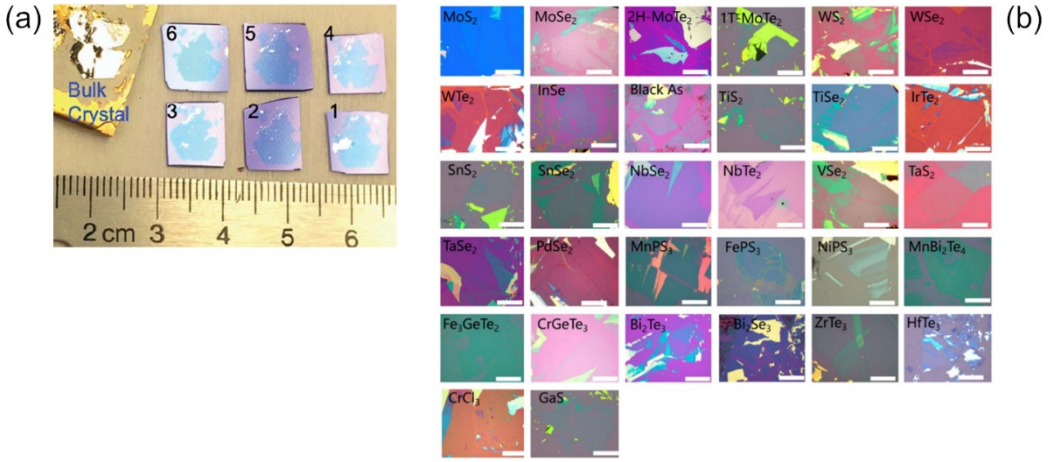

Figure 2.6.- (a) Reproducible process of the mechanical exfoliation assisted by gold from the same bulk crystal. (b) Method applicable to various TMDs materials with high lateral extension. Fig.(a-b) reproduced from Ref. [122].

2.2 MoS_2 PRODUCTION BY BOTTOM-UP APPROACHES

2.2.1 Chemical Vapor Deposition and Sulfurization of Molybdenum film

As discussed in the previous section, the development of scalable methods is necessary for large area scale fabrication of devices based on MoS_2 or other 2D materials. For this reason, wafer-scale synthesis approaches have been already developed in the past for Graphene, such as Chemical Vapor Deposition (CVD) on metal substrates or epitaxial growth on SiC [130,131]. Similar methods have been employed for the synthesis of MoS_2, as the well-known CVD, in which the solid precursors of the Sulphur and Molybdenum react in the vapour phase near or on the heated substrate [132,133]. The scheme of a typical two heating zones CVD system is reproduced in **Figure 2.7** (a), where an argon flux is introduced inside the furnace to transport the evaporated precursors towards the substrate [134]. The nucleation and diffusion of the MoS_2 on the substrate are particularly influenced by different growth

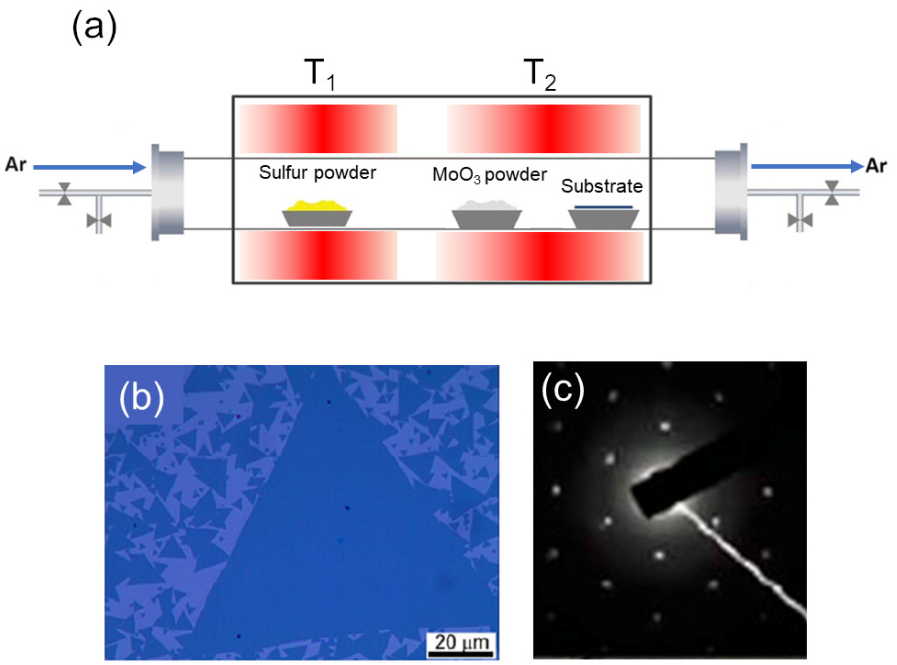

Figure 2.7.- (a) Scheme of the CVD system to realize deposition of MoS_2 from Sulfur and MoO_3 powder. (b) Optical image of triangular MoS_2 realized by CVD. (c) Diffraction of the single-crystal MoS_2 realized by CVD. Fig.(a) reproduced from Ref. [134]. Fig. (b) reproduced from Ref. [145]. Fig.(c) reproduced from Ref. [152].

parameters as temperature of the process [135], carrier gas [136], precursors [137-139] and substrates [140-143]. In fact, it is possible to change the shape and the extension of 1L-MoS_2 flakes from triangular, as shown in **Figure 2.7** (b), to hexagonal geometries by the control of the precursor's ratio [144,145]. Indeed, higher concentration of precursors gives rise to the formation of triangular flakes containing a central nanoparticle constituted by multilayers of MoS_2. Differently, at lower concentration of precursors, monolayer or bilayer are realized in a 2D planar structure without a central multilayer dot [146]. In general, diffraction characterization performed on a single CVD triangular flake shows a high degree of order, as represented in **Figure 2.7** (c). The knowledge of the effects induced on the growth by the different conditions is fundamental to understand and control the mechanism of the process to obtain large area, high crystal quality, single-layer MoS_2 on different substrates. In particular, two main mechanisms have been proposed in literature to describe the phenomenon of MoS_2 growth by CVD technique. In the first, MoO_3 and S vapours react to give an intermediate volatile product $MoO_{3-x}S_y$ that is converted to MoS_2 on the substrate after a further sulfurization process [139,146,147]. A second mechanism proposed does not involve an intermediate reaction process with a reduction of the MoO_3 oxidation state, but the two precursors react in the vapor phase and the MoS_2 products will deposit directly on the substrate [146,148], as illustrated in **Figure 2.8**. In both cases, the reaction products, attaches in preferential regions of the substrate as borders, roughness surface [153], or seed molecules [149,150] forming triangular MoS_2

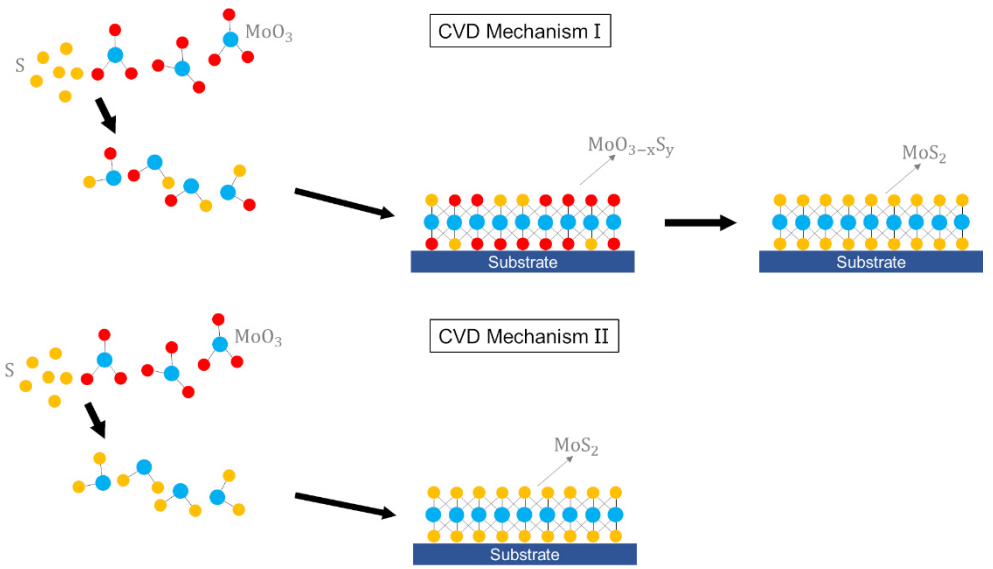

Figure 2.8.- The two CVD mechanism proposed: (I) $MoO_{3-x}S_y$ as an intermediate product between the MoO_3 and S powders. Next the $MoO_{3-x}S_y$ is converted in MoS_2 directly. (II) The two precursors react directly in gas phase forming MoS_2 and next it is deposited on the substrate. Reproduced from Ref. [150].

flakes that maybe coalesce forming a continuous film, as shown in **Figure 2.7** (c). An alternative technique is the two steps CVD, also known as sulfurization of a Mo (or MoO_x) film [150,151]. In this case, an ultra-thin film of Mo (or MoO_x) is pre-deposited on a substrate by physical vapor deposition techniques, as sputtering or thermal evaporation. Next, in a two-zones CVD furnace S powder is evaporated at around 150°C and is transported to the second region (thanks to a flux of carrier gas), where it can react with the MoO_x deposited film, as shown in **Figure 2.9** (a). In this case, the chemisorption of Sulphur occurs directly on this film due to the presence of a large density of MoO_x active sites, which rules the MoS_2 growth until their saturation. The reaction process is illustrated in **Figure 2.9** (b). Despite the better control in terms of thickness and uniformity allowed by the sulfurization process, the MoS_2 film presents a high-level of polycrystallinity with nanograins of the order of 10-30 nm, as observed by the diffraction image of **Figure 2.9**(d), compared to single-crystal flakes obtained from the one-step CVD (**Figure 2.7** (c)). Generally, the crystal quality of the MoS_2 realized by CVD is not the same of that obtained by mechanical exfoliation. In fact, the synthetic approach is source of defects, as grain boundaries and point defects, in the crystal structure of MoS_2 [152-154]. Specifically, we can identify six intrinsic defects induced by the CVD growth, as monosulfur or

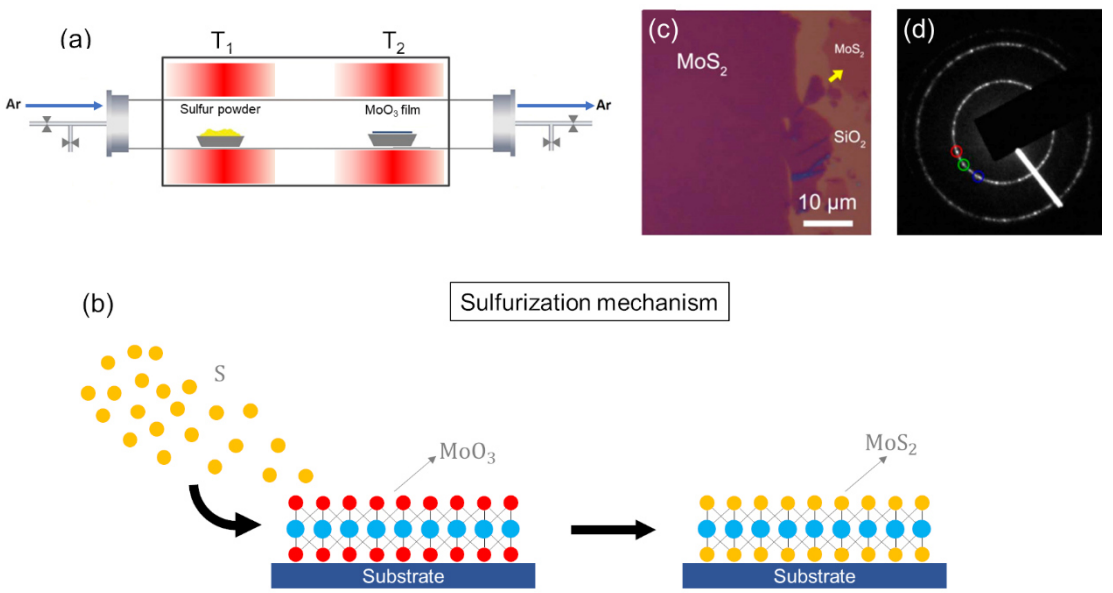

Figure 2.9.- (a) Scheme of the process for sulfurization from a MoO_3 film. (b) Chemisorption mechanism of the sulfurization process(c) Optical image of MoS_2 realized by sulfurization. (c) Diffraction pattern of polycrystalline MoS_2 realized by sulfurization. Fig.(a) reproduced from Ref. [134]. Fig.(b) reproduced from Ref. [150]. Fig.(c-d) reproduced from Ref. [152].

bisulfur vacancies (V_s and V_{S2}) or molybdenum vacancies related to a single or double couple of three nearby sulfur atoms (V_{MoS3} and V_{MoS6}).

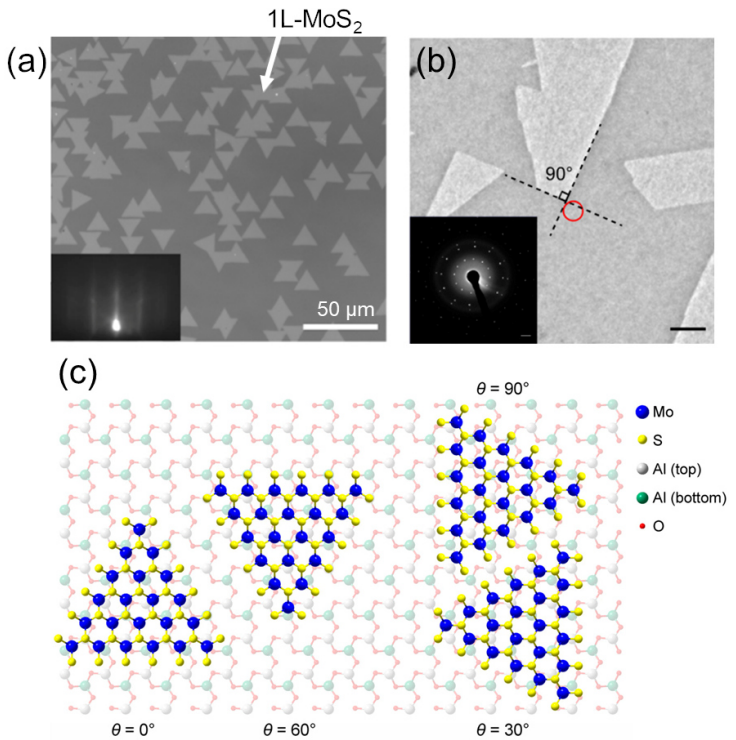

Figure 2.10.-(a) SEM image of 1L-MoS_2 triangles growth by CVD. (b) Low-magnification TEM image and the corresponding diffraction patterns from two merging islands with their edges forming a 90 angle. (c) All the possible orientations of the MoS_2 triangles on the c-sapphire (θ=0°,30°,60° and 90°). Fig.(a-c) reproduced from Ref. [158].

Moreover, antisites defects can be occasionally found when a molybdenum atom replaces a S_2 column or alternatively when a S_2 column substitutes a molybdenum atom (Mo_{S2} and $S2_{Mo}$ respectively) [152,155]. These points defects have consequences on the MoS_2 electronic band structure, introducing unoccupied levels inside the bandgap 0.6 eV below the conduction band[152,155]. Meanwhile grain boundaries can be realized between two different flakes that coalescence during their diffusion over the substrate surface [152,153]. One of the most important consequence of the existence of a high density of points defects and grain boundaries in nanometric regions is the decreasing of the electrical performance (1-2 order of magnitude) of devices realized by sulfurization compared to that realized by mechanical exfoliation [153], estimating high grain boundaries resistance contributions six times higher than that measured in

a single domain [156]. CVD growth of MoS_2 on amorphous SiO_2 substrates gives rise to polycrystalline films with grain boundaries due to the merging of MoS_2 domains with random orientations. The growth on crystalline substrates with hexagonal structure enables the epitaxial growth of MoS_2 domains with precise in-plane orientation, that can be beneficial to reduce the density of grain boundaries when a continuous film is formed. Different authors [157,158] investigated the growth of wafer-scale MoS_2 on c-sapphire by one-step CVD, as illustrated in **Figure 2.10** (a). The RHEED pattern in the inset of **Figure 2.10** (a) demonstrates the structural order of the CVD-growth MoS_2. These monolayer MoS_2 domains show preferential orientations with respect to the c-sapphire. In particular, 0° and 60° edge orientations are the most typical with a small component of domains with an angle of 30° and 90°, as schematically illustrated in **Figure 2.10** (c). It is important to note that triangular groups with the same orientation coalesce forming a continuous MoS_2 film without grain boundaries (**Figure 2.10** (b)), and maintaining the 60°-alignment with the substrates as shown in the inset of **Figure 2.10** (b). Hence, there is a large number of challenges in controlling and understanding the mechanism of MoS_2 CVD growth, to obtain large area single-layer flakes with a high-degree of purity and low-defects density.

2.2.2 Pulsed Laser Deposition

Pulsed laser deposition (PLD) is a valid alternative bottom-up method for the growth MoS_2 on different substrates [159,160]. The principle is a physical deposition that differs from CVD processes in which a chemical reaction occurs before the deposition of the film. The deposition process is carried out in a vacuum chamber where the interaction of a pulsed laser beam with a MoS_2 target gives rise to the formation of a plasma plume. The laser-ablated materials condense on a substrate located on the opposite side of the target, as shown in **Figure 2.11**(a). The main advantage of this approach is the thickness uniformity of the deposited MoS_2 film, that can be realized on different substrates very rapidly, due to the high-deposition rate (10 times higher than the classic sputtering rate) [114]. Serna et al. [161]

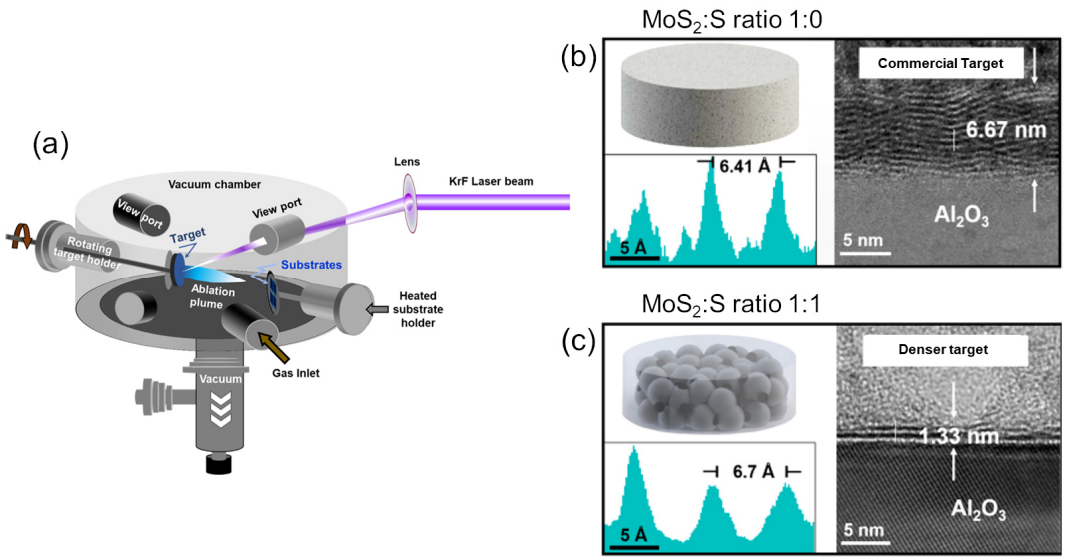

Figure 2.11. – (a) Scheme of the Pulsed Laser Deposition (PLD) system to deposit MoS_2 film on a desired substrate. (b) Effect on the thickness from a conventional commercial target of MoS_2 without sulfur excess (MoS_2:S ratio of 1:0), confirmed by TEM image. The blue spectrum is the interlayer spacing. (c) Effect on the thickness from a denser target of MoS_2 with sulfur excess (MoS_2:S ratio of 1:1), confirmed by TEM image. The blue spectrum is the interlayer spacing. Fig.(a) reproduced from Ref. [109]. Fig(b-c) reproduced from Ref. [161].

demonstrated that is possible to obtain large area (mm^2) MoS_2 indifferently on amorphous, polycrystalline or single-crystal substrates. Optimizing the key parameters such as cooling rate of the substrate, laser fluency, and deposition pressure allows the nucleation and arrangement of the MoS_2 on the desired substrate. In particular, the authors focused their attention on the influence of the MoS_2:S ratio of the target on the features of the deposited layered film. Employing a conventional target (MoS_2:S ratio is 1:0) without sulfur excess, it is simple to obtain vertically

stacked multilayers of MoS_2, as represented in **Figure 2.11**(b). Meanwhile, thinner films of MoS_2 characterized by an interlayer spacing close to the theoretical value of 6.5 A are obtained with the largest MoS_2 particle size and a MoS_2/S ratio of 1:1, as shown in **Figure 2.11**(c). The thickness of the MoS_2 film results inversely proportional to the density of the target, due to the lower ablation rates from denser targets [161]. Indeed, the excess of the sulfur from the target produces a sulfurization environment that allows to realize a more stoichiometric MoS_2 deposited film.

As described for CVD processes, also in this case the main issues are related to the crystal quality and the grains dimensions of the deposited MoS_2 film. In a recent paper, Bertoldo et al. [162] carefully describe the intrinsic defects in MoS_2 grown by PLD through atomic resolution characterizations which have been compared to first-principle calculations. Sulfur vacancies and substitutional Mo defects are the main defects found in PLD grown MoS_2, with an average density of 0.378 nm^{-2} and 0.126 nm^{-2} for V_s and Mo_S, respectively [162]. Differently, the main defects found in MoS_2 prepared by CVD or mechanical exfoliation are intrinsic single sulfur vacancies (V_s) density up to 0.12 nm^{-2} [155,162]. In addition to the vacancies and substitutional defects, the authors observed a wide variety of defects associated with grain boundaries (GBs), as shown in **Figure 2.12**(a-d). These GBs are inherently formed after the coalescence of nanometer size grains and this result is a common feature of one-step synthesis of 2D TMDs by PLD [162]. The growth of the second layer follows the GBs or the edges of the nanometric grains, maintaining typically the orientation of the bottom MoS_2 layer. But the authors found also Moiré patterns with twist angle of 23°, 27°, 33° and 44°, as shown in **Figure 2.12**(c-d). In the false-colored Fast Fourier Transform (FFT) filtered image of **Figure 2.12**(c) is possible to observe three

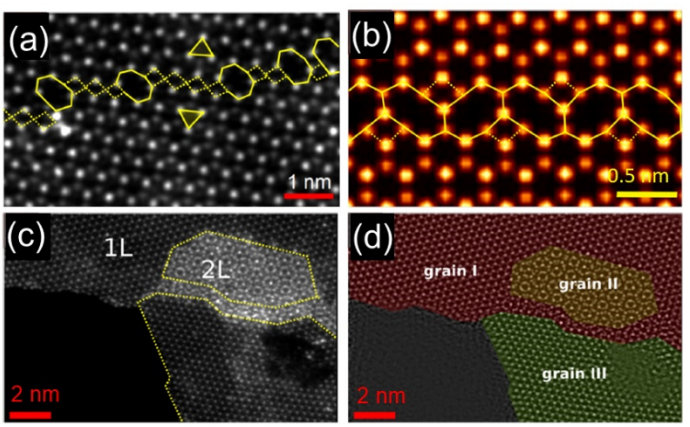

Figure 2.12.- (a) High resolution ADF STEM image and simulation (b) of Grain boundaries lines in MoS_2 grown by PLD. (c) ADF STEM image and (d) false colored Fast Fourier Transform (FFT) in a mono-bilayers MoS_2 region characterized by Moiré fringes. Fig.(a-d) reproduced from Ref. [162].

different grains with Moiré fringes formed after the overlapping of the grain I and II. Thus, the authors confirmed the higher defects density and the small grains dimension in MoS_2 realized by PLD. These remain the main issues of the technique that are still under study to improve the growth method.

2.2.3 Molecular Beam Epitaxy

As previously discussed, both CVD and PLD processes lead to the formation of polycrystalline MoS_2 structures. In particular, MoS_2 films grown by PLD exhibit a higher density of defects and grain boundaries compared to the CVD approach. Molecular Beam Epitaxy (MBE) is an alternative approach for the growth of high purity crystalline films that may be epitaxial over the substrate. The very high purity sources (99.9999%), the ultra-high vacuum (10^{-8}-10^{-12} Torr) environment of the system and the very low growth rate permits to control with atomic layer precision the thickness and the epitaxy of the vertical heterostructures with low defects density[163-165]. In the MBE system, the solid precursors are heated in two different cells (or evaporators) until their sublimation. The evaporated atoms do not interact with each other during their flow in the vacuum chamber, and the two precursors react after the condensation on the substrate [166,167]. The ultra-high vacuum environment allows to realize in situ characterizations of the samples by reflection high energy electron diffraction (RHEED) to control the crystal structure,

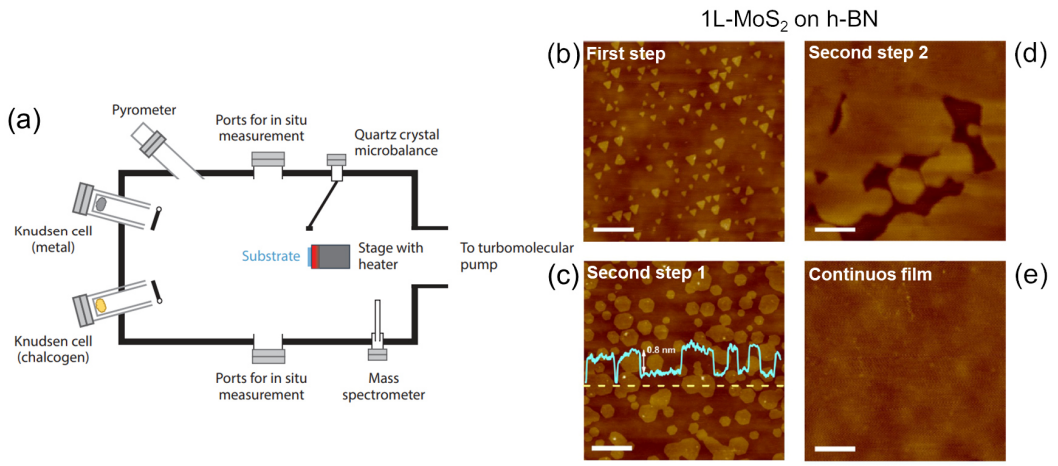

Figure 2.13.- (a) Molecular Beam Epitaxy set-up for TMDs growth. (b) Triangles of MoS_2 on h-BN. (c) Hexagonal MoS_2 grains and their extension (d) on h-BN. (e) Continuous thin film of MoS_2 on h-BN. Fig.(a) reproduced from Ref. [167]. Fig.(b-e) reproduced from Ref. [173].

morphology, and thickness in real time, as shown in **Figure 2.13**(a). It is worth to note that the epitaxy of 2D TMDs characterized by inert surfaces cannot be described by classical three-dimensional materials growth mechanism such as Frank-van der Merwe, Volmer-Weber or Stranski-Krastanov[166,168].

The very weak vdW interaction between the substrate and the epilayer (and also between successive layers) is different compared to the strong covalent in-plane bonding. For this reason, other kinetic considerations, as diffusion and nucleation, have to be added to the classical thermodynamics' models [166]. For this reason, TMDs epitaxial growth is influenced by different growth conditions and kinetics factors, such as adsorption, desorption, diffusion, attachment, and edges diffusion[166]. The full control of these parameters is complex, and this makes MBE a very difficult technique for the growth of TMDs, such as single crystal MoS_2[166,169]. Indeed, the substrate plays a crucial role for the epitaxial growth. It was demonstrated that thin films of TMDs grown on non-vdW substrates seems to have a lower crystal quality compared to other 2D TMDs substrate [166,170-172]. Fu et al. [173] demonstrated the realization of extended single-crystal of 1L-MoS_2 by two-steps MBE growth process. In a first step, the temperature was fixed at 750°C and the Mo and S molecular beams are introduced to react on the substrate surface for 3-4 h, realizing the formation of isolated MoS_2 triangles on h-BN, as shown in **Figure 2.13**(b). Next, a second step is characterized by an increasing of the temperature to 950°C and a decreasing of the Mo flux. And after a control of the flux ratio, the flakes change their shape from triangles to hexagons, as shown in **Figure 2.13**(c).The growth process continues for 6-7h until the entire covering of the h-BN substrate, as represented in **Figure 2.13**(d-e), is reached. Thus, the ability to control the domains orientation to suppress grain boundaries and the optimization of the growth parameters to optimize the process both on passivated substrates and crystalline surfaces are still challenges in the van der Waals epitaxial growth of MoS_2.

2.3 MoS_2 INTEGRATION WITH SEMICONDUCTORS FOR ELECTRONICS AND OPTOELECTRONICS

In the last 50 years, the heterojunctions formed by the combination of semiconductors with different energy bandgap represented the key building blocks of many electronics and optoelectronic devices, including transistors, light emitting diodes and lasers.

Three main band alignment configurations can be obtained at the junction between a narrow-bandgap and wide-bandgap semiconductors, depending on the electron affinities of the two materials, as schematically illustrated in **Figure 2.14. Type-I** (*straddling*) band alignment is obtained when the energy gap of the wide-band gap semiconductor overlaps completely the band gap of a narrow-bandgap semiconductor. Differently, a **type-II** (*staggered*) alignment is realized when the two bandgaps are partially overlapped. Finally, a **type-III** (or "*broken-gap"*) alignment is obtained when the energy band gap of the narrow-bandgap semiconductor is completely external to that of the wide-band gap material.

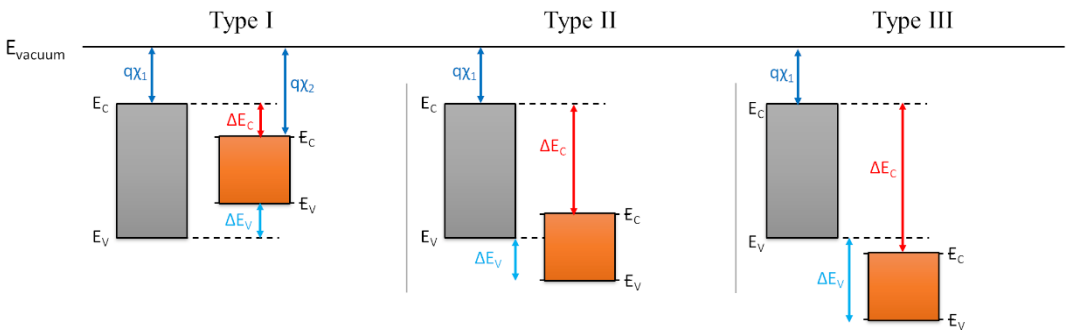

Figure 2.14.-Three types of band gap alignment: (I) Straddling, (II) Staggered and (III) Broken-gap.

When the two semiconducting materials exhibit the same doping type, an isotype (n/n or p/p) heterojunction is formed. On the other hand, for differently doped semiconductors, anisotype heterojunctions (p/n or n/p) are obtained.

These different band-alignment configurations can be conveniently exploited for the realization of electronic/optoelectronic devices with specific functionalities, such as

heterojunction diodes, band-to-band tunnelling diodes, light-emitted diodes (LEDs), photodetectors and solar cells.

Traditionally, semiconductor heterostructures are obtained by epitaxial growth techniques, such as molecular beam epitaxy (MBE), chemical vapour deposition (CVD) or metal-organic-chemical vapour deposition (MOCVD). However, a close matching of in plane lattice parameters is required to achieve a good quality hetero-epitaxial interface between a thin film and a substrate. Lattice constants mismatch typically results in the growth of strained films, with the presence of a certain density of defects, e.g. dislocations. Furthermore, structural relaxation of such films with formation of cracks is typically observed beyond a critical thickness.

The advent of 2D materials, in particular semiconducting TMDs, opened new frontiers for the fabrication of semiconductor heterojunctions, overcoming the limitations of traditional epitaxial growth technique. In fact, due to their ultra-flat and dangling-bond free surface, 2D materials can form vdW heterostructures not only with other layered materials, but also with traditional bulk (3D) semiconductors. These heterostructures can be obtained either by the top-down (exfoliation and transfer) or by the bottom-up approaches discussed in the first part of this chapter. The new properties derived by these 2D/3D vdW combinations are currently intensively explored to develop new device concepts, exploiting the vertical current transport through the heterostructure [174-182].

In the following, the state of the art of MoS_2 integration with silicon and with wide-bandgap hexagonal semiconductors (SiC, GaN) is discussed, showing some relevant examples from the literature.

2.3.1 MoS_2 integration with Silicon

Since silicon is still the leading semiconductor for CMOS applications, several efforts have been carried out in the last years to integrate TMDs, in particular MoS_2 with the Si platform.

Figure 2.15 illustrates the band diagrams of Si and (a) few layers (FL) and (b) 1L of MoS_2 separated by vacuum, calculated considering the relevant parameters (electron affinity χ and energy bandgap E_g) of these material systems [183]. A type-II band alignment can be observed in both cases. A valence band discontinuity $\Delta E_V \approx 0.6$ eV and a conduction band discontinuity $\Delta E_C \approx 0.4$ eV was evaluated for FL-MoS_2/Si

heterojunction, whereas $\Delta E_V \approx 1$ eV and $\Delta E_C \approx 0.2$ eV were obtained for 1L-MoS_2/Si heterojunction.

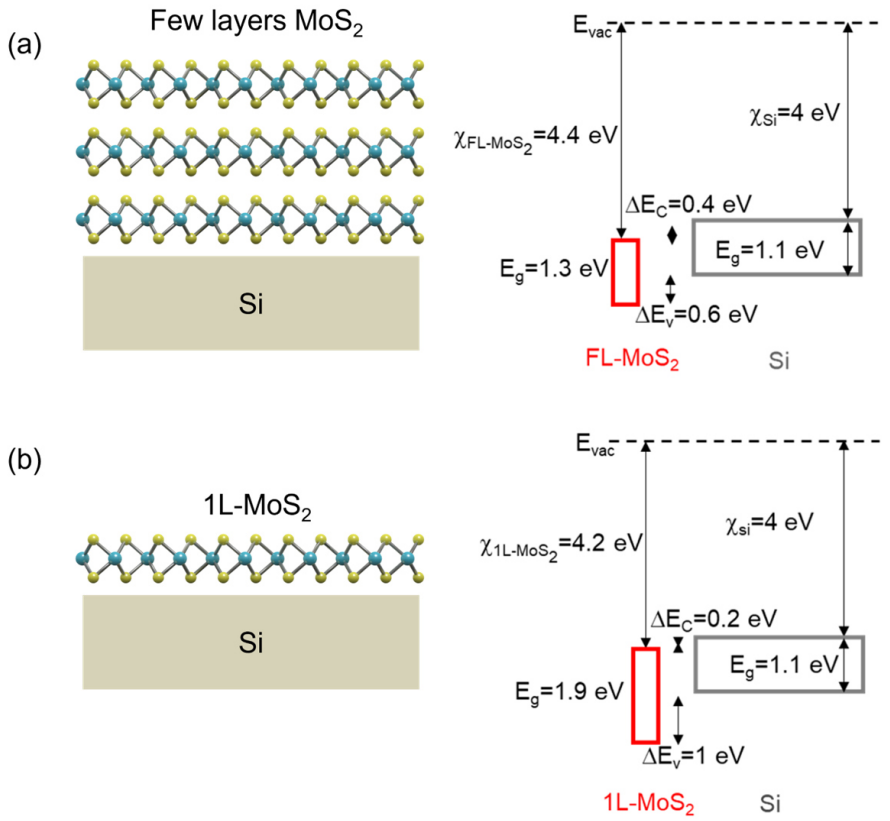

Figure 2.15.- Calculated band alignment at the vdW interface between Si and few layers MoS_2 (a) and 1L-MoS_2 (b).

The valence band discontinuity at the vdW interface between exfoliated FL-MoS_2 and p-type doped Si has been also evaluated experimentally by the combination of X-ray (XPS) and ultraviolet photoelectron spectroscopy (UPS) [184]. **Figure 2.16** (a) and (b) show the core level and valence band spectra for MoS_2 and Si samples before the junction formation, from which the energy separations of the $Mo3d_{5/2}$ and $Si2p_{3/2}$ core levels from the respective valence band maxima (VBM) were obtained:

$$E^{MoS_2}_{Mo3d_{5/2}} - E^{MoS_2}_{VBM} = 228.54 \text{ eV and } E^{Si}_{Si2p_{3/2}} - E^{Si}_{VBM} = 99.03 \text{ eV} \qquad (9)$$

Figure 2.16 (c) shows the Mo 3d and Si 2p core levels for the MoS_2/Si heterojunction, from which the energy separation $E^{MoS_2/Si}_{Mo3d_{5/2}} - E^{MoS_2/Si}_{Si2p_{3/2}}$=130.17 eV was measured. Finally, the valence band discontinuity was evaluated as:

$$\Delta E_v = \left(E^{MoS_2/Si}_{Mo3d_{5/2}} - E^{MoS_2/Si}_{Si2p_{3/2}}\right) - \left[\left(E^{MoS_2}_{Mo3d_{5/2}} - E^{MoS_2}_{VBM}\right) - \left(E^{Si}_{Si2p_{3/2}} - E^{Si}_{VBM}\right)\right] \quad (10)$$

The experimental value of ΔE_V=0.66±0.17 eV obtained by this approach was in close agreement with the calculated value in **Figure 2.15**(a), confirming the type II band alignment between FL-MoS_2 and Si.

To date MoS_2 integration on Si has been mainly obtained by exfoliation from bulk molybdenite or by transfer of CVD grown MoS_2. **Figure 2.17** (a) illustrates a recently demonstrated 1L-MoS_2/p-Si heterojunction device obtained by transfer of

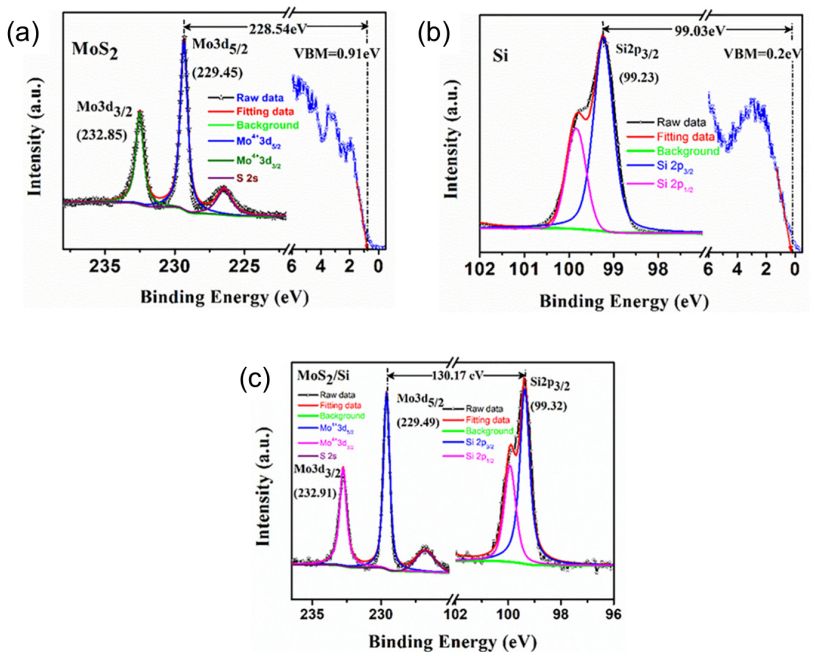

Figure 2.16.- X-ray and ultraviolet photoelectron spectroscopy spectra of (a) Mo 3d and (b) Si 2p core levels from which is estimated the separation $E_{Mo3d5/2}$ - $E_{Si2p3/2}$. (c) Core level and valence band spectra for MoS_2 / Si junction, from which the energy separation of the $Mo3_{d5/2}$ and $Si2_{p3/2}$ is estimated. Fig.(a-c) reproduced from Ref. [184].

MoS_2 on a silicon surface partially covered by a SiO_2 insulating mask [185]. A gold electrode was deposited as a source contact on MoS_2, while the drain contact was fabricated on the p-Si sample. A ~30 nm thick HfO_2 dielectric was used to encapsulate the MoS_2 surface. **Figure 2.17** (b) illustrates the band alignment of the unintentionally n-type doped MoS_2 and p-type Si before the junction formation (i), at equilibrium (ii) and under forward bias polarization (iii). As a result of the built-in potential generated at the anisotype (n-p) heterojunction, the current-voltage (I_d-V_d) characteristic of the device exhibits a rectifying behaviour, as illustrated in in **Figure 2.17** (c). The electroluminescence characteristics of this diode under forward bias polarization were also investigated, and a typical electroluminescence spectrum measured at V_d=5.5 V is reported in **Figure 2.17** (d). Light emission is due to the radiative recombination between electrons and holes injected from the two sides of the heterojunction, as schematically illustrated in the panel (iii) of **Figure 2.17** (b).

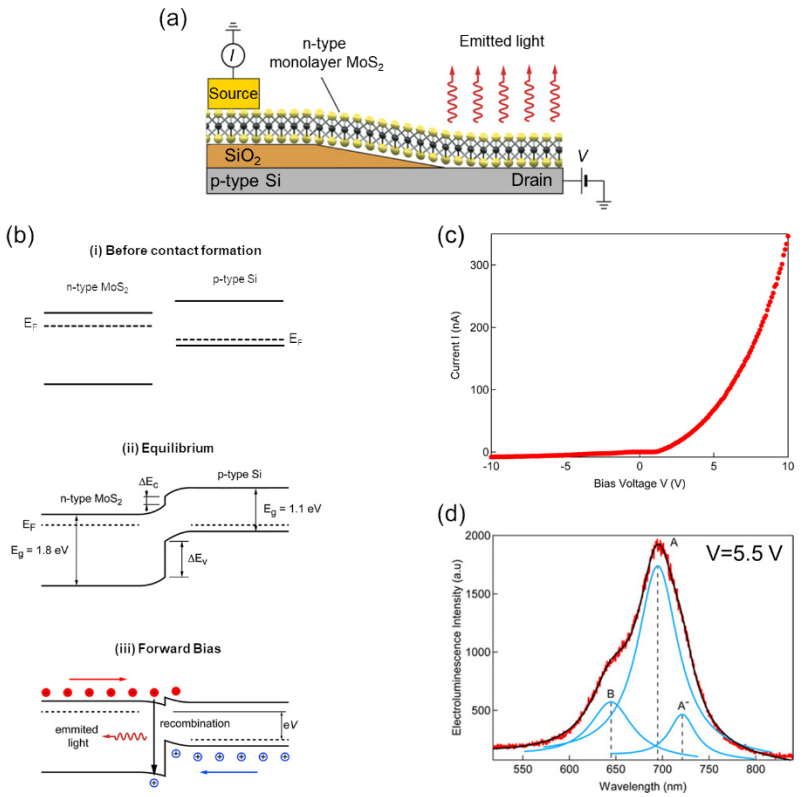

Figure 2.17.- (a) Cross section representation of an heterojunction diode composed by p-Si and n-type 1L-MoS_2. (b) Band diagrams of the heterostructure before the junction formation (i), at equilibrium (ii) and under forward bias polarization (iii). (c) I_d vs V_d characteristics of the diode showing rectifying behavior. (d) Electroluninescence spectrum showing two excitonic components (A, B) and trionic component (A^-). Fig.(a-d) reproduced from Ref. [185].

Noteworthy, the electroluminescence spectrum in **Figure 2.17** (d) resembles a characteristic PL spectrum of MoS_2, with three different spectral contributions associated to the two excitonic peaks A and B and to the trion A^- resonance, respectively. This confirms that the radiative transition occurs in the direct bandgap 1L-MoS_2 rather than in the indirect bandgap Si. This kind of device was also used as a photovoltaic cell able to convert incoming light to electric power with an efficiency of 4.4% [185].

2.3.2 *MoS_2 heterostructures with wide-bandgap semiconductors*

While silicon still remains the leading semiconductor material for logic applications and low-power electronics, the wide bandgap (WBG) semiconductors [186-190], such as 4H-SiC and GaN, are the materials of choice for high-power and high frequency electronics, and for many optoelectronics devices (light emitting diodes, UV photodetectors), due to their excellent physical properties [191], as high critical electric field, thermal conductivity, and large band gap.

In the last years, the integration of TMDs, in particular MoS_2, with GaN and 4H-SiC has been explored by different research groups to realize 2D/3D vdW semiconductor heterojunctions. To date both top-down and bottom-up approaches have been employed to integrate MoS_2 on these WBG materials. These include the transfer of MoS_2 flakes exfoliated from bulk crystals [192-194], or grown on foreign substrates [196-197], and the direct deposition of MoS_2 on GaN [198-200] or 4H-SiC[201,202].

A key aspect which favours the direct epitaxial growth of TMDs on 4H-SiC and GaN is the hexagonal structure with good lattice matching on the (0001) basal plane. **Figure 2.18** reports the energy bandgap and the in-plane lattice constant of bulk hexagonal semiconductors (4H-SiC, GaN and InN) and some members of the layered TMDs family, i.e. MoS_2 (bulk and monolayer), WS_2, ReS_2, TiS_2, ZrS_2 and HfS_2. This plot shows a very good lattice matching of MoS_2 with 4H-SiC and GaN basal planes.

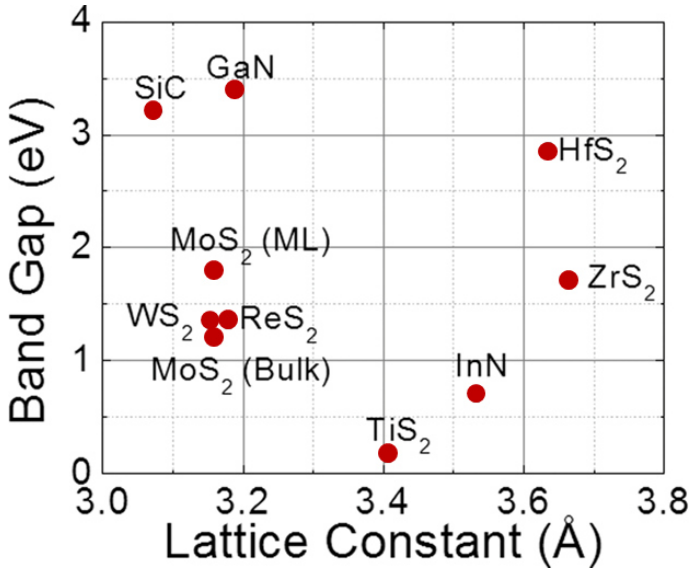

Figure 2.18.- Band gap vs lattice constant. Figure reproduced from Ref. [202].

In particular, the lattice constants of MoS_2 (a_{MoS2}=3.162 Å) and 4H-SiC (a_{4H-SiC}=3.073 Å) exhibit a ~2.9% mismatch. A very low mismatch (<1%) can be also observed for MoS_2 with the GaN basal plane.

Despite lattice matching is not necessary to realize a 2D/3D vdW heterostructure by transfer of a 2D material on a bulk substrate, it has been found to be very beneficial for the direct CVD growth of MoS_2 on hexagonal crystalline substrates. The nucleation and growth of triangular MoS_2 domains with well-defined orientations on crystalline sapphire substrates [200] has been already discussed in the first part of this chapter.

Similarly, the very good lattice matching between MoS_2 and GaN allowed the formation of highly oriented and nearly unstrained triangular MoS_2 domains during single step CVD at temperatures of 700 – 800 °C [200], as shown in **Figure 2.19**. Epitaxial MoS_2 growth on GaN has been also obtained by the pulsed laser deposition (PLD) technique [203]. Few layers or monolayer MoS_2 films on the SiC(0001) surface have been also reported by single step CVD [201] or by the sulfurization of pre-deposited Mo thin films [204]. Highly crystalline few layers MoS_2 on SiC(0001) have been also obtained by PLD at substrate temperature of 700 °C [203].

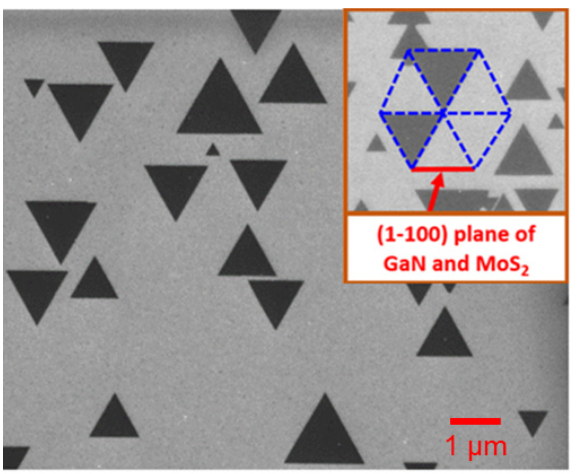

Figure 2.19.- Rotationally aligned epitaxial growth of MoS_2 triangles during CVD on the (0001) basal plane of GaN. All the triangle basis are parallel to the [1-100] direction. Reproduced from Ref. [200].

2.3.2.1 MoS_2/GaN band alignment and heterojunction devices

Figure 2.20 illustrates the band alignment at the vdW interfaces between GaN and few-layers MoS_2 (a) or 1L MoS_2 (b), separated by vacuum (i.e. before contact formation), calculated considering the literature values of the electron affinity (χ) and energy band (E_g) for these materials.

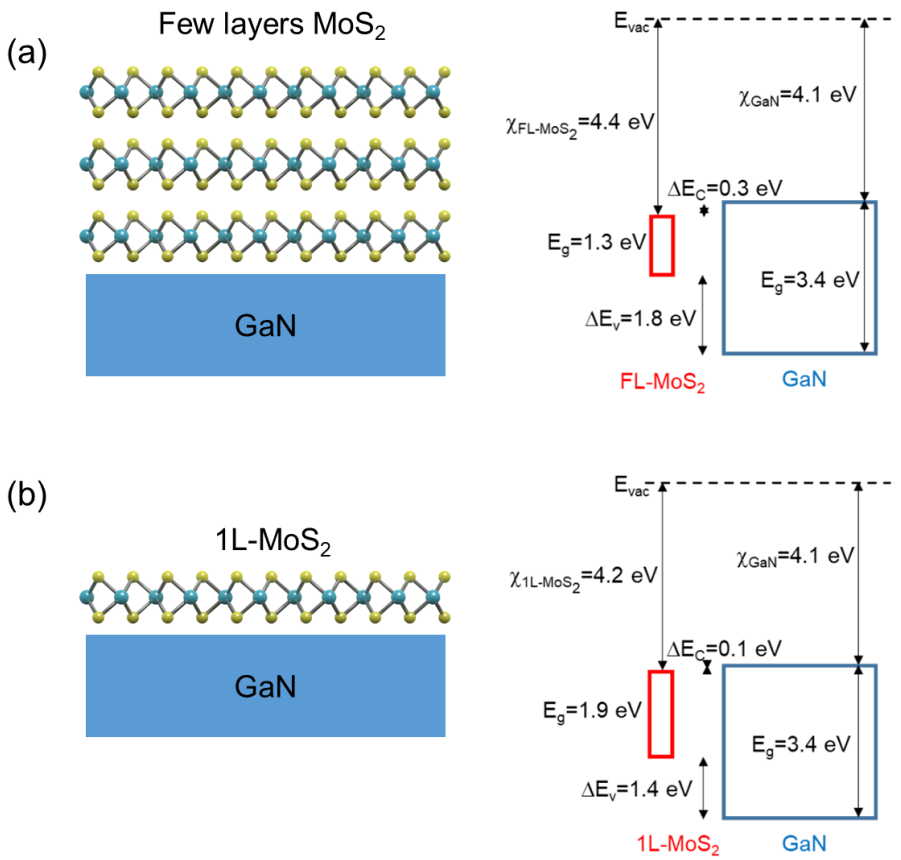

Figure 2.20.- Calculated band alignment at the vdW interface between GaN and few layers MoS_2 (a) and 1L-MoS_2 (b).

According to these diagrams, a type I band alignment is ideally expected after contact formation between GaN and FL-MoS_2 or 1L-MoS_2. Furthermore, a large valence band discontinuity ($\Delta E_v \approx 1.8$ eV for FL-MoS_2/GaN and $\Delta E_v \approx 1.4$ eV for 1L-MoS_2/GaN) and a small conduction band discontinuity ($\Delta E_c \approx 0.3$ eV for FL-

MoS_2/GaN and $\Delta E_v \approx 0.1$ eV for 1L-MoS_2/GaN) is predicted for these heterostructures.

Recently, Zhang et al. [205] employed XPS and UPS analyses to experimentally evaluate the valence band offset ΔE_c in 1L-MoS_2/GaN heterojunctions fabricated by MoS_2 transfer on a GaN surface pre-treated with a remote plasma nitridation. **Figure 2.21** (a) and (b) show the core level spectra (Mo 3d and Ga 2p) and the valence band spectra collected separately on 1L-MoS_2 and GaN samples before the transfer process, whereas the core levels measured on 1L-MoS_2/GaN interface after contact formation are reported in **Figure 2.21** (c). The ΔE_v value is calculated from the energy separation $E^{MoS_2}_{Mo3d_{5/2}} - E^{MoS_2}_{VBM} \approx 228.6 \pm 0.1\ eV$ of the Mo $3d_{5/2}$ peak from the VBM in the MoS_2 sample (a), the separation $E^{GaN}_{Ga2p_{3/2}} - E^{GaN}_{VBM} \approx 1115.2 \pm 0.1\ eV$ of the Ga $2p_{3/2}$ peak from VBM in the GaN sample (b), and the energy difference

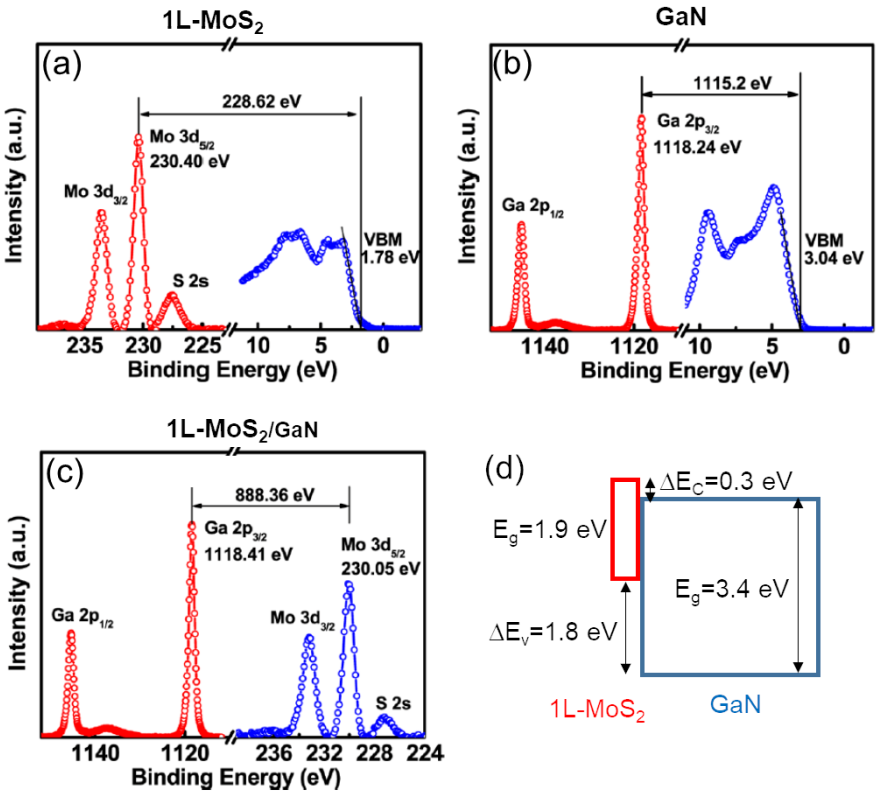

Figure 2.21.- (a) Mo 3d core level and valence band spectra of 1L-MoS_2, (b) Ga 2p and valence band spectra of GaN before junction formation. (c) Core level spectra measured on 1L-MoS_2/GaN after the junction's formation. (d) Band-diagram of the 1L-MoS_2/GaN system evaluated from the experimental ΔE_v value of 1.8 eV, indicating the formation of a type II heterostructure. Figure adapted from Ref. [205].

$E^{MoS_2/GaN}_{Mo3d_{5/2}} - E^{MoS_2/GaN}_{Ga2p_{3/2}} \approx 888.4 \pm 0.1\ eV$ between the Ga $2p_{3/2}$ and Mo $3d_{5/2}$ peak in the 1L-MoS_2/GaN heterostructure, according to the equation:

$$\Delta E_v = \left(E^{MoS_2/GaN}_{Mo3d_{5/2}} - E^{MoS_2/GaN}_{Ga2p_{3/2}}\right) - \left[\left(E^{GaN}_{Ga2p_{3/2}} - E^{GaN}_{VBM}\right) - \left(E^{MoS_2}_{Mo3d_{5/2}} - E^{MoS_2}_{VBM}\right)\right] \approx 1.8 \pm 0.1 \text{ eV} \quad (11)$$

Other experimental investigations reported typical values of the ΔE_v around 1.8 – 1.9 eV both for 1L-MoS_2 and multilayer MoS_2 junctions with GaN [194,206].

Noteworthy this experimental ΔE_v value of ~1.8 eV is significantly larger than the ideal one (~1.4 eV) estimated from the electron affinity and bandgap values of 1L-MoS_2 and GaN (see **Figure 2.20** (b)). This indicates the occurrence of significant charge transfer at the interface during the heterojunction formation. The resulting band diagram of the 1L-MoS_2/GaN system evaluated from the experimental ΔE_v is

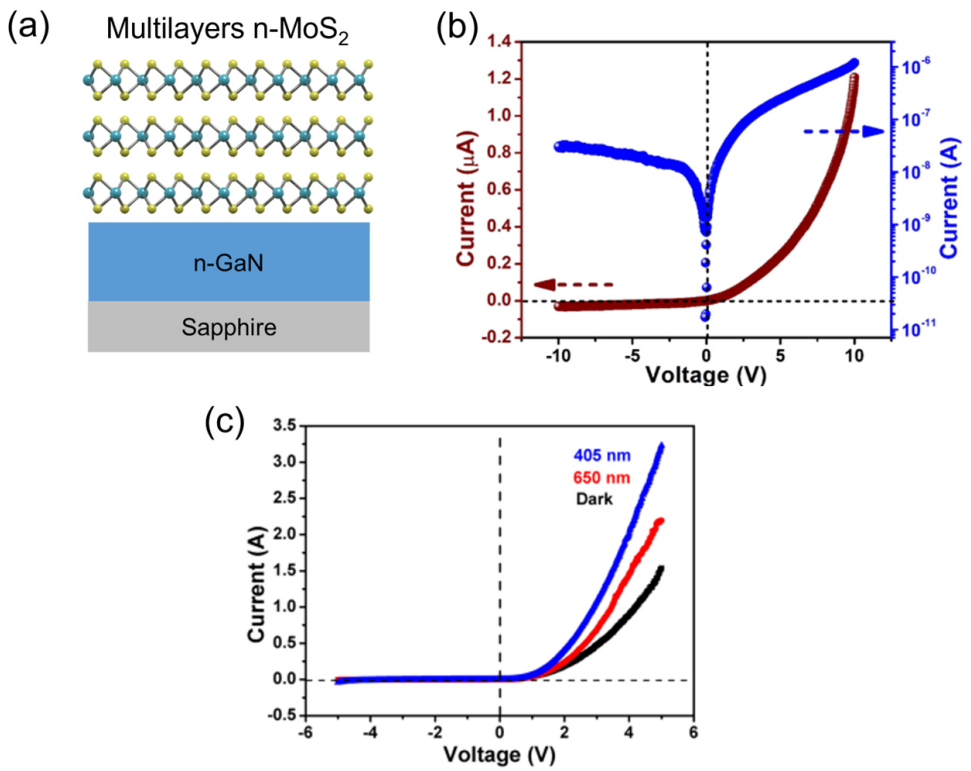

Figure 2.22.- (a) Setup of multilayers n-type MoS_2 exfoliated on n-GaN/sapphire. (b) Current-voltage characteristics of the heterojunction diode in linear (red curve) and semi-log scale (blue curve). (c) Photoelectrical behaviour of the diode under illumination at 405 and 650 nm. Fig.(b-c) reproduced from Ref. [195].

reported in **Figure 2.21**(d), showing the formation of a type II heterojunction with a small conduction band offset $\Delta E_c \approx 0.3$ eV.

An example of MoS_2/GaN heterojunction is described in **Figure 2.22** (a), where the unintentionally n-type doped MoS_2 is obtained by mechanical exfoliation on n-type GaN/sapphire. The doping estimated by Hall measurements is of 4.6×10^{17} cm^{-3} for GaN and $\sim10^{16}$ cm^{-3} for the n-MoS_2. This isotype heterojunction shows a typical rectifying diode behaviour, represented in **Figure 2.22** (b), both in linear (red curve) and semi-log scale (blue curve). Despite a rectifying trend, the diode shows a low rectification ratio ($<10^2$) that can be associated to the low conduction band offset between the n-MoS_2 and the n-GaN. In fact, a lower conduction band offset causes an unavoidable current transport and consequently the diode permits the flow of current both in reverse and forward bias. In particular, the authors estimated a $\Delta Ec \sim 0.23$ eV, comparable to experimental value extracted previously by XPS analysis and associated to type II band alignment. Noteworthy, the current conduction in this n-MoS_2/n-GaN diode increases under illumination with laser wavelengths at 405 and 650 nm, as reported in **Figure 2.22** (c). Hence, this isotype heterojunction shows potential for photodetection applications.

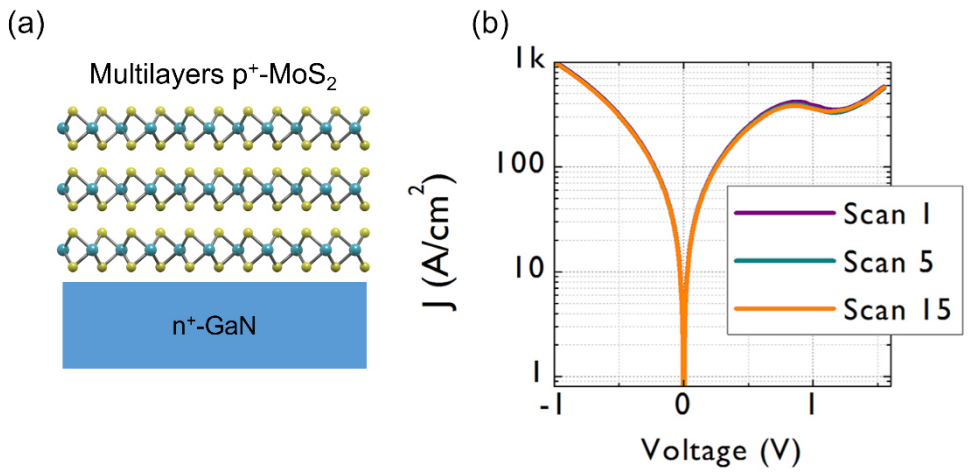

Figure 2.23.- (a) Setup of multilayers p^+-type MoS_2 grown by sulfurization and transferred on n^+-GaN/sapphire. (b) Current-voltage characteristics of the heterojunction diode in semi-log scale for three different scans, showing the negative differential resistance under forward bias. Fig.(b) reproduced by Ref. [196].

In comparison to the previous diode, a different result is obtained in the case of a high-doped anisotype heterojunction composed by p^+-MoS_2 on n^+-GaN, as shown in **Figure 2.23** (a). The n^+-GaN epitaxy, with a doping of $\sim5\times10^{19}$ cm^{-3}, was grown on a n-GaN/sapphire substrate by MBE. The p-type doped MoS_2 was obtained by the

sulfurization of stacked Mo/Nb/Mo thin films on sapphire at 1100°C. In fact, Nb is known to induce p-type doping of MoS_2, as discussed in the Chapter 1. Next, the p-MoS_2 was transferred on n^+-GaN by PMDS transfer process [196]. The electrical characteristic of the diode is represented in **Figure 2.23** (b). Here, the system shows a very high current in reverse bias even at low voltage, while a negative differential resistance is observed under forward bias, which is typical of the interband tunnelling in the Esaki diodes. The authors explained the occurrence of this tunnelling phenomenon by a low conduction band offset of $\Delta E_c \approx 0.2$ eV and the narrow depletion regions of degenerately doped p^+-MoS_2 and n^+-GaN [196]. Hence, substitutional p^+-doping of multilayer MoS_2 by Nb was shown to be appropriate for the realization of Esaki diodes based on the anisotype p^+-MoS_2/n^+-GaN heterojunctions.

2.3.2.2 MoS_2/4H-SiC band alignment and heterojunction devices

Figure 2.24 shows the schemes and the corresponding band alignment of the vdW interfaces before the contact between few-layers of MoS_2 (a) and 1L-MoS_2 (b) on 4H-SiC. Also in this case, the calculation of the band alignment was realized employing theoretical values of electron affinity and of the band gap for both the semiconductors. Similarly to the integration on GaN, FL-MoS_2 seems to give type I band alignment with 4H-SiC, characterized by a low valence band offset ($\Delta E_v \approx 0.7$ eV) and a larger conduction band offset ($\Delta E_c \approx 1.1$ eV). A similar type I configuration is predicted also in the 1L-MoS_2 on 4H-SiC. In this case, the valence band offset ($\Delta E_v \approx 0.3$ eV) is lower compared to the FL-MoS_2/4H-SiC one, while a similar value of $\Delta E_c \approx 1.0$ eV is expected. Differently than for MoS_2/GaN heterojunctions, only few experimental works have been published on the band alignment at MoS_2/4H-

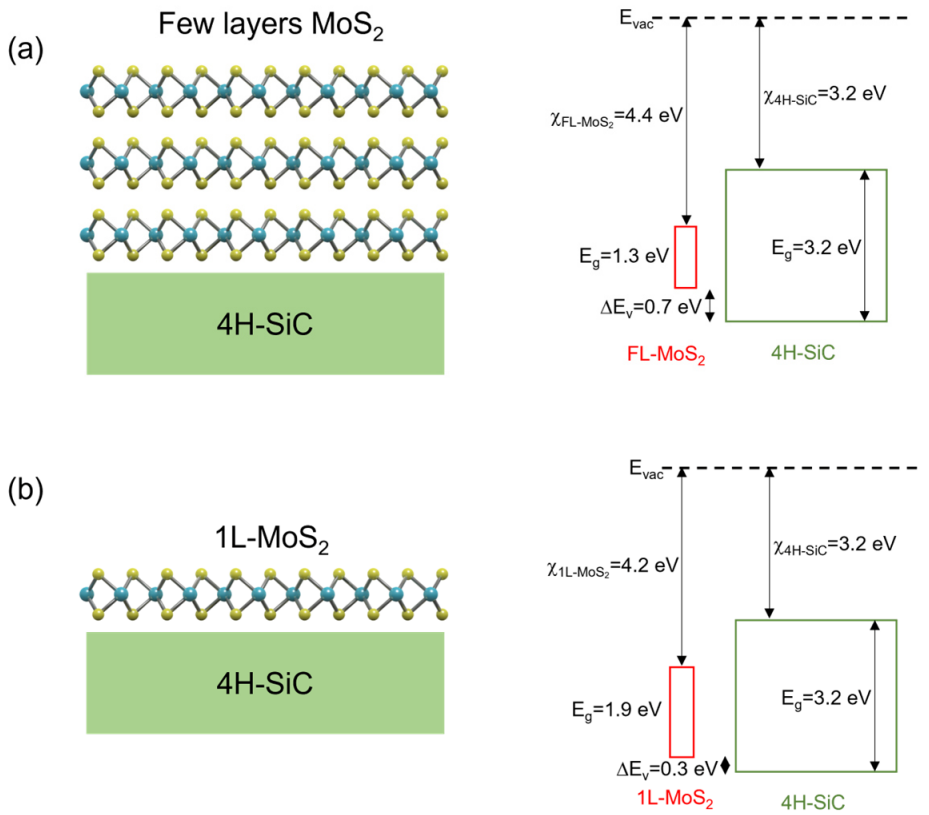

Figure 2.24.- (a) Scheme of the few-layers MoS_2 grown on 4H-SiC and corresponding band alignment. (b) 1L-MoS_2 grown on 4H-SiC and the corresponding band alignment between the two semiconductors.

SiC interface. Recently, Xiao et al. [201] carried out a XPS analysis to determine the valence band spectra of multilayer MoS_2, (**Figure 2.25** (a)), of 4H-SiC (**Figure 2.25** (b)) and their heterostructures (**Figure 2.25** (c)). From this investigation, they deduced $E^{MoS_2}_{Mo3d_{5/2}} - E^{MoS_2}_{VBM} \approx 228.59$ eV, $E^{SiC}_{SiC\ 2p} - E^{SiC}_{VBM} \approx 101.38$ eV, and

$$E^{MoS_2/SiC}_{Mo3d_{5/2}} - E^{MoS_2/SiC}_{SiC\ 2p} \approx 127.45 \text{ eV} \qquad (12)$$

Thus, the authors evaluated a valence band offset of 0.24 eV with the formation of a type II heterojunction, as shown in **Figure 2.25** (d), in contrast with the previous theoretical predictions of a type I heterostructure.

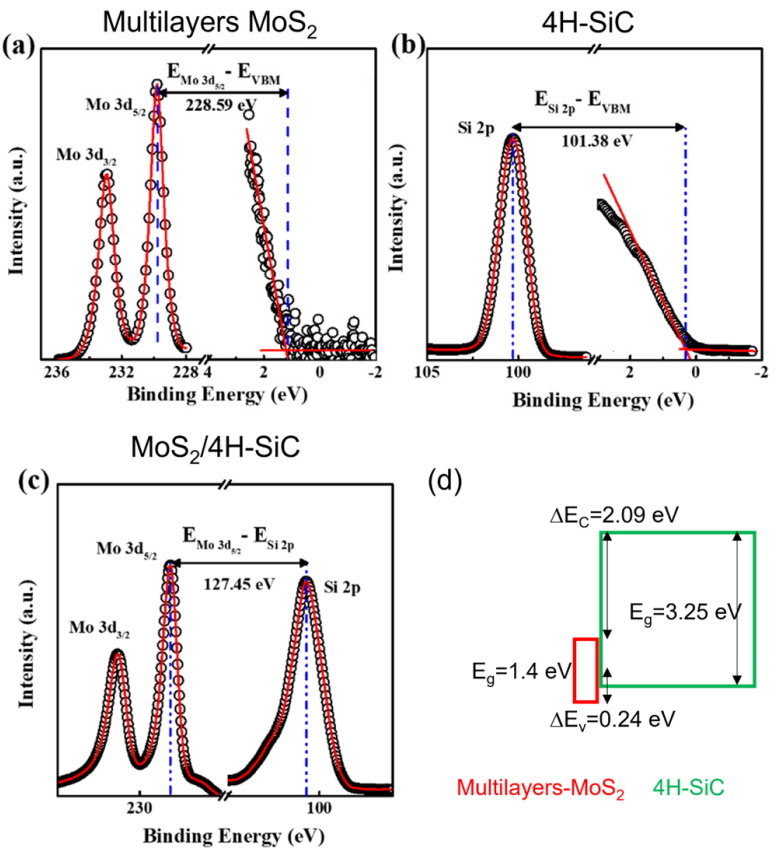

Figure 2.25.- (a) Mo 3d core level and valence band spectra of multilayer MoS_2. (b) Si 2p core level and valence band spectra of bulk SiC. (c) Mo 3d and Si 2p core level spectra obtained from the MoS_2/SiC interface. (d) Bands alignment with the band gap and the derived value of conduction and valence band offset deducted from XPS analysis. Fig.(a-c) reproduced by Ref. [201].

Differently than in the case of MoS_2/GaN heterostructures, fewer studied have been reported on the electrical characterization of MoS_2 heterojunctions with 4H-SiC. The

most investigated heterojunction is the anisotype p-MoS_2 on n-SiC, as represented in **Figure 2.26** (a). In this example, the p-MoS_2 is realized by two-step CVD directly on n^+-4H-SiC at 1100°C, from a stacked Mo/Nb/Mo thin film deposited by sputtering.

Hall measurements indicate that the Nb-doped MoS_2 has a carrier concentration of 3.0×10^{20} cm^{-3} and 8.6×10^{18} cm^{-3} for the n^+-4H-SiC. Both the materials are degenerately doped. The current density-voltage characteristics of the vertical heterojunction diode reported in **Figure 2.26** (b) show six-orders of magnitude rectification ratio, with a slight dependence on the temperature in the range between 6.9 to 300 K. Differently than the previously discussed p^+-MoS_2/n^+-GaN heterojunction, the diode composed by degenerately doped p^+-MoS_2 on n^+-4H-SiC does not show a negative differential resistance behaviour. Instead, the current injection across this junction was found to be dominated by multistep recombination tunnelling through midgap states in SiC, probably associated to interface defects [202]. These results indicate the need of further investigations to improve the quality of the vdW interface between MoS_2 and 4H-SiC. These experimental issues will be addressed in the Chapter 4 of this thesis.

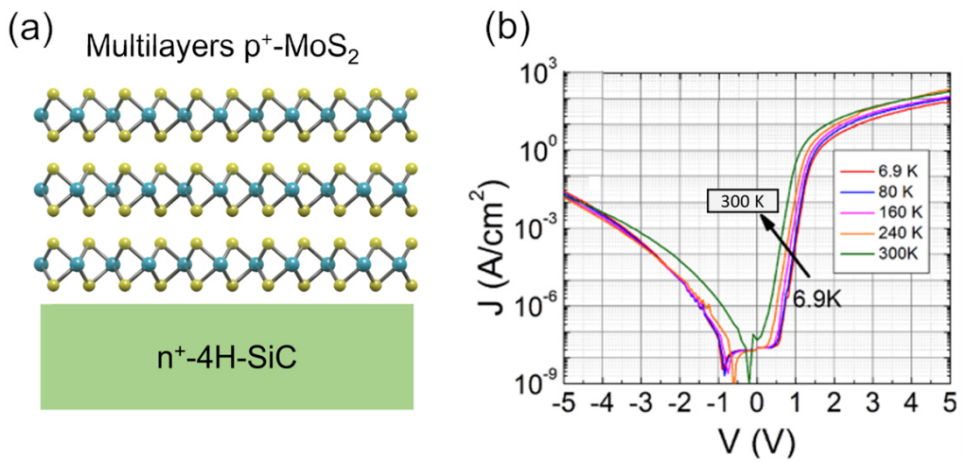

Figure 2.26.- (a) Scheme of multilayers p-MoS_2 on n-4H-SiC and (b) current density-voltage characteristics of the heterojunction. Fig.(b) reproduced from Ref. [202].

2.3.3 High- κ integration on MoS_2

The beneficial role of the high-κ dielectrics on 1L-MoS_2 was mentioned in Chapter 1.3. In fact, this implementation improves the electrical properties of the MoS_2 such as mobility and on/off ratio and decreases the subthreshold swing of FET. The deposition of high-κ dielectric can be obtained in different ways, but the Atomic Layer Deposition (ALD) is the most suitable deposition technique for the growth of ultrathin and conformal dielectric layers on a substrate. The key strength of ALD is related to its peculiar deposition mechanism. It is based on sequential and self-limited chemical reactions between the properly selected chemical precursors and the active sites of the substrate surface, which results in the so-called layer-by-layer growth mode, as shown in **Figure 2.27**(a). This principle permits to obtain uniform, conformal and angstrom-level control of the thickness on an extended area [207,208]. However, as illustrated in **Figure 2.27** (b), the ALD growth mechanism is difficult to be realized on the pristine surface of MoS_2 and other 2D materials, due to the lack of dangling bonds acting as active sites for the adsorption of ALD precursors. Thus, the main consequence of the dangling bonds absence is the formation of inhomogeneous films, as illustrated in **Figure 2.27** (c). The only way to obtain homogenous film is to deposit thicker high-κ films (>30 nm) on the 2D materials, as reported in the previous mentioned work [2]. However, new ALD solutions are necessary in order to achieve scaled electronic devices, differently from chemical functionalization of the 2D surfaces that can induce an increase of the density of defects [209,210]. For this reason, the integration of ultrathin high-κ dielectric on 1L-MoS_2 will be treated with some strategies in the experimental section in Chapter 4-5.

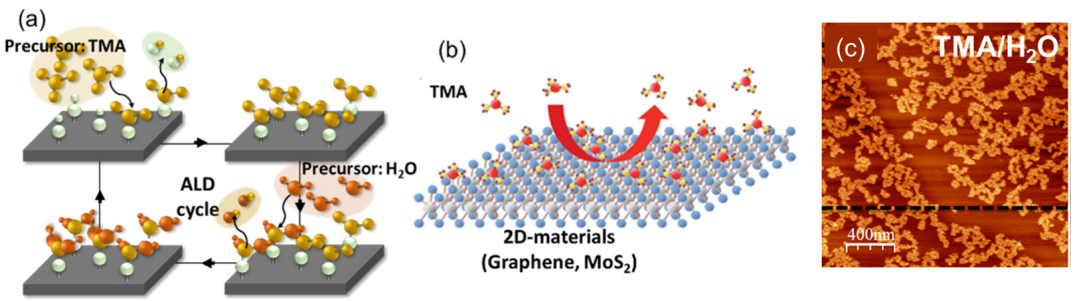

Figure 2.27.- (a) Schematic of a typical cycle in ALD growth. (b) Schematic diagram showing the adsorption and desorption processes of a TMA precursor during the ALD deposition of Al_2O_3 on the 2D materials. (c) AFM image of the ALD-Al_2O_3 layer deposited on a pristine MoS_2 surface. Fig.(a-c) reproduced from Ref. [208].

CHAPTER 3

STRAIN, DOPING AND ELECTRONIC TRANSPORT OF LARGE AREA MoS_2 EXFOLIATED ON GOLD AND TRANSFERRED TO AN INSULATING SUBSTRATE

As discussed in the Chapter 2, the gold-assisted mechanical exfoliation recently emerged as a promising **top-down** approach to produce large area membranes of MoS_2 and other TMDs, mostly composed by monolayers, by exploiting the strong interaction between Au and sulphur atoms. In the present chapter the experimental results obtained during this thesis work in this research field are presented. These include:

- the preparation of very flat Au surfaces, enabling monolayer exfoliation on large area, and an optimized transfer approach of the MoS_2 membrane to an insulating (Al_2O_3 on Si) substrate;

- a detailed characterization of the evolution of the doping, strain and light emission properties of as-exfoliated MoS_2 on Au and after transfer to the insulating substrate, performed by Raman and photoluminescence spectroscopies.

- the advanced electrical characterization of MoS_2 on gold by conductive atomic force microscopy, and of transferred MoS_2 by back-gated field effect transistor.

The obtained results are discussed in the context of the recent literature in the field and provide new insight on the understanding of Au-MoS_2 interaction. Finally, recently obtained experimental evidence on the beneficial effect of the underlying gold substrate on the atomic layer deposition (ALD) of ultra-thin and highly uniform Al_2O_3 films on top of monolayer MoS_2 are presented.

3.1 OPTIMIZED SAMPLES PREPARATION

3.1.1 MoS_2 exfoliation on gold films with optimized low roughness

As discussed in the Chapter 2, recent literature works showed that a low roughness of the gold surface represents a key aspect to achieve optimal monolayer MoS_2 exfoliation. However, achieving the deposition of thin Au films with low roughness by physical deposition techniques (evaporation or sputtering) can be challenging, due to the natural tendency of gold to form clusters.

The approach we adopted to obtain a film with optimized low roughness was to perform a two-steps deposition with a DC magnetron sputtering on a SiO_2/Si substrate, as schematically illustrated in **Figure 3.1**, with the first step consisting in the deposition of a Ni thin film and the second step in the sequential deposition of Au.

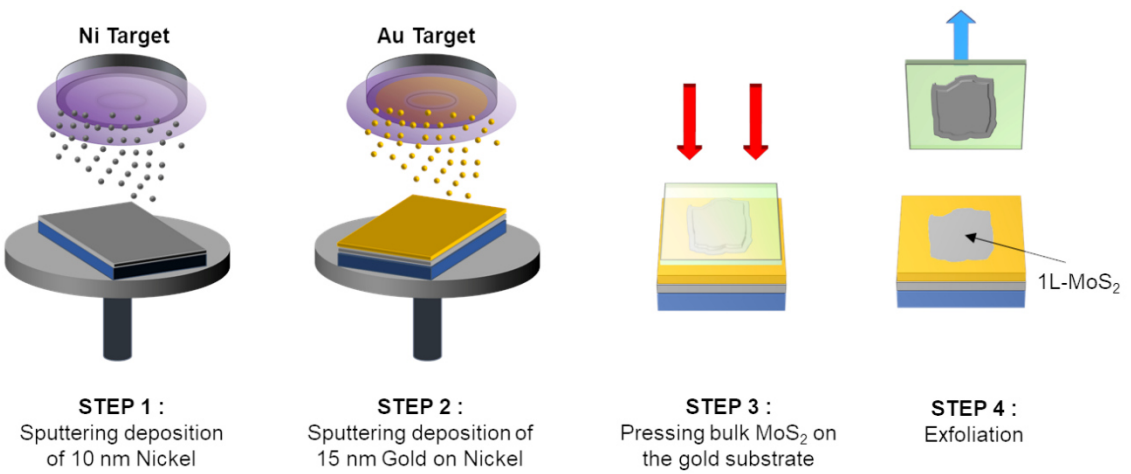

Figure 3.1.- Sputtering deposition of a Ni adhesion layer (step 1) and of the gold thin film (step 2). Pressing of a bulk MoS_2 stamp on the fresh surface of Au immediately after the deposition (step 3) and mechanical exfoliation of extendend 1L-MoS_2 on Au (step 4). Reproduced from Ref. [249].

To this aim, a ~15 nm thick Au film was deposited onto a SiO_2/Si substrate by DC magnetron sputtering. Prior to Au deposition, a 10 nm thick Ni film was sputtered to improve the adhesion onto the SiO_2. Beside ensuring an optimal adhesion to the SiO_2 surface, the Ni interlayer was beneficial to achieve a very smooth surface of the Au

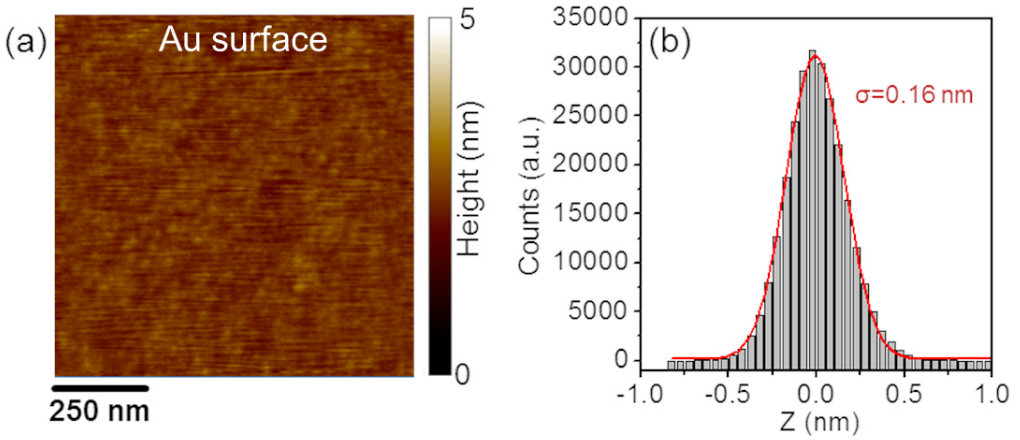

Figure 3.2.- (a) AFM morphology of the fresh Au surface after the magnetron sputtering deposition. (b) Height distribution of the AFM image (a) from which the extracted FWHM indicates the roughness of the gold surface. Reproduced from Ref. [215].

overlayer, with a low root-mean-square (RMS) roughness of 0.16 nm, as deduced from the tapping mode AFM image reported in **Figure 3.2**(a-b).

Mechanical exfoliation of MoS_2 was carried out by pressing a bulk MoS_2 stamp on the fresh Au surface, i.e. immediately after the deposition (see schematic in **Figure 3.1**(step 3)), in order to avoid its contamination with adventitious carbon, which is known to reduce the interaction strength between S and Au atoms [119]. By this procedure, very large area MoS_2 films, mostly composed of monolayer, were separated from the bulk crystal, as schematically illustrated in **Figure 3.1** (step 4) .

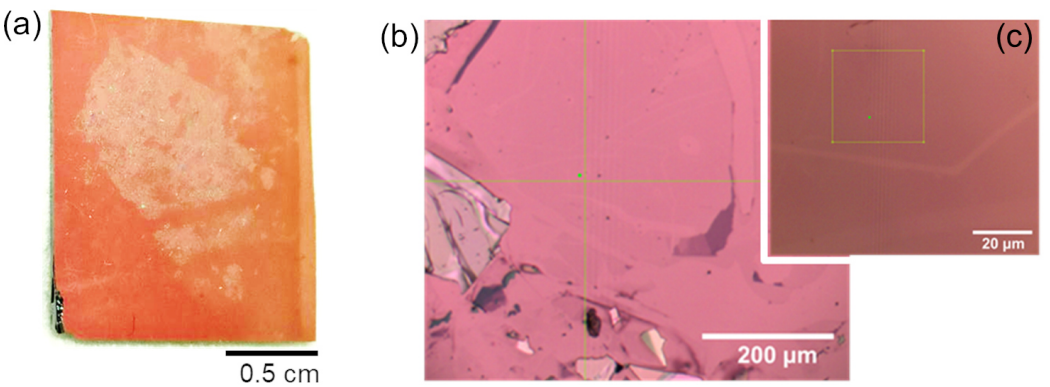

Figure 3.3.- (a) Photograph of the exfoliated 1L-MoS_2 flake on Au. Optical images of the exfoliated 1L-MoS_2 on Au at two different magnifications 10x (b) and 100x (c). Reproduced from Ref. [215].

Figure 3.3 shows an overview photograph of a sample with cm^2 area (a) and two optical images (b,c) at different magnifications (10× and 100×, respectively) of the exfoliated MoS_2 on the Au surface. The presence of an ultra-thin MoS_2 film extending for several hundreds of micrometres can be deduced from the colour contrast in the lower magnification optical image (b), which also shows the presence of thicker MoS_2 areas with smaller size, and of fractures of the MoS_2 membrane (i.e. bare Au regions) due to the exfoliation process. The optical contrast difference between the uniform ultra-thin MoS_2 membrane and one of these fractures can be better visualized in the higher magnification image in **Figure 3.3**(c).

A typical tapping mode AFM image of a fracture of the MoS_2 film is reported in **Figure 3.4**(a). The ~0.7 nm step height measured by the line profile in the insert is a direct confirmation of the 1L thickness of the MoS_2 membrane. Furthermore, a higher resolution AFM image of 1L MoS_2 partially covering the Au surface is reported in **Figure 3.4**(b). The histogram of height distribution extracted from this image shows very similar RMS values for the MoS_2/Au (~0.28 nm) and bare Au

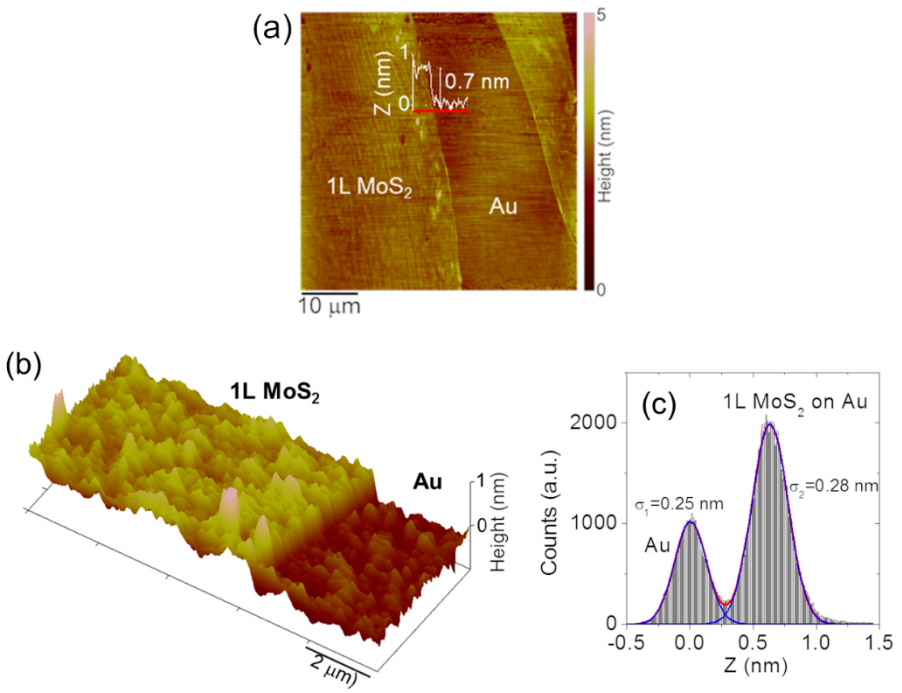

Figure 3.4.- (a) AFM image of the ultra-thin MoS_2 film with a fracture. The ~0.7 nm step height in the height profile along the red line demonstrates the 1L thickness of MoS_2 on Au. (b) AFM morphology of a region where MoS_2 partially covers the Au surface. (c) Corresponding histogram of height distribution, showing two components, associated to the bare Au region and to 1L MoS_2/Au. Very small and comparable values of roughness (σ_1=0.25 nm and σ_2=0.28 nm) can be deduced for both areas. Reproduced from Ref. [215].

areas (~0.25 nm), indicating a very conformal coverage by the MoS_2 membrane (**Figure 3.4**(c)).

In addition to the characterization of sample areas with uniform 1L-MoS_2 thickness, tapping mode AFM was also employed for the characterization of exfoliated regions with variable thickness. **Figure 3.5**(a) shows an AFM image collected in a region comprising both a bare Au area and MoS_2 covered regions with 1L, 2L, FL and multi-layer (bulk) thickness, indicated by different color dashed lines. A phase map collected in the rectangular region indicated by the white dashed line is also reported in **Figure 3.5**(b). This image is complementary to the morphology, as it provides a clear identification of the bare Au areas with respect to the MoS_2 covered ones,

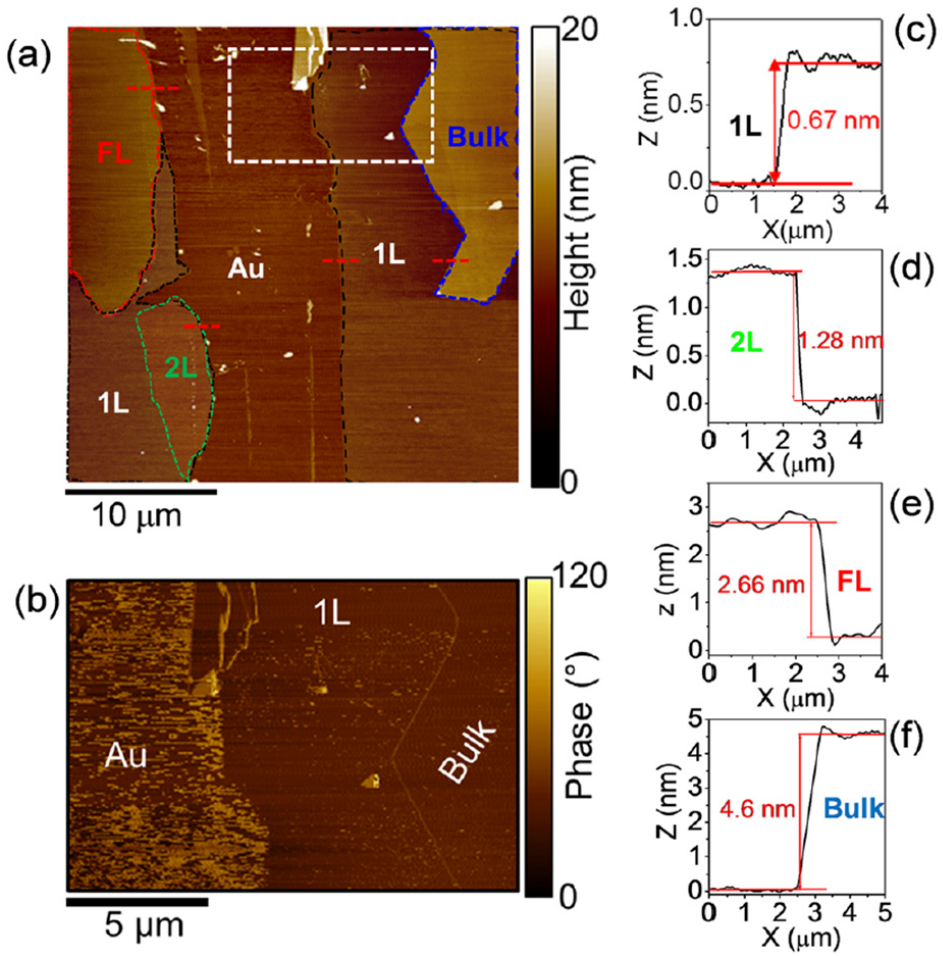

Figure 3.5.- (a) Morphological AFM image of a region of the exfoliated MoS_2 membrane on Au, containing areas with different MoS_2 thicknesses (1L, 2L, FL and bulk) and bare Au areas. (b) Phase image corresponding to the white dashed rectangular region in (a), showing a different contrast between bare Au and MoS_2 covered regions. Height line scans from (c) 1L, (d) 2L, (e) FL and (f) bulk MoS_2 areas in panel (a). Reproduced from Ref. [249].

thanks to the very different phase contrast. **Figure 3.5**(c-f) show the 1L, 2L, Few Layers (FL) and bulk thicknesses of the different areas in the morphological image confirmed by the line-scans, respectively.

3.1.2 Optimized transfer method of Au-exfoliated MoS_2 to an insulating substrate

The transfer of the extended MoS_2 membranes exfoliated on gold to insulating substrates represents a mandatory requirement for most of electronic applications of this material. In the following, an optimized transfer procedure developed within this thesis work is illustrated. A Si substrate covered by 100 nm Al_2O_3 film was employed as the final target substrate, although the transfer procedure can be easily extended

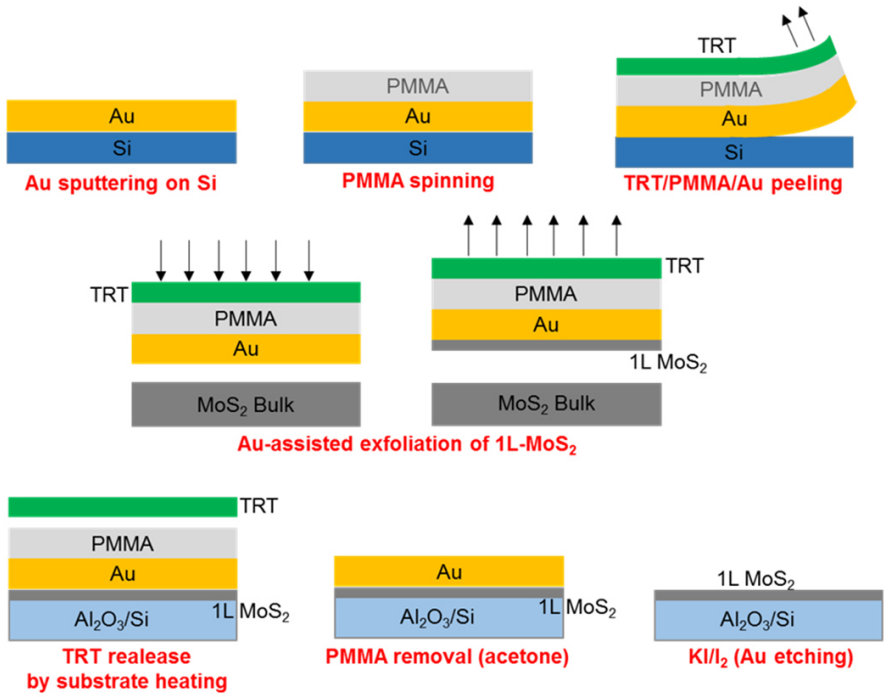

Figure 3.6.- Schematic illustration of the three steps process for Au-assisted exfoliation of 1L MoS_2 and transfer to a Al_2O_3/Si substrate. Reproduced from Ref. [215].

to other semiconductors or dielectric materials.

The developed transfer procedure consisted of three different steps, schematically illustrated in **Figure 3.6**. The first step was the fabrication of an ultra-flat "gold tape", consisting of a gold film on a polymer substrate. To this aim, a ~100 nm thick Au layer was deposited by DC magnetron sputtering on an accurately pre-cleaned silicon sample. Afterwards, the Au surface was spin-coated by a protective PMMA layer and attached to a thermal release tape (TRT). By exploiting the poor adhesion between Au and Si, the TRT/PMMA/Au stack was easily peeled from the silicon

surface, thus obtaining the desired "gold tape". The surface of Au films prepared by this method is typically very flat [211,212] and it has been already demonstrated to be

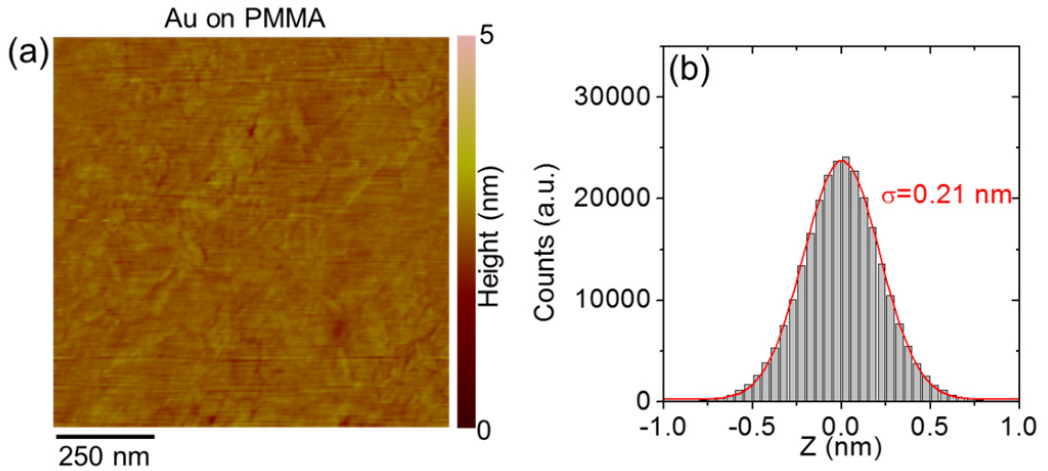

Figure 3.7.- (a) AFM morphology of the peeled gold on PMMA and (b) corresponding histogram of height distribution, showing a very small roughness of 0.21 nm, comparable with that of the Au/Ni film on SiO_2 (see **Figure 3.2**). Reproduced from Ref. [215].

suitable for the exfoliation of large area monolayers of MoS_2 and other TMDs [119]. In particular a RMS roughness of 0.21 nm was evaluated by AFM on the peeled Au films on PMMA in our experiments (**Figure 3.7**(a-b)), which is comparable with that of the Au/Ni film on SiO_2 observed previously in **Figure 3.2**.

The TRT/PMMA/Au stamp with a fresh Au surface, i.e. immediately after peeling from Si, was used to exfoliate 1L MoS_2 from a MoS_2 bulk sample. The final step of the process was the transfer of 1L MoS_2 on the target Al_2O_3/Si surface, as represented in the second part of **Figure 3.6**. This was achieved by pressing the TRT/PMMA/Au/1L MoS_2 stack onto the Al_2O_3/Si substrate while heating at 120 °C to promote the TRT release, followed by PMMA removal and final chemical etching of the Au film (with KI/I_2 solution). **Figure 3.8**(b) reports a typical optical microscopy image of the transferred MoS_2 membrane on the Al_2O_3 surface, this latter presents a low roughness as shown in AFM image reported in **Figure 3.8**(a). As compared to the case of 1L MoS_2 exfoliated on gold (**Figure 3.3**), a much sharper colour contrast can be observed between the regions coated by the extended 1L MoS_2 membrane (blue) and bare Al_2O_3 regions (violet), due to the favourable optical interference with the 100 nm Al_2O_3/Si substrate. Furthermore, the small size regions coated by few-layer or multilayer MoS_2 can be easily identified by the azure or bright colour, respectively. Hence, the optical image provides useful information on the thickness uniformity of the transferred MoS_2 film on large area. **Figure 3.8**(c)

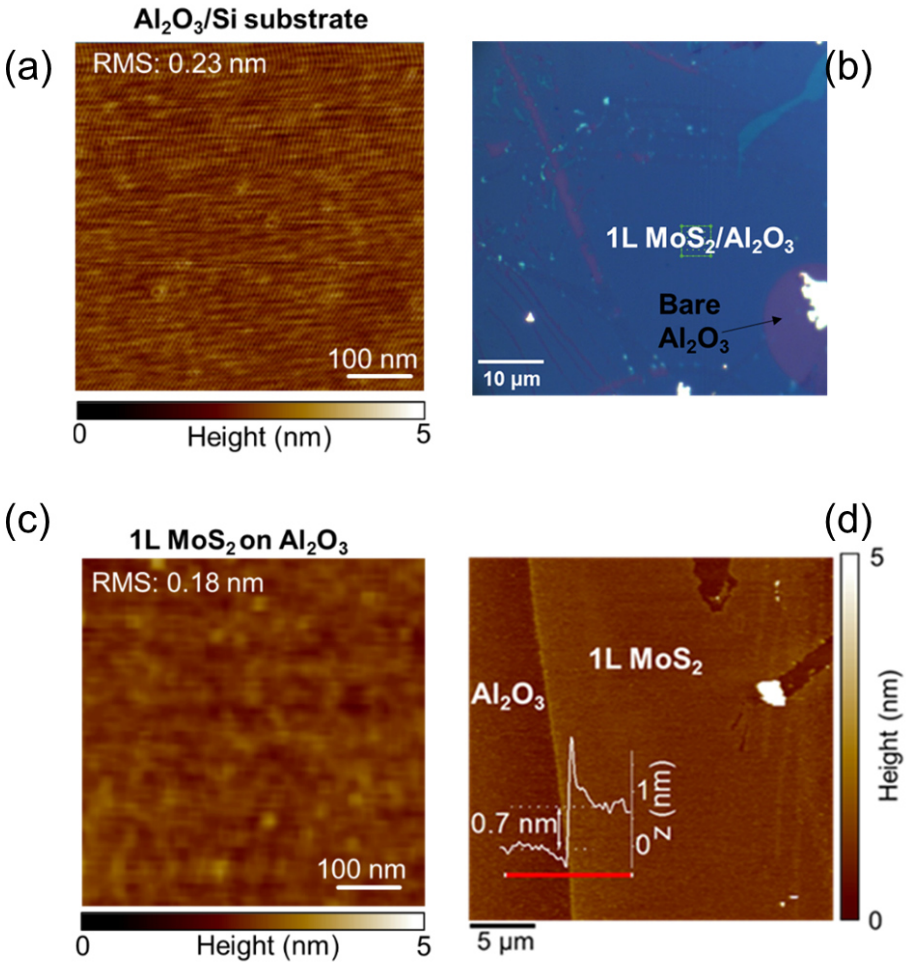

Figure 3.8.- (a) AFM image of the Al_2O_3/Si substrate before the 1L-MoS_2 transfer and the corresponding RMS of 0.23 nm. (b) Optical image of the 1L-MoS_2 transferred on Al_2O_3/Si. (c) AFM image of a submicrometric region of 1L-MoS_2 on Al_2O_3. (d) Corresponding step of 0.7 nm for the 1L-MoS_2 on Al_2O_3/Si. Reproduced from Ref. [215].

represents the morphological image of 1L MoS_2 on Al_2O_3 at high magnification, while the corresponding AFM image in **Figure 3.8**(d) shows a region partially covered by the thin membrane and the corresponding step. These characterizations provide a further confirmation of the low roughness of the 1L-MoS_2 (0.18 nm) and its thickness (0.7 nm) after the transferring.

3.2 SUBSTRATE EFFECTS ON THE VIBRATIONAL AND OPTICAL EMISSION PROPERTIES OF LARGE AREA MoS_2 EXFOLIATED ON AU AND TRANSFERRED TO Al_2O_3

In the following, the impact of the two different substrates (Au and Al_2O_3) on the vibrational and optical emission properties of MoS_2 areas with different thickness has been investigated by μ-Raman and μ-PL spectroscopy.

3.2.1 Raman spectroscopy of Au-exfoliated and transferred MoS_2 membranes with different thickness

Figure 3.9(a) and (b) report a comparison of typical Raman spectra collected on 1L, 2L, few layers (FL) and bulk regions of the MoS_2 membranes exfoliated on Au (a) and transferred onto Al_2O_3 (b). Here, the FL region corresponds to 4 layers of MoS_2, while the bulk region was formed by 10 layers of MoS_2. The characteristic in-plane (E_{2g}) and of the out-of-plane (A_{1g}) vibrational modes are observed in the spectral range from 370 to 420 cm^{-1}. All the spectra were normalized with respect to the A_{1g} peak intensity. Furthermore, vertical dashed lines, corresponding to the E_{2g} and A_{1g} peak positions for 1L MoS_2 on Au and Al_2O_3, have been reported as a guide for the eye in **Figure 3.9**(a) and (b). It can be observed how both the individual peak positions and their separation exhibit a very peculiar dependence on the kind of substrate**.** While a value of $\Delta\omega \approx 18.5$ cm^{-1} is measured for 1L MoS_2 transferred onto Al_2O_3, in the case of 1L MoS_2 exfoliated on Au the E_{2g} and A_{1g} peaks exhibit a significant red and blue shift, respectively, resulting in a larger $\Delta\omega \approx 21.2$ cm^{-1} value . Furthermore, a different behaviour of the in-plane and out of plane vibrational modes is observed on the two different substrates with increasing the number of layers, as shown in **Figure 3.9**(c).

For both substrates, the A_{1g} peak frequencies (filled and empty triangles) exhibit a similar increasing trend with increasing the MoS_2 thickness. In particular, for thin MoS_2 membranes (1L-4L) the A_{1g} peak on MoS_2/Au (filled triangles) is slightly blue shifted with respect to MoS_2/Al_2O_3 (empty triangles), whereas the two frequencies converge to the same value for bulk samples. On the other hand, the E_{2g} peak frequencies (filled and empty squares) show very different trends on the two substrates. While the decreasing E_{2g} peak frequency with increasing the MoS_2 thickness on Al_2O_3 (empty squares) is fully coherent with the reported literature results for MoS_2 on insulating substrates [121], this peak exhibits an anomalous

behavior in the Au case (filled squares). In fact, for 1L MoS_2 on Au the E_{2g} is significantly red-shifted (by ~2 cm^{-1}) with respect to 1L MoS_2 on Al_2O_3. Its frequency increases from 1L to 2L MoS_2 on Au and remains almost constant for thicker membranes.

Noteworthy, for bulk samples, the E_{2g} peak frequencies exhibit the same values on the two substrates. **Figure 3.9**(d) shows an increasing behavior of the peaks frequency difference $\Delta\omega$ as a function of the number of MoS_2 layers for the two different substrates. Furthermore, starting from a significantly larger value of $\Delta\omega$ $\approx$21.2 cm^{-1} for 1L MoS_2 on Au as compared to $\Delta\omega$ $\approx$18.5 cm^{-1} for 1L MoS_2 on Al_2O_3,

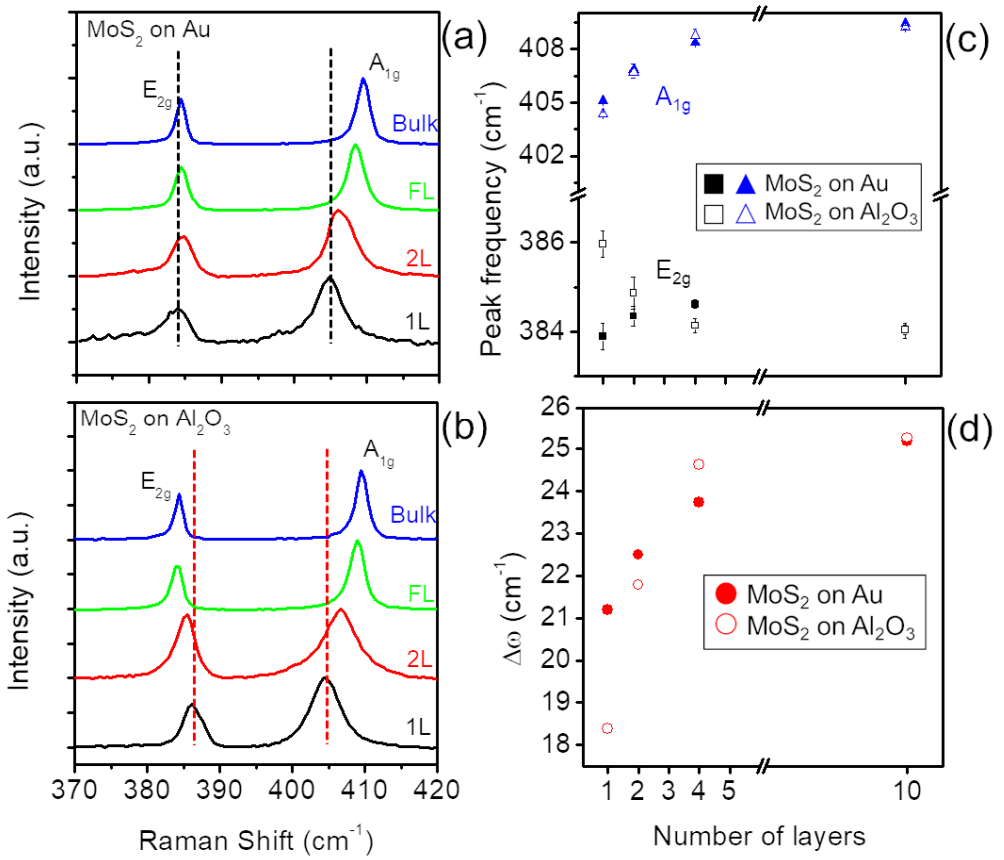

Figure 3.9.- Typical Raman spectra of exfoliated MoS_2 on the Au substrate (a) and transferred onto Al_2O_3/Si (b) measured on 1L, 2L, FL and bulk MoS_2 regions. The black (red) dashed lines indicate the E_{2g} and A_{1g} peaks frequencies for 1L MoS_2 on Au (Al_2O_3). (c) Behavior of the E_{2g} and A_{1g} peak frequencies as a function of the number of layers for MoS_2 on Au (filled squares and triangles) and for MoS_2 on Al_2O_3 (open squares and triangles). (d) Plot of the peaks frequency difference $\Delta\omega$ as a function of the number of layers for MoS_2 on Au (filled red circles) and MoS_2 on Al_2O_3 (empty red circles). Reproduced from Ref. [249].

the difference between the measured Δω values is gradually reduced with increasing the number of layers, reaching approximately the same value of ~25 cm^{-1} for bulk samples. It is worth mentioning that the measured Δω value in the Raman spectra of MoS_2 is generally taken as a straightforward way to estimate the number of layers. In particular, for 1L MoS_2 exfoliated/grown on common insulating substrates (such as SiO_2) the reported values of the separation Δω between E_{2g} and A_{1g} vibrational peaks can range from ~18 cm^{-1} to ~20 cm^{-1} [121]. Hence, the value of 18.5 cm^{-1} for our 1L MoS_2 exfoliated on Au and transferred to the Al_2O_3/Si substrate is in the range of the commonly reported literature values [121,213]. In particular, it is very close to the value measured on 1L MoS_2 flakes directly exfoliated on Al_2O_3 [214]. On the other hand, for as-exfoliated 1L MoS_2 on Au an anomalously large value of Δω=21.2 cm^{-1} is measured. Since the Au-assisted exfoliation is a very clean process (simply achieved by pressing the fresh surface of the bulk MoS_2 stamp onto the as-deposited Au film), the large Δω value cannot be explained by the presence of impurities at MoS_2/Au interface or on MoS_2 surface. On the other hand, its origin is the strong interaction between MoS_2 and the Au substrate [215].

3.2.2 Strain and doping distribution in 1L-MoS_2 membranes by Raman mapping

Focusing our attention on the single layer, **Figure 3.10**(a) shows the comparison between two representative Raman spectra for 1L MoS_2 on Au (black line) and on Al_2O_3/Si (red line), with indicated the characteristic E' and A_1' peaks, associated to the in-plane and out-of-plane 1L-MoS_2 vibrational modes, respectively.
It is well known that E' and A_1' spectral features are highly sensitive to strain and doping of 1L MoS_2 [140,216]. In particular, a red shift of E' peak is typically observed with increasing the tensile strain [90,217]. On the other hand, the A_1' peak is known to be sensitive to doping, and a blue (red) shift of its position is typically reported for p-type (n-type) doping of 1L MoS_2 [87]. Hence, the increase of Δω for 1L MoS_2 on Au/Ni/SiO_2/Si can be ascribed to a change both in the strain and doping of the 2D membrane. In order to extract relevant statistical information on the doping and strain uniformity of the 1L MoS_2 membranes exfoliated on Au and transferred to the Al_2O_3/Si substrate, Raman mapping was carried out on both samples by collecting arrays of 6×6 spectra on a 5×5 μm^2 area. **Figure 3.10**(b) and (c) show the colour maps of the E' peak frequency ($\omega_{E'}$) in the scanned areas for 1L MoS_2 on Au and Al_2O_3, respectively, while the comparison between the histograms of the $\omega_{E'}$ values in the two maps is shown in **Figure 3.10**(d). Similarly, the colour maps of the A_1' peak frequency ($\omega_{A_1'}$) and corresponding histograms are reported in **Figure 3.10**(e),

(f) and (g). Beside the individual peak positions, also their difference $\Delta\omega=\omega_{A_1'}-\omega_{E'}$ was calculated for all the collected Raman spectra. The colour maps of the $\Delta\omega$ values for 1L MoS_2 on Au and Al_2O_3 are shown in **Figure 3.10**(h)-(i), and the histograms of the $\Delta\omega$ values are reported in **Figure 3.10**(j).

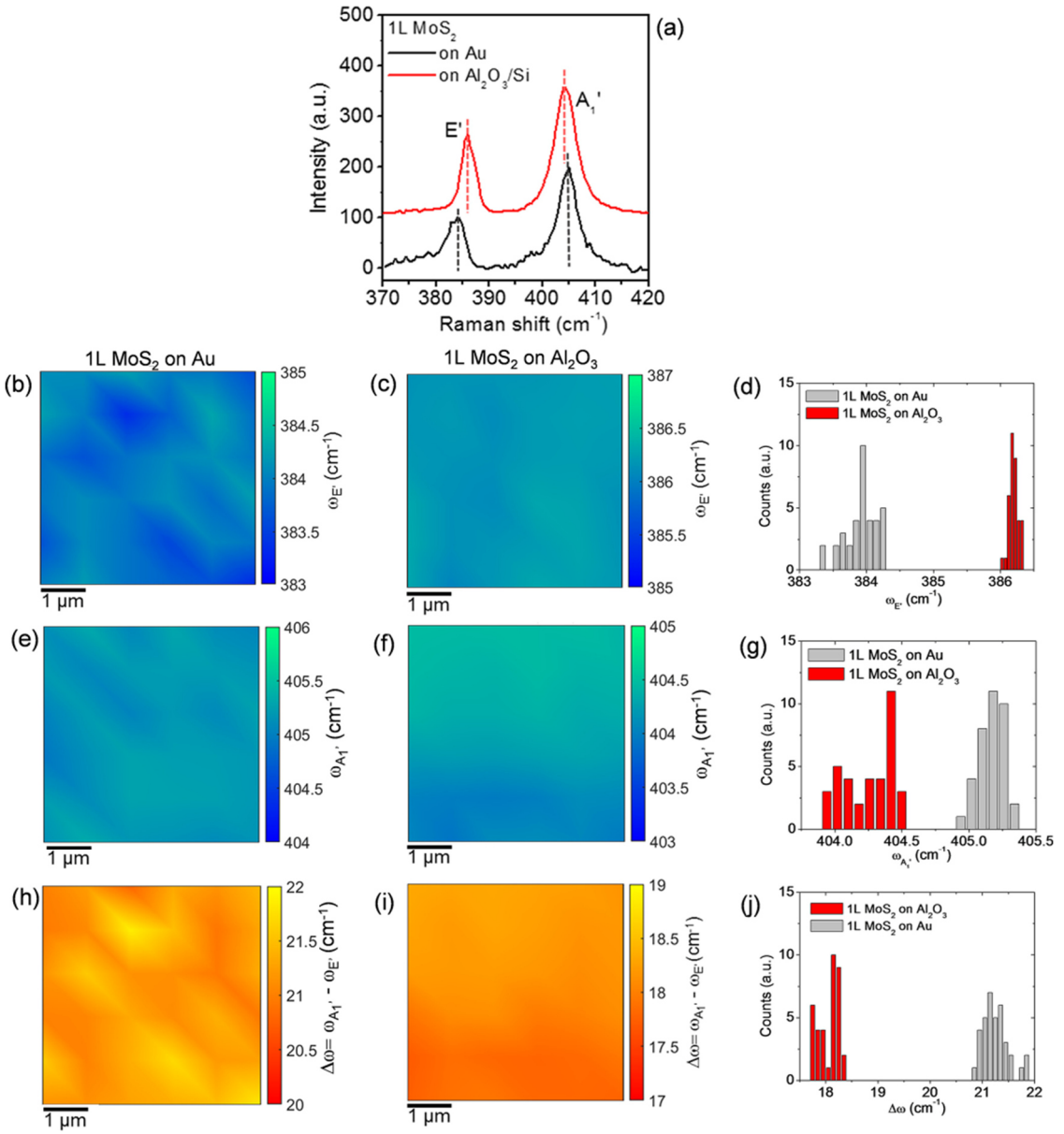

Figure 3.10.- (a) Representative Raman spectra for 1L MoS_2 on Au (black line) and on Al_2O_3/Si (red line). Colour map of the E' peak frequency values ($\omega_{E'}$) for 1L MoS_2 on Au (b) and on Al_2O_3 (c) and corresponding histograms (d). Colour map of the A_1' peak frequency values ($\omega_{A1'}$) for 1L MoS_2 on Au (e) and on Al_2O_3 (f) and corresponding histograms (g). Colour map of the peaks frequency difference ($\Delta\omega=\omega_{A1'}-\omega_{E'}$) for 1L MoS_2 on Au (h) and on Al_2O_3 (i) and corresponding histograms (j). Reproduced from Ref. [215].

The comparison between the colour maps allows to visualize the spatial distribution of the $\omega_{E'}$, $\omega_{A_1'}$ and $\Delta\omega$ spectral features in the two different samples. As an example, it can be clearly deduced that the maxima of $\Delta\omega$ for the Au-supported 1L MoS_2 sample (**Figure 3.10**(h)) are correlated to the minima of the $\omega_{E'}$ map (**Figure 3.10**(b)), where the E' peak is more red-shifted. On the other hand, for the 1L MoS_2 on Al_2O_3, the $\Delta\omega$ map exhibits an almost uniform contrast, and the spatial variations are clearly correlated with those of the A_1' peak. The histograms in **Figure 3.10**(d) and (g) confirm on a large set of data the red-shift of the E' peak and the blue-shift of the A_1' peak for 1L MoS_2 on Au with respect to 1L MoS_2 on Al_2O_3. It is also interesting to observe a significantly narrower spread of E' values for the 1L MoS_2 transferred to Al_2O_3, which can be ascribed to a more uniform strain distribution. By Gaussian fitting of the histograms, the average values and standard deviations of the peak frequencies and their difference have been obtained and reported in **Table 4**.

	$\omega_{E'}$ (cm^{-1})	$\omega_{A1'}$ (cm^{-1})	$\Delta\omega$ (cm^{-1})	ε(%)	n (10^{13} cm^{-2})
1L MoS_2 on Au	383.9±0.3	405.1±0.1	21.2±0.3	0.21±0.06	-0.25±0.06
1L MoS_2 on Al_2O_3	386.2±0.1	404.2±0.1	18.1±0.2	-0.25±0.01	0.5±0.09

Table 4.-Average values and standard deviation of the E', A_1' peaks frequencies ($\omega_{E'}$ and $\omega_{A1'}$) and their difference ($\Delta\omega$), and of the evaluated strain (ε) and doping (n) for 1L MoS_2 on Au and on Al_2O_3.

In the following, the strain ε (%) and doping n (cm^{-2}) for 1L MoS_2 on Au and on Al_2O_3 will be quantitatively evaluated from the correlative plot of the A_1' vs E' peak frequencies of **Figure 3.11** extracted for all the Raman spectra in the maps of **Figure 3.10**. A similar approach, based on the correlative plot of the characteristic 2D and G peaks, has been widely employed for strain and doping quantification of monolayer graphene on different substrates [94,218-221]. More recently such method has been adopted by some authors also for 1L MoS_2 [140,216,222].

In **Figure 3.11**(a), the black open circles represent the A_1' vs E' pairs for all the Raman spectra collected on 1L MoS_2 on Au, while the blue open triangles represent the data pairs for 1L MoS_2 on Al_2O_3. The red and black lines represent the theoretical relations between the frequencies of the two vibrational modes at a laser wavelength of 532 nm in the ideal cases of a purely strained (strain line) and of a purely doped (doping line) 1L MoS_2 [87,90]. The strain and doping lines cross in a point,

corresponding to the $\omega_{E'}^0$ and $\omega_{A1'}^0$ frequencies for ideally unstrained and undoped 1L MoS_2. In the following, the literature values of the peak frequencies for a suspended MoS_2 membrane ($\omega_{E'}^0 = 385\ cm^{-1}$ and $\omega_{A1'}^0 = 405\ cm^{-1}$)[90] have been kept as the best approximation to these ideal values, as substrate effects are excluded in this case. Starting from this reference point, the directions of increasing tensile strain and n-type doping are also indicated by the arrows along the two lines.

The ε and n values for each experimental point in **Figure 3.11** can be evaluated from the combination of the linear relationships between the biaxial strain/charge doping and Raman shifts of the vibrational modes, reported in **Table 4**.

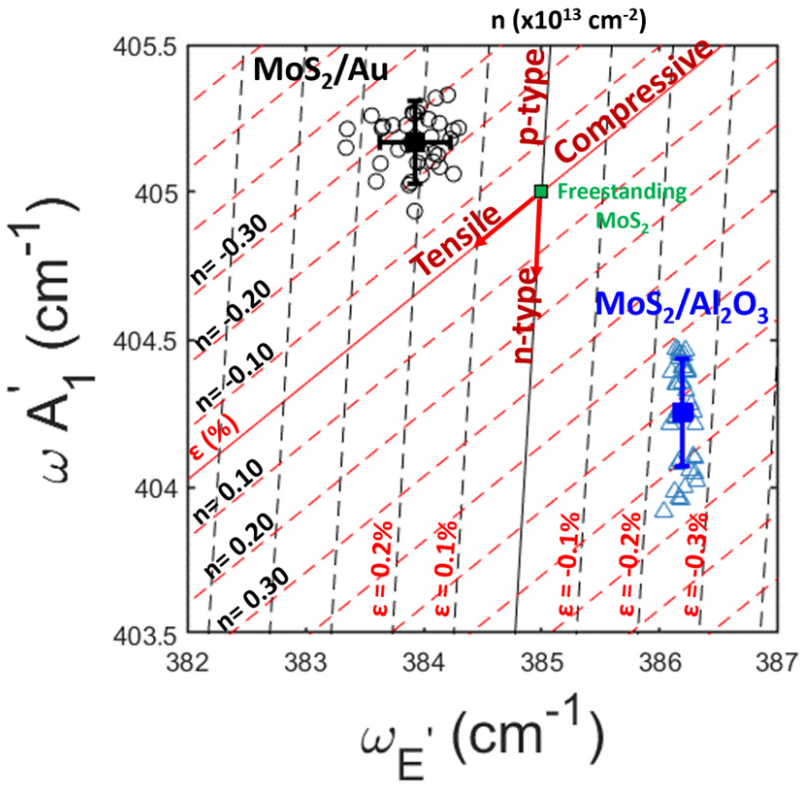

Figure 3.11.- Correlative plot of the A_1' and E' peak frequencies to evaluate the biaxial strain and charge doping distributions in 1L MoS_2 on Au (black circles) and on Al_2O_3 (blue triangles). The red (black) lines represent the strain (doping) lines for ideally undoped (unstrained) 1L MoS_2, meanwhile the green square indicates the $\omega_{E'}^0 = 385\ cm^{-1}$ and $\omega^0{}_{A1'} = 405\ cm^{-1}$ frequencies for freestanding 1L MoS_2, taken as zero reference. The dashed red (black) lines parallel to the strain (doping) lines serve as guides to quantify the doping and strain values, respectively. Reproduced from Ref. [215].

Here, $\gamma_{E'}$=0.68 and $\gamma_{A_1'}$=0.21 are the Grüneisen parameters for the two vibrational modes of 1L MoS_2 [90,92,223]. The $k_{E'}$ = -0.33×10^{-13} cm and $k_{A_1'}$ =-2.2×10^{-13} cm coefficients are the shift rates of Raman peaks as a function of the electron density n

(in cm^{-2}) in 1L MoS_2, obtained by Raman characterization of electrochemically top-gated MoS_2 transistors [87].

In particular, the relation for the strain line can be obtained by solving the system of **Eq.**(5)-(7) in the case of n=0:

$$\omega_{A1'} = \omega_{A1'}^0 + \frac{\gamma_{A1'}\omega_{A1'}^0}{\gamma_{E'}\omega_{E'}^0}\left(\omega_{E'} - \omega_{E'}^0\right) \quad (13)$$

whereas the doping line equation is obtained by the same procedure for ε=0:

$$\omega_{A1'} = \omega_{A1'}^0 + \frac{k_{A1'}}{k_{E'}}\left(\omega_{E'} - \omega_{E'}^0\right) \quad (14)$$

Hence, $\frac{\gamma_{A1'}\omega_{A1'}^0}{\gamma_{E'}\omega_{E'}^0} = 0.32$ and $\frac{k_{A1'}}{k_{E'}} = 6.67$ are the slopes for the strain and doping lines, respectively. The dashed red lines parallel to the strain line (n=0) and the dashed black lines parallel to the doping line (ε=0) serve as guides to quantify the doping and strain values, respectively. They correspond to ±0.1% variations for the strain and $\pm 0.1\times10^{13}$ cm^{-2} variations for the doping. Since the $\omega_{E'}$ is more sensitive to biaxial strain, the spacing between the dashed black lines parallel to the doping line is calculated from the E' mode strain rate $2\gamma_{E'}\omega_{E'}^0$ =5.2 $cm^{-1}/\%$. On the other hand, since the A_1' mode results mainly influenced by charge doping [90], the spacing between the dashed red lines parallel to the strain line is calculated from the A_1' doping rate $k_{A_1'}$=-2.2×10^{-13} cm.

The plot in **Figure 3.11** shows that all the experimental data points for 1L MoS_2 on Au are located above the strain line and in the left side with respect to the doping line. Hence, as compared to the reference case of a free-standing (suspended) 1L MoS_2, our gold-supported 1L MoS_2 films exhibit a tensile strain in the range from ~0.1% to ~0.3% and a p-type doping in the range from $\sim0.1\times10^{13}$ to $\sim0.4\times10^{13}$ cm^{-2}. The average values of the strain (~0.21%) and doping ($\sim0.25\times10^{13}$ cm^{-2}) are

indicated by the black square in **Figure 3.11**. A tensile biaxial strain, originating from the lattice mismatch between MoS_2 and Au,[224,225] has been recently observed in the case of 1L MoS_2 exfoliated on Au also by other authors, [121] that reported very large ε values up to 1.2%. The smaller tensile strain obtained in our samples are probably due to the very smooth surface of the gold films. The observed p-type doping of MoS_2 in contact with Au is consistent with several recent reports of a p-type behavior induced by MoS_2 functionalization with gold nanoparticles, adsorbates or Au-based chemicals [226-228].

On the other hand, the cloud of data for 1L MoS_2 on Al_2O_3 is located in a region of the ε-n plane corresponding to a compressively strained and n-type doped film, with the strain values comprised in a narrow range around ~-0.25% and the electron density ranging from ~0.4×10^{13} to ~0.7×10^{13} cm^{-2}. The compressive strain can be plausibly related to the transfer procedure and the adhesion properties of 1L-MoS_2 with the Al_2O_3 surface. The observed n-type doping is consistent with the unintentional doping typically observed for MoS_2 layer on insulating substrates, and can be ascribed, in part, to charge transfer by adsorbed or interface trapped charges under ambient conditions, as well as to native defects of MoS_2.

Such n-type behaviour is consistent with the unintentional doping type commonly reported for exfoliated or CVD-grown MoS_2, which has been associated to the

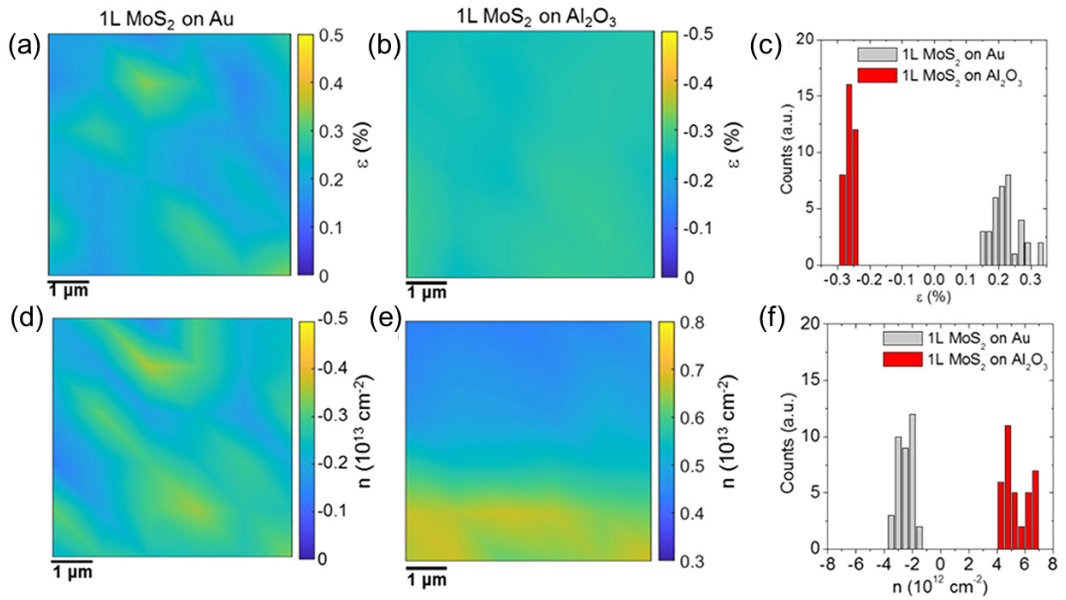

Figure 3.12.- Colour maps of the strain for the 1L MoS_2 on Au (a) and 1L MoS_2 on Al_2O_3 (b) samples and histograms of the strain values (c). Colour maps of the doping for 1L MoS_2 on Au (d) and 1L MoS_2 on Al_2O_3 (e) and histograms of the doping values (f). Reproduced from Ref. [215].

presence of defects (e.g. sulphur vacancies) or other impurities in the MoS_2 lattice[229]. In the case of 1L MoS_2 on Au, a strong electron transfer to the substrate is guessed, which overcompensates the native n-type doping, resulting in a net p-type behaviour. Furthermore, the tensile strain for 1L MoS_2 on Au can be ascribed to the lattice mismatch between MoS_2 and the Au surface, mostly exposing (111) orientation [224,230].

By solving **Eq.**(13)**-**(14**)** for all the data points of the $\omega_{E'}$ and $\omega_{A_1'}$ maps, the corresponding colour maps of the strain (**Figure 3.12** (a)-(b)) and doping (**Figure 3.12** (d)-(e)) for the two samples were obtained. The corresponding histograms of the strain and doping values are reported in **Figure 3.12**(c) and (f), respectively. From the comparison of the strain and doping maps on the 1L MoS_2/Au, a correlation between the regions with higher tensile strain and those with higher p-type doping can be noticed. This suggests that both strain and p-type doping originate from a locally stronger interaction with Au. On the other hand, the compressive strain distribution appears very uniform in the 1L MoS_2 membrane transferred onto Al_2O_3, without any clear correlation with the doping distribution. The average values and standard deviation of the strain and doping for the two different samples have been extracted by Gaussian fitting of the histograms in **Figure 3.12**(c) and (f), and the obtained values have been reported in the **Table 4**. Obviously, the spatial resolution in these maps is limited by the spot size of the Raman laser (~1 μm). Furthermore, the concentration sensitivity (in the order of 10^{12} cm^{-2}) is limited by the shift rate of the A_1' peak with doping concentration. Higher spatial resolution and sensitivity information on the doping distribution in the Au supported 1L MoS_2 will be deduced by nanoscale electrical characterization with conductive atomic force microscopy (C-AFM) analyses, reported later on in this chapter.

3.2.3 *Photoluminescence spectroscopy of Au-exfoliated and transferred MoS_2 membranes with different thickness*

To further investigate the impact of the substrate/MoS_2 interaction on the electronic properties of 1L MoS_2, micro-photoluminescence analyses were also performed using the 532 nm laser probe of the Raman equipment as excitation source. **Figure 3.13** shows the comparison between the representative PL spectra collected on the two different samples under the same illumination conditions.

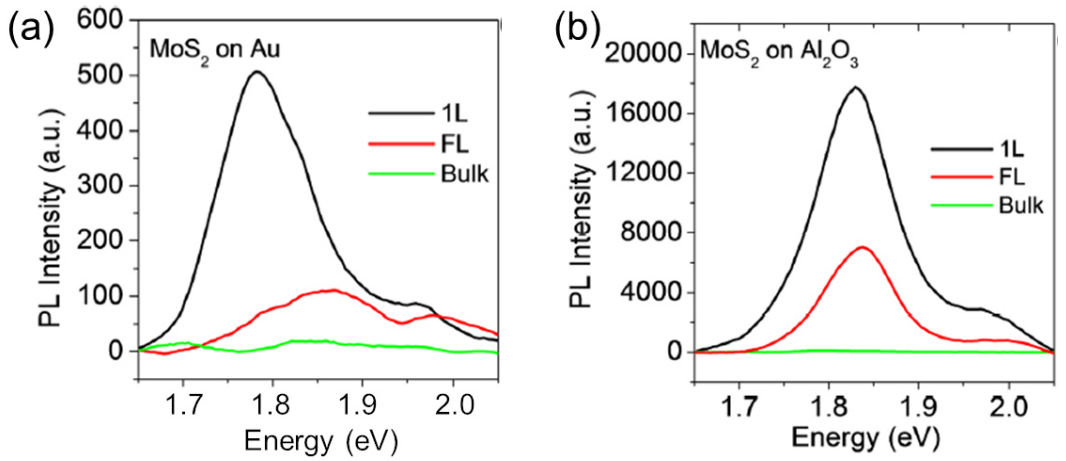

Figure 3.13.- Photoluminescence spectra under 532 nm excitation for 1L, FL and bulk MoS_2 on Au (a) and Al_2O_3 substrate (b). Reproduced from Ref. [215].

Noteworthy, the large 1L MoS_2 membrane produced by gold-assisted exfoliation and finally transferred onto Al_2O_3 exhibits a prominent peak at 1.83 eV (**Figure 3.13**(b)), very similar to that observed in monolayer MoS_2 obtained by the traditional mechanical exfoliation or deposited by CVD. On the other hand, a strongly reduced PL intensity was observed when the exfoliated 1L MoS_2 membrane is still in contact with Au, together with a red-shift of the main PL peak to 1.79 eV (**Figure 3.13**(a)). The strong reduction of the PL intensity is consistent with the emission quenching reported by other authors for 1L MoS_2 exfoliated on Au [119] and for MoS_2 functionalized with Au nanoparticles [231]. This PL quenching can be explained in terms of a preferential transfer of photo-excited charges from MoS_2 to Au. In addition, the tensile strain of the MoS_2 layer in contact with Au can also play a role in the reduction of the PL yield [90]. A further comparison is realized at different thickness for the metallic and for the insulating substrate. In particular, the black, red

and green lines **Figure 3.13** represent the PL spectra for 1L, FL and bulk MoS_2, respectively. In order to perform a reliable comparison of the PL signal on the two different substrates, for each spectrum the intensities were normalized to the intensity of the MoS_2 Raman peaks. A reduction of the relative PL intensities when increasing the MoS_2 thickness from 1L to FL was consistently observed on both kinds of substrates, with the intensity approaching to zero in bulk samples according to the indirect bandgap. Looking more in details at PL emission for 1L MoS_2, for both substrates the PL spectra exhibit a main intense peak at lower energy and another weaker peak at higher energy, associated to the MoS_2 band splitting due to spin-orbit coupling [31,232]. To get a deeper insight in the PL emission mechanisms of 1L MoS_2 on the two different substrates, a deconvolution of the two representative spectra has been carried out, as reported in **Figure 3.14**(a) and (b). In both cases, the best fit was obtained considering three Gaussian peaks, which were associated to a trionic contribution A^- (green dashed line), and two excitonic contributions, i.e. the exciton A^0 (blue) and the exciton B (grey) [55,233,234]. Differently from neutral excitons, consisting of a bound electron/hole pair, trions are charged quasiparticles formed by two electrons and a hole [55]. Noteworthy, while the exciton peak A^0 at 1.84 eV represents the main PL contribution for 1L MoS_2 on Al_2O_3, the trion peak A^- at 1.78 eV appears to be the dominant one in the case of 1L MoS_2 on Au. Finally, the B exciton peak at 1.94 eV for 1L MoS_2 on Al_2O_3 exhibits a significantly higher full width at half maximum (FWHM) with respect to the corresponding peak (at 1.96 eV) for 1L MoS_2 on Au. As indicated in the labels of **Figure 3.14** (a) and (b), the A^-, A^0 and B peaks obtained by the deconvolution are slightly blue-shifted in the case of 1L MoS_2 on Au with respect to 1L MoS_2 on Al_2O_3. However, the overall red shift of the PL spectra for 1L MoS_2 on Au is due to the higher intensity of the trion contribution. As reported in recent theoretical studies [235,236], this effect can be ascribed to the

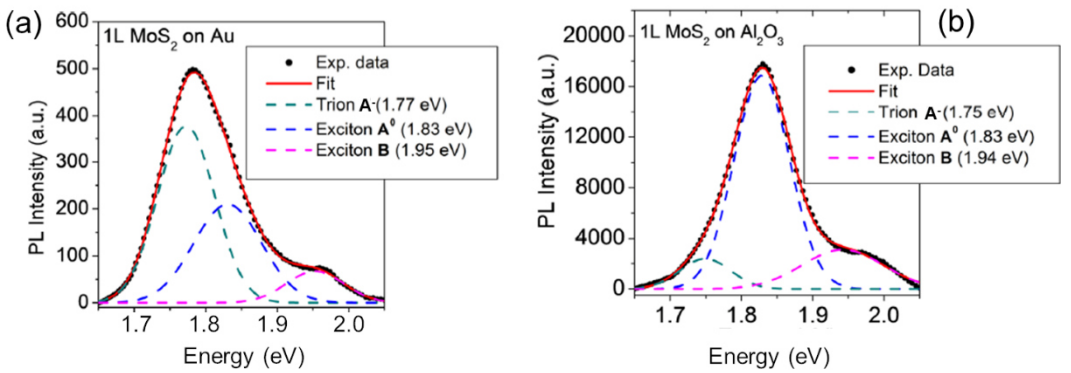

Figure 3.14.- Deconvolution of PL spectra for (a) 1L MoS_2 on Au and (b) 1L MoS_2 on Al_2O_3. Three different components were identified: the trion peak A^-, the exciton peak A^0 and the exciton peak B. Reproduced from Ref. [249].

high polarizability of the metal substrate and to the low MoS_2/Au equilibrium distance enhancing the trion population and at the same time quenching the overall

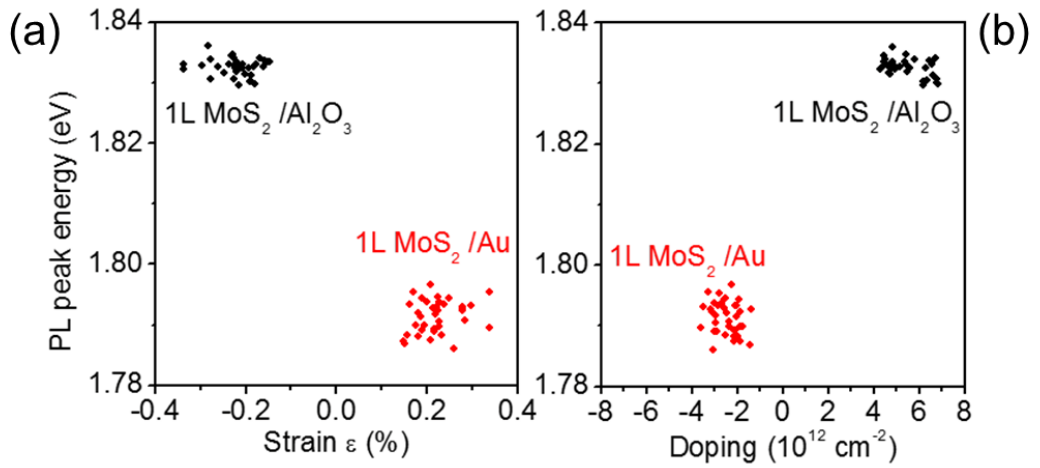

Figure 3.15.- Correlative plots of the PL peak energy with the strain (a) and doping values (b) deduced by PL and Raman mapping on the same sample area. Reproduced from Ref. [215].

emission amplitude [119]. Noteworthy, in the case of FL MoS_2 on Au (**Figure 3.13**(a)) the main PL peak appears to be broader and blue-shifted with respect to the monolayer one, and its energy is closer to that of FL MoS_2 on Al_2O_3. This observation suggests that the increase of the MoS_2 thickness results in a reduced effect of the substrate not only on vibrational properties but also on PL emission.

In order to obtain statistically relevant information, arrays of PL spectra have been collected on the two samples in the same areas previously probed by Raman mapping. Furthermore, **Figure 3.15** (a) and (b) show the correlative plots of the PL peak energy with the strain and doping values deduced from Raman maps. These plots show a narrow distribution of the PL peak energies for both 1L MoS_2/Au and for 1L MoS_2/Al_2O_3 samples. In particular, in **Figure 3.15** (a) the observed peak energy variations observed within each sample and the difference between the average values of the data points collected on the two different substrates are compatible with the PL peak shift rate as a function of the strain (~100 meV/%) reported in the literature [90].

3.3 ELECTRONIC TRANSPORT OF LARGE AREA 1L-MoS_2 EXFOLIATED ON AU AND TRANSFERRED TO Al_2O_3

3.3.1 Vertical transport in 1L-MoS_2 on Au

The Raman mapping experiments reported so far provided information on the doping uniformity of 1L MoS_2/Au basing on the correlation between characteristic vibrational peaks and the carriers type and density. In the following, electrical measurements will be also employed to get further insight on the electronic transport in the 1L MoS_2/Au system and after transfer to the insulating substrate. Recently, other groups used electrical scanning probe methods on TMDs transferred onto noble metal contacts to characterize the buried semiconductor/metal vdW interface [237,238].

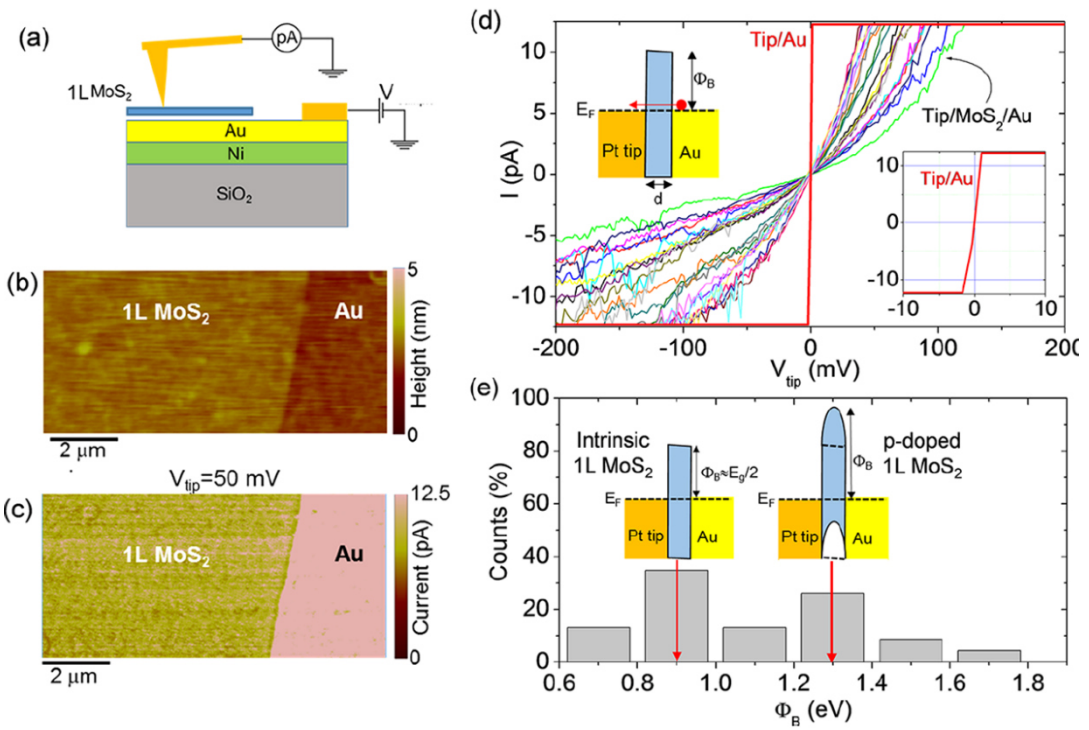

Figure 3.16.- (a) Schematic illustration of the C-AFM setup used for current mapping through the 1L MoS_2 film on Au. (b) Morphology of a sample region with the Au substrate partially covered by the 1L MoS_2 film and (c) simultaneously measured current map on the same area (at V_{tip}=50 mV). (d) Local I-V_{tip} curves measured with the Pt-tip in contact with 1L MoS_2 on Au and with the bare Au surface (red line). A detail of the I-V_{tip} curve measured on Au is reported in the right inset. A schematic band-diagram for the tip/1L MoS_2/Au metal/semiconductor/metal heterojunction is reported in the left inset. (e) Histogram of the tunnelling barrier values Φ_B evaluated from the I-V_{tip} curves in panel (d), according to the direct tunnelling mechanism. The band-diagram for intrinsic and p-type doped 1L MoS_2 are schematically illustrated in the insets of (e). Reproduced from Ref. [215].

Here, we carried out a nanoscale resolution electrical characterization of the Au-supported 1L MoS_2 membrane by C-AFM measurements [239] to get further information on the doping uniformity in this ultra-thin layer. To this aim, the current injection at the interface between the Au substrate and 1L MoS_2 was probed at nanoscale by a Pt-coated Si tip, according to the configuration schematically illustrated in **Figure 3.16**(a). The surface morphology in a sample region partially covered by 1L MoS_2 is reported in **Figure 3.16**(b), showing how the 1L MoS_2 membrane conformally follows the smooth Au morphology. Furthermore, **Figure 3.16**(c) shows the simultaneously measured current map, collected applying a DC bias V_{tip}=50 mV between the Pt tip and the Au electrode (substrate). For this low bias value, the current level measured on the bare Au region reaches the current amplifier saturation limit, whereas appreciable lateral variations of the injected current through the 1L MoS_2 membrane can be observed.

Such local variations of the injected current through the atomically thin membrane can be ascribed to the lateral inhomogeneities of MoS_2 electronic properties. In this respect, it is worth noting that, since C-AFM analyses were performed in ambient conditions, an ultra-thin water layer is adsorbed on the MoS_2 surface, the effective contact area is determined by the size of the water meniscus around the tip [239]. As a matter of fact, the meniscus size is determined by the tip radius, the applied force and the surface roughness. Hence, the smooth Au and MoS_2 surface of our samples and the application of a constant force during measurements results in a nearly constant effective contact area. To further investigate the current transport mechanisms, a set of local current-voltage (I-V_{tip}) characteristics were acquired both on the bare Au surface and at different positions on the MoS_2 film, as reported in **Figure 3.16**(d). The I-V_{tip} curves measured by the Pt tip in contact with Au (see red curve in **Figure 3.16**(d)) are very reproducible and exhibit an Ohmic behaviour with a very steep slope and current saturation at few mV positive and negative bias (as shown in the right inset of **Figure 3.16**(d)). On the other hand, I-V_{tip} curves measured on MoS_2 show significant variations at different positions. A possible reason of such variability can be the presence of nanoscale areas where 1L MoS_2 is locally in contact with Au and areas where it is locally suspended between the Au grains, as recently reported by *Velický et al.* [121]. However, this scenario would imply a splitting of the A_1' peak in the Raman spectra, due to the very different substrate-related doping for the Au-supported and suspended 1L MoS_2 [121]. Since such splitting is not observed in our Raman spectra, we excluded this effect in our 1L MoS_2/Au samples.
In the following, the Pt tip in contact with 1L MoS_2/Au is described as a metal/semiconductor/metal heterojunction, and the local I-V_{tip} curves in **Figure**

3.16(d) have been fitted with relevant current transport mechanisms across the ultra-thin MoS_2 barrier.

In **Figure 3.16**(d) all the curves measured on MoS_2 show a linear behaviour at low V_{tip} values, followed by a deviation from linearity at larger bias values. Furthermore, the slight asymmetry between positive and negative polarizations at larger bias can be ascribed to the different workfunctions of Pt and Au metals.

The linear behaviour of the I-V_{tip} characteristics indicates direct tunnelling (DT) as the most appropriate mechanism ruling current transport at low bias values [240]. In particular, the tunnelling current can be expressed as:

$$I_{DT} = BV_{tip} \times P(\Phi_B, d) = BV_{tip} \exp\left[-\frac{4\pi d\sqrt{2m_{eff}\Phi_B}}{h}\right] \qquad (15)$$

where B is a pre-factor (proportional to the tip contact area) and $P(\Phi_B,d)$ is the direct tunnelling probability, which is a function of the tunnelling barrier thickness d (i.e. the MoS_2 thickness) and its height Φ_B, corresponding to the energy difference between the MoS_2 conduction band and the Au Fermi level (see scheme in the left insert of **Figure 3.16**(d)). Here m_{eff}=0.35 m_0 is the electron effective mass in the transversal direction for 1L MoS_2, [241] and h is the Planck's constant. As a matter of fact, the thickness dependent tunnelling probability becomes unity when the MoS_2 layer is absent (d=0), i.e. when the tip is directly in contact with the Au substrate. Since current mapping and local I-V measurements have been performed using the same tip in a sample area including MoS_2-covered and uncovered Au regions, the same value for the pre-factor B were considered in the two cases. Hence, the experimental values of the local tunnelling probability at different positions on MoS_2 were estimated as the ratio between the slope of the I-V curves measured on MoS_2 and the slope of the I-V characteristics measured on Au. Since the MoS_2 layer is very conformal to the smooth Au morphology, we have assumed a laterally uniform 1L MoS_2 barrier thickness d=0.65 nm (corresponding to the ideal value for 1L MoS_2) over the C-AFM probed area. As a result, the local barrier height values have been extracted from the tunnelling probabilities for each of the I-V curves in **Figure 3.16**(d). The obtained histogram of the Φ_B values, reported in **Figure 3.16**(e), shows a broad distribution, ranging from 0.70±0.08 to 1.70±0.08 eV, with two main components at ~0.9 eV and ~1.3 eV. In particular, the component at $\Phi_B \approx 0.9$ eV corresponds to a Fermi level located approximately at $E_g/2$ with respect to the MoS_2 conduction band, as schematically illustrated in the left insert of **Figure 3.16**(e). Noteworthy, this value is very close to ideal barrier height between Au and charge neutral MoS_2, given by $\Phi_B = W - \chi$, being $W \approx 5.1$ eV the gold work function and $\chi \approx 4.2$

eV the electron affinity of 1L MoS_2 [237]. This charge neutral regions can be ascribed to nanoscale areas where the p-type doping induced by the Au substrate is compensated by the presence of n-type doping impurities/adsorbates on the surface of MoS_2 [242]. Due to the limited sensitivity of Raman peak's shift to doping concentration values $<10^{12}$ cm^{-2}, such low doping areas could not be detected in Raman maps. On the other hand, the component at larger Φ_B values in the distribution of **Figure 3.16**(e) can be ascribed to higher p-type doping of 1L MoS_2, that was detected also by Raman. Such local p-type doping due to the Au substrate induces an upward band bending of the conduction and valence band of MoS_2 (schematically illustrated in the right inset of **Figure 3.16**(e)), which extends over a distance (in the order of few nm) defined by the Debye length in the 2D semiconductor [243].

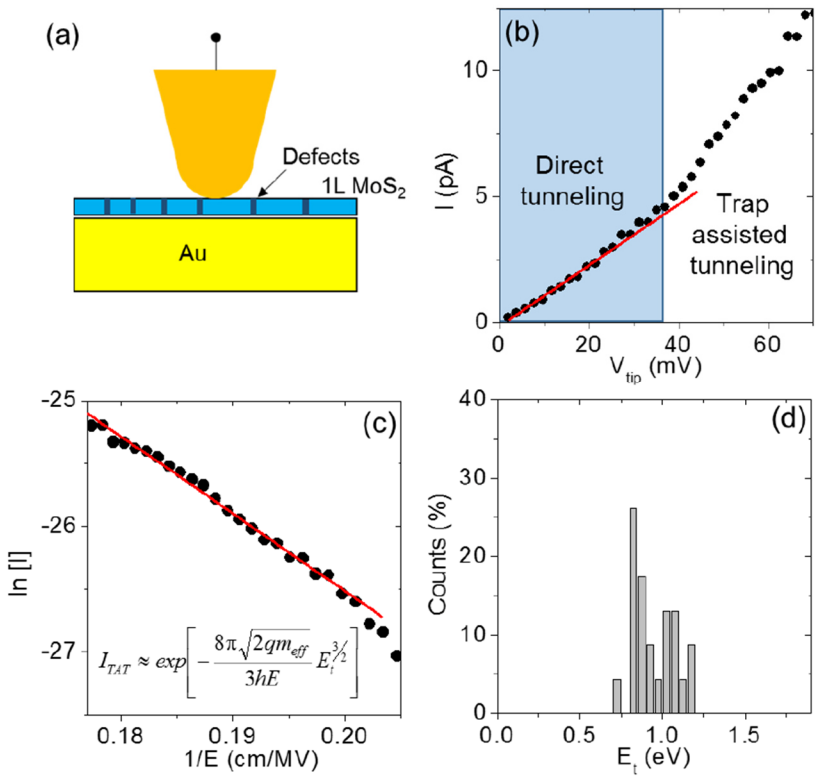

Figure 3.17.- (a) Schematic of the tip/MoS_2/Au system, where the presence of defects (e.g. sulfur vacancies) in the 1L MoS_2 has been indicated. (b) Typical I-V_{tip} curve, where two conduction regimes are indicated: a linear regime (at lower bias) ruled by direct tunnelling, and an exponential regime (at higher bias) ruled by trap-assisted-tunnelling. (c) Plot of ln(I) vs 1/E, demonstrating that current can be described by the trap-assisted-tunnelling equation (in the insert). (d) Histogram of the E_t values obtained by fitting of all the I-V_{tip} curves in **Figure 3.16**(d). Reproduced from Ref. [215].

In addition to DT, trap-assisted-tunneling (TAT) is also expected to significantly contribute to the measured current by the C-AFM tip in exfoliated 1L MoS_2 on Au, as schematized in **Figure 3.17**(a), due to the presence of a large density of native defects, such as sulfur vacancies [244]. In particular, we have found that this transport mechanism is able to describe well the behavior of local I-V_{tip} curves in **Figure 3.17** (b) at higher bias values. **Figure 3.17** (c) show the curves fitting with the TAT equation:

$$I_{TAT} \approx \exp\left[-\frac{8\pi\sqrt{2qm_{eff}}}{3hE}E_t^{3/2}\right] \quad (16)$$

where E is the electric field across 1L MoS_2 and E_t is the trap energy below the conduction band edge. Here, the electric field E was evaluated as $E=(V_{tip}+V_{bb})/d$, where V_{tip} is the tip bias, d=0.65 nm is the thickness of 1L MoS_2 and V_{bb}=0.3V is the average value of the upward band bending of MoS_2 due to p-type doping induced by Au. The resulting distribution of E_t values exhibits a peak at ~0.8 eV (as shown in **Figure 3.17** (d)), consistently with the results of other recent reports [248].

3.3.2 Lateral current transport in 1L-MoS_2 on Al_2O_3 by back-gated field effect transistor characterization

The electronic transport in 1L MoS_2 membrane transferred onto the Al_2O_3 dielectric surface has been investigated by electrical characterization of a field effect transistor (FET) with the Al_2O_3 (100 nm)/Si back-gate and Au source and drain contacts (channel length L=10 μm), as illustrated in the insert of **Figure 3.18**(a). The output characteristics (drain current vs drain bias, I_D-V_D) of the device for different gate bias values ranging from V_G=-20 to 10 V are shown in **Figure 3.18**(a). At low drain bias (V_D<3V) current injection in the MoS_2 channel is limited by the high Schottky barrier at Au/MoS_2 contacts, whereas a linear behaviour of the I_D-V_D characteristics is observed at intermediate V_D values (from 3 to 10 V), followed by current saturation at higher voltages. The transfer characteristic (I_D-V_G) at a drain bias V_D=5V (i.e. in the linear region of I_D-V_D curves) is reported in **Figure 3.18**(b), black line. The monotonic increase of I_D with V_G is the typically observed behaviour for a transistor with an n-type MoS_2 channel. A negative threshold voltage V_{th}≈-8 V was evaluated by linear fitting of the I_D-V_G curve and taking the intercept with the voltage axis, as indicated by the arrow in **Figure 3.18**(b).

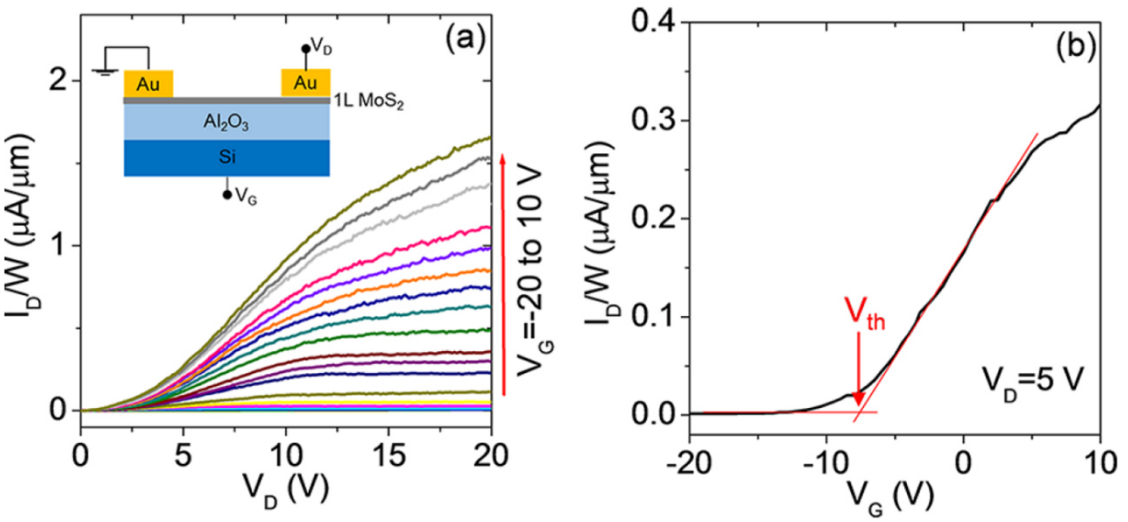

Figure 3.18.- (a) Output and (b) transfer characteristics of a back-gated field effect transistor fabricated with Au-exfoliated 1L MoS_2 transferred on Al_2O_3/Si. The device schematic is shown in the inset of panel (a). Reproduced from Ref. [215].

Since V_{th} represents the bias necessary to deplete the n-type MoS_2 channel, the electron density can be estimated as $n=C_{ox}|V_{th}|/q$, where $C_{ox}=\varepsilon_0\varepsilon_{ox}/t$ is the Al_2O_3 capacitance per unit area, with ε_0 the vacuum permittivity and $\varepsilon_{ox}=8$ is the relative dielectric constant of the Al_2O_3 dielectric. The obtained carrier density $n\approx3.1\times10^{12}$ cm^{-2} is in reasonably good agreement with the carrier density values obtained by Raman mapping. Furthermore, the channel electron mobility has been properly evaluated excluding the effect of the contact resistance. First, the inverse of the on-resistance was extracted from the slop of the linear region of the back-gated 1L-MoS_2 on Al_2O_3 output characteristics, as reported in **Figure 3.19**(a). Next, the extracted R_{on} (at different V_G) was plotted as a function of $1/(V_G-V_{th})$, as represented in **Figure 3.19**(b). A channel electron mobility of $\mu=2.3\pm0.1$ $cm^2V^{-1}s^{-1}$ and a $R_CW\approx2$ MΩμm were extrapolated from the linear fit of the equation:

$$R_{on}W = 2R_CW + L/[\mu C_{ox}(V_G - V_{th})] \quad (17)$$

where R_CW is the contact resistance, L=10 μm the channel length, C_{ox} the capacitance density of 100 nm Al_2O_3 and V_{th}=-8 V the threshold voltage.

Such electron mobility value is not different from the ones reported for back-gated monolayer MoS_2 transistors without high-κ encapsulation [2], where the electron mobility is limited by Coulomb scattering due to charged impurities. In the present case, part of these impurities may originate from the KI/I_2 etching of gold involved in the transfer procedure. In this respect, appropriate strategies should be further elaborated to detach the exfoliated 1L MoS_2 from the Au substrate without using etching procedure. These may include the electrolytic delamination by hydrogen bubbling, used in the past to separate CVD graphene from copper [245] and more recently CVD TMDs from Au foils [246]. Furthermore, a number of potential applications (including memristor devices), directly exploiting the high quality of large area 1L MoS_2 on gold, are currently emerging.

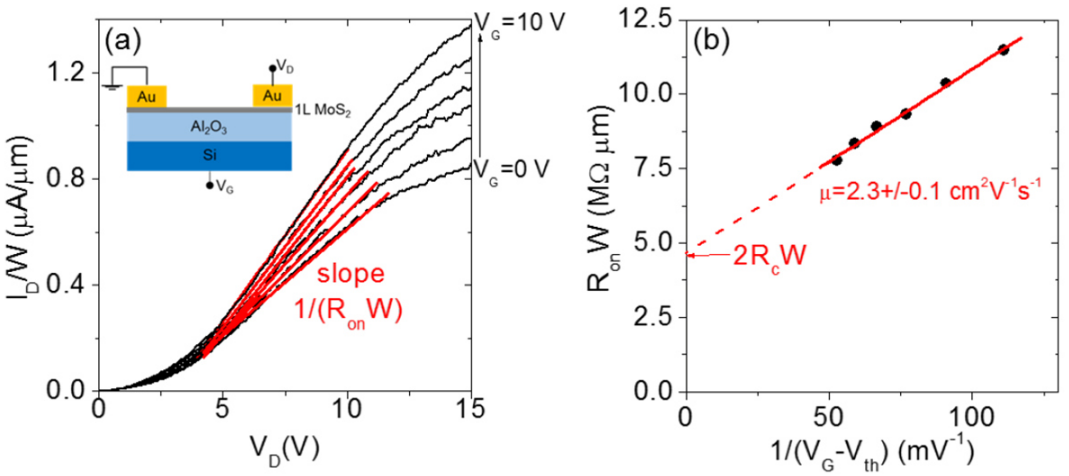

Figure 3.19.- (a) Fitting of the linear region of the output characteristics (I_D/W vs V_D) of the back-gated 1L MoS_2 FET to evaluate the on-resistance $R_{on}W$. (b) Plot of $R_{on}W$ vs $1/(V_G-V_{th})$ and linear fit with the equation $R_{on}W=2R_CW+L/[\mu C_{ox}(V_G-V_{th})]$, with R_CW the contact resistance, L=10 μm the channel length, μ the electron mobility, C_{ox} the capacitance density of 100 nm Al_2O_3, V_{th}=-8 V the threshold voltage. A contact resistance $R_CW\approx2$ MΩμm and a mobility μ=2.3±0.1 $cm^2V^{-1}s^{-1}$ were evaluated from the fit. Reproduced from Ref. [215].

3.4 SUBSTRATE PROMOTED ATOMIC LAYER DEPOSITION OF ULTRA-THIN HIGH-K DIELECTRICS ON GOLD-SUPPORTED 1L-MoS_2

The beneficial role of the high-κ integration on MoS_2 has been treated in Chapter 1 and it was appreciated how this aspect results fundamental for electronic performances improvements such as in field-effect transistors. But at the same time, the growth of ultrathin and uniform dielectric film on 2D materials is very difficult to realize, due to the absence of dangling bonds on their surface. The effects of the interaction between 1L-MoS_2 and the underlying substrate on the ALD growth of ultrathin Al_2O_3 film is here discussed considering two different substrates (Au and on Al_2O_3) [247].

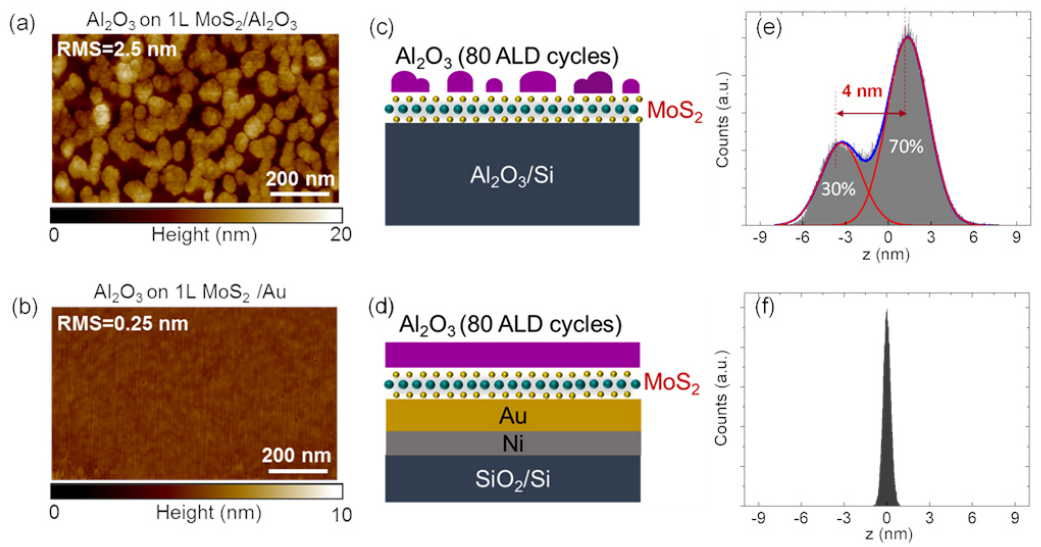

Figure 3.20.- AFM morphologies of Al_2O_3 simultaneously deposited at 250 °C by 80 ALD cycles on the surface of the 1L $MoS_2/Al_2O_3/Si$ sample (a) and of the 1L MoS_2/Au sample (b). The root mean square (RMS) roughness values of the two samples are indicated. The configuration of the deposited Al_2O_3 on 1L $MoS_2/Al_2O_3/Si$ and 1L MoS_2/Au is schematically illustrated in (c) and (d). (e) Histogram of the height distribution obtained from the AFM map of Al_2O_3 on 1L $MoS_2/Al_2O_3/Si$, from which ~70% Al_2O_3 coverage and an average height ~4 nm of Al_2O_3 islands were evaluated. (f) Histogram of the height distribution for Al_2O_3 on 1L MoS_2/Au. Reproduced from Ref. [247].

Figure 3.20 shows the comparison between the AFM surface morphologies of Al_2O_3 simultaneously deposited at 250 °C by 80 ALD cycles on the surface of the 1L $MoS_2/Al_2O_3/Si$ sample (a) and of the 1L MoS_2/Au sample (b), respectively. A high RMS roughness of 2.5 nm was observed for Al_2O_3 deposited on 1L MoS_2 supported by the Al_2O_3/Si substrate. This RMS value is much larger than the ones of the original Al_2O_3 substrate (~0.23 nm) and of 1L MoS_2 on Al_2O_3 (~0.18 nm), indicating

a very inhomogeneous coverage of 1L MoS_2 by the ALD grown Al_2O_3. This scenario, schematically depicted in **Figure 3.20**(c), is consistent with the commonly reported island growth during direct thermal ALD on MoS_2 surface. In order to evaluate the Al_2O_3 coverage, the histogram of height distribution has been reported in **Figure 3.20**(e). This histogram shows two components, related to bare and Al_2O_3 covered MoS_2 areas, from which ~70% coverage and an average Al_2O_3 islands height of ~4 nm was deduced. Differently, for 1L MoS_2 supported by the Au substrate (**Figure 3.20** (b)), a pinhole-free Al_2O_3 layer with a very flat morphology is observed after 80 ALD cycles. The deposited film exhibits a very narrow height distribution (**Figure 3.20**(f)) and low surface roughness (RMS=0.25 nm), only slightly higher

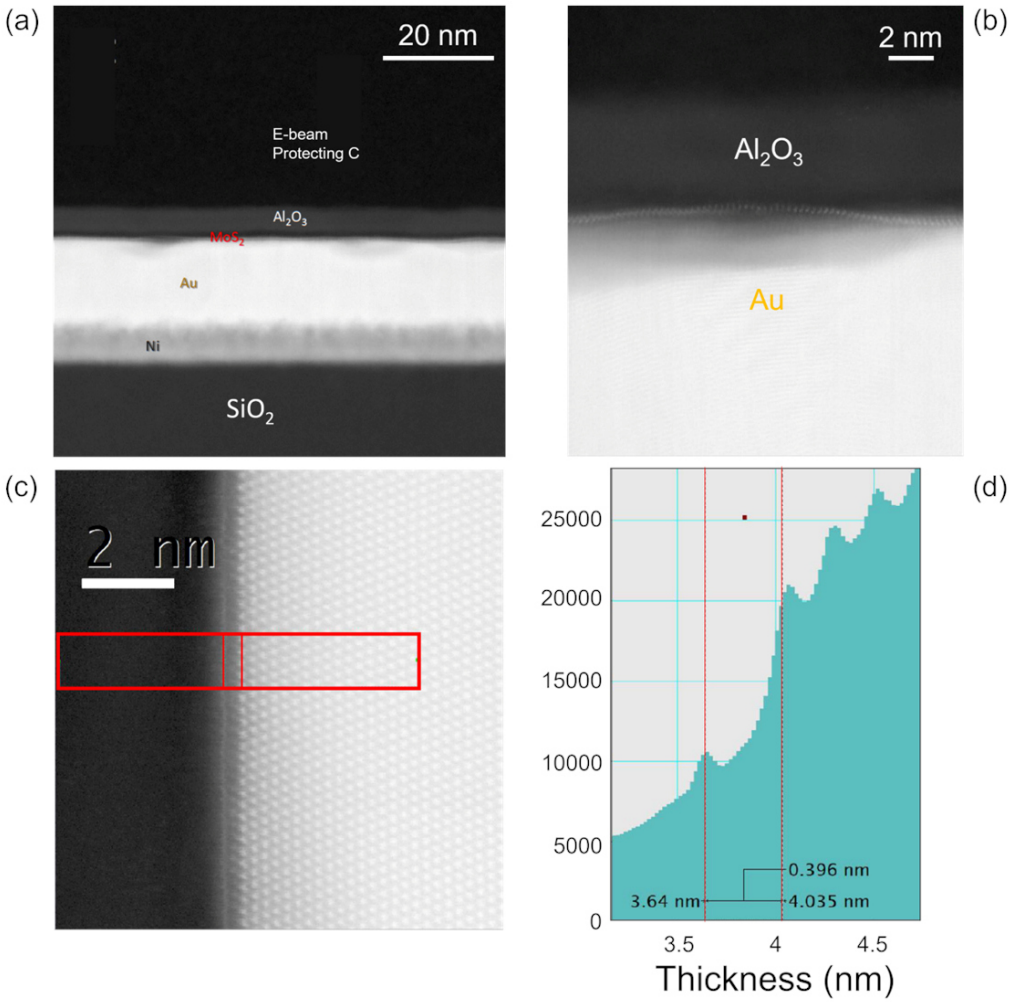

Figure 3.21.- (a) Cross-section TEM image of the lamella realized by the $Al_2O_3/MoS_2/Au/Ni/SiO_2/Si$ sample. (b) Higher magnification of the previous TEM image, in which it is possible to descriminate the 1L-MoS_2 film between the dielectric and the metallic substrate. (c) TEM image showing the distance between the Mo and Au atoms of the sample, whose value is reported in (d).

than the one measured on bare 1L MoS_2 on Au (RMS=0.17 nm) [122]. Such morphological results suggest that, under identical process conditions, an enhanced Al_2O_3 nucleation occurs on the surface of 1L MoS_2 in contact with gold, resulting in the formation of a continuous Al_2O_3 film, as schematically depicted in **Figure 3.20**(d).

Figure 3.21(a) shows the HAADF-STEM analysis on the Al_2O_3 on 1L-MoS_2/Au lamella of the sample described previously. The different contrast permits to evaluate the different elements of the sample, from SiO_2 in the bottom side, to the thin grey sheet of Ni, that results different from bigger white contrast Au film and the light grey Al_2O_3 film above it. Indeed, a sheet of e-beam carbon is employed over the Al_2O_3 film as a protective layer for the lamella. A greater magnification reported in **Figure 3.21**(b) permits to distinguish the thin 1L-MoS_2 film between the Au and the Al_2O_3 dielectric layer. This film results conformal to the Au substrate and a van der Waals gap (black region) can be appreciated between the Al_2O_3 and the MoS_2. Furthermore, **Figure 3.21**(c) is a cross-sectional STEM image in which it is possible to discriminate the crystalline ordered structure of Au (white region) and the single layer of MoS_2. From the red lines in the rectangle reported in **Figure 3.21**(c), the distance of 4.0 ± 0.2 Å between the Mo and the surface Au atoms is extracted and reported in **Figure 3.21**(d). This distance results smaller than that of 5.1 Å reported

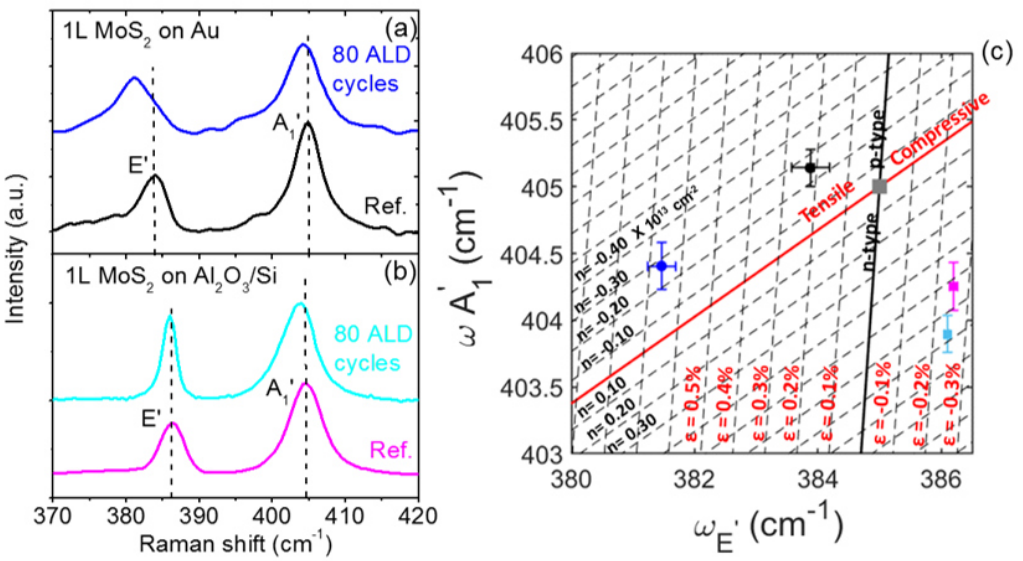

Figure 3.22.- Representative Raman spectra collected on 1L MoS_2 on Au (a) and 1L MoS_2 on Al_2O_3/Si (b) before (reference) and after 80 Al_2O_3 ALD cycles. (c) Correlative plot of the A_1' vs E' peak frequencies of the Raman spectra acquired on the 1L MoS_2 on Au before (black circle) and after (blue circle) ALD deposition and for 1L MoS_2 on Al_2O_3/Si before (magenta square) and after (cyan square) ALD deposition, allowing to evaluate the type and average values of strain and doping of 1L MoS_2 membrane. Reproduced from Ref. [247].

in other recent literature works [119], confirming the very strong nature of the interaction between the MoS_2 and Au also in our situation.

Furthermore, the significant tensile strain experienced by the 1L MoS_2 membrane exfoliated on Au can also play an important role, as discussed in the following. Micro-Raman spectroscopy analyses have been performed to investigate the strain and doping status of 1L MoS_2 residing on Au and Al_2O_3 substrates before and after the ALD growth. **Figure 3.22**(a) reports two representative Raman spectra for as exfoliated 1L MoS_2 on Au (reference) and after 80 TMA/H_2O ALD cycles. The corresponding Raman spectra for 1L MoS_2 transferred onto the Al_2O_3/Si substrate (reference) and after the 80 ALD cycles are shown in **Figure 3.22**(b). Interestingly, the E' peak redshift is further increased and the A_1' peak blue-shift is slightly reduced after ALD of the uniform Al_2O_3 film on the gold supported membrane. On the other hand, only a slight red shift of the A_1' peak was observed after 80 ALD cycles on the Al_2O_3 supported 1L MoS_2, probably due to the inhomogeneous Al_2O_3 coverage (as shown in **Figure 3.20**(a)). In order to achieve a quantification of the strain ε (%) and doping n (cm^{-2}) for the 1L MoS_2 membranes on the two different substrates before and after the ALD process, a correlative analysis of the A_1' vs E' peak frequencies has been carried out and reported in **Figure 3.22**(c), according to the procedure recently discussed in Ref. [215]. The red and black lines in **Figure 3.22**(c) represent the theoretical behaviour of the peaks' frequencies for 1L MoS_2 subjected only to a biaxial strain (tensile or compressive) or to doping (n-type or p-type), respectively. The crossing point (gray square) of these lines corresponds to literature values of the E' and A_1' positions for a free-standing 1L MoS_2, taken as the best approximation for ideally unstrained and undoped MoS_2. The spacing of the dashed lines parallel to the ideal strain and doping lines is associated with carrier density changes of 0.1×10^{13} cm^{-2} and strain changes of 0.1%, respectively. The black point is the average value of the A_1' vs E' frequencies from several (>20) Raman spectra measured on the reference 1L MoS_2/Au sample, whereas the error bars are the standard deviations from this statistical analysis. The magenta point is the average value obtained from Raman analyses on several points of the reference 1L MoS_2/Al_2O_3 sample. For this sample, the A_1' frequency exhibits a significant dispersion (indicated by the error bar), whereas the small E' frequency dispersion is within the data point. The observed tensile strain of 1L MoS_2 exfoliated on Au substrates, combined with the presence of a very high density of native S vacancies in the material [248], can also contribute to the enhanced Al_2O_3 nucleation during the early stages of thermal ALD. Furthermore, recent investigations of the vibrational properties for MoS_2/Au samples

with variable MoS_2 thickness showed a significantly reduced effect of the MoS_2/Au interaction on 2L MoS_2 as compared to 1L samples [249].

Noteworthy, the blue point in **Figure 3.22**(c) obtained from Raman analyses after 80 ALD cycles on 1L MoS_2/Au indicates a further increase of the tensile strain ($\varepsilon \approx 0.65\%$), as compared to the original value of 0.21%, which can be associated to the formation of a compact Al_2O_3 film on top of MoS_2. On the other hand, no significant changes with respect to the original p-type doping value was observed after the ALD growth, confirming that the doping status of the film is strongly dominated by the strong Au-1L MoS_2 interaction. Finally, the data-point for the 1L MoS_2/Al_2O_3 sample after the 80 ALD cycles indicates no significant changes in the compressive strain, consistently with the highly inhomogeneous Al_2O_3 coverage, and an increase of the n-type doping to $n \approx 0.6 \times 10^{13}$ cm^{-2}. This latter can be ascribed to positively charged defects [250] at the interface between the poor quality Al_2O_3 film and 1L MoS_2.

In **Figure 3.23**, micro-PL spectra acquired on the two reference 1L MoS_2 samples and after 80 cycles ALD growth are also reported, to further elucidate the impact of the substrate and of the deposition process on the optical emission properties of the direct bandgap 1L MoS_2 membrane. A prominent emission peak located at 1.84 eV

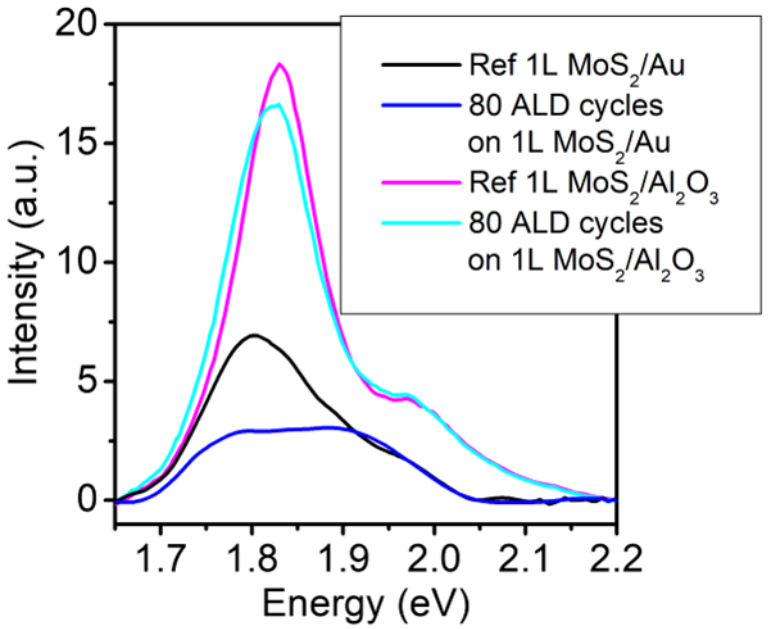

Figure 3.23.- Micro-PL spectra acquired on 1L MoS_2/Al_2O_3 and on 1L MoS_2/Au samples before (ref. spectra) and after 80 Al_2O_3 ALD cycles. Reproduced from Ref. [247].

can be observed for 1L MoS_2 supported by Al_2O_3/Si, whereas a significant reduction of the PL intensity accompanied by a red shift of the main peak position at 1.79 eV is found for the reference sample on Au. A similar quenching of the PL intensity has been reported for 1L MoS_2 exfoliated on Au [119,215] and for MoS_2 functionalized with Au nanoparticles [231]. This behavior can be explained in terms of a preferential transfer of photoexcited charges from MoS_2 to Au. In addition, the tensile strain of 1L MoS_2 in contact with Au can also play a role in the reduction of the PL yield [90].

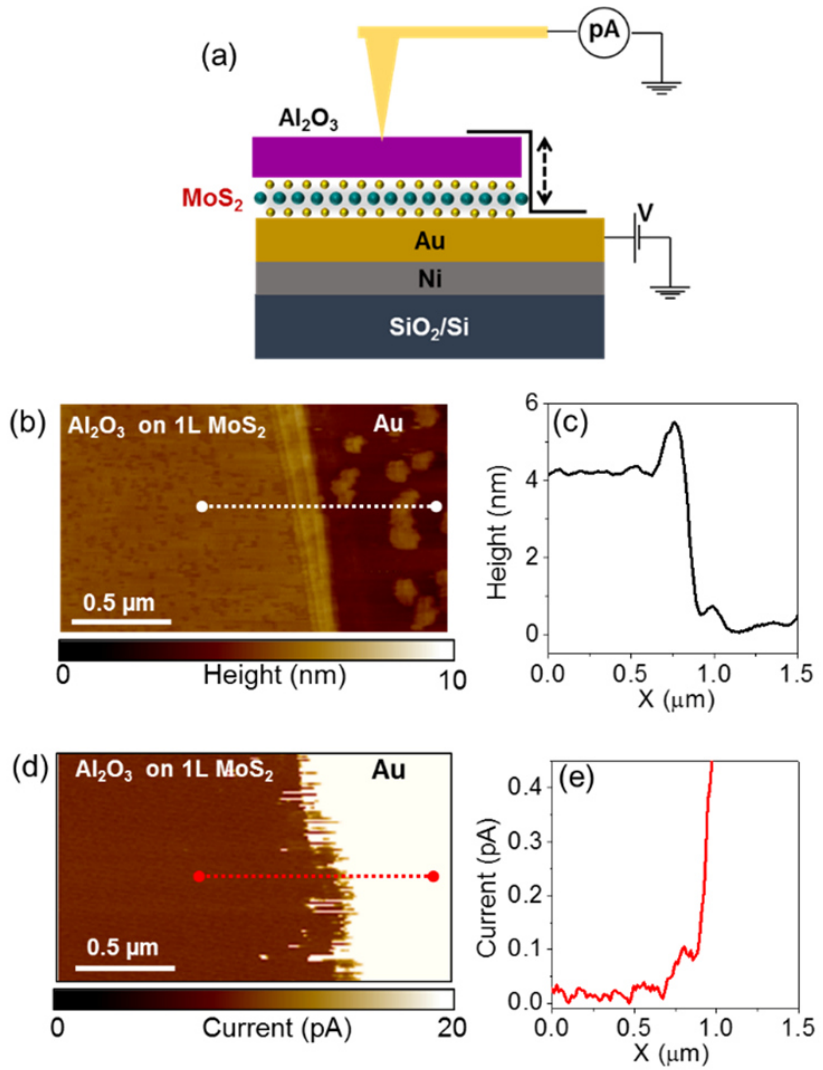

Figure 3.24.- (a) Schematic of the step between the Al_2O_3/1L MoS_2 stack and the underlying Au substrate. (b) AFM image and (c) height line-profile of the step, from which a deposited Al_2O_3 thickness of ~3.6 nm was estimated, after subtracting 1L MoS_2 thickness (~0.7 nm) (d) C-AFM current map simultaneously acquired with a bias V=3V and (e) current profile, demonstrating a good insulating quality of the deposited Al_2O_3 film onto 1L MoS_2 on Au. Reproduced from Ref. [247].

After 80 ALD cycles, only a small reduction of the PL intensity was observed for the 1L MoS_2/Al_2O_3 sample, which can be explained by the highly inhomogeneous Al_2O_3 coverage and to the small interaction of MoS_2 with the dielectric substrate. On the other hand, further quenching of the PL intensity was found in the case of 1L MoS_2/Au sample covered by the ~3.6 nm uniform Al_2O_3 film. This observation can be consistent with the increase of the tensile strain observed by Raman analyses and the consequent increase of the interaction with the Au substrate due to the material added on top of MoS_2.

In order to evaluate the thickness and the electrical insulating quality of the uniform Al_2O_3 film deposited on 1L MoS_2/Au, C-AFM morphology and current maps were simultaneously acquired by scanning the metal tip across a step between the Al_2O_3/1L MoS_2 stack and the underlying Au substrate, as schematically depicted in **Figure 3.24**(a). **Figure 3.24**(b) shows a morphological image collected in the proximity of a crack in the 1L MoS_2 membrane. The growth of a uniform and compact Al_2O_3 film on 1L MoS_2 and a poor ALD growth on the bare Au surface can be deduced from this image. Furthermore, the height line-profile in **Figure 3.24** (c) displays a total thickness of the Al_2O_3/MoS_2 stack of ~4.3 nm, from which a deposited Al_2O_3 thickness of ~3.6 nm can be estimated, by subtracting the thickness of 1L MoS_2 on Au (~0.7 nm) [215]. The slightly increased height observed at the step edge can be ascribed to the folding of the broken 1L MoS_2 membrane. The electrical

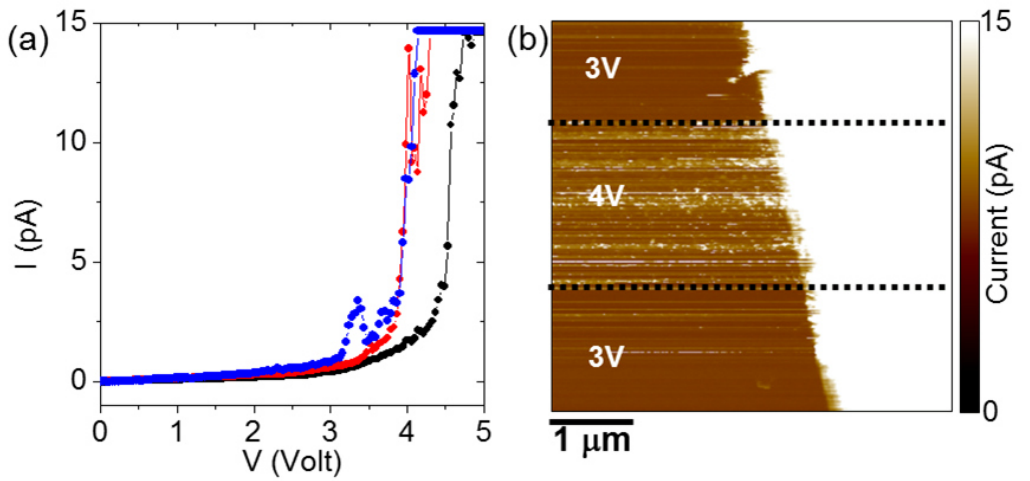

Figure 3.25.- (a) Local current-voltage (I-V) characteristics collected at three different positions (different color points) on the Al_2O_3/MoS_2/Au stack, showing current breakdown at biases between 3.7 and 4.5 V. (b) C-AFM current map collected on the Al_2O_3/MoS_2/Au stack at bias values of 3V (upper region), 4V (middle region) and 3V (lower region). A significant increase of the current leakage, with the appearance of localized breakdown spots is observed at 4 V. Reproduced from Ref. [247].

insulating properties of the 3.6 nm Al_2O_3 film deposited onto 1L MoS_2 on Au are demonstrated by the current map in **Figure 3.24**(d), acquired by applying a bias of 3 V between the tip and the gold substrate. In particular, the line-profile in **Figure 3.24**(e) shows very low current values in the Al_2O_3/1L MoS_2 region, whereas the saturation value of the current sensor was reached on Au region. The current conduction in the region close to the step edge suggests lower insulating properties of Al_2O_3 deposited on the locally folded MoS_2 membrane.

To get further insight on the electrical insulating quality of the 3.6 nm Al_2O_3 film, local current-voltage (I-V) characteristics were acquired by the C-AFM tip on the Al_2O_3/1L MoS_2/Au stack. **Figure 3.25**(a) shows three representative I-V curves measured at three different positions on the Al_2O_3 surface by ramping the bias from 0 to 5 V. While very low leakage current values are observed up to ~3 V, an abrupt rise of current up to the compliance level (indicating a localized dielectric breakdown) occurs at bias values in the range from 3.7 to 4.5 V, depending on the local I-V curve. For the Al_2O_3 film thickness t_{ox}=3.6 nm, these breakdown voltage (V_{BD}) values correspond to a breakdown electric field ($E_{BD}=V_{BD}/_{tox}$) of ~10 – 12 MV/cm. These values are comparable to those reported for the state-of-the-art high-κ dielectrics with similar equivalent oxide thickness (EOT) deposited by ALD on MoS_2 [251]. The localized nature of the breakdown events is further confirmed by the current map in **Figure 3.25**(b), acquired on the surface of the Al_2O_3/1L MoS_2/Au stack while changing the bias from 3V (in the upper part of the image) to 4V (in the middle part) and then back to 3V (bottom part). An increase of the leakage current level is observed when increasing the bias from 3 to 4V, with the appearance of conduction instability and some localized breakdown spots. After reducing the bias down to 3V (bottom part of the image), the current level becomes identical to the one in the upper part, confirming the localized character of the breakdown behavior.

Brief Conclusion

In conclusion, the optimization of the gold-assisted exfoliation allowed the preparation of large-area (cm^2) 1L-MoS_2 on Au and the subsequent transferring to an insulating substrate of Al_2O_3/Si. Raman spectra for 1L-MoS_2 on Au revealed an anomalous large value of $\Delta\omega \approx 21.2 \pm 0.3$ cm^{-1} compared to the typical one of 18.1 $\pm$ 0.2 cm^{-1} when transferred on Al_2O_3/Si. Such differences gradually decreased while increasing the number of MoS_2 layers. This anomalous behavior is associated to the strong interaction between the 1L-MoS_2 and Au. In particular, Raman mapping

showed an inhomogeneous distribution of p-type doping ($p \approx 0.1\text{-}0.4 \times 10^{13}$ cm^{-2}) and tensile strain (in a range between $\varepsilon \approx 0.1\text{-}0.3\%$). The electrical properties of 1L-MoS_2 on Au characterized by C-AFM, described a direct tunneling transport mechanism through the ultrathin membrane, and deduced a broad Φ_B distribution (between 0.7-1.7 eV), in agreement with the inhomogenous p-type doping. After the transfer to Al_2O_3/Si, the p-type doping and the tensile strain were converted in n-type doping ($n \approx 0.5 \times 10^{13}$ cm^{-2}) and compressive strain ($\varepsilon \approx -0.25\%$). These results are confirmed by electrical measurements on the back-gated 1L-MoS_2 transistor, showing a of n-type channel and a mobility $\mu = 2.3 \pm 0.1$ $cm^2V^{-1}s^{-1}$, comparable to MoS_2 transistor without high-κ dielectrics encapsulation. Furthermore, the PL of the 1L-MoS_2 on Au exhibited a strong quenching and a red-shift to 1.79 eV compared to the 1.84 eV peak position of the 1L-MoS_2 on Al_2O_3/Si. This red-shift is associated to a different trion/exciton intensity ratio, indicating how the relative population of the quasiparticles generation is influenced by the strong interaction between the 1L-MoS_2 and gold. The beneficial role of the metallic substrate was demonstrated to improve the high-κ dielectrics growth by ALD on the 1L-MoS_2. In fact, an homogenous and ultrathin (3.6 nm) of Al_2O_3 has been grown on 1L-MoS_2 on Au compared to the insulating substrate.

These results provide a deeper understanding of the properties of 1L-MoS_2 realized by mechanical exfoliation assisted by Au. Indeed, they will contribute to the widespread application of this outstanding quality material in the demonstration of novel device concepts and synthetic van der Waals heterostructures. However, the demonstrated high-quality ALD growth of high-κ dielectrics on large-area 1L MoS_2 produced by the Au-assisted exfoliation can find important device applications, including the fabrication of FETs or the passivation of non-volatile switching memory devices based on Au/1L MoS_2/Au junctions [128].

CHAPTER 4

INTEGRATION OF LARGE-AREA MoS_2 ON WIDE-BANDGAP SEMICONDUCTORS BY SULFURIZATION OF ULTRATHIN MO FILMS

The gold-assisted mechanical exfoliation described in the previous chapter currently represents the most advanced top-down approach for the production of high crystalline quality and extended 1L-MoS_2 membranes. However, due to the limited size of commercially available bulk MoS_2 stamps and the complexity of the transfer process, this method can be useful just for the investigation of basic physical phenomena and the demonstration of devices prototypes.

Differently, bottom-up approaches (such as chemical vapour deposition), remains the most suitable method to deposit large area ultra-thin MoS_2 films on insulating or semiconducting substrates. In particular, the two-steps CVD approach, based on the physical vapor deposition of a thin Mo (or Mo-oxide) film and its subsequent annealing under sulfur flow, is highly compatible with the state-of-the-art fabrication approaches in microelectronics. Furthermore, it potentially allows excellent control on the number of MoS_2 layers by controlling the initial film thickness.

In this chapter, the sulfurization approach has been investigated in detail and applied for the integration of ultra-thin (1L or 2L) MoS_2 on wide bandgap hexagonal semiconductors, i.e. 4H-SiC, GaN-on-sapphire and bulk GaN. After thickness calibration and compositional analysis of the Mo films deposited by DC magnetron sputtering, the sulfurization conditions leading to the formation of 1L-2L MoS_2 on these substrates have been discussed. The grown MoS_2 layers have been extensively characterized by the combination of morphological (AFM), structural/chemical (TEM with EDS and XPS) and vibrational (Raman) methods.

After assessing the quality of the layers, the vertical current injection at the interfaces of MoS_2 with 4H-SiC (n- and n^+ doped), and bulk GaN crystals has been investigated by conductive atomic force microscopy (CAFM), providing a detailed description of the electronic transport mechanisms.

4.1 Ultra-thin Mo films deposition and sulfurization process

The ultra-thin Mo films (1-2 nm thickness) used for the sulfurization process were deposited by DC magnetron sputtering from a Mo-target using a Quorum Q300-TD system. A compositional analysis by XPS and the accurate calibration of the deposited film thickness as a function of the main deposition parameters, i.e. current and time, represented the preliminary steps of this experimental study.

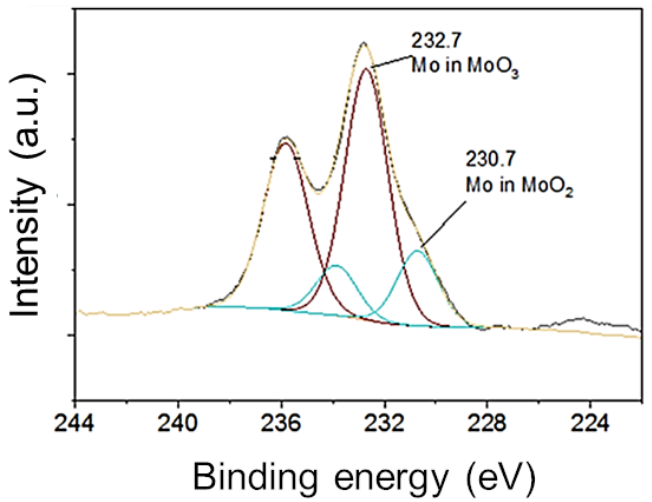

Figure 4.1.- Core level XPS spectra of as-deposited Mo on SiO_2, indicating the complete oxidation of the film. Reproduced from Ref. [40].

Figure 4.1 reports a typical XPS compositional analyses performed on the as-deposited ultra-thin Mo films, which shows their complete oxidation, being predominantly composed by MoO_3, with a smaller MoO_2 contribution. Recently, other authors [150] also reported the complete oxidation (ascribed to air exposure after the deposition) of evaporated Mo films with similar thickness, used for subsequent MoS_2 growth by sulfurization. Based on these results, from now on, the deposited

Target	Time (s)	Distance from target (cm)	Base pressure (mbar)	DC current (mA)
Mo (99.99%)	From 5-10	Fixed at 5	2.0×10^{-5}	10

Table 5.- Summary of the magnetron sputtering condition to obtain ultrathin (1-1.8 nm) of Mo films.

Mo-oxide films will be indicated as MoO_x. After initial studies, the best conditions to obtain ultrathin and reproducible Mo films are reported in **Table 5**.

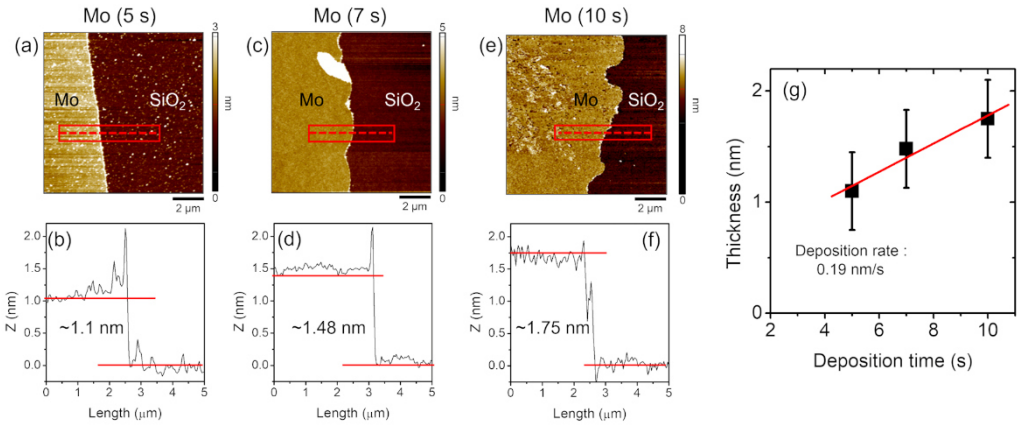

Figure 4.2.- AFM morphologies of deposited MoO_x film on SiO_2 at different time: (a) 5 seconds, (c) 7 seconds, (e) 10 seconds. Corresponding line profiles for each deposition (b) 5 s, (d) 7s, (f) 10s. Plot of the deposited Mo thickness vs the deposition time, from which a deposition rate of ~0.2 nm/s was deduced.

The thickness of the as-deposited Mo films was evaluated by AFM step height measurements performed on intentionally scratched regions of the films. **Figure 4.2** (a,c,e) show the morphologies and corresponding line profiles (b,d,f) for films deposited with different sputtering times (5 s, 7 s and 10 s), resulting in ~1.1 nm, ~1.48 nm and ~1.75 nm thickness respectively. Finally, **Figure 4.2** (g) illustrates the increase of the deposited film thickness as a function of the sputtering time (5, 7 and

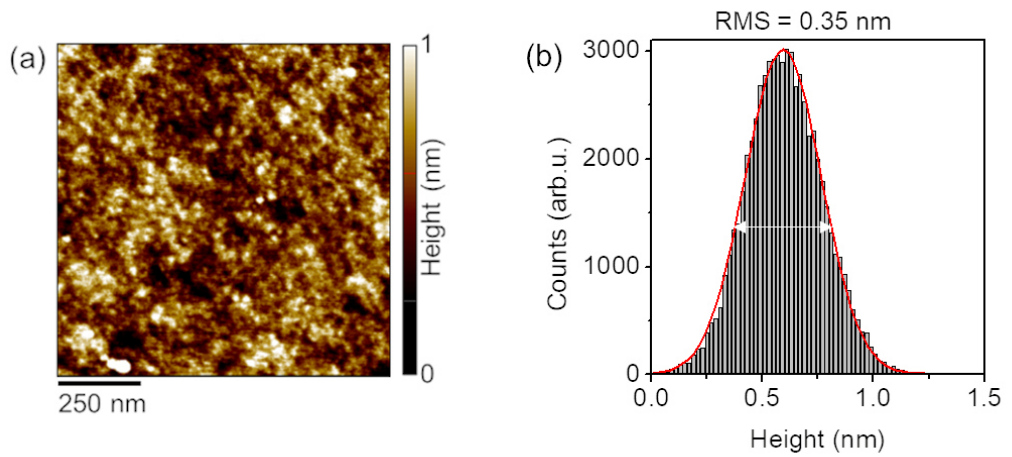

Figure 4.3.- (a) Typical AFM morphology of as-deposited MoOx thin films with sputtering time 7 s on SiO_2. (b) Histogram of the height distribution with the indication of the root mean square (RMS) roughness with respect to the SiO_2. Reproduced from Ref. [252].

10s), from which a deposition rate of around 0.19-0.20 nm/s was deduced by the linear fit of the experimental data.

Figure 4.3(a) shows a typical AFM morphology of the as-deposited film on the SiO_2/Si substrate using a sputtering time of 7 s. This analysis indicates a very low root mean square (RMS) surface roughness of 0.35 nm, as observed in **Figure 4.3**(b). Similar roughness values have been measured for films deposited at higher and lower sputtering times.

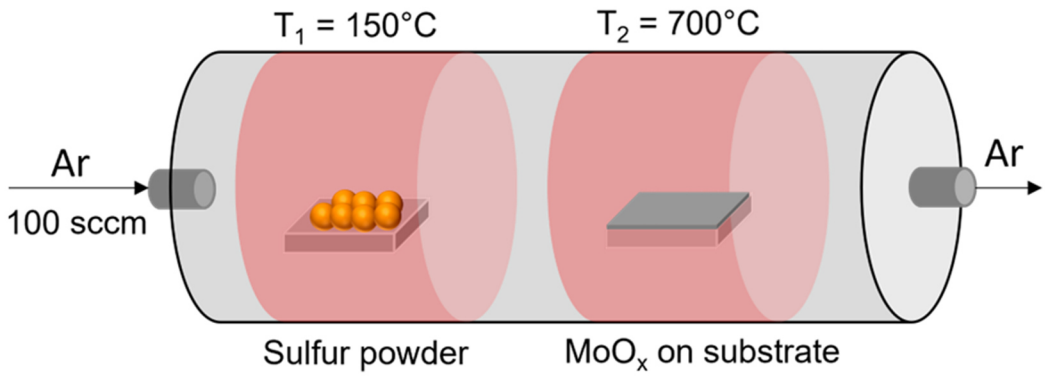

Figure 4.4.- Schematic illustration of MoS_2 growth by sulfurization of a pre-deposited MoOx film, T_2 is fixed at 700°C. Reproduced from Ref. [40].

The sulfurization process was carried out in a two heating-zones furnace, represented in **Figure 4.4**. The first zone hosts a crucible with 300 mg of sulfur (purity 99.9%) heated at 150°C, while the MoO_x/SiO_2 samples are located in the second zone (at temperature of 700°C) with a flux of argon carrier gas (100 standard cubic centimeters per minute (sccm)) with the purpose to transport the sulfur vapors from the first to the second zone. The process is realized in 60 minutes.

In a recent work the authors [150] explained the conversion of MoO_3 to MoS_2 upon exposure to sulfur according to the following chemical reaction:

$$2MoO_3\ (s) + 7\ S\ (g) \rightarrow 2\ MoS_2\ (s) + 3\ SO_2\ (g) \qquad (18)$$

which is the result of two intermediate steps:

$$MoO_3\ + (x/2)\ S\ \rightarrow MoO_{3-x}\ + (x/2)\ SO_2 \qquad (19)$$

$$MoO_{3-x}\ + [(7-x)/2)\ ]\ S\ \rightarrow MoS_2\ + [(3-x)/2)\ ]\ SO_2 \qquad (20)$$

i.e. the S-induced reduction of the MoO_3 to a sub-stoichiometric oxide MoO_{3-x} Eq.(19), followed by its conversion to MoS_2 Eq.(20), with the formation of gaseous SO_2 as a by-product. During this process, the evaporation of MoO_3 from the surface can play a significant role, depending on the temperature [150].

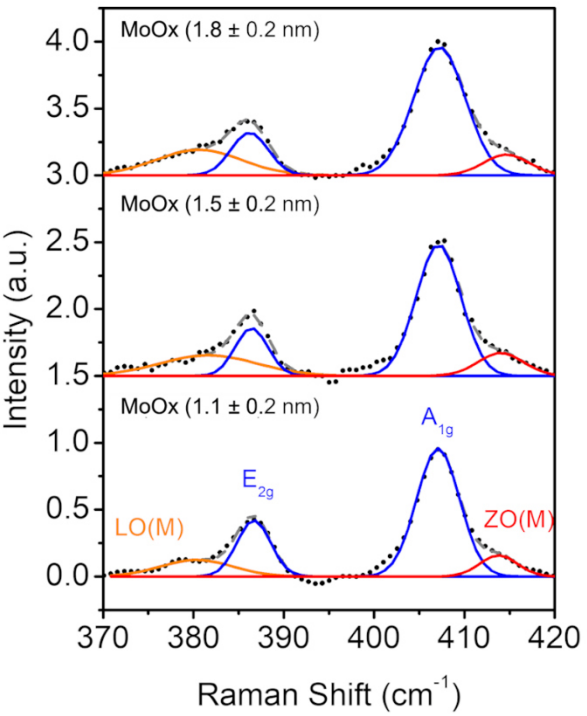

Figure 4.5.- Raman spectra for MoS_2 on SiO_2 growth by sulfurization from different starting MoOx thickness (1.1, 1.5, 1.8 nm).

In our experiments, the temperature of 700°C for the second zone was chosen as an optimal trade-off for the conversion of the as-deposited MoO_x into MoS_2, while minimizing MoO_x evaporation phenomena that inevitably would compromise the uniformity of the MoS_2 film.

The formation of MoS_2 after this process was evaluated by the Raman spectra. As reported in **Figure 4.5**, the two main vibrational peaks at different thickness of the starting MoO_x are found. Besides the two main vibrational peaks E_{2g} and A_{1g}, the deconvolution analysis permits to observe two additional peaks defined LO(M) and ZO(M), outlined by orange and red lines respectively. As described in the previous

chapter, these two peaks are associated with the defective nature of the MoS_2 produced by sulfurization, but also to the polycrystalline and nanometric dimension of film grains. In particular, LO(M) contribution seems to increase in width and intensity as a function of the thickness of the MoO_x film, while the ZO(M) peak remains practically constant at different MoO_x thickness. A further information extracted by Raman spectra is the thickness of the MoS_2 film, that was realized by a statistical study on the difference between the two main vibrational peaks positions, E_{2g} and A_{1g}, as reported in **Figure 4.6**. The MoS_2 realized by a starting Mo thickness of 1.1 and 1.5 nm shows a $\Delta\omega$ of around 20.3 ± 0.7 cm^{-1}, while a little change of the distribution is observed when the sulfurization is realized on 1.8 nm of MoOx (with $\Delta\omega$~ 21.1 ± 0.7 cm^{-1}). However, these statistical distributions are always centered in the region of 1L-2L of MoS_2, as underlined by the red dashed lines in **Figure 4.6**.

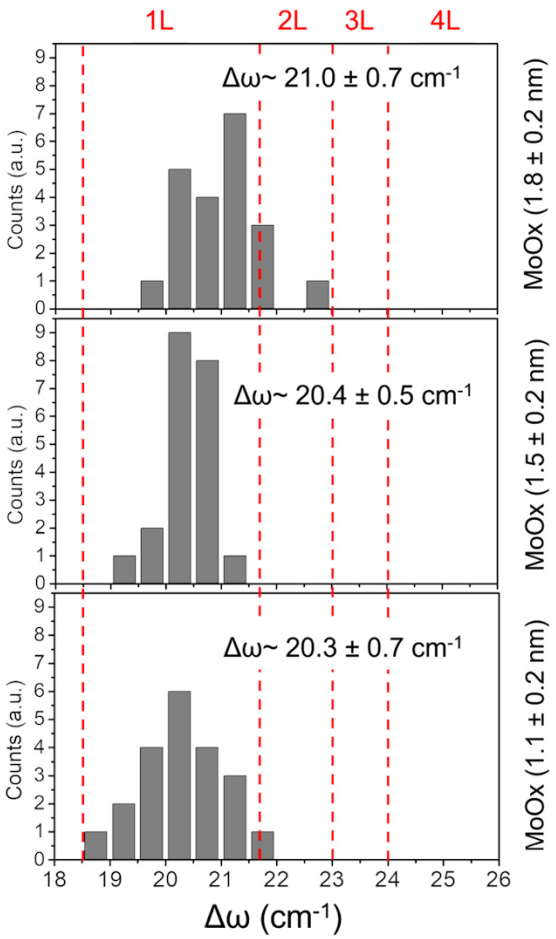

Figure 4.6.- Distribution of the difference between the two vibrational MoS_2 Raman peaks, E_{2g} and A_{1g}, at different starting MoO_x thickness (1.1, 1.5 and 1.8 nm).

These preliminary evaluations on the MoS_2 produced on SiO_2, provided us the correct conditions of growth to obtain a single or two-layers of MoS_2. The same sulfurization conditions were employed for the MoS_2 growth on wide bandgap semiconductors, as will be described in next paragraph.

4.2 MoS_2 INTEGRATION WITH 4H-SiC

4.2.1 MoS_2 heterostructures with n^- and n^+ doped 4H-SiC(0001)

MoS_2 was grown on the surface of highly n^+-doped (~10^{19} cm^{-3}) 4H-SiC(0001) 4°-off substrates and of n^--doped (~10^{16} cm^{-3}) 4H-SiC epi-layers by sulfurization of pre-deposited ultra-thin MoO_x films. The as-deposited MoO_x films, with ~1.2 nm thickness evaluated by AFM step height measurements, were investigated by XPS analysis. As previously illustrated in **Figure 4.4**, the sulfurization process was carried out in quartz tube with two-heating zones. The samples placed in the second zone (at a temperature T_2=700 °C) were exposed to sulfur vapors transported by the carrier gas (Ar) from the crucible in the first zone (at T_1=150 °C).

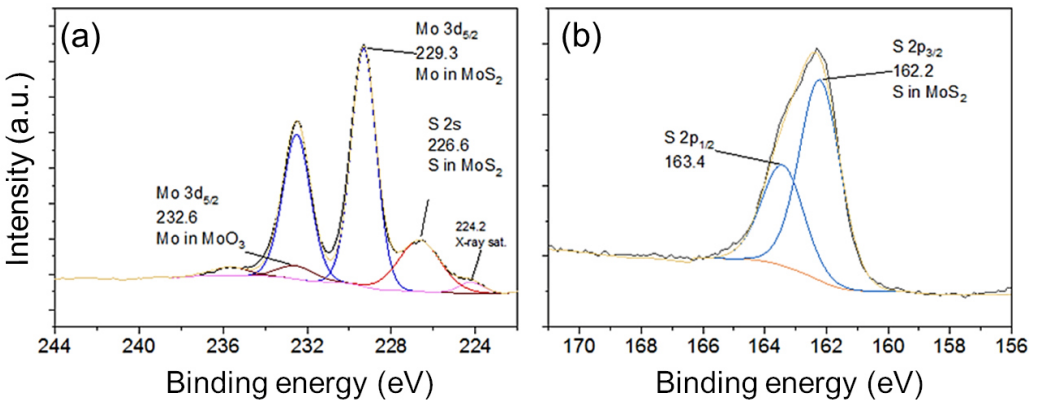

Figure 4.7.- Mo 3d and S 2s (a) and S sp (b) core level XPS spectra of MoS_2 thin films obtained by sulfurization of MoO_x on 4H-SiC. Reproduced from Ref. [40].

Figure 4.7 shows the results of XPS analyses performed after the sulfurization process ((a) and (b)). The expected Mo3d, S2s and S2p contributions associated to MoS_2 can be observed in **Figure 4.7**(a) and (b), accompanied by minor contributions associated to unreacted MoO_3. This MoO_3 component is found to play a crucial role in the electrical behavior of the MoS_2/4H-SiC heterostructure, as discussed later on in this chapter.

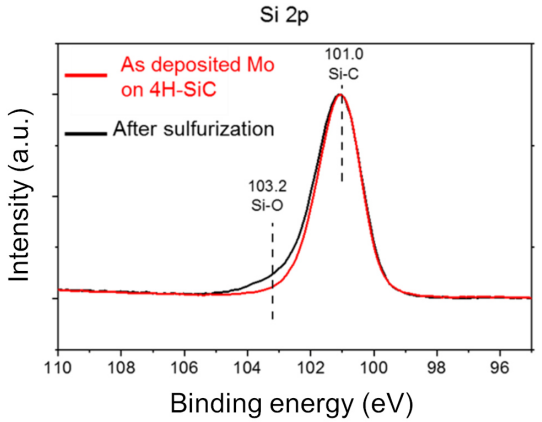

Figure 4.8.- Core level XPS spectrum of Si 2p for 4H-SiC with as-deposited MoO_x and after the sulfurization process for MoS_2 formation. For both samples, the main peak energy corresponds to the Si-C bonding in 4H-SiC. A contribution associated to a slight oxidation of Si can be observed after the sulfurization process. Reproduced from Ref. [40].

According to other recent reports [150,252], the sulfurization of ~1 nm MoO_x is expected to result in the formation of 1L MoS_2. No reaction between Mo or S and 4H-SiC occurs during the sulfurization process, while a slight oxidation of 4H-SiC

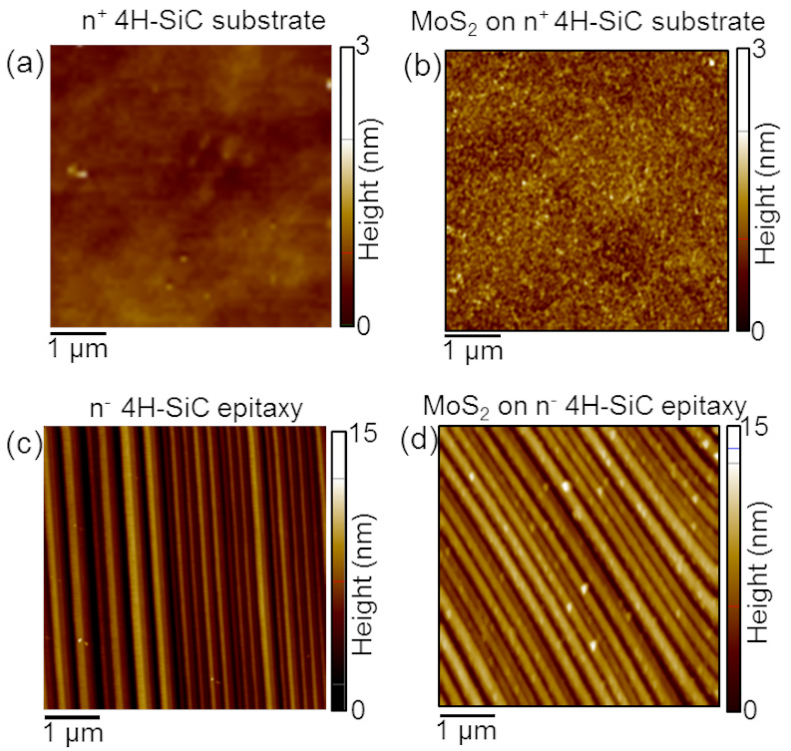

Figure 4.9.- AFM morphologies of the bare surfaces for n^+ 4H-SiC substrate (a) and n^- 4H-SiC epitaxy (c), and after the MoS_2 growth on the two samples ((b), (d)). Reproduced from Ref. [40].

is observed, as indicated by Si 2p core level spectra of the as deposited and annealed samples, as reported in **Figure 4.8**.

Figure 4.9(a) and (b) show the surface morphology of the pristine 4H-SiC n^+ substrate and after MoS_2 formation. The conformal coverage of the SiC surface by a nanocrystalline film, with average grain size of ~50 nm, can be deduced from **Figure 4.9**(b). The morphology of the bare n^- 4H-SiC epitaxial layer exhibits the typical step bunching associated to the 4°-off miscut angle (**Figure 4.9**(c)), and the coverage by the nanocrystalline MoS_2 film can be argued after the MoO_x thin film sulfurization (**Figure 4.9**(d)).

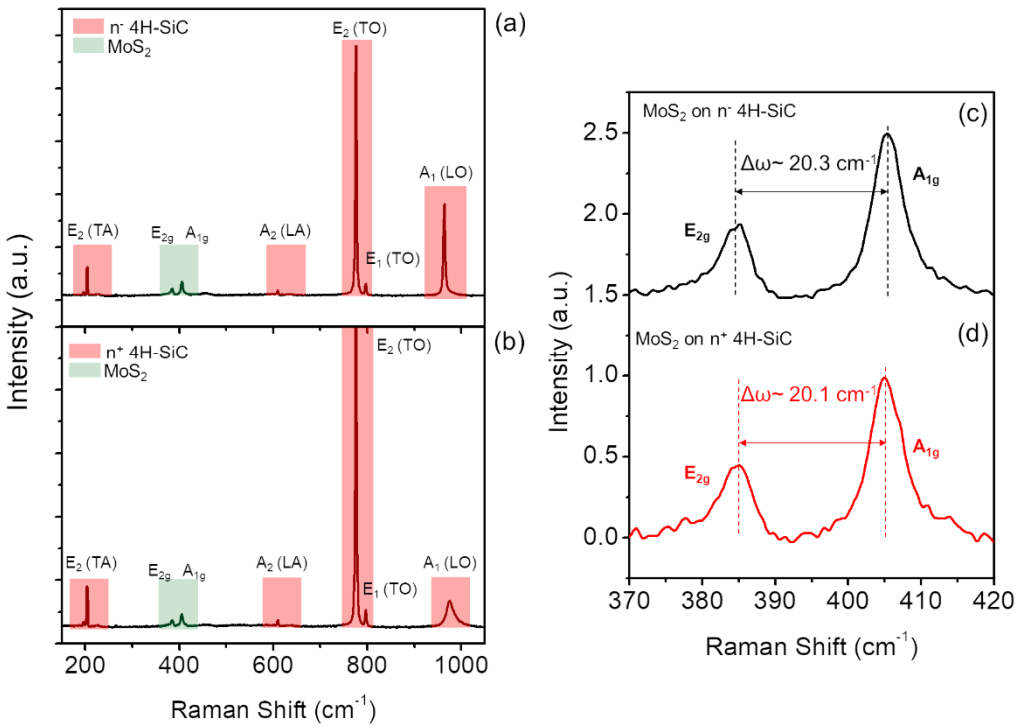

Figure 4.10.- Typical Raman spectrum of (a) MoS_2 on n^- 4H-SiC and (b) on n^+ 4H-SiC with the identification of the MoS_2 (green square) and 4H-SiC components (red squares). Detail of the MoS_2 vibrational modes, E_{2g} and A_{1g}, and their difference ($\Delta\omega$) on n^- 4H-SiC (c) and on n^+ 4H-SiC (d). Reproduced from Ref. [40].

The MoS_2 thickness uniformity on the n^+ and n^- 4H-SiC was quantitatively evaluated by Raman mapping. Typical Raman spectra collected with a laser source of 532 nm on the MoS_2/n^--SiC and MoS_2/n^+-SiC sample are reported in **Figure 4.10**(a-b), where the main vibrational features of the 4H-SiC substrate (i.e., E_2(TA), A_2(LA), E_2(TO),

E_1(TO), A_1(LO)) and of 2H-MoS_2 (E_{2g} and A_{1g}) have been highlighted. **Figure 4.10**(c-d) show a closer view of the in-plane (E_{2g}) and out-of-plane (A_{1g}) vibrational modes of MoS_2, with the indication of the peaks wavenumber difference $\Delta\omega \approx 20.1$ cm^{-1} and 20.3 cm^{-1}, which is consistent with monolayer (1L) MoS_2 thickness [2,84]. **Figure 4.11**(a) and (b) display color map and the histogram of the $\Delta\omega$ values extracted from an array of 50×50 Raman spectra collected on 10 μm×10 μm of MoS_2/n^+-4H-SiC sample area. From this statistical analysis, an average value of $\Delta\omega \approx 20.1$ cm^{-1} with a standard deviation of 0.8 cm^{-1} has been deduced, indicating that the film produced by sulfurization is predominantly formed by 1L-MoS_2, with a small fraction of 2L or 3L areas. The same kind of analysis (reported in **Figure 4.11**(c)-(d)) was carried out on the MoS_2/n^--SiC sample, showing a very similar distribution of MoS_2 number of layers (average $\Delta\omega \approx 20.3$ cm^{-1} with a standard

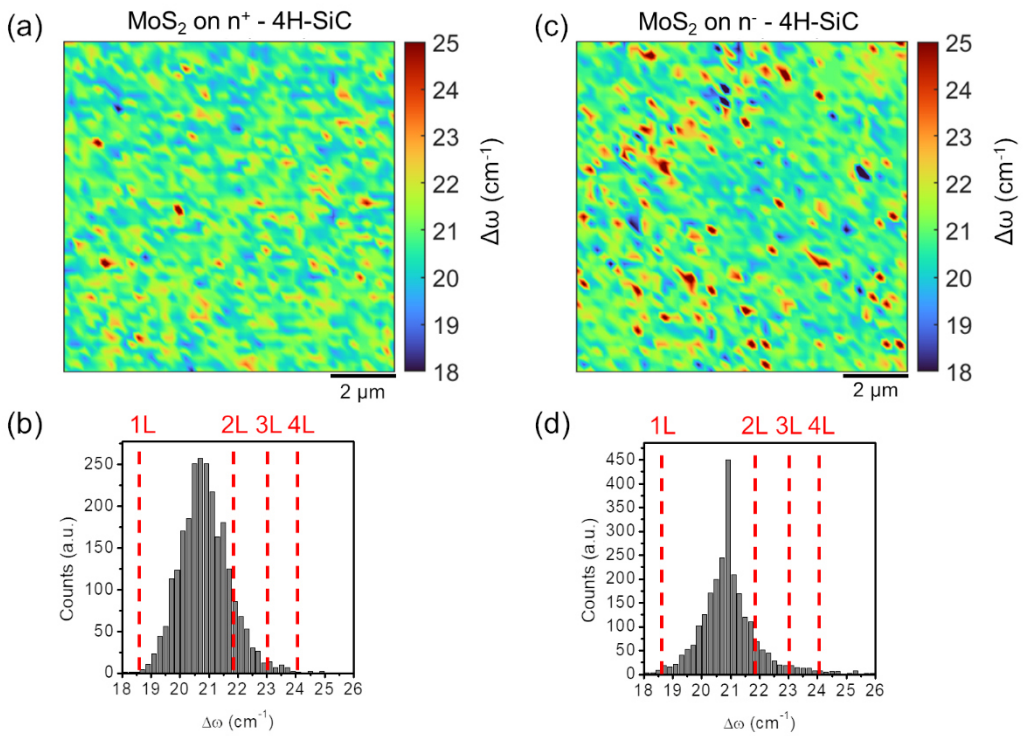

Figure 4.11.- Colour map (a-c) and histogram (b-d) of the $\Delta\omega$ values extracted from an array of 50×50 Raman spectra collected on 10 μm×10 μm of MoS_2 on n^+-4H-SiC and on n^- -4H-SiC, respectively. Reproduced from Ref. [40].

deviation of 0.5 cm^{-1}), in spite of the differences in the surface morphology between the n^+-SiC substrate and the epitaxy observed in **Figure 4.9**.

Figure 4.12(a) shows a low magnification cross-sectional scanning transmission electron microscopy (STEM) image in the high angle annular dark field (HAADF) mode of the ultra-thin MoS_2 film grown on the n^+ 4H-SiC substrate. In this imaging mode, based on Z contrast, MoS_2 appears as a single or double layer with bright contrast. It is covered by a carbon film (with low Z contrast) with a top-most Pt layer, used as protective layers during Focused Ion Beam (FIB) preparation. Furthermore,

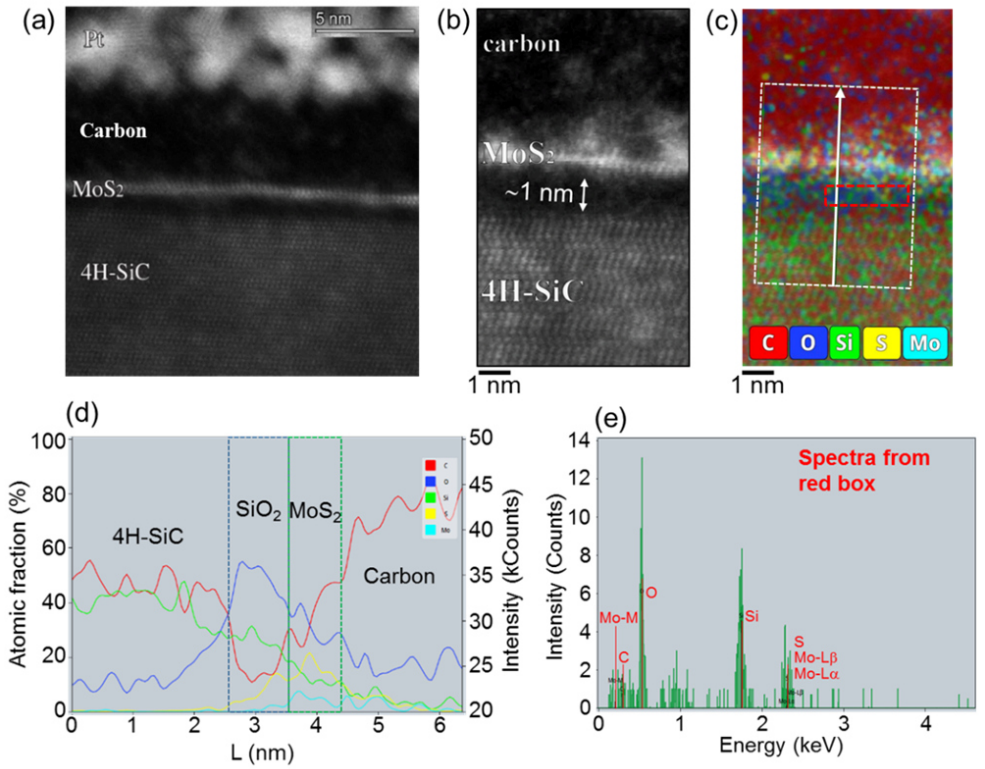

Figure 4.12.- (a) HAADF-STEM of the MoS_2 heterojunction with n^+ 4H-SiC. Comparison between atomic resolution HAADF (b) and EDS elemental map (c), demonstrating the presence of ~1 nm SiO_2 at MoS_2/SiC interface. (d) Line profile of the atomic fraction vs position extracted from the EDS map. (e) X-ray spectra collected from the red-box area in the EDS map (c), from which SiO_2 composition can be deduced. Reproduced from Ref. [40].

a dark stripe is typically present at the interface between MoS_2 and 4H-SiC. **Figure 4.12**(b) shows an atomic resolution HAADF-STEM, from which ~1 nm thickness of this dark stripe is evaluated.

To get information on the composition of this interfacial region, an EDS spectrum image (**Figure 4.12**(c)) was simultaneously collected, showing the elemental distribution of carbon, oxygen, silicon, molybdenum, and sulfur. Furthermore, a

depth profile of atomic fractions extracted from the spectrum image is reported in

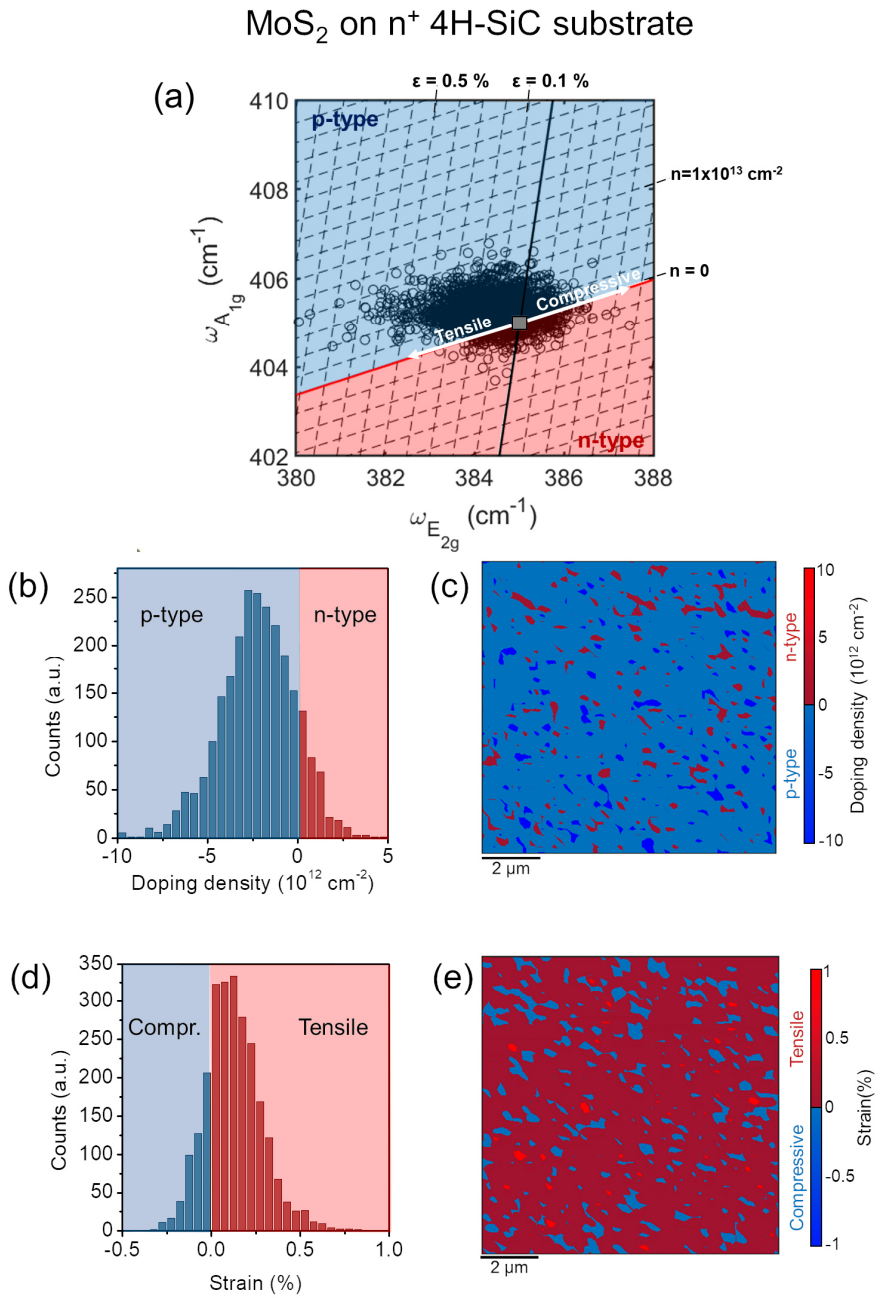

Figure 4.13.- (a) Correlative plot of the A_{1g} and E_{2g} Raman peaks' wavenumbers extracted from the array of 50×50 Raman spectra on 10 μm×10 μm sample area in **Figure 4.11**(a). Histogram and (c) map of the MoS_2 doping density. (d) Histogram and (e) map of the MoS_2 strain. Reproduced from Ref. [40].

Figure 4.12(d). On the left we can see a composition, which belongs to the 4H-SiC substrate. Then, in the middle, where oxygen concentration (blue line) increased, we observe a SiO_2 composition. Then one can observe the MoS_2 stripe, covered by the protective carbon film. Furthermore, **Figure 4.12** shows a X-Ray spectrum collected in the rectangular box region in (c), corresponding to the dark stripe in the Z contrast image (b). This compositional analysis clarifies that the ~1 nm dark stripe between MoS_2 and 4H-SiC observed in the HAADF image (**Figure 4.12**(b)) is SiO_2, formed during the high temperature sulfurization of the original metal (oxide), as indicated also by XPS analyses (**Figure 4.8**).

Focusing our attention to the MoS_2 sample grown on n^+-4H-SiC, a correlative plot of the A_{1g} and E_{2g} Raman peaks' wavenumbers (ω_{A1g} vs. ω_{E2g}), obtained from a large array of 2500 spectra measured on MoS_2 on n^+-SiC is reported in **Figure 4.13**(a). This plot provides quantitative information on the doping and strain status of the MoS_2 film, by comparing the distribution of experimental data (open circles) with the theoretical ω_{A1g}-ω_{E2g} relations for a purely unstrained 1L MoS_2 (strain line) and for a purely undoped 1L MoS_2 (doping line) [215]. The strain (doping) lines are represented by the red (black) solid lines in **Figure 4.13**(a). In particular, the strain line separates the p-type and n-type doping regions in the ω_{A1g}-ω_{E2g} plot, whereas the doping line separates the tensile and compressive strain regions.

Hence, the experimental data distribution in **Figure 4.13**(a) clearly shows that the MoS_2 film produced by Mo sulfurization exhibits a p-type doping in most of the probed area and is affected by a small tensile strain (<0.5%). Furthermore, the dashed lines parallel to the strain (doping) lines allow to estimate on the doping (strain) values associated at each data point. The histogram and the corresponding map of the doping density values have been reported in **Figure 4.13**(b) and (c), respectively. Their combination indicates the occurrence of p-type doping on ~86.4% of the probed MoS_2 area, with an average holes density of 2.5×10^{12} cm^{-2} and a standard deviation of 2×10^{12} cm^{-2}. Analogously, the occurrence of a small tensile strain on ~79.8% of the probed area, with an average ε=0.12% and a standard deviation of 0.14%, have been deduced from the histogram and the color map in **Figure 4.13**(d) and (e). Furthermore, the comparison of the two maps in **Figure 4.13**(c) and (e) indicates the lack of correlation between the doping and strain spatial distributions in the MoS_2 film.
The same kind of analysis has been carried out on the array of Raman spectra collected on MoS_2 grown on the n^- 4H-SiC epitaxy, and similar mean values of MoS_2 doping and strain were obtained as reported in **Figure 4.14**.

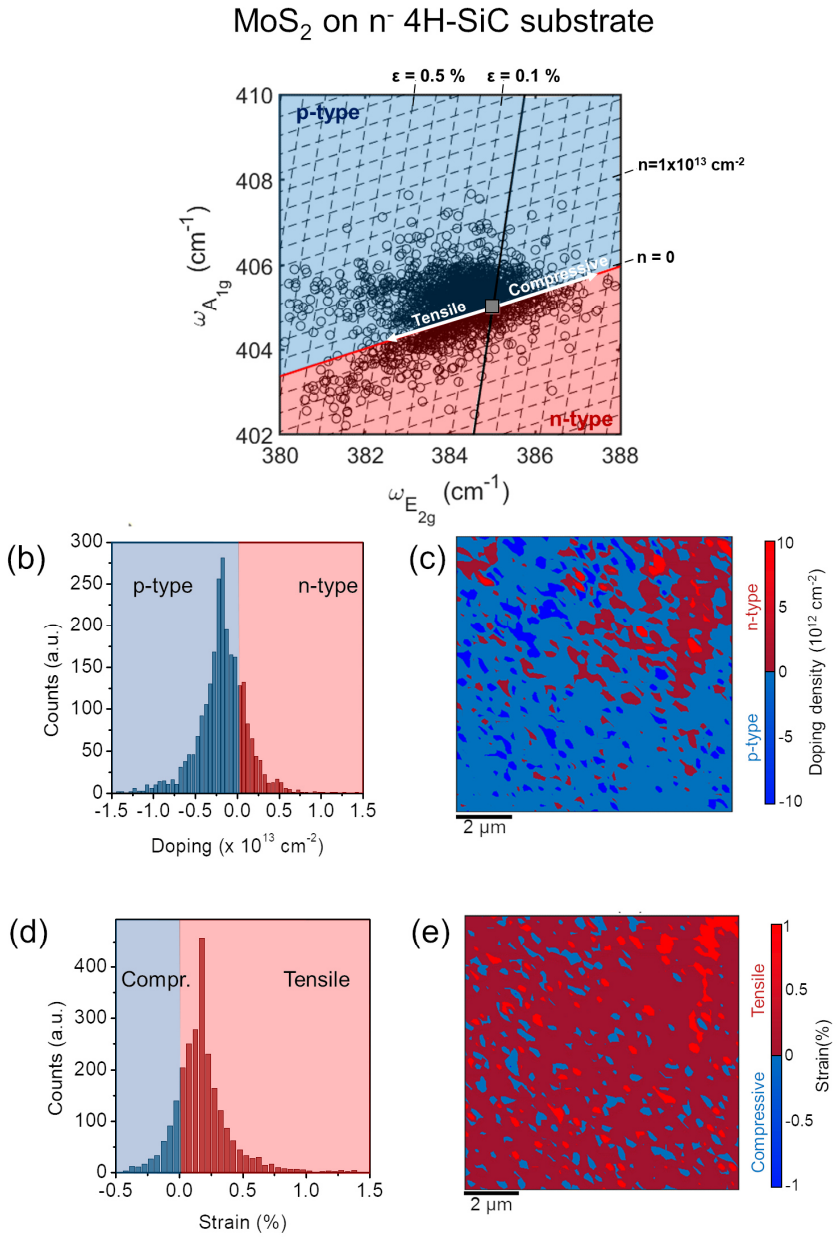

Figure 4.14.- Correlative plot of the A_{1g} and E_{2g} Raman peaks' wavenumbers extracted from the array of 50x50 Raman spectra on 10µm x 10 µm sample area of MoS_2 on n^--4H-SiC. (b) Histogram and (c) map of the MoS_2 doping density. (d) Histogram and (e) map of the MoS_2 strain. Reproduced from Ref. [40].

4.2.2 *Vertical current transport at MoS_2 heterojunctions with n^- and n^+ doped 4H-SiC(0001)*

After assessing the morphological properties and the thickness uniformity of the as-grown MoS_2 films, the current transport across their heterojunctions with the n^+ -4H-SiC and n^- -4H-SiC has been investigated using conductive atomic force microscopy (C-AFM) with Pt coated tips, according to the configurations schematically illustrated in **Figure 4.15**(a) and (d). As compared to conventional current voltage (I-V) measurements on vertical devices with deposited macroscopic electrodes, C-AFM analyses [239] provides spatially resolved information on the injected current with nanoscale resolution, corresponding to the effective contact area of the metal tip. Furthermore, this analysis is non-destructive and allows to probe the intrinsic electrical properties of the MoS_2/4H-SiC heterojunctions, avoiding any effect of contaminations (lithography-induced resist residuals) and modification of the monolayer MoS_2 films by metal deposition during devices fabrication. These metal deposition effects can be particularly relevant, as discussed in recent reference papers[253,254].

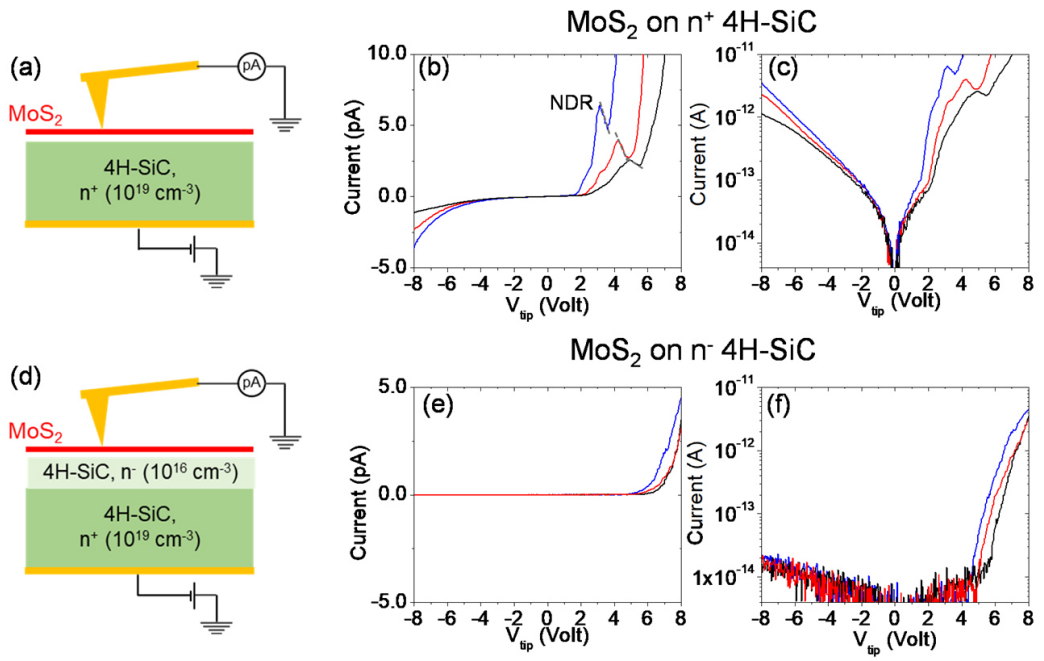

Figure 4.15.- Schematic illustration of the C-AFM setup to probe the current transport through the MoS_2 heterojunctions with the n^+ -4H-SiC (a) and n^- -4H-SiC (d). Comparison of three typical I-V characteristics on linear (b) and semilog-scale (c), collected by the Pt tip at different positions on the surface of the MoS_2/n^+ 4H-SiC heterojunction. Comparison of three typical I-V characteristics on linear (e) and semilog-scale (f), at different tip positions on the MoS_2/n^- 4H-SiC heterojunction. Reproduced from Ref. [40].

Figure 4.15(b) shows three I-V characteristics collected by the Pt tip at different positions on the surface of the MoS_2/n^+ SiC heterojunction. The same curves have been reported in a semilog-scale in **Figure 4.15**(c). Similarly, three I-V characteristics at different surface positions of the MoS_2/n^- SiC heterojunction are reported in **Figure 4.15**(e) and (f) on linear scale and semilog-scale, respectively. A noise level in the measured current <50 fA can be observed in the semilog-scale characteristics in **Figure 4.15**(c) and (f). The MoS_2 junction with the lightly n-type doped (10^{16} cm^{-3}) 4H-SiC epitaxy exhibits a strongly rectifying behavior, with negligible current injection at negative (reverse) bias and exponential current after a turn on voltage of 4 -5 V under positive (forward bias). On the other hand, the I-V characteristics of the MoS_2 heterojunction with the n^+-SiC substrate show much higher current both under reverse and forward bias polarization, as expected by tunneling phenomena across the very narrow depletion region in the degenerately doped 4H-SiC. However, the most noticeable feature in all the curves of **Figure 4.15**(b),(c) is the presence of a pronounced negative differential resistance (NDR) under forward polarization, with some variability in the peak voltage (V_P) and peak current (I_P) at the different tip positions. The NDR behavior is typically ascribed to band-to-band-tunneling (BTBT) between degenerately n^+ and p^+ doped semiconductors. Hence, the observation of this phenomenon in the I-V characteristics of the MoS_2/n^+ SiC system at room temperature indicates not only the formation of a very sharp 2D/3D heterojunction, but also a degenerate p-type doping of 1L-MoS_2 obtained by the sulfurization process. The comparison of the three characteristics in **Figure 4.15**(b), (c) shows an interesting correlation between the V_P and I_P values under forward bias and the reverse current level, with lower V_P and higher I_P corresponding to a higher reverse current. As discussed in the following, such variability in the local NDR behavior can be ascribed to local changes in the MoS_2 p-type doping.

In the following, the forward bias I-V characteristic of the p^+-$MoS_2/SiO_2/n^+$-SiC heterojunction are discussed in detail, considering the different mechanisms ruling current injection at the interfaces. The equivalent circuit of this system, schematically depicted in **Figure 4.16**(a), can be described by the series combination of the contact resistance R_c associated to the tip/MoS_2 Schottky barrier [229] and of the p^+-$MoS_2/SiO_2/n^+$-SiC tunnel (Esaki) diode. Hence, the applied tip bias $V_{tip}>0$ partially drops across the contact resistance and partially across the diode. **Figure 4.16**(b) shows a typical forward bias I-V characteristic measured on the heterojunction. At low forward bias values ($V_{tip}<3$ V), the current injection is limited

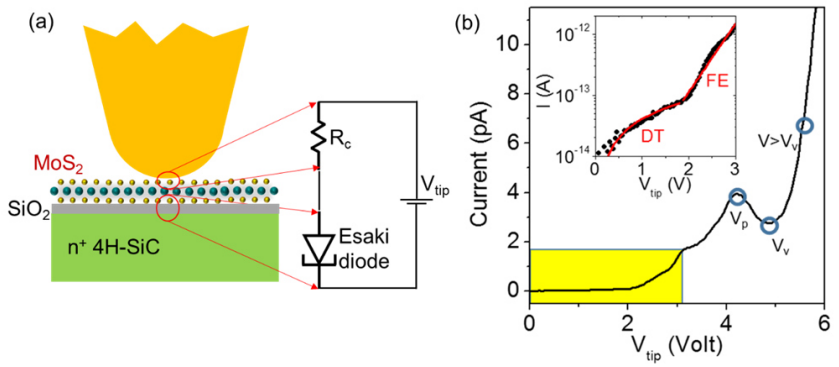

Figure 4.16.- (a) Schematic illustration of the Pt tip/MoS_2/SiO_2/SiC junction, with its equivalent circuit, consisting of the series combination of the Pt/MoS_2 contact resistance (R_C) and the Esaki diode. (b) Forward bias I-V characteristic with the indication of the different transport regimes. A semilog scale plot of the I-V curve in the low bias regime, marked by a yellow box, dominated by R_C, is reported in the insert. Reproduced from Ref. [40].

by the Pt tip/MoS_2 contact resistance. The semilog-scale plot of the I-V curve in this low current regime, reported in insert of **Figure 4.16**(b), shows that current transport is limited by direct tunneling (DT) across the Pt/MoS_2 Schottky barrier from 0 to 2 V, being $I_{DT} \propto V_{tip} T$ with T the tunnel probability. Field emission (FE) across the barrier becomes the dominant mechanism between 2 and 3V. In particular, the FE current increases with the forward bias as $I_{FE} \propto \exp[qV_{tip}/E_{00}]$, being the q the electron charge and E_{00} a characteristic energy related to the holes concentration N_h in the p^+-MoS_2 layer:

$$E_{00} = \frac{h}{\pi}\sqrt{\frac{N_h}{m_h \varepsilon_0 \varepsilon_r}} \qquad (21)$$

with ε_0 the vacuum dielectric constant, $\varepsilon_r \approx 6$ the relative permittivity [255] and m_h the holes effective mass for 1L MoS_2. A value of $E_{00} \approx 377$ meV was obtained from the I-V curve fit in the insert of **Figure 4.16**(b), from which a hole concentration $N_h \approx 6.9\times10^{19}$ cm^{-3} (i.e. a holes density $p \approx 4.5\times10^{12}$ cm^{-2}) is determined, in agreement with the range of values deduced by Raman mapping.

At forward bias V_{tip}>3V, the band-to-band tunneling at the heterojunction becomes the dominant transport mechanism, resulting first in the current increase up to the peak value (I_P) at the voltage V_P, followed by the decrease at the valley current (I_V) at the bias V_v, as indicated in **Figure 4.16**(b).

To better illustrate the band-to-band-tunneling phenomenon, **Figure 4.17**(a) shows the alignment between the bands of p^+ doped 1L MoS_2, SiO_2 and n^+ 4H-SiC separated by vacuum, evaluated using the literature values of electron affinity and energy bandgap for these materials, whereas the energy band-diagrams of the p^+-MoS_2/SiO_2/n^+-SiC system under different biasing conditions are reported in **Figure 4.17**(b)-(e).

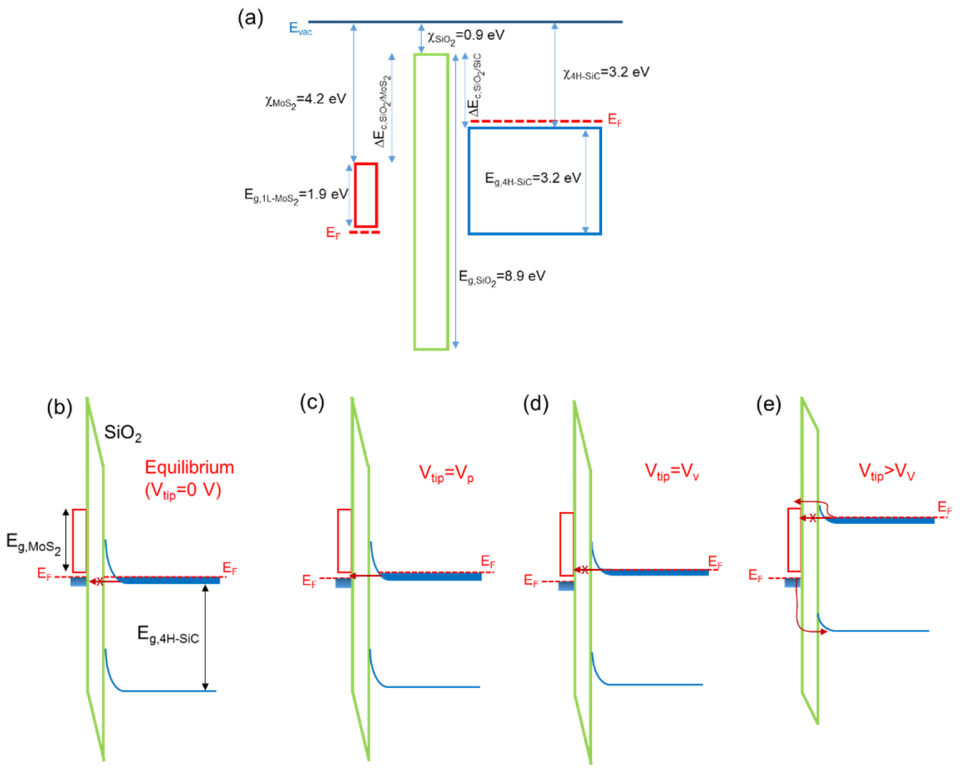

Figure 4.17.- (a) Alignment between the bands of p^+doped 1L-MoS_2, SiO_2 and n^+ 4H-SiC separated by vacuum, evaluated using the literature values of electron affinity (χ) and energy bandgap (E_g) for these materials. Band diagrams of the p^+-MoS_2/SiO_2/n^+-SiC junction under equilibrium conditions (b), at a bias V_P corresponding to the peak current (c), at a bias V_V corresponding to the valley current (d), and for $V_{tip}>V_V$ (e). Reproduced from Ref. [40].

Under equilibrium conditions, i.e. at V_{tip}=0 V (**Figure 4.17** (b)), the Fermi levels of the two degenerate semiconductors are aligned. The thickness of the tunnel barrier between the two semiconductors is the sum of the SiO_2 interfacial layer (~1 nm) and the depletion region of the n^+-SiC at V_{tip}=0 V, corresponding to the Debye length $L_D=(\varepsilon_0\,\varepsilon_{SiC}kT/qN_D)^{1/2}\approx$1.1 nm for $N_D\approx10^{19}$ cm^{-3}, where ε_{SiC} is the 4H-SiC dielectric permittivity and N_D is the donor concentration. Under equilibrium, the filled states

of the n^+-SiC conduction band are aligned with the filled states of p^+-MoS_2 valence band and BTBT is forbidden. When high enough positive bias is applied, filled states on the SiC side and unoccupied states on the MoS_2 side are partially overlapped, thus the electrons can tunnel through the barrier from n-SiC to p-MoS_2.The BTBT current reaches its maximum (peak current I_p) at the bias $V_{tip}=V_{P,}$ when the overlap between the filled and empty states at the two sides of the barrier reaches its maximum, as illustrated in **Figure 4.17** (c). By further increasing the V_{tip} the overlap starts to decrease, giving rise to a decrease of the BTBT current, i.e. to the NDR part of the curve. Ideally, the BTBT current is expected to decrease to zero at the bias $V_{tip}=V_{V,}$ when the conduction band edge of SiC and the valence band edge of MoS_2 are aligned (as illustrated in **Figure 4.17** (d)). However, the actual measured value of I_V and, hence, the peak-to-valley current ratio of ~1.5, can be explained by the occurrence of other competitive transport mechanisms, such as current tunneling mediated by defects states at the interface [256]. For larger bias values ($V_{tip}>V_V$), current transport is ruled by a combined thermionic-tunneling mechanism through the tunnel barrier, as schematically depicted in **Figure 4.17** (e).

The reported results demonstrate an efficient method to obtain large area and uniform p^+ MoS_2 films on 4H-SiC, which is compatible with semiconductor industry process flows. Furthermore, the observation of room temperature NDR behavior in MoS_2/SiC heterojunctions paves the way to the implementation of Esaki diodes on the silicon carbide platform, extending its range of potential applications to fast switching devices and circuits.

4.3 MoS_2 INTEGRATION WITH GaN

4.3.1 MoS_2 heterostructures with GaN-on-sapphire

Most of the recent investigations about MoS_2 integration with GaN have been carried out on low-cost commercially available GaN-on-sapphire substrates. Hence, for benchmarking purposes, we performed a preliminary study applying the optimized growth of MoS_2 by the sulfurization approach on this kind of substrates.

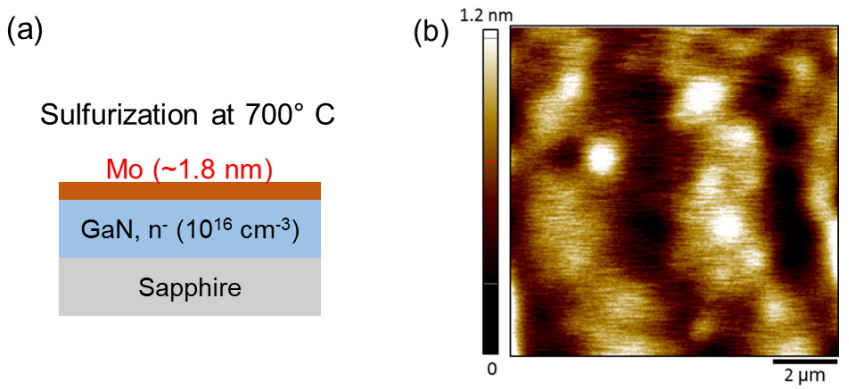

Figure 4.18.- (a) Scheme of the two steps process used to obtain MoS_2 by sulfurization of MoOx film sputtered on GaN/Sapphire. (b) AFM image of as grown MoS_2 on GaN.

Figure 4.18 (a) shows a schematic of a n-type doped (10^{16} cm^{-3}) GaN-on-sapphire epitaxial layer, with an ultra-thin MoO_x (1.8 nm) deposited film. The surface morphology of the sample after the sulfurization process at 700°C, reported in **Figure 4.18** (b), resembles the typical morphology of GaN-on-sapphire, indicating a conformal coverage of the MoS_2 film. The MoS_2 formation was confirmed by Raman spectroscopy. **Figure 4.19** (a) shows a typical Raman spectrum for MoS_2 on GaN-on-sapphire, which exhibits the two main MoS_2 vibrational modes and the GaN counterpart (E_2 high energy and A_1(LO)) underlined by red and light-blue squares respectively. A detail of the MoS_2 vibrational spectrum is reported in **Figure 4.19** (b), where a $\Delta\omega \sim 21.1$ cm^{-1} is estimated from the difference of the A_{1g} and E_{2g} peaks located at 407.0 ± 1.0 cm^{-1} and 385.5 ± 0.8 cm^{-1}, respectively. Similarly to **Figure 4.5**, the two peaks show a small asymmetric shape due to the nanocrystalline nature of the sulfurized MoO_x film. A statistical study on the difference between the two peaks is represented by the colour map in **Figure 4.19** (c) and the corresponding histogram (d). The $\Delta\omega$ distribution is peaked at 21.5 ± 1.2 cm^{-1} with a small tail at

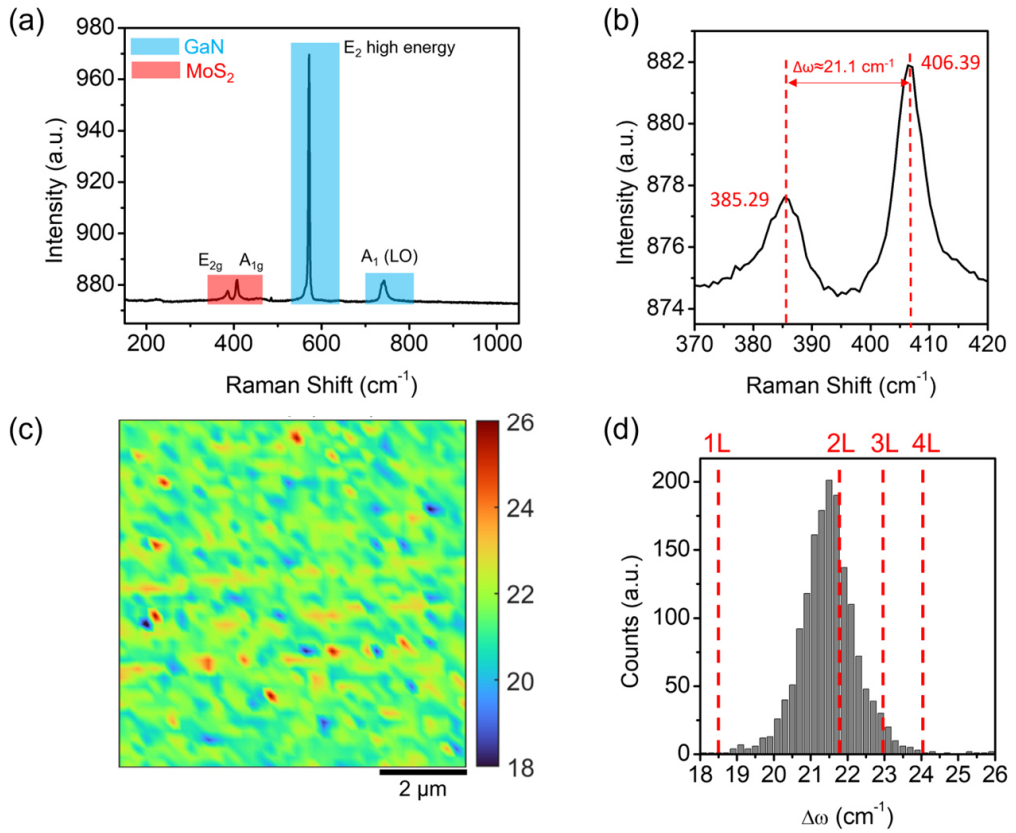

Figure 4.19.- (a) Typical Raman spectrum of MoS_2 on GaN/Sapphire with the corresponding peaks. Blue squares indicate the Raman peaks of GaN while the red-ones those of MoS_2. (b) Corresponding MoS_2 Raman spectrum on GaN/sapphire with a difference of 21.1 cm^{-1} between the main peaks. (c) Map of the main Raman peaks difference of MoS_2 ($\Delta\omega$) in a 10x10 μm^2 area and the corresponding distribution (d) that identifies a number of layer between 1-2.

higher $\Delta\omega$ values, indicating that the MoS_2 film is mostly composed by 1 or 2L, with a small fraction of 3L. A further confirmation of the number of layers of this sample is obtained by TEM images reported in **Figure 4.20**. The intensity contrast in the HAADF-STEM image (**Figure 4.20** (a)) allows to identify the continuous MoS_2 film, composed by 1L or 2L of MoS_2, separated by a vdW gap from the crystalline GaN substrate. Furthermore, atomic resolution HAADF- and the annular bright field (ABF) - STEM images of heterostructure are reported in **Figure 4.20** (b-c). Due to the different contrast formation mechanism in the two STEM imaging modes, only atoms (Mo, Ga) with high atomic number Z can be visualized in the HAADF image, whereas both atoms with high (Mo, Ga) and lower Z (N and S) are identifies in the ABF image, confirming the presence of few-layers of MoS_2.

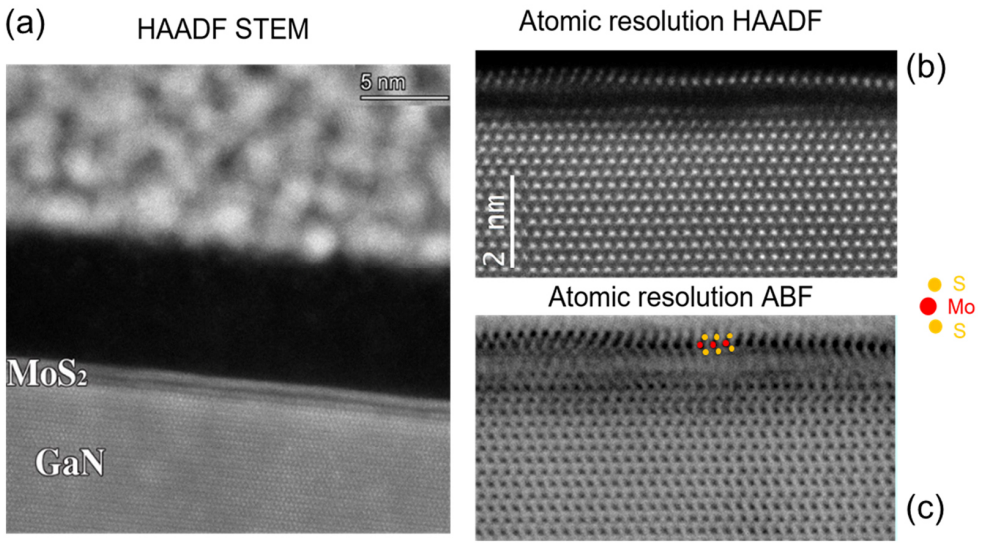

Figure 4.20.- (a) HAADF STEM image of MoS_2 on GaN/Sapphire and (b) atomic resolution HAADF and (c) ABF.

4.3.2 MoS_2 heterostructures with bulk GaN

After the preliminary study of the MoS_2 growth on GaN/sapphire, the process was extended to the bulk GaN substrates. The interest toward this samples is due to the excellent crystalline quality and extremely low defectivity of GaN epilayers on bulk GaN substrates, making them suitable for high performance switching devices with very low leakage current.
Starting from a thin film of MoOx (~1.5 nm) deposited by sputtering, as shown in **Figure 4.21** (a), a thin film of MoS_2 was obtained on GaN after one hour of sulfurization process at 700°C. The corresponding AFM of the MoS_2 on GaN bulk with the well-defined GaN steps is reported in **Figure 4.21** (b). A typical Raman spectrum of the heterostructure is shown in **Figure 4.22** (a), where the main contributions of MoS_2 (E_{2g} and A_{1g}) and GaN (E_2 high energy and A_1(LO)) are identified by red and light blue squares, respectively.

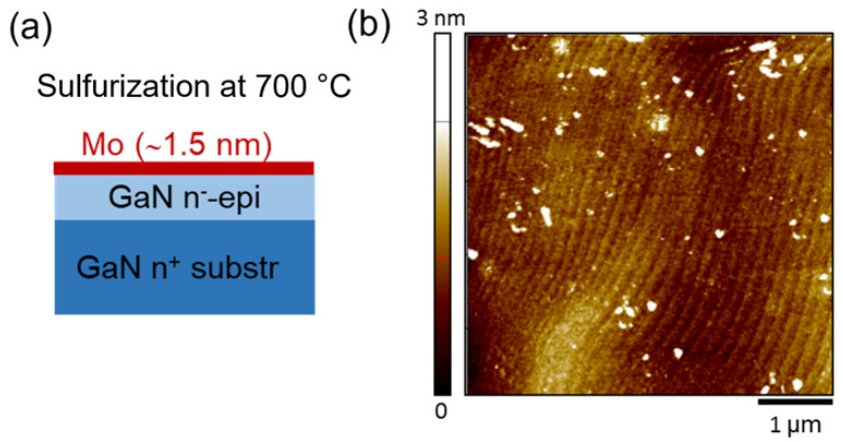

Figure 4.21.- (a) Scheme of the two steps process used to obtain MoS_2 by sulfurization of MoOx film sputtered on bulk GaN. (b) AFM image of as grown MoS_2 on bulk GaN.

A detail of the MoS_2 spectrum is reported in **Figure 4.22** (b), where the in-plane and the out-of-plane mode are respectively located at 384.6 ± 0.6 cm^{-1} and 406.0 ± 0.6 cm^{-1}, with a wavenumber difference $\Delta\omega \approx$ 21.4 ± 0.8 cm^{-1}. This value can be associated to a single or a bilayer of MoS_2. To better evaluate the MoS_2 uniformity on GaN, we performed a statistical study, collecting Raman maps on sample areas of 10 µm ×10 µm. **Figure 4.22** (c) shows the colour map of the $\Delta\omega$ values indicating the dominance of 1L and 2L of MoS_2 (green colour), with a smaller fraction of multilayers (red color). This can be better observed in the $\Delta\omega$ histogram, reported in **Figure 4.22** (d), which is centred at 21.4 ± 0.8 cm^{-1}, with an asymmetric shape and a tail extending to $\Delta\omega$ values >23 cm^{-1}. Similarly to the case of MoS_2 on 4H-SiC, a

correlative E_{2g}-A_{1g} plot was also performed for MoS_2 on bulk GaN in order to extract information on the doping and strain of MoS_2. As illustrated in **Figure 4.23** (a), the cloud of experimental points is mostly located in the region of the plot above the strain line (blue region), corresponding to the p-type doped MoS_2. The charge density in MoS_2 on bulk GaN can be better evaluated from the histogram (**Figure 4.23** (b))

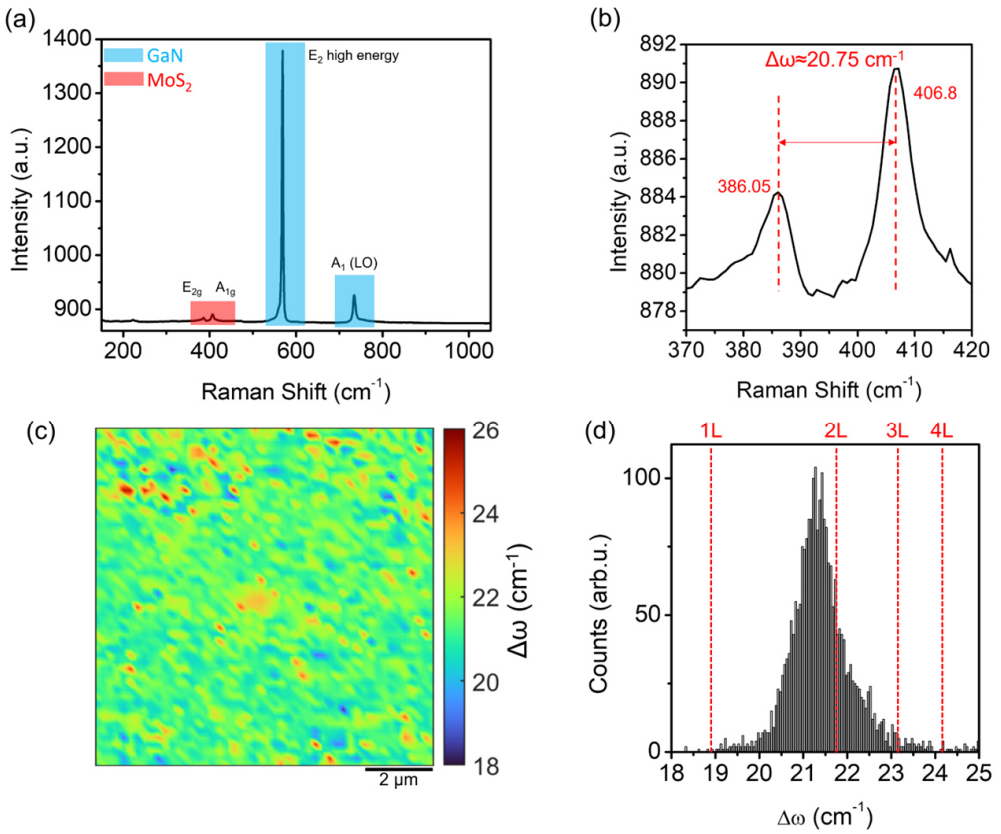

Figure 4.22.- (a) Typical Raman spectrum of MoS_2 on GaN bulk with the corresponding peaks indicated by red (for MoS_2) and blue squares (for GaN). (b) Corresponding Raman spectrum of MoS_2 on GaN with a difference between the two peaks of 20.75 cm^{-1}. (c) Color map of the difference between the two Raman peaks of MoS_2 and the corresponding histogram (d), that indicate a number of layers between 1-2.

and the corresponding color map (**Figure 4.23** (c)). From these figures, a p-type doping of ~5×10^{12} cm^{-2} can be deduced, which is two times higher than that obtained for MoS_2 grown on 4H-SiC (**Figure 4.13** (a)) under the same conditions. Similarly to the case of MoS_2 grown on 4H-SiC, the p-type doping can be ascribed to the MoO_x residuals from the starting deposited film. **Figure 4.23** (d-e) shows the distribution of the biaxial strain in the MoS_2 film, which indicates the presence of a very low tensile strain (<0.1%). This small value of strain is consistent with the very small

mismatch of the lattice constant between the two materials, as discussed in the **Figure 2.18** of Chapter 2. This is a further proof of the good suitability of wide-bandgap semiconductors such as SiC and GaN for the growth of extended ultrathin MoS_2.

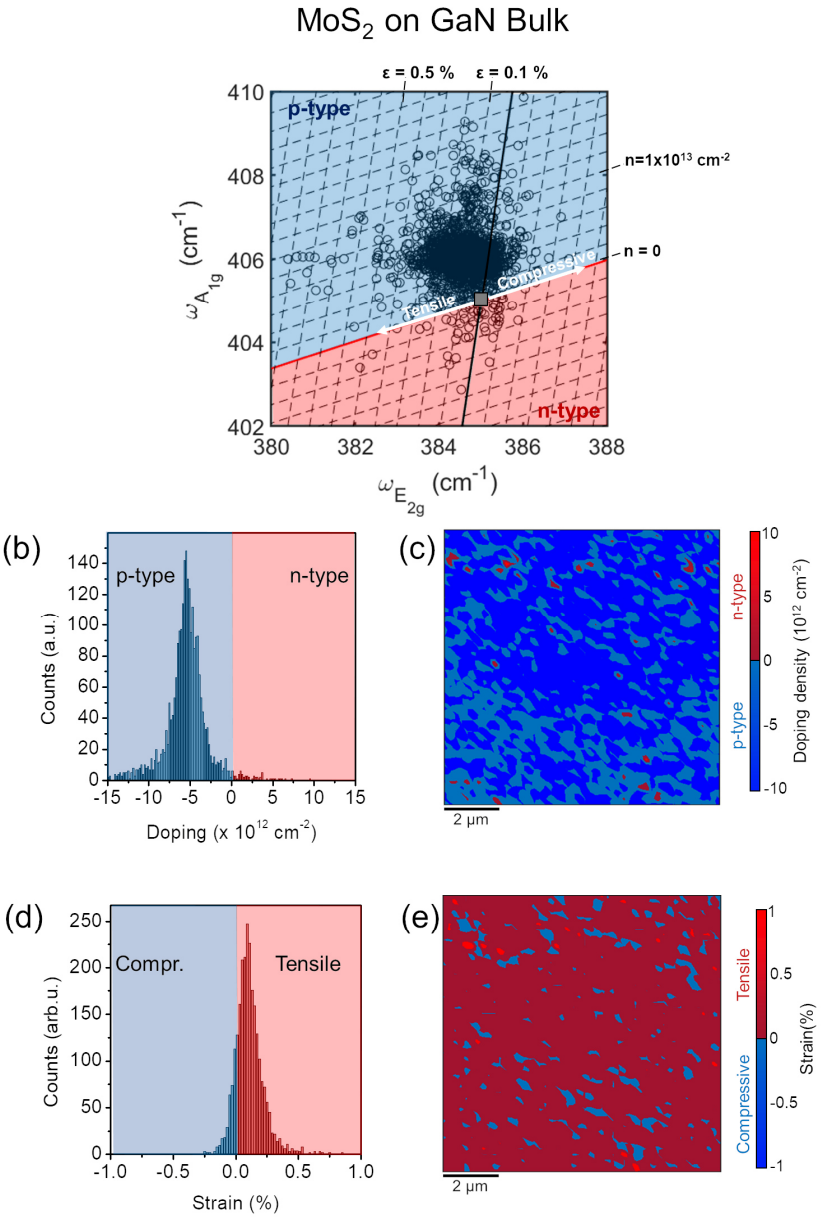

Figure 4.23.- (a) Correlative plot of the two main peaks positions of MoS_2 to estimate the strain and doping on MoS_2 supported on GaN bulk. (b) Distribution of calculated doping on MoS_2 on GaN bulk and the corresponding colour map (c). (d) Distribution of strain induced on MoS_2 on GaN bulk and the corresponding colour map (e).

4.3.3 Vertical current transport at MoS_2 heterojunctions with bulk GaN

After assessing the structural properties, doping and strain of ultra-thin MoS_2 membranes on bulk GaN, the vertical current transport across the vdW heterojunction of these materials was investigated in detail by nanoscale resolution current-voltage analyses based on C-AFM. **Figure 4.24** (a) illustrates the experimental setup used for front-to-back current measurements on a MoS_2 heterojunction with a n^- doped epitaxial layer on n^+ doped bulk GaN. A dc bias ramp is applied between the nanoscale Pt-coated tip contact on MoS_2 and a macroscopic contact on bulk GaN, while the flowing current is measured by a current amplifier connected to the tip. **Figure 4.24** (b) reports a set of local I-V curves measured on

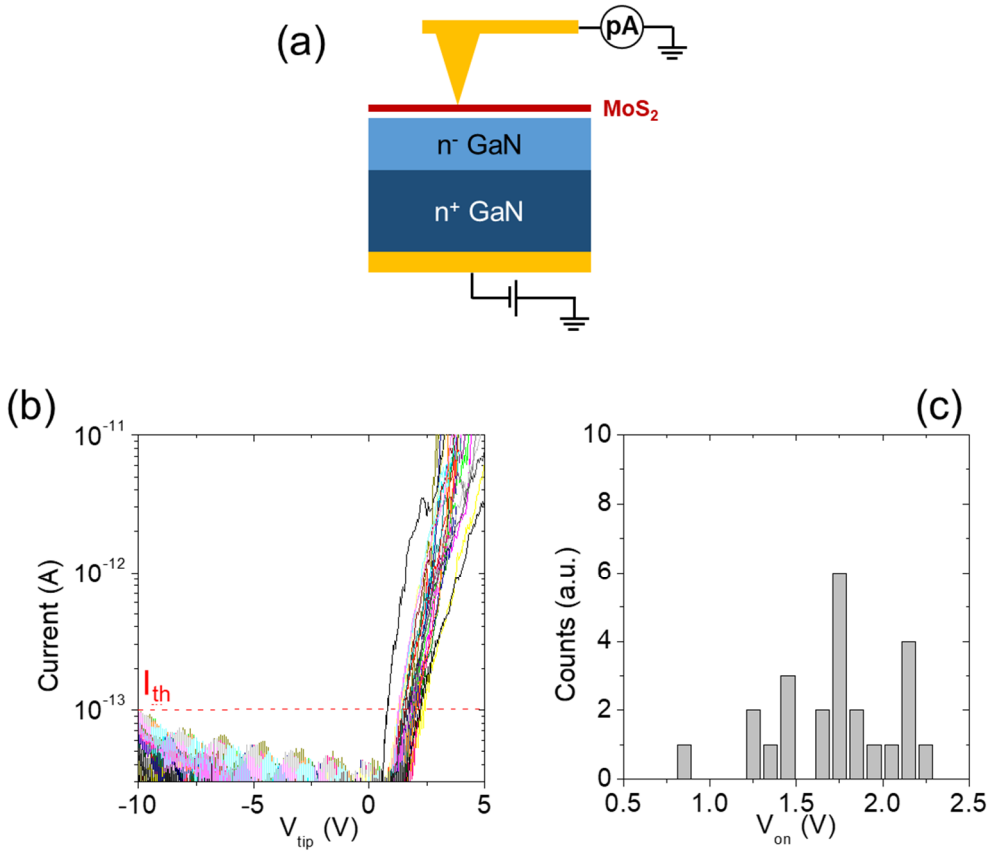

Figure 4.24.- (a) Setup of the vertical current measurements on MoS_2/GaN bulk with C-AFM. (b) Semilog scale Current-voltage characteristics collected on an array of 5×5 positions on 5 μm × 5 μm area of the Pt tip on MoS_2. (c) Distribution of the onset voltage values V_{on} extracted from the array of I-V curves at a threshold current value of $I_{th}=10^{-13}$ A.

an array of 5×5 tip positions on a 5 µm × 5 µm area. The curves, reported in a semilog scale, clearly show a rectifying behavior, negligible current under negative (reverse) bias and exponential rise of the current under positive (forward) polarization above an onset voltage (V_{on}). To quantitatively evaluate the V_{on} for this heterojunction, a threshold current of 10^{-13} A (above the noise level) was fixed, and the corresponding voltage was extracted from each I-V curve in **Figure 4.24** (b). The resulting distribution of V_{on} values is reported in the histogram of **Figure 4.24** (c), with an average value of ~1.7±0.4 V. The very low reverse current and this high onset voltage indicate a high energy barrier between the p^+-type doped MoS_2 grown by Mo sulfurization and GaN. The energy band diagram configuration of this anisotype 2D/3D heterojunction between highly p-type doped MoS_2 and n-GaN is schematically illustrated in **Figure 4.25** before (a) and after contact formation (b) under equilibrium conditions. In **Figure 4.25** (a), a type II heterojunction with $\Delta E_c \approx 0.3$ eV is considered, following the XPS/UPS literature results reported in **Figure 2.21** of Chapter 2. The Fermi levels have been evaluated from the p^+ and n^- doping of MoS_2 and GaN, respectively. Finally, the energy barrier Φ_B, formed under

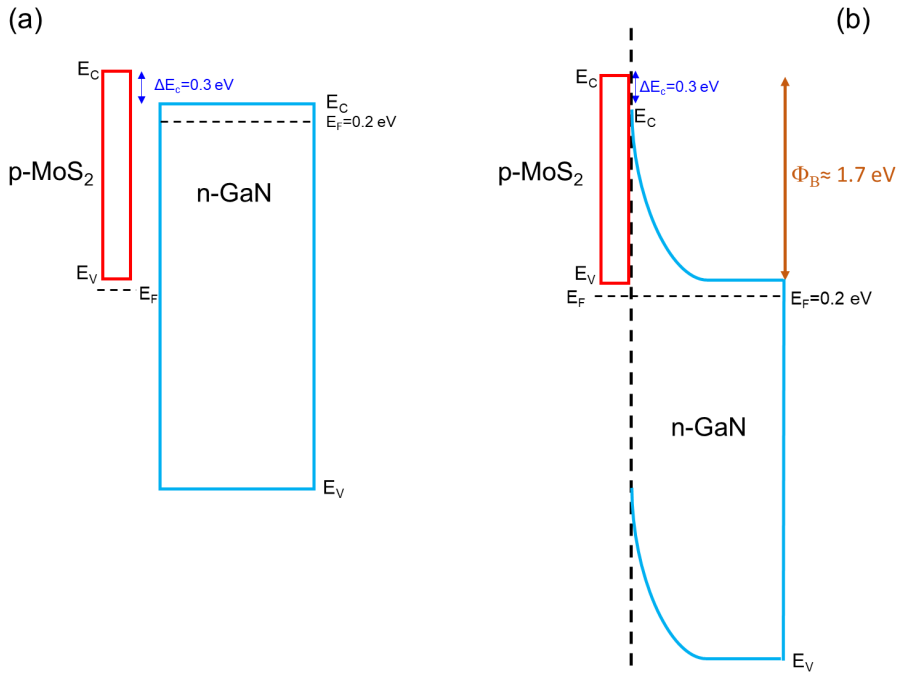

Figure 4.25.- Scheme of the band alignement before (a) and after (b) contact between the MoS_2 and GaN bulk.

equilibrium conditions after alignment of the Fermi levels, is indicated. Its value, $\Phi_B \approx 1.7$ eV, is consistent with the average V_{on} value extracted from electrical characterization.

Brief Conclusion

The two-steps CVD approach, demonstrated to be a suitable method to deposit large and ultra-thin MoS_2 on insulating or semiconductive substrates. Indeed, it resulted highly compatible with the state-of-the-art fabrication approaches in microelectronics. A preliminary optimization of the sputtering deposition was necessary to realize low-roughness (RMS = 0.35 nm) and ultrathin Mo films (1.2-1.8 nm) on SiO_2, which resulted oxidated after the exposition at air (after XPS analyses). The sulfurization process was carried-out in a two-zone CVD furnace at two different temperatures (150°C for the sulfur and 700°C for the sample zone respectively). The realized MoS_2 films have been characterized by AFM and Raman, from which was deducted a nanocrystalline dimensions of grains and $\Delta\omega$ ranging between 20.3-21.0 cm^{-1}, indicating 1-2 layers of MoS_2 on SiO_2. At the same conditions, the MoS_2 was grown on n^+-4H-SiC and n^--4H-SiC, which are characterized by a charge density of $\sim10^{19}$ cm^{-3} and $\sim10^{16}$ cm^{-3}, respectively. Raman mapping and TEM characterizations confirmed the realization of 1-2 layers of MoS_2 on 4H-SiC, with the formation of a thin film of SiO_2 between them, probably induced by the growth conditions. Following, a p-type doping of around 2.5×10^{12} cm^{-2} with a standard deviation of 2.0×10^{12} cm^{-2}, and a very small tensile strain ($\varepsilon\approx0.12\%$ with a standard deviation of 0.14%) are deducted from the correlative A_{1g} vs E_{2g} plot of the MoS_2/ n^+-4H-SiC and the corresponding distributions. The residuals of MoO_3 after the sulfurization, confirmed by XPS analysis, are the origin of the p-type doping induced on the MoS_2. While the small tensile strain is associated to the very small lattice mismatch between the two semiconductors. Similar values are found on the MoS_2 on n-4H-SiC, confirming the reproducibility of the sulfurization process. Vertical electrical measurements were carried-out by C-AFM on MoS_2 junction with the lightly n-type doped (10^{16} cm^{-3}) 4H-SiC epitaxy, which exhibited a strongly rectifying behavior, with negligible current injection at negative (reverse) bias and exponential current after a turn on voltage of 4 -5 V under positive (forward bias). Differently, a pronounced negative differential resistance (NDR) was observed on the MoS_2 junction with the highly doped 4H-SiC, ascribed to the band-to-band tunneling (BTBT) between two degenerately doped semiconductors (p^+-MoS_2 and n^+-4H-SiC). At low forward bias, the dominant transport mechanism is the direct tunneling across the Pt tip/ MoS_2 Schottky barrier from 0 to 2 V. While field-emission resulted the dominant mechanism between 2-3 V. For $V_{tip}>3$ V the transport mechanism at the heterojunctions resulted dominated by the BTBT, caused by the

overlapping between the filled states on the SiC side and unoccupied states on the MoS_2 side. At higher value of bias, the overlap between the states decreases causing the decreasing of the BTBT.

At the same conditions, the MoS_2 films were also grown by sulfurization on GaN-sapphire and GaN Bulk. The first substrate was employed for a preliminary study, confirming the formation of large-area 1-2 layers of MoS_2 on GaN-sapphire by Raman and TEM characterization. Passing to the MoS_2 on GaN-Bulk heterojunction, a p-type doping of $\sim 5\times10^{12}$ cm^{-2} was deducted, two times higher than that obtained on 4H-SiC. Also in this case, a small tensile strain ($\varepsilon<0.1\%$) is derived, due to the small mismatch between the MoS_2 and GaN. The electrical characterization between the vdW heterojunction was carried-out by C-AFM. The I-V_{tip} characteristics showed a rectifying behavior, negligible current under negative (reverse) bias and exponential rise of the current under positive (forward) polarization above an onset voltage (V_{on}). The average value of V_{on} ~1.7±0.4 V was extracted from the current-voltage curves. The very low reverse current and this high onset voltage indicated a high energy barrier between the p^+-type doped MoS_2 grown by Mo sulfurization and GaN. From the band-diagram of the vdW heterojunction, an energy barrier of $\Phi_B\approx1.7$ eV was deducted, resulting consistent with the average V_{on} value extracted from electrical characterization. The reported results demonstrate an efficient method to obtain large area and uniform p^+ MoS_2 films on 4H-SiC and on GaN Bulk, which is compatible with semiconductor industry process flows. Indeed, the integration of MoS_2 with WBG permitted to extend the MoS_2 range of potential applications to fast switching devices and circuits.

SUMMARY

The peculiar physical properties, such as the semiconductive behavior and the band gap tunability as a function of the thickness, make the MoS_2 an excellent candidate to applications in the "Moore" and "More than Moore" electronics domains and in the optoelectronics field. In particular, MoS_2 can be employed as an ultrathin channel material in MOSFET devices for logic and switching applications, due to the high on/off state current ratio (I_{on}/I_{off} ~10^8) and the good carrier mobility.

The main contributions of this thesis work in this research field consist in the development of advanced top-down and bottom-up methods for the preparation of large area MoS_2 films on different substrates, and in the detailed structural and electrical characterization of the obtained heterostructures. Indeed, the MoS_2 integration with high-κ dielectrics, such as Al_2O_3, and wide-bandgap (WBG) semiconductors, such as SiC and GaN, has been addressed. The former permits to enhance the MoS_2 mobility in MOSFET devices, while the latter extends the MoS_2 applicability to innovative devices for the high-frequency and high-power electronics.

In order to bring MoS_2 closer to future industrial developments in the fields of electronics and optoelectronics, the following issues have been addressed in this thesis:

(i) The improvement of the gold-assisted mechanical exfoliation to produce extended membranes of MoS_2 with high crystalline quality on Au and next transferred to an insulating substrate for the realization of a back-gated FET.
(ii) The growth optimization by two-steps CVD (sulfurization) of ultrathin and large area (cm^2) membranes of MoS_2 on WGB semiconductors.
(iii) The optimized growth of ultra-thin films of high-κ dielectrics (Al_2O_3) on large-area MoS_2 by atomic layer deposition (ALD), exploiting the beneficial role of the gold substrate.
(iv) The detailed investigation, using Raman and Photoluminescence analysis, of the strain, doping and defects' density, induced in the MoS_2 films by the preparation/growth conditions or by the interaction with the substrate.
(v) The electrical characterization of vertical current injection in MoS_2 heterojunctions with WBG substrates, using nanoscale-resolved conductive atomic force microscopy (C-AFM). These electrical features have been correlated to the structural properties of the 2D/3D systems.

Chapter 1 and *Chapter 2* provided an introduction on the MoS_2 physical properties and the state-of-the-art approaches to produce 1L-MoS_2. In particular, the integration

of MoS_2 with Si, WBG semiconductors and high-κ dielectrics have been included, discussing relevant properties and issues.

Chapter 3 and *4* reported the experimental results obtained during the PhD thesis. Specifically, *Chapter 3* described the preparation and characterization of the 1L-MoS_2 obtained by gold-assisted mechanical exfoliation and transferred on an insulating substrate. The deposition of Au/Ni films with optimized small roughness played a key role to increase the efficiency of exfoliation of 1L-MoS_2 from a molybdenite bulk crystal. Furthermore, an efficient method to transfer the large area (cm^2) MoS_2 membranes from gold to an insulting substrate has been developed. This procedure allowed to obtain large-area 1L-MoS_2 on Al_2O_3 preserving the high-quality of the exfoliated crystals. The impact of the metallic (Au) and the insulating (Al_2O_3) substrates on the vibrational and optical properties of MoS_2 were characterized by Raman and PL spectroscopy. The in-plane (E_{2g}) and out-of-plane (A_{1g}) vibrational peaks of 1L-MoS_2 transferred onto Al_2O_3 showed a frequency difference of 18.1 ± 0.2 cm^{-1}, consistently with literature results for 1L-MoS_2 on insulating substrates. On the other hand, an anomalous increase of $\Delta\omega$ mean value to 21.2 ± 0.3 cm^{-1} was observed for as-exfoliated 1L-MoS_2 on gold and ascribed to strain and doping of the 2D membrane induced by the interaction with the substrate. Specifically, Au-supported 1L-MoS_2 was affected by a biaxial tensile strain ($\varepsilon_{biax} \approx 0.21 \pm 0.06$ %), which was converted in a compressive strain ($\varepsilon_{biax} \approx -0.25 \pm 0.01$ %) after the transferring on the insulating Al_2O_3 substrate. Furthermore, as-exfoliated 1L-MoS_2 on Au showed a p-type doping $p \approx (-0.25 \pm 0.06) \times 10^{13}$ cm^{-2}, which was converted into a n-type doping $n \approx (0.5 \pm 0.09) \times 10^{13}$ cm^{-2} after transfer onto Al_2O_3. The interaction with the substrate also influenced the optical emission properties of 1L-MoS_2. In fact, 1L-MoS_2 transferred onto Al_2O_3 showed a prominent peak centered at an energy of 1.84 eV, consistently with the typical PL spectra of MoS_2 obtained by mechanical exfoliation or CVD growth. Differently, a red-shift of the PL peak to 1.79 eV and a significant quenching of the PL intensity is observed for as-exfoliated 1L-MoS_2 on gold. A detailed investigation by deconvolution analysis of PL spectra allowed to identify three main components, associated to the trion (A^-) and exciton contributions (A^0 and B). Interestingly, the exciton A^0 at 1.83 eV represented the main contribution in the PL spectra for 1L-MoS_2 on Al_2O_3, whereas the trion contribution at 1.78 eV was the dominant one for 1L-MoS_2 on Au. The enhancement of the trions' population and the quenching of the emission amplitude for Au-supported MoS_2 was ascribed to the high polarizability of the metallic substrate and the very low MoS_2/Au equilibrium distance.

Finally, the electrical transport properties of as-exfoliated 1L-MoS_2 on Au were investigated by conductive atomic force microscopy (C-AFM) measurements, whereas a back-gated MoS_2 field effect transistor was fabricated and characterized

after MoS_2 transfer onto an Al_2O_3/Si substrate. Nanoscale resolution electrical measurements on 1L-MoS_2/Au by C-AFM indicated the direct tunneling as the main vertical current transport mechanism at the MoS_2/Au interface, and the evaluated barrier height was consistent with the substrate-induced p-type doping of MoS_2. After the transferring of the 1L-MoS_2 on Al_2O_3, the lateral electronic transport was evaluated by electrical characterization of the FET with Al_2O_3/Si back-gate. The output characteristics showed the typical transistor behavior, in which at low drain bias ($V_D < 3V$), the electrons injections were limited by the high Schottky barrier at Au/MoS_2 contacts, while a linear behavior in a range of drain bias between 3-10 V and a consequent current saturation at higher voltage were observed. The transfer characteristics showed the behavior of a transistor with a n-type MoS_2 channel with a carrier density of $n \approx 3.1 \times 10^{12}$ cm^{-2} in good agreement with the previous Raman analysis.

In the final section of *Chapter 3*, the integration of the high-κ dielectrics (Al_2O_3 in this case) on 1L-MoS_2 was addressed. For the first time, we reported the growth of an ultrathin Al_2O_3 film (3.6 nm) by atomic layer deposition (ALD) on large-area 1L-MoS_2 obtained by gold-assisted mechanical exfoliation. Very different Al_2O_3 coverage was observed by performing the ALD Al_2O_3 growth under identical conditions (temperature of 250 °C and pulses number) on 1L-MoS_2 supported by Au and by an insulting substrate. In fact, while a highly inhomogeneous Al_2O_3 coverage was obtained on 1L-MoS_2 onto Al_2O_3/Si, the growth of an homogenous, flat and ultrathin Al_2O_3film (3.6 nm) was obtained for 1L-MoS_2 on Au. These results clearly indicated a beneficial effect of the MoS_2/Au interaction, resulting in the enhanced Al_2O_3 nucleation during the first stages of the ALD process, followed by a layer-by-layer growth. A further insight on the insulating properties of the deposited high-κ film was provided by C-AFM current mapping of the Al_2O_3/1L-MoS_2/Au stack, showing a very low leakage current and a breakdown electric field of 10-12 MV/cm. These results on the high-quality growth of high-κ dielectrics on MoS_2/Au can find important device applications, including the fabrication of FETs and passivation of non-volatile switching memory devices based on Au/1L-MoS_2/Au junctions.

Chapter 4 reported the results on the integration of large area MoS_2 on WBG semiconductors by sulfurization of ultrathin (1-2 nm) molybdenum oxide (MoO_x) films, obtained by optimized DC magnetron sputtering from a Mo target, followed by natural oxidation under ambient conditions. The composition of these films was preliminary evaluated by XPS analyses, which revealed their completed oxidation with the presence of MoO_3 and MoO_2 contributions. Furthermore, a very flat morphology low roughness (RMS=0.35 nm) characterized by nanocrystalline domains was observed by AFM. The sulfurization process was carried out in a two-heating zones furnace, where a crucible with sulfur powders was placed in the low

temperature zone (T_1=150°C) and the sample in the high temperature zone (T_2=700°C), and a flux of Ar was used as carrier gas to transport the S vapors from the first to the second zone. The sulfurization process was first assessed on MoOx films on SiO_2/Si reference substrates, and therefore extended to 4H-SiC and GaN wide bandgap semiconductors. The formation of uniform 1L-2L MoS_2 by sulfurization of the starting MoOx films (1-2 nm thick) was confirmed by Raman spectroscopy and mapping. AFM analyses confirmed a highly uniform and conformal coverage by MoS_2 layers, with a nanocrystalline morphology (10-30 nm grain size), reminiscent of the original MoOx film's structure. The presence of the LO(M) and ZO(M) contributions in the Raman spectra of MoS_2 obtained by the sulfurization approach was correlated to the presence of defects and to the nanocrystalline nature of the film.

Subsequently, MoS_2 was grown on two different doped 4H-SiC: n^+-4H-SiC and n^--4H-SiC with a doping of ~10^{19} cm^{-3} and ~10^{16} cm^{-3}, respectively. After the sulfurization process, the samples were analyzed by XPS, that revealed the incomplete conversion of MoO_x to MoS_2, due to the presence of MoO_3 residues. No reaction between Mo or S and 4H-SiC occurred during the sulfurization, but the formation of an ultra-thin film (~1 nm) of SiO_2 was observed between the MoS_2 and 4H-SiC, confirmed by XPS and TEM characterizations. From the correlative A_{1g} vs E_{2g} plot, a p-type MoS_2 ($p \approx 2.5 \pm 2\times10^{12}$ cm^{-2}) subjected to a small tensile strain ($\varepsilon_{biax} \approx 0.12 \pm 0.14\%$) was deduced. The p-type doping was correlated to the MoO_3 residues after the sulfurization process, while the small tensile strain to the small lattice mismatch between MoS_2 and SiC (~2.9%). The electrical properties of the MoS_2/n-4H-SiC heterojunctions were analyzed by C-AFM local current-voltage (I-V) measurements, exhibiting a strongly rectifying behavior, a negligible current injection in reverse bias and an exponential current after a turn on voltage of 4-5V (forward bias). Differently, the MoS_2 on n^+-4H-SiC characteristics reported a higher current both under forward and reverse bias. The most notable feature for the MoS_2 on n^+-4H-SiC heterojunction was the observation of a negative differential resistance peak (NDR) under forward bias, associated to the band-to-band tunneling (BTBT) between two degenerately n^+ and p^+ doping semiconductors, occurring when the filled states of the n^+-4H-SiC conduction band are overlapped with the unoccupied states of the p^+-MoS_2 valence band. Some variability in the NDR peak was ascribed to local changes in the MoS_2 p-type doping. This first observation of the NDR behavior in MoS_2/4H-SiC heterojunctions confirmed the high electronic quality of the interface. Furthermore, it opens the possibility to develop Esaki diodes on the silicon carbide platform, for fast switching devices and circuits.

The last section of *Chapter 4* reported the results of MoS_2 growth on GaN-on-sapphire and bulk GaN substrates by the sulfurization of pre-deposited ultra-thin

MoOx films. Highly uniform coverage of GaN with 1-2L MoS_2 films was demonstrated by the combination of Raman mapping, AFM and TEM/STEM analyses. In particular, atomic resolution STEM images showed a high quality vdW interface between MoS_2 and GaN. The strain and charge density distributions in MoS_2 films grown on bulk GaN, evaluated by the correlative analyses of A_{1g} and E_{2g} Raman peaks, showed a p-type doping ($p \approx 5 \times 10^{12}$ cm^{-2}) and a very small tensile strain (<0.1%), coherent with the very small lattice mismatch between MoS_2 and GaN. Finally, the vertical current transport in the MoS_2 heterojunction with n-doped bulk GaN was investigated by C-AFM. The I-V_{tip} characteristics showed a rectifying behavior with a negligible current under reverse bias and an exponential rise of the current under forward bias above an onset voltage $V_{on} \approx (1.7 \pm 0.4)$ V. The very low reverse current and the high onset voltage was associated to a high energy barrier ($\Phi_B \approx 1.7$ eV) according to the energy band-diagram of the p^+-MoS_2/n-GaN heterojunction.

PERSPECTIVES

The results of the research activities carried out in this PhD thesis opens new perspectives in the emerging field of vdW semiconductor heterostructures.

The gold assisted mechanical exfoliation and optimized transfer approach presented in the *Chapter 3* can be extended to other 2D materials beyond MoS_2 and employed to realize large area (mm^2 to cm^2) 2D/2D heterostructures (such as MoS_2/WS_2, $MoS_2/MoSe_2$, MoS_2/WSe_2, $MoSe_2/WSe_2$, $MoSe_2/WS_2$, WS_2/WSe_2..) for basic studies and the demonstration of prototype electronic/optoelectronic devices.

The gold substrate was demonstrated to play a beneficial role in the atomic layer deposition (ALD) of uniform and ultrathin Al_2O_3 films on top of the 1L-MoS_2/Au stack. In the future, the ALD growth of dielectrics with higher permittivity (such as HfO_2) on Au-supported 1L-MoS_2 is planned, in order to elucidate similarities and differences in the nucleation/growth mechanisms. Furthermore, a key requirement for practical applications of this system will be the development of optimized methods to transfer the high-κ dielectric/1L-MoS_2 stack from Au to insulating or semiconductor substrates, without degrading the structural/electrical properties of MoS_2 and the dielectric. This will be the object of next experiments.

In the *Chapter 4*, the sulfurization of pre-deposited ultrathin MoOx films has been demonstrated as an efficient approach to produce 1L-2L MoS_2 films with uniform coverage on different substrates, from SiO_2/Si to WBG semiconductors (SiC and GaN). These films present high quality vdW heterostructures with SiC and GaN, resulting in interesting vertical current transport behavior at the interface. However, their nanocrystalline structure, with a very large density of grain boundaries, limits the in-plane current transport in the 2D material. In this respect, alternative large area growth methods such as single-step chemical vapour deposition (CVD), Pulsed Laser Deposition (PLD) and Molecular Beam Epitaxy (MBE) are currently explored, in the framework of the EU project ETMOS, for the epitaxial growth of MoS_2 on sapphire, SiC, GaN and AlN. The result of these experiments will be compared with those reported in this PhD thesis, in order to define optimal deposition methods for specific applications.

Following the basic investigations of the current transport in MoS_2/4H-SiC and MoS_2/GaN based on nanoscale C-AFM analyses, prototypes of vertical diodes will be realized by fabrication of macroscopic metal contacts on the MoS_2 surface. The electrical behavior of these devices will be compared as a function of the employed metallic contacts, or the method used to fabricate them (direct deposition or transfer on the MoS_2 surface). Furthermore, the electrical characteristics of these

macroscopic devices will be correlated with those obtained at the nanoscale by C-AFM. Electro-optical characterization of the MoS_2 heterojunctions with SiC and GaN is planned, for future optoelectronic applications (such as UV-vis photodetectors). Furthermore, the integration of MoS_2 onto Nitride semiconductor heterostructures, such as AlGaN/GaN, will be explored for advanced applications in high electron mobility transistors.

APPENDIX

CHARACTERIZATION METHODS

Atomic Force Microscopy

During this PhD thesis, two different instruments for the Atomic Force Microscopy (AFM) have been employed: *DI3100 System by Bruker with Nanoscope V electronics* and *PSIA XE-300*. Both the instruments were used in tapping mode (with a Si tip of ~5 nm curvature radius) for the morphological measurements, while the AFM by Bruker was also employed in conductive mode for the electrical characterizations (a Pt-coated Si tips and of ~5 nm curvature radius was employed) with the TUNA module equipped to the system.

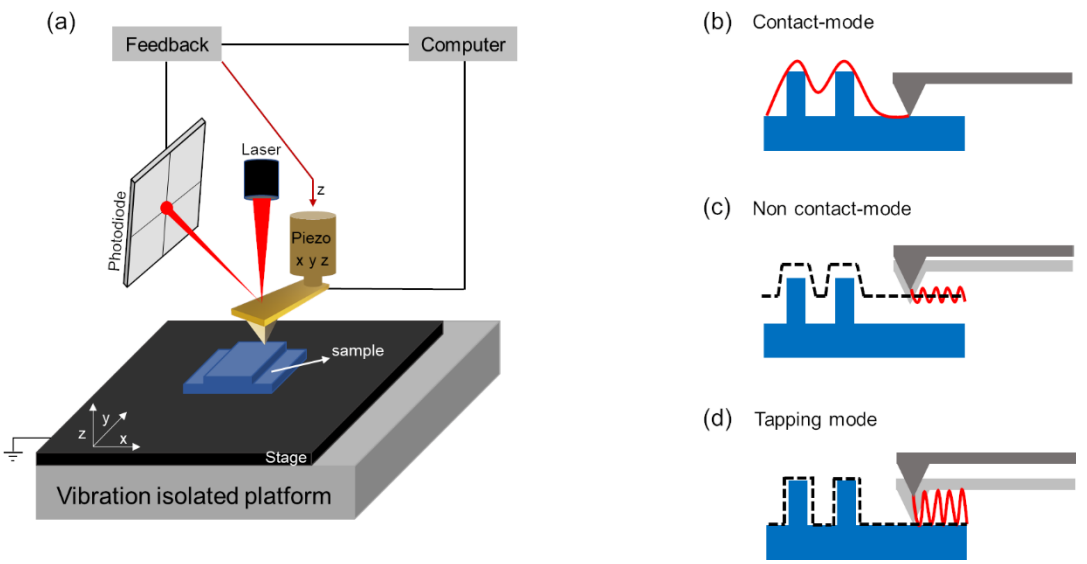

Figure A1.- (a) Scheme of the AFM setup with the typical components. The three main operational modes: (b) contact-mode, (c) non-contact mode and (d) tapping mode.

The Atomic Force Microscopy (AFM) is a special kind of microscope that employs a mechanical sampling method to realize a real image of the surface of a sample at the nanoscale [257]. The scan of the sample is realized through an atomically sharp tip on the surface by controlling the force between the sample and the tip. This nanosized tip is mounted on a microfabricated cantilever characterized by a spring constant k.

The length of the cantilever is around few or hundred micrometers and with a thickness of around 1 μm, while the tip radius is generally lower than 10 nm. Piezoelectric actuators positioned at the end of the cantilever allow to control the positioning and the scanning of the tip on the surface. In fact, these piezoelectric materials realize picometer variation in response to electrical stimuli [257]. The deflection of the cantilever during the sample scan is detected employing a laser beam that is reflected on the backside of the tip towards a four-quadrant photodiode, as represented in fig. In this way, it is possible to monitor the tip-surface motion by recording the laser beam reflection changing the output of the photodiode. Thus, AFM is equipped by a feedback loop using the deflection of the laser to control the force and the tip position, when the system is in *contact mode*, or using the cantilever oscillation amplitude when the system is in *Tapping Mode*. This instrument permits to maintain constant the feedback parameter (cantilever deflection or cantilever oscillation amplitude) to a setpoint value by adjusting the z-piezoelectric actuators. Indeed, all the measurements need an isolated platform to eliminate the acoustic and vibration contributions during the scan. Finally, it is possible to realize the topographic image of the sample surface on a desired scan area. AFM can work in three classes of operation that differ from the nature of probe to surface interaction:

I. **Contact Mode**, when the tip is directly in contact with the surface and the deflection of the cantilever is the feedback parameter to measure the physical variation of the contact with the sample, as shown in **Fig.A1**(b)**.**
II. **Non-contact Mode**, when dynamic oscillations of the cantilever are used to probe the surface and the tip is not physically in contact with the sample, as shown in **Fig.A1**(c)
III. **Tapping mode**, when the tip switches between contact and non-contact during its oscillation on the sample surface. In this case, the feedback parameter is the oscillation amplitude of the cantilever, as shown in **Fig.A1**(d).

Thus, in general an AFM system is constituted by the following elements:

1. A vibration and acoustic platform isolation
2. A tip-cantilever connected to piezoelectric transducers
3. A laser to detect tip-sample interaction
4. A feedback electronic control system
5. A computer and a software to monitor and control the scan

Additional AFM modes were concerned in the last years to characterize different physical quantities depending on the force detected during the tip-sample interaction. This includes the possibility to sense resistance, capacitance, electrical and magnetic fields at the nanometric scale. Focusing on the Conductive Atomic Force Microscopy (C-AFM), this technique is employed to characterize the electrical properties of the sample surface. The C-AFM system requires an AFM conventional setup equipped with a conductive tip and a current detection system. The working principle is like that previously described but a voltage between the tip and the sample is applied during the scan. Thus, the tip acts as a mobile metal contact connected to a current-to-voltage amplifier that allows to detect currents in the pico- or femto-ampere range.

μ-Raman and μ-Photoluminescence Spectroscopy

The *Horiba LabRam HR-Evolution Spectrometer* was employed both for μ-Raman and μ-Photoluminescence Spectroscopy during this PhD course.

Raman spectroscopy is a technique used to determine the vibrational modes of the molecules and it is based on Raman scattering. This latter is an inelastic scattering of the light after the interaction with molecular vibrations or phonons. The light excites the molecules to virtual excited states for a short time and next they recombine in a different vibrational state from the starting one. This causes the emission of a photon with a lower or higher energy than that of the incident one. If the final vibrational state is higher in energy than the initial state, the scattered photon will have a lower energy (and lower frequency) and this shift is defined Stokes-shift. Differently, when the molecular final state is lower in energy, the scattered photon will have a higher energy (and higher frequency) and this is defined Anti-Stokes shift.

A typical Raman setup is composed by a laser source at a fixed wavelength that can be modulated in power by a series of neutral filters, as shown in **Fig.A2**. The light passes through a series of mirrors before being focused on the sample by a microscope lens and an appropriate objective. The same objective recoils the scattered component of light and guides it towards the spectrometer through opportune mirrors and lenses. The elastic component of light (Rayleigh scattering) is stopped by a laser filter, thus the Raman scattering component pass through a confocal pinhole, where only the part of light from the confocal plane is selected.

This aspect permits to enhance the lateral and the vertical space resolutions. In the end, the scattered light is diffracted by an appropriate diffraction grating and recorded by a Charge-Couple Device (CCD). In our apparatus, both Raman and PL measurements were performed using a laser excitation wavelength of 532 nm (2.33 eV) in a confocal mode microscope system with a 100x objective. The power of the laser has been filtered to 1% or 3.2% of the nominal power of 100 mW. Specifically, the μ-Raman spectroscopy was realized with a diffraction grating of 1800 lines/mm in a range from 150 to 650 cm^{-1}, while a grating of 600 lines/mm was employed for μ-PL measurements (in a range from 10 to 5500 cm^{-1}). PL characterizations have been made possible increasing the binning of the CCD pixels from the default value to 30. In this way, the CCD has the possibility to record a greater number of photons at the expense of a minor spectral resolution (not necessary for PL compared to Raman Spectroscopy).

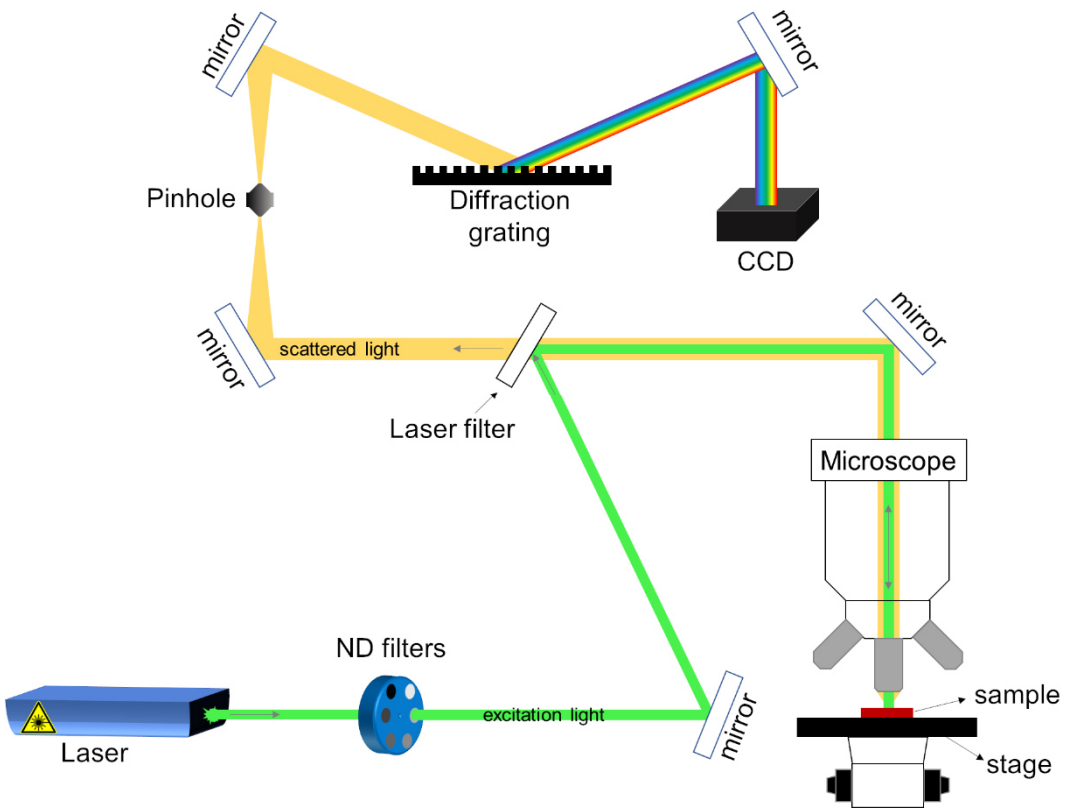

Figure A2.- Raman spectroscopy setup.

Transmission Electron Microscopy (TEM)

Transmission Electron Microscopy is a powerful technique employed in material science to obtain real image of a sample trough a transmitted beam of electrons. Generally, the beam of electrons is at high energy and interacts with a very thin sample. From this interaction is possible to observe the sample's crystal structure, its grain boundaries, dislocations, or further crystal features. Indeed, in this specific case, TEM offers the possibility to analyze the number of layers of 2D materials, as well as their quality, the vdW gap and the defects at the interfaces when the sample is analyzed in cross-section. This kind of beam overcomes the limit imposed by the wavelengths of the light that are used in traditional microscopies, and consequently to realize image at higher resolutions. This is due to the smaller De Broglie wavelength of electrons compared to that of photons.

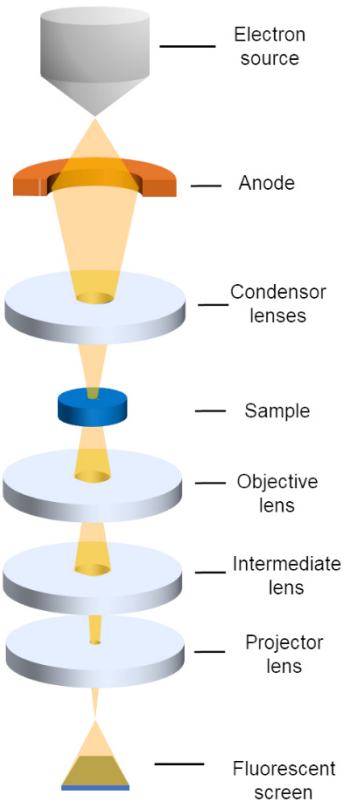

Figure A3.- Set up of a conventional Transmission Electron Microscopy.

The electrons beam is emitted from an electrons source, as a tungsten filament, after the application of a sufficient current **Fig.A3**. The electrons will be emitted by

thermionic emission or field electron emission mechanism. Using a condenser lens, the beam is restricted excluding the high-angle electrons. Next the beam strikes the specimen located in a stage and part of the beam will be transmitted through the sample. A higher number of electrons will be transmitted for transparent and thinnest samples. Thus, the transmitted component will be focused by a series of lenses (objective, intermediate and projector) on a phosphorus screen or CCD camera to realize the final image. This image will be featured by darker and lighter areas that correspond to areas of the sample where fewer, and more electrons were transmitted through respectively. In addition to this classical configuration, TEM can also be employed in scanning mode, defined STEM. In this modality, the beam of electrons is focused to a very thin spot (0.05-0.2 nm) on the sample that will be scanned at each small point illuminated. Typically, the conventional TEM are equipped by scanning coils that allow to switch from TEM to STEM configuration. The diffracted component of the electron beam can be used to realize the *Selected Area Diffraction* (SAD or SAED) technique that permits to obtain information on the crystallographic structure of the sample analyzed. In particular, for crystalline samples, the image consists of a structure of ordered dots, while for amorphous or polycrystalline samples a series of rings will be produced. Differently, the *Energy-dispersive X-ray Spectroscop*y (EDS or EDX) permits to realize the elemental or chemical analysis of the sample, when X-ray are emitted from the sample after the interaction with the high-energy electrons beam. TEM analyses are carried out in a high vacuum mainly to increase the mean free path of electrons but also to prevent several electrical problems during the characterization. In this thesis, high resolution transmission electron microscopy (HR-TEM), high angle annular dark field scanning transmission electron microscopy (HAADF-STEM) and energy dispersion spectroscopy (EDS) analyses of the MoS_2 thin films were carried out with an aberration-corrected Titan Themis 200 microscope. To this aim, cross-sectioned samples were prepared by Focused Ion Beam (FIB).

X-Ray photoelectron Spectroscopy

The X-Ray photoelectron Spectroscopy (XPS) belongs to the photoemission spectroscopy that exploits the photoelectric effect to identify the chemical composition and the chemical states of the elements present on a sample surface. It is effectively a quantitative spectroscopy technique. In particular, employing an X-

ray wavelength whose energy is well-known (E_{photon}), and measuring the emitted electrons kinetic energies ($E_{Kinetic}$), it is possible to extract the binding energy of each emitted electrons (E_{BE}) from the photoelectric equation:

$$E_{BE} = E_{photon} - (E_{Kinetic} + \emptyset) \quad \text{(EA1)}$$

where $\emptyset$ is the corrected work function of the surface, considering the corrections due to the instrument's configuration. The scheme of the instrument is represented in **Fig.A4,** where a photon source of x-ray irradiates a sample surface from which are emitted photoelectrons from 1 to 10 nm of analyzed material. The photoelectrons are recoiled through a system of electron optical lens that define the acceptance angle for collecting electrons from the sample. Next, a hemispherical analyzer (that has a

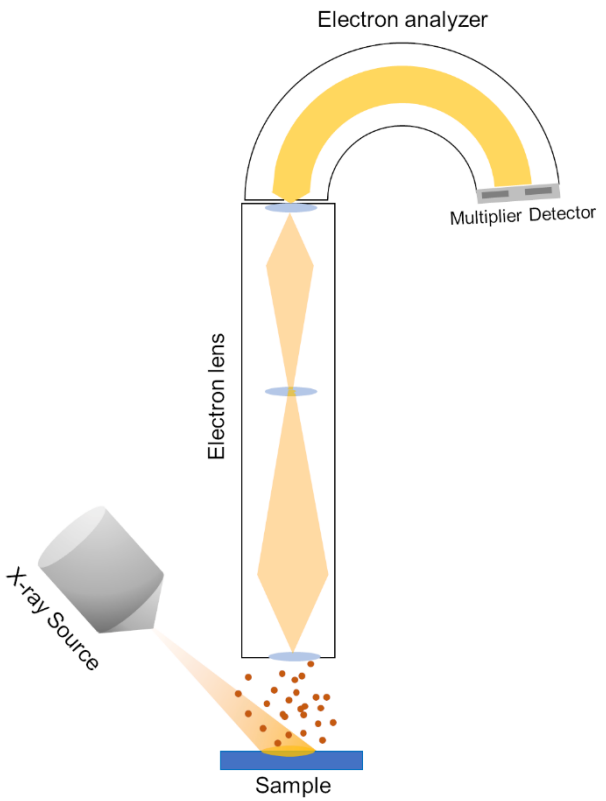

Figure A4.- X-ray photoelectron spectroscopy setup.

better performance compared to the cylindrical mirrors' analyzer) permits to filter the electrons with a specific energy imposed by the voltage applied between the two hemispheres. Changing the voltage, it is possible to recoil electrons with different energies. A better resolution is obtained with a larger radius analyzer. In the end, electrons are recoiled from the analyzer exit slit by multipliers detectors that allow

to increase the collection efficiency. All the XPS instruments are housed within ultra-high vacuum environments (10^{-9} – 10^{-10} mbar) to prevent the scattering of the photoelectrons with the air molecules and to avoid the surface contaminations. In this thesis, the compositional properties of the MoS_2 were evaluated by X-ray photoelectron spectroscopy (XPS) using Escalab Xi+ equipment by Thermo Fisher (Waltham, MA, USA), with a monochromatic Al Kα X-ray source (energy = 1486.6 eV). The spectra were collected at a take-off angle of 90° relative to the sample surface and pass energy of 20 eV. The instrument resolution was 0.45 eV (FWHM of the Ag $3d_{5/2}$ peak). The spectra were aligned using C1s (285 eV) as reference.

BIBLIOGRAPHY

1. A. K. Geim, I. V. Grigorieva. Van der Waals heterostructures. Nature **499**(7459), 419-425 (2013).
2. B. Radisavljevic, A. Radenovic, J. Brivio, V. Giacometti, A. Kis. Single-layer MoS_2 transistors. Nature nanotechnology **6**(3), 147-150 (2011).
3. K. S. Novoselov, A. K. Geim, S. V. Morozov, D. E. Jiang, Y. Zhang, S. V. Dubonos, I. V. Grigorieva, A. A. Firsov. Electric field effect in atomically thin carbon films. Science **306**(5696), 666-669 (2004).
4. K. S. Novoselov, D. Jiang, F. Schedin, T. J. Booth, V. V. Khotkevich, S. V. Morozov, A. K. Geim. Two-dimensional atomic crystals. Proceedings of the National Academy of Sciences **102**(30), 10451-10453 (2005).
5. H. S. S. Ramakrishna Matte, A. Gomathi, A. K. Manna, D. J. Late, R. Datta, S. K. Pati, C. N. R. Rao. MoS_2 and WS_2 analogues of graphene. Angewandte Chemie International Edition **49**(24), 4059-4062, (2010).
6. A. V. Kolobov, J. Tominaga. Two-dimensional transition-metal dichalcogenides (Vol. 239). Springer (2016).
7. S. Zeng, Z. Tang, C. Liu, P. Zhou. Electronics based on two-dimensional materials: Status and outlook. Nano Research **14**(6), 1752-1767 (2021).
8. A. Kara, H. Enriquez, A. P. Seitsonen, L. L. Y. Voon, S. Vizzini, B. Aufray, H. Oughaddou. A review on silicene—new candidate for electronics. Surface science reports **67**(1), 1-18 (2012).
9. A. Acun, L. Zhang, P. Bampoulis, M. V. Farmanbar, A. van Houselt, A. N. Rudenko, M. Lingenfelder, G. Brocks, B. Poelsema, M. I. Katsnelson, H. J. Zandvliet. Germanene: the germanium analogue of graphene. Journal of physics: Condensed matter **27**(44), 443002 (2015).
10. Z. Q. Wang, T. Y. Lü, H. Q. Wang, Y. P. Feng, J. C. Zheng. Review of borophene and its potential applications. Frontiers of Physics **14**(3), 1-20 (2019).

11. B. Anasori, Y. Xie, M. Beidaghi, J. Lu, B. C. Hosler, L. Hultman, P. R. C. Kent, Y. Gogotsi, M. W. Barsoum. Two-dimensional, ordered, double transition metals carbides (MXenes). ACS nano **9**(10), 9507-9516 (2015).
12. K. I. Bolotin, K. J. Sikes, Z. Jiang, M. Klima, G. Fudenberg, J. Hone, P. Kim, H. L. Stormer. Ultrahigh electron mobility in suspended graphene. Solid state communications **146**, 351-355 (2008).
13. D. Jariwala, A. Srivastava, P. M. Ajayan. Graphene synthesis and band gap opening. Journal of nanoscience and nanotechnology **11**(8), 6621-6641 (2011).
14. S. Y. Zhou, G. H. Gweon, A. V. Fedorov, P. D. First, W. A. De Heer, D. H. Lee, F. Guinea, A. H. Castro Neto, A. Lanzara. Substrate-induced bandgap opening in epitaxial graphene. Nature materials **6**(10), 770-775 (2007).
15. Z. H. Ni, T. Yu, Y. H. Lu, Y. Y. Wang, Y. P. Feng, Z. X. Shen. Uniaxial strain on graphene: Raman spectroscopy study and band-gap opening. ACS nano **2**(11), 2301-2305 (2008).
16. M. Y. Han, B. Özyilmaz, Y. Zhang, P. Kim. Energy band-gap engineering of graphene nanoribbons. Physical review letters **98**(20), 206805 (2007).
17. X. Li, X. Wang, L. Zhang, S. Lee, H. Dai. Chemically derived, ultrasmooth graphene nanoribbon semiconductors. Science **319**(5867), 1229-1232 (2008).
18. L. Jiao, L. Zhang, X. Wang, G. Diankov, H. Dai. Narrow graphene nanoribbons from carbon nanotubes. Nature **458**(7240), 877-880 (2009).
19. F. Sols, F. Guinea, A. C. Neto. Coulomb blockade in graphene nanoribbons. Physical Review Letters **99**(16), 166803 (2007).
20. Y. Yoon, J. Guo. Effect of edge roughness in graphene nanoribbon transistors. Applied Physics Letters **91**(7), 073103 (2007).
21. B. Obradovic, R. Kotlyar, F. Heinz, P. Matagne, T. Rakshit, M. D Giles, M. A. Stettler D. E. Nikonov. Analysis of graphene nanoribbons as a channel material for field-effect transistors. Applied Physics Letters **88**(14), 142102 (2006).

22. Y. Zhang, T. T. Tang, C. Girit, Z. Hao, M. C. Martin, A. Zettl, M. F. Crommie, Y. R. Shen, F. Wang. Direct observation of a widely tunable bandgap in bilayer graphene. Nature **459**(7248), 820-823 (2009).

23. F. Xia, D. B. Farmer, Y. M. Lin, P. Avouris. Graphene field-effect transistors with high on/off current ratio and large transport band gap at room temperature. Nano letters **10**(2), 715-718 (2010).

24. M. Yankowitz, J. Xue, B. J. LeRoy. Graphene on hexagonal boron nitride. Journal of Physics: Condensed Matter **26**(30), 303201 (2014).

25. J. Wang, F. Ma, M. Sun. Graphene, hexagonal boron nitride, and their heterostructures: properties and applications. RSC advances **7**(27), 16801-16822 (2017).

26. C. R. Dean, A. F. Young, I. Meric, C. Lee, L. Wang, S. Sorgenfrei, K. Watanabe, T. Taniguchi, P. Kim, K. L. Shepard, J. Hone. Boron nitride substrates for high-quality graphene electronics. Nature nanotechnology **5**(10), 722-726 (2010).

27. D. Jariwala, V. K. Sangwan, L. J. Lauhon, T. J. Marks, M. C. Hersam. Emerging device applications for semiconducting two-dimensional transition metal dichalcogenides. ACS nano **8**(2), 1102-1120 (2014).

28. T. Nawz, A. Safdar, M. Hussain, D. Sung Lee, M. Siyar. Graphene to advanced MoS_2: a review of structure, synthesis, and optoelectronic device application. Crystals **10**(10), 902 (2020).

29. G. Eda, H. Yamaguchi, D. Voiry, T. Fujita, M. Chen, M. Chhowalla. Photoluminescence from chemically exfoliated MoS_2. Nano letters **11**(12), 5111-5116 (2011).

30. K. E. Dungey, M. D. Curtis, J. E. Penner-Hahn. Structural characterization and thermal stability of MoS_2 intercalation compounds. Chemistry of Materials **10**(8), 2152-2161 (1998).

31. K.F. Mak, C. Lee, J. Hone, J. Shan, T.F. Heinz. Atomically thin MoS_2: a new direct-gap semiconductor. Physical review letters **105**(13), 136805 (2010).

32. A. Splendiani, L. Sun, Y. Zhang, T. Li, J. Kim, C. Y. Chim, G. Galli, F. Wang. Emerging photoluminescence in monolayer MoS_2. Nano letters **10**(4), 1271-1275 (2010).

33. W. Choi, N. Choudhary, G. H. Han, J. Park, D. Akinwande, Y. H. Lee. Recent development of two-dimensional transition metal dichalcogenides and their applications. Materials Today **20**(3), 116-130 (2017).

34. E. Singh, P. Singh, K. S. Kim, G. Y. Yeom, H. S. Nalwa. Flexible molybdenum disulfide (MoS_2) atomic layers for wearable electronics and optoelectronics. ACS applied materials & interfaces **11**(12), 11061-11105 (2019).

35. D. J. Late, Y. K. Huang, B. Liu, J. Acharya, S. N. Shirodkar, J. Luo, A. Yan, D. Charles, U. V. Waghmare, V. P. Dravid, C. N. R. Rao. Sensing behavior of atomically thin-layered MoS_2 transistors. ACS nano **7**(6), 4879-4891 (2013).

36. K. Chang, Z. Mei, T. Wang, Q. Kang, S. Ouyang, J. Ye. MoS_2/graphene cocatalyst for efficient photocatalytic H_2 evolution under visible light irradiation. ACS nano **8**(7), 7078-7087 (2014).

37. T. Roy, M.Tosun, X. Cao, H. Fang, D. H. Lien, P. Zhao, Y. Z. Chen, Y. L. Chueh, J. Guo, A. Javey. Dual-gated MoS_2/WSe_2 van der Waals tunnel diodes and transistors. ACS nano **9**(2), 2071-2079 (2015).

38. M. Choi, Y. J. Park, B. K. Sharma, S. R. Bae, S. Y. Kim, J. H. Ahn. Flexible active-matrix organic light-emitting diode display enabled by MoS_2 thin-film transistor. Science advances **4**(4), eaas8721 (2018).

39. D. Kufer, G. Konstantatos. Highly sensitive, encapsulated MoS2 photodetector with gate controllable gain and speed. Nano letters 15(11), 7307-7313 (2015).

40. F. Giannazzo, S. E. Panasci, E. Schilirò, F. Roccaforte, A. Koos, M. Nemeth, B. Pécz. Esaki Diode Behavior in Highly uniform MoS_2/Silicon Carbide Heterojunctions. Advanced Materials Interfaces, **9**(22), 2200915 (2022).

41. F. Giannazzo, R. Dagher, E. Schilirò, S. E. Panasci, G. Greco, G. Nicotra, F. Roccaforte, S. Agnello, J. Brault, Y. Cordier, A. Michon. Nanoscale structural

and electrical properties of graphene grown on AlGaN by catalyst-free chemical vapor deposition. Nanotechnology **32**, 015705 (2020).

42. F. Giannazzo, S. E. Panasci, E. Schilirò, P. Fiorenza, G. Greco, F. Roccaforte, M. Cannas, S. Agnello, A. Koos, B. Pécz, M. Spankova, S. Chromik. Highly homogeneous 2D/3D heterojunction diodes by pulsed laser deposition of MoS_2 on ion implantation doped 4H-SiC. Advanced Materials Interfaces, 2201502, (2022).

43. Y. Liu, Y. Huang, X. Duan. Van der Waals integration before and beyond two-dimensional materials. Nature **567**(7748), 323-333 (2019).

44. K. Autumn, M. Sitti, Y. A. Liang, A. M. Peattie, W. R. Hansen, S. Sponberg, T. W. Kenny, R. Fearing, J. N. Israelachvili, R. J. Full. Evidence for van der Waals adhesion in gecko setae. Proceedings of the National Academy of Sciences **99**(19), 12252-12256 (2002).

45. M. Yi, Z. Shen. A review on mechanical exfoliation for the scalable production of graphene. Journal of Materials Chemistry A **3**(22), 11700-11715 (2015).

46. I. Song, C. Park, H. C. Choi. Synthesis and properties of molybdenum disulphide: from bulk to atomic layers. Rsc Advances **5**(10), 7495-7514 (2015).

47. U. Krishnan, M. Kaur, K. Singh, M. Kumar, A. Kumar. A synoptic review of MoS_2: Synthesis to applications. Superlattices and Microstructures **128**, 274-297 (2019).

48. F. Wypych, R. Schöllhorn, 1T-MoS_2, a new metallic modification of molybdenum disulfide. Journal of the Chemical Society, Chemical Communications **19**, 1386-1388 (1992).

49. F. Wypych, T. Weber, R. Prins. Scanning tunneling microscopic investigation of 1T-MoS_2. Chemistry of materials **10**(3), 723-727 (1998).

50. A. N. Enyashin, L. Yadgarov, L. Houben, I. Popov, M. Weidenbach, R. Tenne, M. Bar-Sadan, G. Seifert. New Route for Stabilization of 1T-WS_2 and MoS_2 Phases. The Journal of Physical Chemistry C **115**(50), 24586-24591 (2011).

51. S. Bertolazzi, J. Brivio, A. Kis. Stretching and breaking of ultrathin MoS_2. ACS nano **5**(12), 9703-9709 (2011).

52. C. Berger, Z. Song, T. Li, X. Li, A. Y. Ogbazghi, R. Feng, Z. Dai, A. N. Marchenkov, E. H. Conrad, P. N. First, W. A. De Heer. Ultrathin epitaxial graphite: 2D electron gas properties and a route toward graphene-based nanoelectronics. The Journal of Physical Chemistry B **108**(52), 19912-19916 (2004).

53. M. C. Lemme, T. J. Echtermeyer, M. Baus, H. Kurz. A graphene field-effect device. IEEE Electron Device Letters **28**(4), 282-284 (2007).

54. A. Ayari, E. Cobas, O. Ogundadegbe, M. S. Fuhrer. Realization and electrical characterization of ultrathin crystals of layered transition-metal dichalcogenides. Journal of Applied Physics **101**, 14507–14507 (2007).

55. K. F. Mak, K. He, C. Lee, G. H. Lee, J. Hone, T. F. Heinz, J. Shan. Tightly bound trions in monolayer MoS_2. Nature materials **12**(3), 207-211 (2013).

56. S. Mouri, Y. Miyauchi, K. Matsuda. Tunable photoluminescence of monolayer MoS_2 via chemical doping. Nano letters **13**(12), 5944-5948 (2013).

57. P. Willke, J. A. Amani, A. Sinterhauf, S. Thakur, T. Kotzott, T. Druga, S. Weikert, K. Maiti, H. Hofsass, M. Wenderoth. Doping of graphene by low-energy ion beam implantation: structural, electronic, and transport properties. Nano letters **15**(8), 5110-5115 (2015).

58. Y. Zhao, K. Xu, F. Pan, C. Zhou, F. Zhou, Y. Chai. Doping, contact and interface engineering of two-dimensional layered transition metal dichalcogenides transistors. Advanced Functional Materials **27**(19), 1603484 (2017).

59. N. Kaushik, D. Karmakar, A. Nipane, S. Karande, S. Lodha. Interfacial n-doping using an ultrathin TiO2 layer for contact resistance reduction in MoS_2. ACS applied materials & interfaces **8**(1), 256-263 (2016).

60. J. Y. Lee, J. H. Kim, Y. Jung, J. C. Shin, Y. Lee, K. Kim, N. Kim, A. M. van der Zende, J. Son, G. H. Lee. Evolution of defect formation during atomically precise

desulfurization of monolayer MoS_2. Communications Materials **2**(1), 1-10 (2021).

61. S. Das, M. Demarteau, A. Roelofs. Nb-doped single crystalline MoS_2 field effect transistor. Applied Physics Letters **106**(17), 173506 (2015).
62. M. R. Laskar, D. N. Nath, L. Ma, E. W. Lee, C. H. Lee, T. Kent, Z. Yang, R. Mishra, M. A. Roldan, J. C. Idrobo, S. T. Pantelides, S. J. Pennycook, R. C. Myers, Y. Wu, S. Rajan. p-type doping of MoS_2 thin films using Nb. Applied Physics Letters **104**(9), 092104 (2014).
63. J. Suh, T. E. Park, D. Y. Lin, D. Fu, J. Park, H. J. Jung, Y. Chen, C. Ko, C. Jang, Y. Sun, R. Sinclair, J. Chang, S. Tongay, J. Wu. Doping against the native propensity of MoS_2: degenerate hole doping by cation substitution. Nano letters **14**(12), 6976-6982 (2014).
64. S. G. Ramaraj, S. Nundy, P. Zhao, D. Elamaran, A. A. Tahir, Y. Hayakawa, M. Muruganathan, H. Mizuta, S. W. Kim. RF Sputtered Nb-Doped MoS_2 Thin Film for Effective Detection of NO_2 Gas Molecules: Theoretical and Experimental Studies. ACS omega **7**(12), 10492-10501 (2022).
65. P. Bampoulis, R. van Bremen, Q. Yao, B. Poelsema, H. J. Zandvliet, K. Sotthewes. Defect dominated charge transport and fermi level pinning in MoS_2/metal contacts. ACS applied materials & interfaces **9**(22), 19278-19286 (2017).
66. S. Das, H. Y. Chen, A. V. Penumatcha, J. Appenzeller. High performance multilayer MoS2 transistors with scandium contacts. Nano letters **13**(1), 100-105 (2013).
67. H. Zhong, R. Quhe, Y. Wang, Z. Ni, M. Ye, Z. Song, Y. Pan, J. Yang, L. Yang, M. Lei, J. Shi, J. Lu. Interfacial properties of monolayer and bilayer MoS_2 contacts with metals: beyond the energy band calculations. Scientific reports **6**(1), 1-16 (2016).

68. C. Gong, L. Colombo, R. M. Wallace, K. Cho. The unusual mechanism of partial Fermi level pinning at metal–MoS_2 interfaces. Nano letters **14**(4), 1714-1720 (2014).

69. R. Fivaz, E. J. P. R. Mooser. Mobility of charge carriers in semiconducting layer structures. Physical Review **163**(3), 743 (1967).

70. D. Jena, A. Konar. Enhancement of carrier mobility in semiconductor nanostructures by dielectric engineering. Physical review letters **98**(13), 136805 (2007).

71. F. Chen, J. Xia, D. K. Ferry, N. Tao. Dielectric screening enhanced performance in graphene FET. Nano letters **9**(7), 2571-2574 (2009).

72. V. A. Fonoberov, A. A. Balandin. Giant enhancement of the carrier mobility in silicon nanowires with diamond coating. Nano Letters **6**(11), 2442-2446 (2006).

73. M. T. Bohr, R. S. Chau, T. Ghani, K. Mistry. The high-κ solution. IEEE spectrum **44**(10), 29-35 (2007).

74. K. Kobayashi, J. Yamauchi. Electronic structure and scanning-tunneling-microscopy image of molybdenum dichalcogenide surfaces. Physical Review B **51**(23), 17085 (1995).

75. T. Li, G. Galli. Electronic properties of MoS_2 nanoparticles. The Journal of Physical Chemistry C **111**(44), 16192-16196 (2007).

76. A. Kuc, N. Zibouche, T. Heine. Influence of quantum confinement on the electronic structure of the transition metal sulfide TS_2. Physical Review B **83**(24), 245213 (2011).

77. Z. Y. Zhu, Y. C. Cheng, U. Schwingenschlögl. Giant spin-orbit-induced spin splitting in two-dimensional transition-metal dichalcogenide semiconductors. Physical Review B **84**(15), 153402 (2011).

78. N. Scheuschner, O. Ochedowski, A. M. Kaulitz, R. Gillen, M. Schleberger, J. Maultzsch. Photoluminescence of freestanding single-and few-layer MoS_2. Physical Review B **89**, 125406 (2014).

79. M. Drüppel, T. Deilmann, P. Krüger, M. Rohlfing. Diversity of trion states and substrate effects in the optical properties of an MoS_2 monolayer. Nature communications **8**(1), 1-7 (2017).

80. W. Jin, P. C. Yeh, N. Zaki, D. Zhang, J. T. Sadowski, A. Al-Mahboob, A. M. van der Zande, D. A. Chenet, J. I. Dadap, I. P. Herman, P. Sutter, J. Hone, R. M. Osgood Jr. Direct measurement of the thickness-dependent electronic band structure of MoS_2 using angle-resolved photoemission spectroscopy. Physical review letters **111**(10), 106801 (2013).

81. N. Alidoust, G. Bian, S. Y. Xu, R. Sankar, M. Neupane, C. Liu, I. Belopolski, D.-X. Qu, J. D. Delinger, F.-C. Chou, M. Z. Hasan. Observation of monolayer valence band spin-orbit effect and induced quantum well states in MoX_2. Nature communications **5**(1), 1-9 (2014).

82. R. S. Sundaram, M. Engel, A. Lombardo, R. Krupke, A. C. Ferrari, Ph. Avouris, M. Steiner. Electroluminescence in Single Layer MoS_2. Nano Letters **13**, 1416 (2013).

83. Z. Yin, H. Li, H. Li, L. Jiang, Y. Shi, Y. Sun, G. Lu, Q. Zhang, X. Chen, H. Zhang. Single-layer MoS_2 phototransistors ACS Nano **6**, 74 (2012).

84. C. Lee, H. Yan, L. E. Brus, T. F. Heinz, J. Hone, S. Ryu. Anomalous lattice vibrations of single-and few-layer MoS_2. ACS nano **4**(5), 2695-2700 (2010).

85. S. Bertolazzi, J. Brivio, A. Kis. Stretching and breaking of ultrathin MoS_2. ACS nano **5**(12), 9703-9709 (2011).

86. T. Korn, S. Heydrich, M. Hirmer, J. Schmutzler, C. Schüller. Low-temperature photocarrier dynamics in monolayer MoS_2. Applied Physics Letters **99**(10), 102109 (2011).

87. B. Chakraborty, A. Bera, D. V. S. Muthu, S. Bhowmick, U. V. Waghmare, A. K. Sood. Symmetry-dependent phonon renormalization in monolayer MoS_2 transistor. Physical Review B **85**(16), 161403 (2012).

88. R. J. Angel, M. Murri, B. Mihailova, M. Alvaro. Stress, strain and Raman shifts. Zeitschrift für Kristallographie-Crystalline Materials **234**(2), 129-140 (2019).

89. C. R. Zhu, G. Wang, B. L. Liu, X. Marie, X. F. Qiao, X. Zhang, X. X. Wu, H. Fan, P. H. Tan, T. Amand, B. Urbaszek. Strain tuning of optical emission energy and polarization in monolayer and bilayer MoS_2. Physical Review B **88**(12), 121301 (2013).

90. D. Lloyd, X. Liu, J. W. Christopher, L. Cantley, A. Wadehra, B. L. Kim, B. B. Goldberg, A. K. Swan, J. S. Bunch. Band gap engineering with ultralarge biaxial strains in suspended monolayer MoS_2. Nano letters **16**(9), 5836-5841 (2016).

91. G. Grimvall. Thermophysical properties of materials. Elsevier (1999).

92. N. Ferralis. Probing mechanical properties of graphene with Raman spectroscopy. Journal of materials science **45**(19), 5135-5149 (2010).

93. N. Mounet, N. Marzari. First-principles determination of the structural, vibrational and thermodynamic properties of diamond, graphite, and derivatives. Physical Review B **71**(20), 205214 (2005).

94. T. M. G. Mohiuddin, A. Lombardo, R. R. Nair, A. Bonetti, G. Savini, R. Jalil, N. Bonini, D. M. Basko, C. Galiotis, N. Marzari, K. S. Novoselov, A. K. Geim, A. C. Ferrari. Uniaxial strain in graphene by Raman spectroscopy: G peak splitting, Grüneisen parameters, and sample orientation. Physical Review B **79**(20), 205433 (2009).

95. N. Ferralis, R. Maboudian, C. Carraro. Evidence of structural strain in epitaxial graphene layers on 6H-SiC (0001). Physical review letters **101**(15), 156801 (2008).

96. H. J. Conley, B. Wang, J. I. Ziegler, R. F. Haglund Jr, S. T. Pantelides, K. I. Bolotin. Bandgap engineering of strained monolayer and bilayer MoS_2. Nano letters **13**(8), 3626-3630 (2013).

97. G. Plechinger, A. Castellanos-Gomez, M. Buscema, H. S. Van Der Zant, G. A. Steele, A. Kuc, T. Heine, C. Schüller, T. Korn. Control of biaxial strain in single-layer molybdenite using local thermal expansion of the substrate. 2D Materials **2**(1), 015006 (2015).

98. E. Scalise, M. Houssa, G. Pourtois, V. Afanas'ev, A. Stesmans. Strain induced semiconductor to metal transition in the two-dimensional honeycomb structure of MoS_2. Nano Research **5**, 43–48 (2012).

99. B. Chakraborty, A. Das, A. K. Sood. The formation of ap–n junction in a polymer electrolyte top-gated bilayer graphene transistor. Nanotechnology **20**(36), 365203 (2009).

100. C. Attaccalite, L. Wirtz, M. Lazzeri, F. Mauri, A. Rubio. Doped graphene as tunable electron-phonon coupling material. Nano letters **10**(4), 1172-1176 (2010).

101. J. Yan, Y. Zhang, P. Kim, A. Pinczuk. Electric field effect tuning of electron-phonon coupling in graphene. Physical review letters **98**(16), 166802 (2007).

102. S. Pisana, M. Lazzeri, C. Casiraghi, K. S. Novoselov, A. K. Geim, A. C. Ferrari, F. Mauri. Breakdown of the adiabatic Born–Oppenheimer approximation in graphene. Nature materials **6**(3), 198-201 (2007).

103. J. Yan, E. A. Henriksen, P. Kim, A. Pinczuk. Observation of anomalous phonon softening in bilayer graphene. Physical review letters **101**(13), 136804 (2008).

104. J. Zhang, Y. Zhu, M. Tebyetekerwa, D. Li, D. Liu, W. Lei, L. Wang, Y. Zhang, Y. Lu. Vanadium-Doped Monolayer MoS_2 with Tunable Optical Properties for Field-Effect Transistors. ACS Applied Nano Materials **4**(1), 769-777 (2020).

105. S. Mignuzzi, A. J. Pollard, N. Bonini, B. Brennan, I. S. Gilmore, M. A. Pimenta, D. Richards, D. Roy. Effect of disorder on Raman scattering of single-layer MoS_2. Physical Review B **91**(19), 195411 (2015).

106. E. Del Corro, H. Terrones, A. Elias, C. Fantini, S. Feng, M. A. Nguyen, T. E. Mallouk, M. Terrones, M. A. Pimenta. Excited excitonic states in 1L, 2L, 3L, and bulk WSe_2 observed by resonant Raman spectroscopy. ACS Nano **8**(9), 9629-9635 (2014).

107. N. Kang, H. P. Paudel, M. N. Leuenberger, L. Tetard, S. I. Khondaker. Photoluminescence quenching in single-layer MoS_2 via oxygen plasma treatment. Journal of Physical Chemistry C **118**, 21258–21263 (2014).

[108.] K. M. McCreary, A. T. Hanbicki, S. V. Sivaram, B. T. Jonker. A- and Bexciton photoluminescence intensity ratio as a measure of sample quality for transition metal dichalcogenide monolayers. APL Materials **6**, 111106 (2018).

[109.] D. Mouloua, A. Kotbi, G. Deokar, K. Kaja, M. El Marssi, M. A. El Khakani, M. Jouiad. Recent progress in the synthesis of MoS_2 thin films for sensing, photovoltaic and plasmonic applications: a review. Materials **14**(12), 3283 (2021).

[110.] J. N. Coleman, M. Lotya, A. O'Neill, S. D. Bergin, P. J. King, U. Khan, K. Young, A. Gaucher, S. De, R. J. Smith, I. V. Shvets, S. K. Arora, G. Stanton, H. Y. Kim, K. Lee, G. T. Kim, G. S. Duesberg, T. Hallam, J. J. Boland, J. J. Wang, J. F. Donegan, J. C. Grunlan, G. Moriarty, A. Shmeliov, R. J. Nicholls, J. M. Perkins, E. M. Grieveson, K. Theuwissen, D. W. Mccomb, P. D. Nellist, V. Nicolosi. Two-dimensional nanosheets produced by liquid exfoliation of layered materials. Science **331**, 568–571 (2011).

[111.] Q. D. Truong, M. Kempaiah Devaraju, Y. Nakayasu, N. Tamura, Y. Sasaki, T. Tomai, I. Honma. Exfoliated MoS_2 and $MoSe_2$ Nanosheets by a supercritical fluid process for a hybrid Mg–Li-ion battery. ACS omega **2**(5), 2360-2367 (2017).

[112.] P. Joensen, R. F. Frindt, S. R. Morrison. Single-layer MoS_2. Materials research bulletin **21**(4), 457-461 (1986).

[113.] M. Osada, T. Sasaki. Exfoliated oxide nanosheets: new solution to nanoelectronics. Journal of Materials Chemistry **19**, 2503–2511 (2009).

[114.] X. Fan, P. Xu, D. Zhou, Y. Sun, Y. C. Li, M. A. T. Nguyen, M. Terrones, T. E. Mallouk. Fast and Efficient Preparation of Exfoliated 2H MoS_2 Nanosheets by Sonication-Assisted Lithium Intercalation and Infrared Laser-Induced 1T to 2H Phase Reversion. Nano Letters **15**, 5956−5960 (2015).

[115.] Y. Q. Yang, C. T. Tye, K. J. Smith. Influence of MoS_2 catalyst morphology on the hydrodeoxygenation of phenols. Catalysis Communications **9**(6), 1364-1368 (2008).

116. A. Ambrosi, Z. Sofer, M. Pumera. Lithium intercalation compound dramatically influences the electrochemical properties of exfoliated MoS_2. Small **11**(5), 605-612 (2015).

117. G. Z. Magda, J. Pető, G. Dobrik, C. Hwang, L. P. Biró, L. Tapasztó. Exfoliation of large-area transition metal chalcogenide single layers. Scientific reports **5**(1), 1-5 (2015).

118. S. B. Desai, S. R. Madhvapathy, M. Amani, D. Kiriya, M. Hettick, M. Tosun, Y. Zhou, M. Dubey, J. W. Ager III, D. Chrzan, A. Javey. Gold-mediated exfoliation of ultralarge optoelectronically-perfect monolayers. Advanced Materials **28**(21), 4053-4058 (2016).

119. M. Velicky, G. E. Donnelly, W. R. Hendren, S. McFarland, D. Scullion, W. J. DeBenedetti, G. C. Correa, Y. Han, A. J. Wain, M. A. Hines, D. A. Muller, K. S. Novoselov, H. D. Abruña, R. M. Bowman, E. J. G. Santos, F. Huang. Mechanism of gold-assisted exfoliation of centimeter-sized transition-metal dichalcogenide monolayers. ACS nano **12**(10), 10463-10472 (2018).

120. M. Heyl, D. Burmeister, T. Schultz, S. Pallasch, G. Ligorio, N. Koch, E. J. List-Kratochvil. Thermally Activated Gold-Mediated Transition Metal Dichalcogenide Exfoliation and a Unique Gold-Mediated Transfer. physica status solidi (RRL)–Rapid Research Letters **14**(11), 2000408 (2020).

121. M. Velicky, A. Rodriguez, M. Bousa, A. V. Krayev, M. Vondracek, J. Honolka, M. Ahmadi, G. E. Donnelly, F. Huang, H. D. Abruña, K. S. Novoselov, O. Frank. Strain and charge doping fingerprints of the strong interaction between monolayer MoS_2 and gold. The journal of physical chemistry letters **11**(15), 6112-6118 (2020).

122. Y. Huang, Y.-H. Pan, R. Yang, L.-H. Bao, L. Meng, H.-L. Luo, Y.-Q. Cai, G.-D. Lui, W.-J. Zhao, Z. Zhou, L.-M. Wu, Z.-L. Zhu, M. Huang, L.-W. Liu, L. Liu, P. Cheng, K.-H. Wu, S.-B. Tian, C.-Z. Gu, Y.-G. Shi, Y.-F. Guo, Z. G. Cheng, J.-J. Hu, L. Zhao, G.-H. Yang, E. Sutter, P. Sutter, Y..L. Wang, W. Ji, X.-J. Zhou,

H.-J. Gao. Universal Mechanical exfoliation of large-area 2D crystals. Nature communications **11**(1), 1-9 (2020).

123. F. Liu, W. Wu, Y. Bai, S. H. Chae, Q. Li, J. Wang, J. Hone, X. Y. Zhu. Disassembling 2D van der Waals crystals into macroscopic monolayers and reassembling into artificial lattices. Science **367**(6480), 903-906 (2020).

124. E. Pollmann, S. Sleziona, T. Foller, U. Hagemann, C. Gorynski, O. Petri, L. Madauß, L. Breuer, M. Schleberger. Large-Area, Two-Dimensional MoS2 Exfoliated on Gold: Direct Experimental Access to the Metal–Semiconductor Interface. ACS omega **6**(24), 15929-15939 (2021).

125. B. Zou, Z. Wu, Y. Zhou, Y. Zhou, J. Wang, L. Zhang, F. Cao, H. Sun. Spectroscopic Ellipsometry Investigation of Au-Assisted Exfoliated Large-Area Single-Crystalline Monolayer MoS_2. physica status solidi (RRL)–Rapid Research Letters **15**(11), 2100385 (2021).

126. P. Brus, V. Zatko, M. Galbiati, F. Godel, S. Collin, B. Servet, S. Xavier, R. Aubry, P. Garabedian, M. B. Martin, B. Dlubak, P. Seneor, O. Bezencenet. Large-Scale-Compatible Stabilization of a 2D Semiconductor Platform toward Discrete Components. Advanced Electronic Materials **7**(4), 2001109 (2021).

127. H. Häkkinen. The gold–sulfur interface at the nanoscale. Nature chemistry **4**(6), 443-455 (2012).

128. S. M. Hus, R. Ge, P. A. Chen, L. Liang, G. E. Donnelly, W. Ko, F. Huang, M. H. Chiang, A. P. Li, D. Akinwande. Observation of single-defect memristor in an MoS_2 atomic sheet. Nature Nanotechnology **16**(1), 58-62 (2021).

129. Y. Zeng, X. Li, W. Chen, J. Liao, J. Lou, Q. Chen. Highly enhanced photoluminescence of monolayer MoS_2 with self-assembled Au nanoparticle arrays. Advanced Materials Interfaces **4**(21), 1700739 (2017).

130. X. Li, W. Cai, J. An, S. Kim, J. Nah, D. Yang, R. Piner, A. Velamakanni, I. Jung, E. Tutuc, S. K. Banerjee, L. Colombo, R. S. Ruoff. Large-area synthesis of high-quality and uniform graphene films on copper foils. Science **324**(5932), 1312-1314 (2009).

131. J. Hass, W. A. De Heer, E. H. Conrad. The growth and morphology of epitaxial multilayer graphene. Journal of Physics: Condensed Matter **20**(32), 323202 (2008).

132. H. O. Pierson. Handbook of chemical vapor deposition: principles, technology and applications. William Andrew (1999).

133. Y. H. Lee, X. Q. Zhang, W. Zhang, M. T. Chang, C. T. Lin, K. D. Chang, Y. C. Yu, J. T. W. Wang, C. S. Chang, L. J. Li, T. W. Lin. Synthesis of large-area MoS_2 atomic layers with chemical vapor deposition. Advanced materials **24**(17), 2320-2325 (2012).

134. L. Tang, J. Tan, H. Nong, B. Liu, H. M. Cheng Chemical vapor deposition growth of two-dimensional compound materials: controllability, material quality, and growth mechanism. Accounts of Materials Research **2**(1), 36-47 (2020).

135. Z. Zhu, S. Zhan, J. Zhang, G. Jiang, M. Yi, J. Wen. Influence of growth temperature on MoS_2 synthesis by chemical vapor deposition. Materials Research Express **6**(9), 095011 (2019).

136. Y. Cao, X. Luo, S. Han, C. Yuan, Y. Yang, Q. Li, T. Yu, S. Ye. Influences of carrier gas flow rate on the morphologies of MoS_2 flakes. Chemical Physics Letters **631**, 30-33 (2015).

137. P. Kumar, B. Viswanath. Effect of sulfur evaporation rate on screw dislocation driven growth of MoS_2 with high atomic step density. Crystal Growth & Design **16**(12), 7145-7154 (2016).

138. A. Ubaldini, J. Jacimovic, N. Ubrig, E. Giannini. Chloride-driven chemical vapor transport method for crystal growth of transition metal dichalcogenides. Crystal Growth & Design **13**(10), 4453-4459 (2013).

139. G. H. Han, N. J. Kybert, C. H. Naylor, B. S. Lee, J. Ping, J. H. Park, J. Kang, S. Y. Lee, R. Agarwal, A. T. Johnson. Seeded growth of highly crystalline molybdenum disulphide monolayers at controlled locations. Nature communications **6**(1), 1-6 (2015).

[140.] W. H. Chae, J. D. Cain, E. D. Hanson, A. A. Murthy, V. P. Dravid. Substrate-induced strain and charge doping in CVD-grown monolayer MoS_2. Applied Physics Letters **111**(14), 143106 (2017).

[141.] H. Yin, X. Zhang, J. Lu, X. Geng, Y. Wan, M. Wu, P. Yang. Substrate effects on the CVD growth of MoS_2 and WS_2. Journal of Materials Science **55**(3), 990-996 (2020).

[142.] S. Wang, M. Pacios, H. Bhaskaran, J. H. Warner. Substrate control for large area continuous films of monolayer MoS_2 by atmospheric pressure chemical vapor deposition. Nanotechnology **27**(8), 085604 (2016).

[143.] J. Sitek, J. Plocharski, I. Pasternak, A. P. Gertych, C. McAleese, B. R. Conran, M. Zdrojek, W. Strupinski. Substrate-induced variances in morphological and structural properties of MoS_2 grown by chemical vapor deposition on epitaxial graphene and SiO_2. ACS Applied Materials & Interfaces **12**(40), 45101-45110 (2020).

[144.] S. Wang, Y. Rong, Y. Fan, M. Pacios, H. Bhaskaran, K. He, J. H. Warner. Shape evolution of monolayer MoS_2 crystals grown by chemical vapor deposition. Chemistry of Materials **26**(22), 6371-6379 (2014).

[145.] S. Y. Yang, G. W. Shim, S. B. Seo, S. Y. Choi. Effective shape-controlled growth of monolayer MoS_2 flakes by powder-based chemical vapor deposition. Nano Research **10**(1), 255-262 (2017).

[146.] D. Zhou, H. Shu, C. Hu, L. Jiang, P. Liang, X. Chen. Unveiling the growth mechanism of MoS_2 with chemical vapor deposition: from two-dimensional planar nucleation to self-seeding nucleation. Crystal Growth & Design **18**(2), 1012-1019 (2018).

[147.] D. Zhu, H. Shu, F. Jiang, D. Lv, V. Asokan, O. Omar, J. Yuan, Z. Zhang, C. Jin. Capture the Growth Kinetics of CVD Growth of Two-Dimensional MoS_2. npj 2D Materials and Applications **1**, 8−15 (2017).

148. Q. Ji, Y. Zhang, Y. Zhang, Z. Liu. Chemical Vapor Deposition of Group-VIB Metal Dichalcogenide Monolayers: Engineered Substrates from Amorphous to Single Crystalline. Chemical Society Review **44**, 2587−2602 (2015).

149. Y. H. Lee, X. Q. Zhang, W. Zhang, M. T. Chang, C. T. Lin, K. D. Chang, Y.C. Yu, J. T. W. Wang, C.S. Chang, L. L. Li, T. W. Lin. Synthesis of large-area MoS_2 atomic layers with chemical vapor deposition. Advanced materials **24**(17), 2320-2325 (2012).

150. S. Vangelista, E. Cinquanta, C. Martella, M. Alia, M. Longo, A. Lamperti, R. Mantovan, F. B. Basset, F. Pezzoli, A. Molle. Towards a uniform and large-scale deposition of MoS_2 nanosheets via sulfurization of ultra-thin Mo-based solid films. Nanotechnology **27**(17), 175703 (2016).

151. Y. C. Lin, W. Zhang, J. K. Huang, K. K. Liu, Y. H. Lee, C. T. Liang, C. W. Chu, L. J. Li. Wafer-scale MoS_2 thin layers prepared by MoO_3 sulfurization. Nanoscale **4**(20), 6637-6641 (2012).

152. S. Najmaei, J. Yuan, J. Zhang, P. Ajayan, J. Lou. Synthesis and defect investigation of two-dimensional molybdenum disulfide atomic layers. Accounts of Chemical Research **48**(1), 31-40 (2015).

153. S. Najmaei, Z. Liu, W. Zhou, X. Zou, G. Shi, S. Lei, B. I. Yakobson, J. C. Idrobo, P. M. Ajayan, J. Lou. Vapour phase growth and grain boundary structure of molybdenum disulphide atomic layers. Nature materials **12**(8), 754-759 (2013).

154. L. Tao, K. Chen, Z. Chen, W. Chen, X. Gui, H. Chen, X. Li, J. B. Xu. Centimeter-scale CVD growth of highly crystalline single-layer MoS_2 film with spatial homogeneity and the visualization of grain boundaries. ACS applied materials & interfaces **9**(13), 12073-12081 (2017).

155. W. Zhou, X. Zou, S. Najmaei, Z. Liu, Y. Shi, J. Kong, J. Lou, P. M. Ajayan, B. I. Yakobson, J. C. Idrobo. Intrinsic structural defects in monolayer molybdenum disulfide. Nano letters **13**(6), 2615-2622 (2013).

156. F. Giannazzo, M. Bosi, F. Fabbri, E. Schilirò, G. Greco, F. Roccaforte. Direct Probing of Grain Boundary Resistance in Chemical Vapor Deposition-Grown

Monolayer MoS_2 by Conductive Atomic Force Microscopy. physica status solidi (RRL)–Rapid Research Letters **14**(2), 1900393 (2020).

157. H. Yu, M. Liao, W. Zhao, G. Liu, X. J. Zhou, Z. Wei, X. Xu, K. Liu, Z. Hu, K. Deng, S. Zhou, J. A. Shi, L. Gu, C. Shen, T. Zhang, L. Du, L. Xie, J. Zhu, W. Chen, R. Yang, D. Shi, G. Zhang. Wafer-scale growth and transfer of highly-oriented monolayer MoS_2 continuous films. ACS nano **11**(12), 12001-12007 (2017).

158. D. Dumcenco, D. Ovchinnikov, K. Marinov, P. Lazic, M. Gibertini, N. Marzari, O. L. Sanchez, Y. C. Kung, D. Krasnozhon, M. W. Chen, S. Bertolazzi, P. Gillet, A. F. i Morral, A. Radenovic, A. Kis. Large-area epitaxial monolayer MoS_2. ACS nano **9**(4), 4611-4620 (2015).

159. T. A. Loh, D. H. Chua. Growth mechanism of pulsed laser fabricated few-layer MoS_2 on metal substrates. ACS applied materials & interfaces **6**(18), 15966-15971 (2014).

160. D. J. Late, P. A. Shaikh, R. Khare, R. V. Kashid, M. Chaudhary, M. A. More, S. B. Ogale. Pulsed laser-deposited MoS_2 thin films on W and Si: field emission and photoresponse studies. ACS applied materials & interfaces **6**(18), 15881-15888 (2014).

161. M. I. Serna, S. H. Yoo, S. Moreno, Y. Xi, J. P. Oviedo, H. Choi, H. N. Alshareef, M. J. Kim, M. Minary-Jolandan, M. A. Quevedo-Lopez. Large-area deposition of MoS_2 by pulsed laser deposition with in situ thickness control. Acs Nano **10**(6), 6054-6061 (2016).

162. F. Bertoldo, R. R. Unocic, Y. C. Lin, X. Sang, A. A. Puretzky, Y. Yu, D. Miakota, C. M. Rouleau, J. Schou, K. S. Thygesen, D. B. Geohegan, S. Canulescu. Intrinsic Defects in MoS_2 Grown by Pulsed Laser Deposition: From Monolayers to Bilayers. ACS nano **15**(2), 2858-2868 (2021).

163. J. Y. Tsao. Materials fundamentals of molecular beam epitaxy. Academic Press (2012).

[164.] A. Koma, K. Sunouchi, T. Miyajima. Fabrication and characterization of heterostructures with subnanometer thickness. Microelectronic Engineering **2**(1-3), 129-136 (1984).

[165.] S. Tiefenbacher, H. Sehnert, C. Pettenkofer, W. Jaegermann. Epitaxial films of WS2 by metal organic van der Waals epitaxy (MO-VDWE). Surface science **318**(1-2), L1161-L1164 (1994).

[166.] L. A. Walsh, R. Addou, R. M. Wallace, C. L. Hinkle. Molecular beam epitaxy of transition metal dichalcogenides. Molecular Beam Epitaxy (pp. 515-531). Elsevier (2018).

[167.] T. H. Choudhury, X. Zhang, Z. Y. A. Balushi, M. Chubarov, J. M. Redwing. Epitaxial growth of 2D layered transition metal dichalcogenides. arXiv preprint arXiv:1909.03502, (2019).

[168.] J. Venables. Introduction to surface and thin film processes. Cambridge University Press (2000).

[169.] S. Vishwanath, X. Liu, S. Rouvimov, L. Basile, N. Lu, A. Azcatl, K. Magno, R. M. Wallace, M. Kim, J. C. Idrobo, J. K. Furdyna, D. Jena, H. G. Xing. Controllable growth of layered selenide and telluride heterostructures and superlattices using molecular beam epitaxy. Journal of Materials Research **31**(7), 900-910 (2016).

[170.] S. Tiefenbacher, C. Pettenkofer, W. Jaegermann. Moiré pattern in LEED obtained by van der Waals epitaxy of lattice mismatched $WS_2/MoTe_2$ (0001) heterointerfaces. Surface science **450**(3), 181-190 (2000).

[171.] H. C. Diaz, Y. Ma, S. Kolekar, J. Avila, C. Chen, M. C. Asensio, M. Batzill. Substrate dependent electronic structure variations of van der Waals heterostructures of $MoSe_2$ or $MoSe_{2(1-x)}$ Te_{2x} grown by van der Waals epitaxy. 2D Materials **4**(2), 025094 (2017).

[172.] T. Hotta, T. Tokuda, S. Zhao, K. Watanabe, T. Taniguchi, H. Shinohara, R. Kitaura. Molecular beam epitaxy growth of monolayer niobium diselenide flakes. Applied Physics Letters **109**(13), 133101 (2016).

[173.] D. Fu, X. Zhao, Y. Y. Zhang, L. Li, H. Xu, A. R. Jang, S. I. Yoon, P. Song, S. M. Poh, T. Ren, Z. Ding, W. Fu, T. J. Shin, H. S. Shin, S. T. Pantelides, W. Zhou, K. P. Loh. Molecular beam epitaxy of highly crystalline monolayer molybdenum disulfide on hexagonal boron nitride. Journal of the American Chemical Society **139**(27), 9392-9400 (2017).

[174.] Q. H. Wang, K. Kalantar-Zadeh, A. Kis, J. N. Coleman, M. S. Strano. Electronics and optoelectronics of two-dimensional transition metal dichalcogenides. Nature nanotechnology **7**(11), 699-712 (2012).

[175.] F. Bonaccorso, A. Lombardo, T. Hasan, Z. Sun, L. Colombo, A. C. Ferrari. Production and processing of graphene and 2d crystals. Materials today **15**(12), 564-589 (2012).

[176.] L. Britnell, R. M. Ribeiro, A. Eckmann, R. Jalil, B. D. Belle, A. Mishchenko, Y.-J. Kim, R. V. Gorbachev, T. Georgiou, S. V. Morozov, A. N. Grigorenko, A. K. Geim, C. Casiraghi, A. H. Castro Neto, K. S. Novoselov. Strong light-matter interactions in heterostructures of atomically thin films. Science **340**(6138), 1311-1314 (2013).

[177.] M. Bernardi, M. Palummo, J. C. Grossman. Extraordinary sunlight absorption and one nanometer thick photovoltaics using two-dimensional monolayer materials. Nano letters **13**(8), 3664-3670 (2013).

[178.] C. H. Lee, G. H. Lee, A. M. Van Der Zande, W. Chen, Y. Li, M. Han, X. Cui, G. Arefe, C. Nuckolls, T. F. Heinz, J. Guo, J. Hone, P. Kim. Atomically thin p–n junctions with van der Waals heterointerfaces. Nature nanotechnology **9**(9), 676-681 (2014).

[179.] O. Lopez-Sanchez, D. Lembke, M. Kayci, A. Radenovic, A. Kis. Ultrasensitive photodetectors based on monolayer MoS_2. Nature nanotechnology **8**(7), 497-501 (2013).

[180.] J. Miao, X. Liu, K. Jo, K. He, R. Saxena, B. Song, H. Zhang, M.-G. Han, W. Hun, D. Jariwala. Gate-tunable semiconductor heterojunctions from 2D/3D van der Waals interfaces. Nano Letters **20**(4), 2907-2915 (2020).

[181.] Z. Wang, A. Hemmetter, B. Uzlu, M. Saeed, A. Hamed, S. Kataria, R. Negra, D. Neumaier, M. C. Lemme. Graphene in 2D/3D Heterostructure Diodes for High Performance Electronics and Optoelectronics, Advanced Electronics Materials **7**, 2001210 (2021).

[182.] F. Giannazzo, G. Greco, F. Roccaforte, S. S. Sonde. Vertical Transistors Based on 2D Materials: Status and Prospects, Crystals **8**, 70 (2018).

[183.] Y. Zhao, G. Ouyang, Thickness-dependent photoelectric properties of MoS_2/Si heterostructure solar cells, Scientific Reports **9**, 17381 (2019).

[184.] N. Goel, R. Kumar, M. Mishra, G. Gupta, M. Kumar, Determination of band alignment at two-dimensional MoS_2/Si van der Waals Heterojunction, Journal of Applied Physics **123**, 225301 (2018).

[185.] O. Lopez-Sanchez, E. Alarcon Llado, V. Koman, A. Fontcuberta i Morral, A. Radenovic, A. Kis. Light generation and harvesting in a van der Waals heterostructure. Acs Nano **8**(3), 3042-3048 (2014).

[186.] M. N. Yoder. Wide bandgap semiconductor materials and devices. IEEE Transactions on Electron Devices **43**(10), 1633-1636 (1996).

[187.] K. Takahashi, A. Yoshikawa, A. Sandhu. Wide bandgap semiconductors. Verlag Berlin Heidelberg (2007).

[188.] J. Millan, P. Godignon, X. Perpiñà, A. Pérez-Tomás, J. Rebollo. A survey of wide bandgap power semiconductor devices. IEEE transactions on Power Electronics **29**(5), 2155-2163 (2013).

[189.] A. A. Burk Jr, M. J. O'Loughlin, R. R. Siergiej, A. K. Agarwal, S. Sriram, R. C. Clarke, M. F. MacMillan, V. Balakrishna, C. D. Brandt. SiC and GaN wide bandgap semiconductor materials and devices. Solid-State Electronics **43**(8), 1459-1464 (1999).

[190.] F. Roccaforte, P. Fiorenza, G. Greco, R. Lo Nigro, F. Giannazzo, F. Iucolano, M. Saggio. Emerging trends in wide band gap semiconductors (SiC and GaN) technology for power devices. Microelectronic Engineering **187**, 66-77 (2018).

[191.] T. Kimoto, J. A. Cooper. Fundamentals of silicon carbide technology: growth, characterization, devices and applications. John Wiley & Sons (2014).

[192.] C. Y. Huang, C. Chang, G.-Z. Lu, W.-C. Huang, C.-S. Huang, M.-L. Chen, T.-N. Lin, J.-L. Shen, T.-Y. Lin, Hybrid 2D/3D MoS_2/GaN heterostructures for dual functional photoresponse, Applied Physics Letters **112**, 233106 (2018).

[193.] M. Moun, R. Singh, Exploring conduction mechanism and photoresponse in p-GaN/n-MoS_2 heterojunction diode. Journal of Applied Physics **127**, 135702 (2020).

[194.] S. K. Jain, R. R. Kumar, N. Aggarwal, P. Vashishtha, L. Goswami, S. Kuriakose, A. Pandey, M. Bhaskaran, S. Walia, G. Gupta, Current Transport and Band Alignment Study of MoS_2/GaN and MoS_2/AlGaN Heterointerfaces for Broadband Photodetection Application, ACS Applied Electronic Materials **2**, 710−718 (2020).

[195.] M. Moun, M. Kumar, M. Garg, R. Pathak, R. Singh, Understanding of MoS_2/GaN heterojunction diode and its photodetection properties, Scientific Reports **8**, 1-10 (2018).

[196.] S. Krishnamoorthy, E. W. Lee, C. H. Lee, Y. Zhang, W. D. McCulloch, J. M. Johnson, J. Hwang, Y. Wu, S. Rajan. High current density 2D/3D MoS_2/GaN Esaki tunnel diodes, Applied Physics Letters **109**(18), 183505 (2016).

[197.] H. Jeong, S. Bang, H. M. Oh, H. J. Jeong, S.-J. An, G. H. Han, H. Kim, K. K. Kim, J. C. Park, Y. H. Lee, G. Lerondel, M. S. Jeong, Semiconductor Insulator Semiconductor Diode Consisting of Monolayer MoS_2, h-BN, and GaN Heterostructure, ACS Nano **9**, 10032–10038 (2015).

[198.] D. Ruzmetov, K. Zhang, G. Stan, B. Kalanyan, G. R. Bhimanapati, S. M. Eichfeld, R. A. Burke, P. B. Shah, T. P. O'Regan, F. J. Crowne, A. G. Birdwell, J. A. Robinson, A. V. Davydov, T. G. Ivanov, Vertical 2D/3D Semiconductor Heterostructures Based on Epitaxial Molybdenum Disulfide and Gallium Nitride. ACS Nano **10**, 3580−3588 (2016).

[199.] T. P. O'Regan, D. Ruzmetov, M. R. Neupane, R. A. Burke, A. A. Herzing, K. Zhang, A. G. Birdwell, D. E. Taylor, E. F. C. Byrd, S. D. Walck, A. V. Davydov, J. A. Robinson, T. G. Ivanov, Structural and electrical analysis of epitaxial 2D/3D vertical heterojunctions of monolayer MoS_2 on GaN, Applied Physics Letters **111**, 051602 (2017).

[200.] D. Ruzmetov, K. Zhang, G. Stan, B Kalanyan, G. Bhimanapati, S.M. Eichfeld, R.A. Burke, P.B. Shah, T.P. O'Regan, F.J. Crowne, A.G. Birdwell, J.A. Robinson, A.V. Davydov, T.G. Ivanov. Vertical 2D/3D semiconductor heterostructures based on epitaxial molybdenum disulfide and gallium nitride, ACS Nano **10**, 3580–3588 (2016).

[201.] Y. Xiao, L. Min, X. Liu, W. Liu, U. Younis, T. Peng, X. Kang, X. Wu, S. Ding, D. W. Zhang, Facile integration of MoS_2/SiC photodetector by direct chemical vapor deposition, Nanophotonics **9**, 3035–3044 (2020).

[202.] E. W. Lee II, L. Ma, D. N. Nath, C. H. Lee, A. Arehart, Y. Wu, S. Rajan. Growth and electrical characterization of two-dimensional layered MoS_2/SiC heterojunctions, Applied Physics Letters **105**, 203504 (2014).

[203.] C. R. Serrao, A. M. Diamond, S.-L. Hsu, L. You, S. Gadgil, J. Clarkson, C. Carraro, R. Maboudian, C. Hu, S. Salahuddin, Highly crystalline MoS_2 thin films grown by pulsed laser deposition, Applied Physics Letters **106**, 052101 (2015).

[204.] E. W. Lee, L. Ma, D. N. Nath, C. H. Lee, A. Arehart, Y. Wu, S. Rajan. Growth and electrical characterization of two-dimensional layered MoS_2/SiC heterojunctions. Applied Physics Letters **105**(20), 203504 (2014).

[205.] Z. Zhang, Q. Qian, B. Li, K. J. Chen, Interface Engineering of Monolayer MoS_2/GaN Hybrid Heterostructure: Modified Band Alignment for Photocatalytic Water Splitting Application by Nitridation Treatment. ACS Applied Materials & Interfaces **10**, 17419−17426 (2018).

[206.] M. Tangi, P. Mishra, T. K. Ng, M. N. Hedhili, B. Janjua, M. S. Alias, D. H. Anjum, C.-C. Tseng, Y. Shi, H. J. Joyce, L.-J. Li, B. S. Ooi, Determination of

band offsets at GaN/single-layer MoS_2 heterojunction. Applied Physics Letters **109**, 032104 (2016).

207. P. O. Oviroh, R. Akbarzadeh, D. Pan, R. A. M. Coetzee, T. C. Jen. New development of atomic layer deposition: processes, methods and applications. Science and technology of advanced materials **20**(1), 465-496 (2019).

208. E. Schilirò, R. Lo Nigro, F. Roccaforte, F. Giannazzo. Substrate-Driven Atomic Layer Deposition of High-κ Dielectrics on 2D Materials. Applied Sciences **11**(22), 11052 (2021).

209. A. Azcatl, S. McDonnell, S. KC, X. Peng, H. Dong, X. Qin, R. Addou, G. I. Mordi, N. Lu, J. Kim, M. J. Kim, K. Cho, R. M. Wallace. MoS_2 functionalization for ultra-thin atomic layer deposited dielectrics. Applied Physics Letters **104**(11), 111601 (2014).

210. S. McDonnell, B. Brennan, A. Azcatl, N. Lu, H. Dong, C. Buie, J. Kim, C. L. Hinkle, M. J. Lee, R. M. Wallace. HfO_2 on MoS_2 by atomic layer deposition: adsorption mechanisms and thickness scalability. ACS Nano **7**(11), 10354-10361 (2013).

211. M. Hegner, P. Wagner, G. Semenza. Ultralarge Atomically Flat Template-Stripped Au Surfaces for Scanning Probe Microscopy. Surface Science **291**, 39–46 (1993).

212. N. Vogel, J. Zieleniecki, I. Köper. As Flat as it Gets: Ultrasmooth Surfaces from Template-stripping Procedures. Nanoscale **4**, 3820–3832 (2012).

213. Y. Zhan, Z. Liu, S. Najmaei, P. M. Ajayan, J. Lou. Large-Area Vapor-Phase Growth and Characterization of MoS_2 Atomic Layers on a SiO_2 Substrate. Small **8**(7), 966-971 (2012).

214. J. Xu, L. Chen, Y.-W. Dai, Q. Cao, Q.-Q. Sun, S.-J. Ding, H. Zhu, D. W. Zhang. A two-dimensional semiconductor transistor with boosted gate control and sensing ability. Science Advances **3**, e1602246 (2017).

215. S. E. Panasci, E. Schilirò. G. Greco, M. Cannas, F. M. Gelardi, S. Agnello, F. Roccaforte, F. Giannazzo. Strain, Doping and electronic transport of large area

monolater MoS_2 exfoliated on gold and transferred to an insulating substrate. ACS Applied Materials & Interfaces **13**, 31248-31259 (2021).

216. A. Michail, N. Delikoukos, J. Parthenios, C. Galiotis, K. Papagelis. Optical detection of strain and doping inhomogeneities in single layer MoS_2. Applied Physics Letters **108**(17), 173102 (2016).

217. A. McCreary, R. Ghosh, M. Amani, J. Wang, K. A. N. Duerloo, A. Sharma, K. Jarvis, E. J. Reed, A. M. Dongare, S. K. Banerjee, M. Terrones, R. R. Namburu, M. Dubey. Effects of Uniaxial and Biaxial Strain on Few-Layered Terrace Structures of MoS_2 Grown by Vapor Transport. ACS Nano **10**, 3186-3197 (2016).

218. J. E. Lee, G. Ahn, J. Shim, Y. S. Lee, S. Ryu. Optical Separation of Mechanical Strain From Charge Doping in Graphene. Nature communications **3**(1), 1-8 (2012).

219. A. Armano, G. Buscarino, M. Cannas, F. M. Gelardi, F. Giannazzo, E. Schilirò, S. Agnello. Monolayer Graphene Doping and Strain Dynamics Induced by Thermal Treatments in Controlled Atmosphere. Carbon **127**, 270-279 (2018).

220. Ch. Androulidakis, G. Tsoukleri, N. Koutroumanis, G. Gkikas, P. Pappas, J. Parthenios, K. Papagelis, C. Galiotis. Experimentally Derived Axial Stress–Strain Relations for Two-Dimensional Materials such as Monolayer Graphene. Carbon **81**, 322-328 (2015).

221. E. Schilirò, R. Lo Nigro, S. E. Panasci, F. M. Gelardi, S. Agnello, R. Yakimova, F. Roccaforte, F. Giannazzo. Aluminum Oxide Nucleation in the Early Stages of Atomic Layer Deposition on Epitaxial Graphene. Carbon **169**, 172-181 (2020).

222. R. Rao, A. E. Islam, S. Singh, R. Berry, R. K. Kawakami, B. Maruyama, J. Katoch. Spectroscopic Evaluation of Charge-Transfer Doping and Strain in Graphene/MoS_2 Heterostructures. Physical Review B **99**, 195401 (2019).

223. A. Jorio, M. S. Dresselhaus, R. Saito, G. Dresselhaus. Raman Spectroscopy in Graphene Related Systems. John Wiley & Sons (2011).

224. C. Gong, C. Huang, J. Miller, L. Cheng, Y. Hao, D. Cobden, J. Kim, R. S. Ruoff, R. M. Wallace, K. Cho, X. Xu, Y. J. Chabal. Metal Contacts on Physical Vapor Deposited Monolayer MoS_2. ACS Nano **7**, 11350−11357 (2013).

225. S. G. Sørensen, H. G. Füchtbauer, A. K. Tuxen, A. S. Walton, J. V. Lauritsen. Structure and Electronic Properties of In Situ Synthesized Single-Layer MoS2 on a Gold Surface. ACS Nano **8**, 6788−6796 (2014).

226. A. K. Singh, R. K. Pandey, R. Prakash, J. Eom, Tailoring the Charge Carrier in Few Layers MoS_2 Field-Effect Transistors by Au Metal Adsorbate, Applied Surface Science **437**, 70–74 (2018).

227. H. Liu, D. Grasseschi, A. Dodda, K. Fujisawa, D. Olson, E. Kahn, F. Zhang, T. Zhang, Y. Lei, R. B. N. Branco, A. L. Elías, R. C. Silva, Y.-T. Yeh, C. M. Maroneze, L. Seixas, P. Hopkins, S. Das, C. J. S. de Matos, M. Terrones. Spontaneous Chemical Functionalization Via Coordination of Au Single Atoms on Monolayer MoS_2, Science Advances **6**, abc9308 (2020).

228. X. Liu, D. Qu, J. Ryu, F. Ahmed, Z. Yang, D. Lee, W. J. Yoo. P-Type Polar Transition of Chemically Doped Multilayer MoS_2 Transistor, Advanced Materials **28**, 2345–2351 (2016).

229. F. Giannazzo, G. Fisichella, A. Piazza, S. Agnello, F. Roccaforte. Nanoscale inhomogeneity of the Schottky barrier and resistivity in MoS_2 multilayers. Physical Review B **92**, 081307(R) (2015).

230. A. Bruix, J. A. Miwa, N. Hauptmann, D. Wegner, S. Ulstrup, S. S. Grønborg, C. E. Sanders, M. Dendzik, A. Grubisic Cabo, M. Bianchi, J. V. Lauritsen, A. A. Khajetoorians, B. Hammer, P. Hofmann. Single-layer MoS_2 on Au (111): Band gap renormalization and substrate interaction. Physical Review B **93**, 165422 (2016).

231. U. Bhanu, M. R. Islam, L. Tetard, S. I. Khondaker. Photoluminescence Quenching in Gold-MoS_2 Hybrid Nanoflakes. Scientific Reports **4**, 5575 (2014).

232. A. Molina-Sánchez, D. Sangalli, K. Hummer, A. Marini, L. Wirtz. Effect of spin-orbit interaction on the optical spectra of single-layer, double-layer, and bulk MoS_2. Physical Review B **88**, 045412 (2013).

233. K. Kheng, R. T. Cox, M. Y. d'Aubigné, F. Bassani, K. Saminadayar, S. Tatarenko. Observation of negatively charged excitons X^- in semiconductor quantum wells. Physical Review Letters **71**, 1752 (1993).

234. N. Scheuschner, O. Ochedowski, A. M. Kaulitz, R. Gillen, M. Schleberger, J. Maultzsch. Photoluminescence of freestanding single-and few-layer MoS_2. Physical Review B **89**, 125406 (2014).

235. M. Drüppel, T. Deilmann, P. Krüger, M. Rohlfing. Diversity of trion states and substrate effects in the optical properties of an MoS_2 monolayer. Nature Communication **8**, 1-7 (2017).

236. Y. V. Zhumagulov, A. Vagov, D. R. Gulevich, P. E. Faria Junior, V. Perebeinos. Trion induced photoluminescence of a doped MoS_2 monolayer Journal of Chemical Physics **153**, 044132 (2020).

237. H. Lee, S. Deshmukh, J. Wen, V. Z. Costa, J. S. Schuder, M. Sanchez, A. S. Ichimura, E. Pop, B. Wang, A. K. M. Newaz. Layer-Dependent Interfacial Transport and Optoelectrical Properties of MoS_2 on Ultraflat Metals, ACS Applied Materials & Interfaces **11**, 31543–31550 (2019).

238. A. Krayev, C. S. Bailey, K. Jo, S. Wang, A. Singh, T. Darlington, G.-Y. Liu, S. Gradecak, P. J. Schuck, E. Pop, D. Jariwala. Dry Transfer of van der Waals Crystals to Noble Metal Surfaces To Enable Characterization of Buried Interfaces, ACS Applied Materials & Interfaces **11**, 38218−38225 (2019).

239. F. Giannazzo, E. Schilirò, G. Greco, F. Roccaforte. Conductive Atomic Force Microscopy of Semiconducting Transition Metal Dichalcogenides and Heterostructures, Nanomaterials **10**, 803 (2020).

240. D. Fu, J. Zhou, S. Tongay, K. Liu, W. Fan, T.-J. K. Liu, J. Wu. Mechanically Modulated Tunneling Resistance in Monolayer MoS_2, Applied Physics Letters **103**, 183105 (2013).

241. T. Cheiwchanchamnangij, W.R.L. Lambrecht. Quasiparticle Band Structure Calculation of Monolayer, Bilayer, and Bulk MoS_2, Physical Review B **85**, 205302, 2012.

242. T. Komesu, D. Le, I. Tanabe, E. F. Schwier, Y. Kojima, M. Zheng, K. Taguchi, K. Miyamoto, T. Okuda, H. Iwasawa, K. Shimada, T. S. Rahman, P. A. Dowben. Adsorbate doping of MoS_2 and WSe_2: the influence of Na and Co. Journal of Physics: Condensed Matter **29**, 285501 (2017).

243. A. R. Bechhofer, A. Ueda, A. Nipane, J. T. Teherani. The 2D Debye length: An analytical study of weak charge screening in 2D semiconductors, Journal of Applied Physics **129**, 024301 (2021).

244. P. Vancsó, G. Z. Magda, J. Pető, J.-Y. Noh, Y.-S. Kim, C. Hwang, L. P. Biró, L. Tapasztó. The intrinsic defect structure of exfoliated MoS_2 single layers revealed by Scanning Tunneling Microscopy, Scientific Reports **6**, 29726 (2016).

245. G. Fisichella, S. Di Franco, F. Roccaforte, S. Ravesi, F. Giannazzo. Microscopic mechanisms of graphene electrolytic delamination from metal substrates, Applied Physics Letters **104**, 233105 (2014).

246. Y. Gao, Z. Liu, D.-M. Sun, L. Huang, L.-P. Ma, L.-C. Yin, T. Ma, Z. Zhang, X.-L. Ma, L.-M. Peng, H.-M. Cheng, W. Ren. Large-area synthesis of high-quality and uniform monolayer WS_2 on reusable Au foils. Nature Communications **6**, 8569 (2015).

247. E. Schilirò, R. Lo Nigro, S. E. Panasci, S. Agnello, M. Cannas, F. M. Gelardi, F. Roccaforte, F. Giannazzo. Direct Atomic Layer Deposition of Ultrathin Aluminum Oxide on Monolayer MoS_2 Exfoliated on Gold: The Role of the Substrate. Advanced Materials & Interfaces **8**, 2101117 (2021).

248. S. Bhattacharjee, E. Caruso, N. McEvoy, C. Ó. Coileáin, K. O'Neill, L. Ansari, G. S. Duesberg, R. Nagle, K. Cherkaoui, F. Gity, P. K. Hurley, Insights into Multilevel Resistive Switching in Monolayer MoS_2, ACS Applied Materials & Interfaces **12**, 6022−6029 (2020).

[249.] S. E. Panasci, E. Schilirò, F. Migliore, M. Cannas, F. M. Gelardi, F. Roccaforte, F. Giannazzo, S. Agnello. Substrate impact on the thickness dependence of vibrational and optical properties of large area MoS_2 produced by gold-assisted exfoliation. Applied Physics Letters **119**(9), 093103 (2021).

[250.] E. Schilirò, P. Fiorenza, C. Bongiorno, C. Spinella, S. Di Franco, G. Greco, R. Lo Nigro, F. Roccaforte, Correlating electron trapping and structural defects in Al_2O_3 thin films deposited by plasma enhanced atomic layer deposition, AIP Advances **10**, 125017 (2020).

[251.] W. Li, J. Zhou, S. Cai, Z. Yu, J. Zhang, N. Fang, T. Li, Y. Wu, T. Chen, X. Xie, H. Ma, K. Yan, N. Dai, X. Wu, H. Zhao, Z. Wang, D. He, L. Pan, Y. Shi, P. Wang, W. Chen, K. Nagashio, X. Duan, X. Wang, Uniform and ultrathin high-κ gate dielectrics for two-dimensional electronic devices. Nature Electronics **2**, 563–571 (2019).

[252.] S. E. Panasci, A. Koos, E. Schilirò, S. Di Franco, G. Greco, P Fiorenza, F. Roccaforte, S. Agnello, M. Cannas, F. M. Gelardi, A. Sulyok, M. Nemeth, B. Pécz, F. Giannazzo, Multiscale Investigation of the Structural, Electrical and Photoluminescence Properties of MoS_2 Obtained by MoO_3 Sulfurization, Nanomaterials **12**, 182 (2022).

[253.] Y. Liu, J. Guo, E. Zhu, L. Liao, S.-J. Lee, M. Ding, I. Shakir, V Gambin, Y Huang, X. Duan, Approaching the Schottky–Mott limit in van der Waals metal–semiconductor junctions, Nature **557**, 696 (2018).

[254.] Y. Wang, J. C. Kim, R. J. Wu, J. Martinez, X. Song, J. Yang, F. Zhao, A. Mkhoyan, H. Y. Jeong, M. Chhowalla, Van der Waals contacts between three-dimensional metals and two-dimensional semiconductors, Nature **568**, 70 (2019).

[255.] A. Laturia, M. L. Van de Put, W. G. Vandenberghe, Dielectric properties of hexagonal boron nitride and transition metal dichalcogenides: from monolayer to bulk, npj 2D Materials and Applications **2**, 6 (2018).

256. S. M. Sze, K. K. Ng, Physics of semiconductor devices, 3r Ed., John Wiley & Sons (2007).

257. U. Celano. Electrical Atomic Force Microscopy for Nanoelectronics, Springer International Publishing (2019).

Curriculum Vitae

Personal Information

Surname	Panasci
Name	Salvatore Ethan
Date of Birth	1992, January, 27
Nationality	Italian
E-mail	salvoethanpanasci@libero.it

Education

2022, December	PhD in Material Science and Nanotechnology at University of Catania. **Thesis**: *Molybdenum disulfide heterostructures: preparation and electronic transport.* **Tutors**: Dr. Filippo Giannazzo; Prof. Franco Gelardi; Prof. Simonpietro Agnello.
2020, September	NanoInnovation2020: School on Scanning Probe Microscopy and on Nanotechnologies.
2019, October	Master's Degree in Material Science and nanotechnology at University of Padova. **Thesis**: *Two-dimensional ordered nanostructure arrays for plasmonic nanolaser devices.* **Supervisors**: Prof. Tiziana Cesca; Prof. Giovanni Mattei. (Evaluation 109/110)

2017, March	Bachelor's Degree in Physics at University of Palermo **Thesis**: *Studio in situ del processo fotocatalitico indotto da nanoparticelle di TiO_2.* **Supervisor**: Prof. Simonpietro Agnello
2011-2012	Bachelor's Degree in Astronomy at University of Bologna. not completed.
2011, June	Scientific High School Stanislao Cannizzaro of Palermo, Italy. (Evaluation 94/100)

List of PhD courses

Name of the course	**Professor**	**CFU**
Tecniche numeriche di simulazione	Prof. Piccitto	3
Basic physics of Semiconductors	Prof. Mirabella	3
Advanced synthetic methodologies for thin film and monolayer	Prof. Malandrino	2
Ion beam modification and analysis of materials	Prof. Mirabella	2
Scanning Probe Microscopies	Prof. Ruffino	2
Spectroscopic techniques for materials characterization	Prof. Reitano	2

Conferences

Oral presentation: "**Strain, doping and electronic properties of large area MoS_2 exfoliated on gold substrates**", E-MRS Spring Meeting 2021, virtual conference, 31 May- 4 June 2021.

Oral presentation: "**Structural and electrical properties of ultra-thin MoS_2 films obtained by MoO_3 sulfurization on SiO_2, sapphire and 4H-SiC**", E-MRS Fall Meeting 2022, Warsaw, 18^{th} – 23^{th} September 2022.

Awards

Best student award E-MRS Fall Meeting Symposium G: "New frontiers in wide band-gap semiconductors and heterostructures for electronics, optoelectronics and sensing".

Reviewer activities

Reviewer activities have been carried out for the following journals:

- Micro and Nanostructures (I. F. 2.658)
- IEEE Transactions on Electron Devices (I. F. 3.319)
- ACS Applied Materials & Interfaces (I. F. 9.229)

List of Publications

[1] F. Giannazzo, R. Dagher, E. Schilirò, **S. E. Panasci**, G. Greco, G. Nicotra, F. Roccaforte, S. Agnello, J. Brault, Y. Cordier, A. Michon. Nanoscale structural and electrical properties of graphene grown on AlGaN by catalyst-free chemical vapor deposition. Nanotechnology, 32(1), 015705, 2020.

[2] E. Schilirò, R. Lo Nigro, **S. E. Panasci**, F. M. Gelardi, S. Agnello, R. Yakimova,F. Roccaforte, F. Giannazzo. Aluminum oxide nucleation in the early stages of atomic layer deposition on epitaxial graphene. Carbon, 169, 172-181, 2020.

[3] L. Seravalli, M. Bosi, P. Fiorenza, **S. E. Panasci**, D. Orsi, E. Rotunno, L. Cristofolini, F. Rossi, F. Giannazzo, F. Fabbri. Gold nanaparticles assisted synthesis of MoS_2 monolayers by chemical vapor deposition. Nanoscale Advances, 3(16), 4826-2833, 2021.

[4] **S. E. Panasci**, E. Schilirò, G. Greco, M. Cannas, F. M. Gelardi, S. Agnello, F. Roccaforte, F. Giannazzo. Strain, Doping, and Electronic Transport of Large Area Monolayer MoS_2 Exfoliated on Gold and Transferred to an Insulating Substrate. ACS Applied Materials & Interfaces, 13(26), 31248-31259, 2021.

[5] **S. E. Panasci**, E. Schilirò, F. Migliore, M. Cannas, F. M. Gelardi, F. Roccaforte, F. Giannazzo, S. Agnello. Substrate impact of the thickness dependence of vibrational and optical properties of large area MoS_2 produced by gold-assisted exfoliation. Applied Physics Letters, 119(9), 093103, 2021.

[6] E. Schilirò, R. Lo Nigro, **S. E. Panasci**, S. Agnello, M. Cannas, F. M. Gelardi, F. Roccaforte, F. Giannazzo. Direct Atomic Layer Deposition of Ultrathin Aluminum Oxide on Monolayer MoS_2 Exfoliated on Gold: The Role of the Substrate. Advanced Materials Interfaces, 8(21), 2101117, 2021

[7] **S. E. Panasci**, A. Koos, E. Schilirò, S. Di Franco, G. Greco, P. Fiorenza, F. Roccaforte, S. Agnello, M. Cannas, F. M. Gelardi, A. Sulyok, M. Nemeth, B. Pécz, F. Giannazzo. Multiscale Investigation of the Structural, Electrical and Photoluminescence Properties of MoS_2 obtained by MoO_3 sulfurization. Nanomaterials, 12(2), 182, 2022.

[8] F. Giannazzo, **S. E. Panasci**, E. Schilirò, F. Roccaforte, A. Koos, M. Nemeth, B. Pécz. Esaki Diode Behavior in Highly Uniform MoS_2/Silicon Carbide Heterojunctions. Advanced Materials Interfaces 9, 2200915, 2022.

[9] **S. E. Panasci**, A. Alessi, G. Buscarino, M. Cannas, F. M. Gelardi, E. Schilirò, F. Giannazzo, S. Agnello. Electron irradiation effects on single layer MoS_2 obtained by gold assisted exfoliation. Physica Status Solidi (a), 2200096, 2022. DOI: 10.1002/pssa.202200096.

[10] M. Vivona, F. Giannazzo, G. Bellocchi, **S. E. Panasci**, S. Agnello, P. Badala, A. Bassi, C. Bongiorno, S. Di Franco, S. Rascunà, F. Roccaforte. Effects of excimer laser irradiation on the morphological, structural and electrical properties of Aluminum-implanted 4H-SiC. ACS Applied Electronic Materials, 4(9), 4514, 2022. DOI: 10.1021/acsaelm.2c00748.

[11] F. Giannazzo, **S. E. Panasci**, E. Schilirò, P. Fiorenza, G. Greco, F. Roccaforte, M. Cannas, S. Agnello, A. Koos, B. Pécz, M. Spankova, S. Chromik. Highly homogeneous 2D/3D heterojunction diodes by pulsed laser deposition of MoS_2 on ion implantation doped 4H-SiC. Advanced Materials Interfaces, 2201502, 2022. DOI: 10.1002/admi.202201502

Acknowledgements

These research activities were carried out into the PhD course in Materials Science and Nanotechnology of the University of Catania, and supported by the Epitaxial Transition dichalcogenides onto wide band gap hexagonal Semiconductors for advanced electronics (ETMOS) project, funding within the FlagEra 2019 "Graphene- Applied research and innovation" transnational call for proposals coordinated by CNR-IMM.

The PhD course was splitted in two consequential phases. The first was centred on the academic formation conducted at the Chemistry Department of the University of Catania. The second phase regarding the research activity, has been carried out entirely at the Microelectronics and Microsystems Institution of CNR (CNR-IMM) laboratories of Catania and at the Physics and Chemistry Department of the University of Palermo.

First of all, I would like to thank Dr. Filippo Giannazzo, my CNR-IMM Supervisor, for the trust, the support, the teachings, the great opportunities he gave me, and the transmitted passion for the research activity. He is inspiring me both professionally and humanly. I'm honoured to have known him. Indeed, I would like to thank my University Tutor, Prof. Franco Gelardi of the University of Palermo, for the help and the advice given during my PhD course. I would like to thank Prof. Simonpietro Agnello, who believed in me since the bachelor's degree and for bringing me in this world, I'll be forever grateful.

I would give thanks to each member of the CNR-IMM group to which I belong. I would thank Dr. Fabrizio Roccaforte, whose leadership, determination, sympathy and passion are basic resources to guide the entire group. A special thank goes to Dr. Salvo Di Franco, support, and reference column for the entire Institute, for the patience he had, and the advice given in Clean Room. A big thank goes to Dr. Emanuela Schilirò, for the enormous patience and help, and from which I draw inspiration for the tenacity and determination to pursuing a purpose. I would thank Dr. Giuseppe Greco for the advice, the great sympathy and the exciting football matches. Thanks also to Dr. Marilena Vivona, for the advice and the kindness who showed me since the first PhD day. Indeed, I would thank Dr. Patrick Fiorenza, for the advice, the sympathy and the enormous help with the electrical characterizations. I would thank also Dr. Raffaella Lo Nigro, for the kindness and the help given to me.

In the end, I would thank Bruno Galizia, to whom I wish the best for the continuation of his PhD course.

I give thanks the previous Director Dr. Guglielmo Fortunato, and Dr. Vittorio Privitera, present Director of CNR-IMM, for the opportunity to carry out the research activities at CNR-IMM of Catania.

I would thank all the ETMOS partners: Prof. Béla Pécz, Dr. Antal Koos, Dr. Miklos Nemeth, Prof. Štefan Chromik, Dr. Marianna Španková, Dr. Antonino La Magna, Prof. Marco Cannas, Dr. Adrien Michon, Dr. Yvon Cordièr, Dr. Mohamed Al Khalfioui and Chiara Mastropasqua.

I would thanks Dr. Antonio Mio, Dr. Gianfranco Sfuncia and Dr. Giuseppe Nicotra for the TEM analysis carried out at CNR-IMM of Catania.

A special thank goes to all my friends in the world of science and not only: Salvo Valastro, Annalisa Cannizzaro, Alessandro Meli, Mattia Pizzone and all the XXXV cycles PhD students. Thanks to all the colleagues of MP8 boxes: Corrado Bongiorno and Emanuele Smecca. I would like to thank also Monia Spera, who helped me since the first day in Catania, and Seby Caccamo, Inàki Garcia-Lopez and Giuseppe Caruso for the sympathy and the rides on the football fields.

I would thank my wonderful group in Palermo: Anna, Chiara, Daniele, Dario, Francesco, Paolo, Roberta, RLG, Riccardo L, Rosi, to be always there and show me every day how much they care about me. I will always be there for you. A big thank goes also to all my friends in Palermo: Enrico, Gabriele, Giuseppe F., Giulio, Gowsi, Lupo, Sofia C., you are always present in my life.

I would thank my friend in the magic Padova: Diego, Domenico, Ionut, Mario and Valerio, to share everything, despite time and distances. I'm grateful to have known you and to share with you an important part of my life.

I would thank my Padova family: Ignazio, Ivan, Marialaura, Mary and Tony, because of them, I reached my master's degree but also the future that has ensued. I will always be grateful for what you have done for me.

I would thank my new friends in Catania: Chiara, Davide, Daniele C., Daniele M., Federica A., Federica F., Giulia M., Marco, Martina, Seby S., for giving me a home and welcoming me in the big Controvento's family.

I would thank my family: my father, my mother, my sister and Lupetta, for supporting me in both in the darkest night and in the brightest days. I would thank

you for giving me confidence and freedom of choice. I would thank you for showing me the Music, that will be always a haven in the joys and sorrows of life. In the end, I would thank you for teaching me the greatest of the resources that I find in me: the will to rise again and to overcome my limits.

Finally, I would thank Angelica, for all the things she does for me, despite all. Thank to be my best friend, my biggest power and my biggest resource. I'll get better and grow with and for you, always.

In conclusion, a particular thing goes to everyone like me, that will have failed several times in life, and then rise with a little more awareness. To you, I advise to getting up and smiling, because failures are the biggest lessons of life. There is not greater victory.

Ringraziamenti

Queste attività di ricerca sono state svolte all'interno del corso di Dottorato in Scienza dei materiali e Nanotecnologie dell'Università di Catania e supportato dal progetto Epitaxial Transition Metal dichalcogenides onto wide band gap hexagonal Semiconductors for advanced electronics (ETMOS) finanziato nell'ambito del bando transnazionale FlagERA 2019 "Grafene - Ricerca applicata e innovazione" coordinato dal CNR-IMM.

Il percorso di Dottorato è stato suddiviso in due fasi consequenziali. La prima fase è stata incentrata sulla formazione accademica svolta presso il Dipartimento di Chimica dell'Università di Catania. La seconda fase riguardo l'attività di ricerca, è stata svolta interamente presso i laboratori dell'Istituto di Microelettronica e Microsistemi del CNR (CNR-IMM) di Catania.

Voglio ringraziare il mio Supervisore del CNR-IMM, il Dr. Filippo Giannazzo, per la fiducia, il supporto, gli insegnamenti, la passione trasmessa per la ricerca e le grandi opportunità che mi ha dato. Sono onorato di averlo conosciuto. È e sarà sempre fonte di ispirazione sia dal punto di vista umano che professionale. Inoltre, voglio ringraziare il Prof. Franco Gelardi dell'Università di Palermo e Tutor Universitario per il confronto e i consigli dati durante il percorso di dottorato. Voglio ringraziare il Prof. Simonpietro Agnello per aver creduto in me fin dalla prima tesi di laurea triennale e per avermi introdotto in questo mondo, ne sarò grato per sempre.

Voglio dedicare inoltre dei ringraziamenti a ciascun membro del gruppo di ricerca a cui appartengo. Voglio ringraziare il Dr. Fabrizio Roccaforte, la cui leadership, determinazione, simpatia e passione sono risorse fondamentali per guidare l'intero gruppo di ricerca. Un ringraziamento speciale va al Dr. Salvo Di Franco, colonna portante e riferimento per l'intero istituto, per la pazienza che ha avuto e gli insegnamenti dati in Clean Room. Un grande grazie va alla Dr.ssa Emanuela Schilirò, per l'enorme pazienza e aiuto, e dalla quale traggo ispirazione per la tenacia e la determinazione nell'inseguire un obiettivo. Ringrazio anche il Dr. Giuseppe Greco per i consigli, la grande simpatia e le entusiasmanti partite a calcetto. Un ringraziamento va anche alla Dr.ssa Marilena Vivona per i consigli e la gentilezza che mi ha mostrato fin dal primo giorno di dottorato. Ringrazio inoltre il Dr. Patrick Fiorenza per i consigli, la simpatia e l'enorme aiuto con le misure elettriche. Ringrazio anche la Dr.ssa Raffaella Lo Nigro per la gentilezza e l'aiuto che mi ha dato. Ringrazio infine Bruno Galizia, a cui auguro il meglio per il proseguimento del suo percorso di Dottorato.

Ringrazio il precedente Direttore Dr. Guglielmo Fortunato, e Dr. Vittorio Privitera, attuale Direttore del CNR-IMM, per l'opportunità di poter svolgere le attività di ricerca presso la sede CNR-IMM di Catania.

Un ringraziamento va anche a tutti i partner del Progetto ETMOS: Prof. Béla Pécz, Dr. Antal Koos, Dr. Miklos Nemeth, Prof. Štefan Chromik, Dr. Marianna Španková, Dr. Antonino La Magna, Prof. Marco Cannas, Dr. Adrien Michon, Dr. Yvon Cordièr, Dr. Mohamed Al Khalfioui e Chiara Mastropasqua.

Vorrei ringraziare Dr. Antonio Mio, Dr. Gianfranco Sfuncia e Dr. Giuseppe Nicotra per le analisi TEM realizzate presso il CNR-IMM di Catania.

Un grazie speciale ai miei compagni di avventure nel mondo della Scienza e non solo: Salvo Valastro, Annalisa Cannizzaro, Alessandro Meli, Mattia Pizzone e a tutti i dottorandi del XXXV ciclo. Ai colleghi del CNR dei box in MP8: Corrado Bongiorno e Emanuele Smecca. Ringrazio anche Monia Spera per il grande aiuto che mi ha dato fin dai primi giorni a Catania e Seby Caccamo, Inaki Garcia-Lopez e Giuseppe Caruso per la simpatia e le cavalcate sui campi di calcio.

Vorrei ringraziare il mio fantastico gruppo di Palermo: Anna, Chiara, Daniele, Dario, Francesco, Paolo, Roberta, RLG, Riccardo L., Rosi, per esserci sempre e per dimostrarmi ogni giorno quanto tengano a me. Ci sarò sempre per voi. Un enorme grazie anche agli altri miei amici di Palermo: Enrico, Gabriele, Giuseppe F., Giulio, Gowsi, Lupo e Sofia C., siete sempre presenti nella mia vita.

Vorrei ringraziare gli amici della magica Padova: Diego, Domenico, Ionut, Mario e Valerio, per condividere tutto nonostante il tempo e le distanze. Sono grato di avervi conosciuto e di condividere con voi una parte importante della mia vita.

Vorrei ringraziare la mia famiglia di Padova: Ignazio, Ivan, Marialaura, Mary e Tony, grazie ai quali ho raggiunto l'obiettivo della laurea magistrale ma anche il futuro che ne è conseguito. Vi sarò sempre grato per quello che avete fatto per me.

Vorrei ringraziare i miei nuovi amici di Catania: Chiara, Davide, Daniele C., Daniele M., Federica A., Federica F., Giulia M., Marco, Martina, Seby S., per avermi dato una casa e avermi accolto nella grande famiglia di Controvento.

Vorrei ringraziare la mia famiglia: mio padre, mia madre, mia sorella e Lupetta per avermi supportato sia nelle notti più buie che nelle giornate più splendenti. Vi ringrazio per avermi dato fiducia e la libertà di scelta. Vi ringrazio anche per avermi mostrato la Musica, che rimarrà sempre un porto sicuro sia nelle gioie che nel dolore della vita. Infine, vi ringrazio per avermi insegnato la più grande delle risorse che oggi mi ritrovo: la volontà di rialzarmi e di superare i miei limiti.

Infine, vorrei ringraziare Angelica, per tutto quello che fa per me, nonostante tutto. Grazie per essere la mia migliore amica, la mia più grande forza e la mia più grande risorsa. Migliorerò e crescerò con te e per te, sempre.

Per concludere, un pensiero particolare va a chiunque che come me, avrà fallito più volte nella vita per poi rialzarsi con un pizzico di consapevolezza in più. A te, consiglio di continuare a rialzarti e di sorridere, perché i fallimenti sono i più grandi insegnamenti della vita. Non esiste vittoria più grande.